

UC San Diego

UC San Diego Electronic Theses and Dissertations

Title

Thermal degradation of the performance of elastomeric bearings for seismic isolation

Permalink

<https://escholarship.org/uc/item/6j3486gj>

Author

Shirazi, Ali

Publication Date

2010

Peer reviewed|Thesis/dissertation

UNIVERSITY OF CALIFORNIA, SAN DIEGO

**Thermal Degradation of the Performance of Elastomeric Bearings for
Seismic Isolation**

A dissertation submitted in partial satisfaction of the
requirements for the degree
Doctor of Philosophy

in

Structural Engineering

by

Ali Shirazi

Committee in Charge:

Chia-Ming Uang, Chair
Gianmario Benzoni
Steve Cande
Francesco Lanza di Scalea
Vlado Lubarda
Benson Shing

2010

The Dissertation of Ali Shirazi is approved, and it is acceptable in quality and form for publication on microfilm and electronically:

Chair

University of California, San Diego

2010

Table of Contents

SIGNATURE PAGE	iii
TABLE OF CONTENTS	iv
LIST OF FIGURES	vii
LIST OF TABLES	xiv
VITA	xvi
ABSTRACT OF THE DISSERTATION	xvii

1 SEISMIC ISOLATION AND SEISMIC RESPONSE MODIFICATION DEVICES, AN INTRODUCTION	1
---	----------

1.1 Seismic Isolation, Principle and Primary Objective	1
1.2 Seismic Response Modification Devices	6
1.3 History and Application	7
1.4 Problem Statement	10
1.5 The State of Art	11
1.6 Goal of This Research	13
1.7 Outline	14
1.7.1 Step-1, Test of Full Scale Devices.....	16
1.7.2 Step-2, Thermal Behavior of Laminated Rubber Bearing	17
1.7.3 Step-3, Assessment of Tensile Strength of Lead.....	19

2 TYPES OF SEISMIC RESPONSE MODIFICATION DEVICES	20
---	-----------

2.1 Elastomeric Bearings	22
2.1.1 Laminated Rubber Bearings	22
2.1.2 Lead Core Rubber Bearings (LRB)	28
2.2 Sliding Bearings	32
2.2.1 Friction Pendulum	32
2.3 Hybrid Bearings	35
2.4 Yielding Bearings	36
2.5 Viscous Dampers (VDs)	37

3 MATERIALS USED IN MANUFACTURING ELASTOMERIC BEARINGS	44
---	-----------

3.1 Introduction to Polymers	44
3.1.1 Thermoplastic Polymers	45
3.1.2 Thermoset Polymers	48
3.1.3 Elastomeric Polymers.....	49
3.1.4 Strain-Stress Curves of Common Polymers	52

3.2 Rubber	53
3.2.1 Rubber Compounding Ingredients	55
3.2.2 Mechanical Characteristic of Rubbers	62
3.2.3 High and Low Damping Rubbers	68
3.3 Lead	70
3.3.1 Damping Mechanism of Lead	71
3.3.2 Mechanical Properties of Lead	72
3.4 Steel	74
 4 DETERIORATION OF ELASTOMERIC BEARINGS FROM MATERIAL POINT OF VIEW	 79
4.1 Deterioration of Rubber.....	80
4.1.1 Hardening of Rubber and the Effect of Temperature	81
4.1.2 Cracking and Debond	83
4.1.3 Fatigue of Rubber	85
4.1.4 Scragging	86
4.2 Deterioration of Lead	88
4.2.1 Oxidation of Lead	88
4.2.2 Fatigue of Lead	89
4.2.3 Distortion of Lead Plug	90
4.3 Degradation of Steel	92
4.3.1 Corrosion	92
4.4 Highlight of the Chapter.....	93
 5 DEGRADATION PHENOMENON IN ELASTOMERIC BEARINGS AND THE CONTRIBUTING FACTORS	 96
5.1 Property Deterioration and Connection with Heat.....	97
5.2 Experiment-1	100
5.2.1 Specification of Test Bearings	102
5.2.2 Test Set Up	109
5.2.3 Test Protocols and Results	110
5.2.4 Observations and Remarks	117
5.2.5 Empirical Model for EDC in Terms of Input Characteristics	137
5.2.6 Highlights of Experiment-1	142
 6 THERMAL BEHAVIOR AND MODELING	 145
6.1 Study of the Thermal Behavior of Elastomeric Bearings	149
6.2 Experiment-2.....	151

6.2.1	Instrumentation of the Test Bearing	151
6.2.2	Test Procedure and Result	155
6.2.3	Analysis and Conclusions.....	158
6.2.4	Highlights of Experiment-2	167
6.3	Mechanical Properties of Laminated Rubber.....	168
6.4	Finite Element Modeling	186
6.5	Steady State Heat Transfer.....	190
6.5.1	Qualitative Observation	192
6.5.2	Quantitative Assessments and Conclusions	200
6.6	Validation of F.E.M. Using Theoretical Approach.....	205
6.6.1	Results of Direct and Indirect FEM	206
6.6.2	Observations and Results.....	207
6.7	Phase-1, Steady State Heat Transfer Model.....	213
6.8	Phase-2, Transient Heat Transfer Analysis	215
6.9	Phase-3, Stress Analysis (Post-yield behavior of Lead)	218
6.9.1	Complexity of the Phenomenon	219
6.9.2	Defining Engineering Properties of Constituent Materials	221
6.10	Highlight of the Chapter.....	229
7	ASSESSMENT OF THERMAL DETERIORATION OF LEAD PLUGS	231
7.1	Relation between Temperature and Tensile Strength of Lead	233
7.2	Proposed Model	235
7.3	Implementation of the Proposed Model	236
7.3.1	Reproduction of Tests Performed on Robinson Bearing	236
7.3.2	Estimation of per Cycle Degradation.....	246
7.4	Conclusion and Remarks	255
8	SUMMARY, CONCLUSION AND SUGGESTION FOR FUTURE STUDIES .	256
8.1	Summary and Conclusion	256
8.2	Suggestion for Future Studies.....	259
APPENDICES		260
REFERENCES.....		312

List of Figures

FIGURE 1-1: SCHEMATIC OF COMPARISON OF DEFORMATION OF A FIXED-BASE AND A BASE ISOLATED STRUCTURE.....	2
FIGURE 1-2: APPLICATION OF BASE ISOLATION ON BRIDGES	3
FIGURE 1-3: DYNAMIC RESPONSE OF A STRUCTURE FOR DIFFERENT VALUES OF DAMPING RATIO	5
FIGURE 1-4: APPLICATION OF SEISMIC ISOLATION IN DIFFERENT TYPES OF STRUCTURES. HOSPITALS, FIRE DEPARTMENTS, POWER STATIONS AND BRIDGES ARE THE TYPES OF STRUCTURES WHICH ARE CRITICAL TO REMAIN OPERATIONAL DURING AND AFTER SEISMIC EVENTS	9
FIGURE 1-5: OUTLINE OF THE PROGRAM PRESENTED IN THIS RESEARCH FOR DEGRADATION ANALYSIS OF ELASTOMERIC BEARINGS	15
FIGURE 1-6: OBJECTIVES PURSUED IN STEP-1	17
FIGURE 1-7: OBJECTIVES PURSUED IN STEP-2	18
FIGURE 2-1: DIFFERENT TYPES OF SEISMIC RESPONSE MODIFICATION DEVICES	21
FIGURE 2-2: SECTION VIEW OF A TYPICAL LAMINATED RUBBER BEARING	23
FIGURE 2-3: EFFECTIVE CROSS SECTION THAT RESISTS COMPRESSIVE STRESS.....	24
FIGURE 2-4: SECTIONAL VIEW OF A LEAD CORE RUBBER BEARING	29
FIGURE 2-5: AN IDEALIZED FORCE-DISPLACEMENT LOOP OF AND ISOLATION BEARING ...	30
FIGURE 2-6: GENERAL COMPONENTS OF A FRICTION PENDULUM. NOT SHOWN IN THE IMAGE IS A SEALING SYSTEM THAT REST BETWEEN THE TWO CIRCULAR EDGES WHEN THE BEARING IS ASSEMBLED, THIS HELPS IN PREVENTING DIRT AND DEBRIS FROM GETTING INTO THE SLIDING ZONE	34
FIGURE 2-7: A FRICTION PENDULUM DAMPER SYSTEM INSTALLED ON SEAHAWKS STADIUM. IT DECOUPLES THE ROOF WHICH ATTAINS THE HIGHEST ACCELERATION AT A SEISMIC EVENT FROM THE REST OF THE STRUCTURE. SOURCE: HTTP://WWW.DJC.COM/NEWS/CO/11134804.HTML	34
FIGURE 2-8: SCHEMATIC OF HYSTERESIS LOOP OF A SINGLE CONCAVE FRICTION PENDULUM BEARING	35
FIGURE 2-9: A COMMON TYPE OF HYBRID BEARING CONSISTING OF A LAMINATED RUBBER BEARING AND A SLIDING BEARING	36
FIGURE 2-10: HYSTERETIC LOOP OF A HYBRID BEARING COMPRISED OF ELASTOMER AND SLIDING SURFACE	36
FIGURE 2-11: FLEXURAL YIELDING BEARINGS	37
FIGURE 2-12: IDEALIZED (PERFECTLY BILINEAR) HYSTERESIS LOOP OF A YIELDING DEVICE	37
FIGURE 2-13: VISCOUS DAMPER TESTED AT THE CALTRANS SRMD TEST FACILITIES AT UCSD.....	38
FIGURE 2-14: A TYPICAL VISCOUS DAMPER.....	38
FIGURE 2-15: SECTION VIEW OF A TYPICAL VISCOUS DAMPER AND ITS MAJOR COMPONENTS	39
FIGURE 3-1: GENERAL CLASSIFICATION OF POLYMER FAMILY	45

FIGURE 3-2: SCHEMATIC OF FCC CRYSTALLINE STRUCTURE	47
FIGURE 3-3: SCHEMATIC OF CROSSLINKING PHENOMENON	51
FIGURE 3-4: STRAIN-STRESS BEHAVIOR OF DIFFERENT TYPES OF POLYMERS.....	52
FIGURE 3-5: CHEMICAL STRUCTURE OF NEOPRENE RUBBER.....	54
FIGURE 3-6: COMPARISON BETWEEN STRESS-STRAIN CURVES OF NATURAL AND THE CHEMICAL PROCESS OF VULCANIZED RUBBER	58
FIGURE 3-7: VULCANIZATION OF NATURAL RUBBER.....	58
FIGURE 3-8: DUROMETER TESTING METHOD	64
FIGURE 3-9: SCHEMATIC OF THE ASSEMBLY USED TO OBTAIN MODULUS OF SHEAR FOR ELASTOMERIC MATERIALS. A SHEAR STRAIN OF 50% IS SUSTAINED WHILE MODULUS OF SHEAR IS CALCULATED (NCHRP 449)	67
FIGURE 3-10: SPRING-DASHPOT EXAMPLE REPRESENTING DIFFERENCE BETWEEN HIGH AND LOW DAMPING RUBBER.....	69
FIGURE 3-11: USING STEEL SHIMS LAMINATED WITH RUBBER IMPROVES STABILITY OF ELASTOMERIC BEARINGS SIGNIFICANTLY	75
FIGURE 4-1: FORMATION OF COVALENT BOND THROUGH OUT VULCANIZATION PROCESS	81
FIGURE 4-2: CHANGE IN ENGINEERING PROPERTIES OF RUBBER AS CROSS LINK DENSITY INCREASES	82
FIGURE 4-3: VARIATION OF MODULUS OF ELASTICITY AND DAMPING RATIO OF RUBBER SAMPLES WHEN EXPOSED TO VARIOUS DEGREES OF TEMPERATURE [10]	83
FIGURE 4-4: RUBBER AT VICINITY OF STEEL SHIMS IS EXPOSED TO HIGHER TEMPERATURE I.E. HARDENING HAPPENS AT HIGHER RATE	84
FIGURE 4-5: HIGH RATE OF VULCANIZATION MAKES RUBBER LOSE ITS ELASTICITY AND BECOME MORE VULNERABLE TO CRACKING AND DEBONDING AT THE AREAS AROUND STEEL SHIMS	84
FIGURE 4-6: HIGH RATE OF VULCANIZATION MAKE RUBBER LOSE ITS ELASTICITY AND MORE VULNERABLE TO CRACKING AND DEBONDING. THIS PHENOMENON EVENTUALLY RESULTS IN COMPLETE FAILURE OF THE BEARING. SOURCE: YOSHITO ITOH, DEPT OF CIVIL ENG., NAGOYA UNIVERSITY, JAPAN [1].....	85
FIGURE 4-7: VARIATION OF NORMALIZED STIFFNESS AS A FUNCTION OF NUMBER OF CYCLES LOAD APPLIED TO A RUBBER SAMPLE AT VELOCITY OF 5MM/SEC AND 50% SHEAR STRAIN	86
FIGURE 4-8: HYSTERESIS LOOPS SHOWING SCRAPING EFFECT AT LOW FREQUENCY CYCLIC LOAD.....	87
FIGURE 4-9: HYSTERESIS LOOPS SHOWING SCRAPING EFFECT AT HIGH FREQUENCY CYCLIC LOAD.....	87
FIGURE 4-10: ANALYTICAL SPRING MODEL OF ELASTOMERIC BEARING SUGGESTED BY KELLY AND KOH	91
FIGURE 4-11: FAILURE OF A BEARING DUE TO SHEAR FAILURE ALONG THE AXIS. (SOURCE: REPORT NO. 289, S.M BUILT, DEPT. OF CIVIL ENGINEERING, UNIVERSITY OF AUCKLAND, NEW ZEALAND)	91

FIGURE 4-12: FORMATION OF CORROSION SYSTEM IN SALINE ENVIRONMENT	93
FIGURE 5-1: LOADING AND ENVIRONMENTAL CONDITIONS CREATE TRANSIENT AND STEADY STATE MOTION TO IN-SERVICE ELASTOMERIC BEARINGS	97
FIGURE 5-2: COMPLETE FLOW DIAGRAM OF STEPS TAKEN FOR DEGRADATION ANALYSIS.	99
FIGURE 5-3: HARMONIC SINUSOIDAL WAS THE TYPE EXCITATION APPLIED TO ALL OF THE BEARINGS THROUGH THE EXPERIMENT-1	101
FIGURE 5-4: SCHEMATIC OF TESTING SET UP	102
FIGURE 5-5: DRAWING OF SECTION VIEW OF LRB700	103
FIGURE 5-6: DRAWING OF SECTION VIEW OF LRB1300	105
FIGURE 5-7: DRAWING OF SECTION VIEW OF NRB1300	106
FIGURE 5-8: DRAWING OF SECTION VIEW OF THE ROBINSON BEARING	108
FIGURE 5-9: DISPLACEMENT TRANSDUCER CONFIGURATION	110
FIGURE 5-10: CHARACTERISTIC OF A HYSTERESIS LOOP USED FOR ANALYSIS	112
FIGURE 5-11: PLOT OF DISPLACEMENT VERSUS TIME OF THE LOAD PROTOCOL APPLIED TO NRB1300, LRB1300 AND LRB700.....	113
FIGURE 5-12: ENERGY DISSIPATED PER CYCLE FOR LRB1300.....	119
FIGURE 5-13: ENERGY DISSIPATED PER CYCLE FOR LRB700.....	120
FIGURE 5-14: ENERGY DISSIPATED PER CYCLE AS A FUNCTION OF TIME FOR THE ROBINSON BEARING	123
FIGURE 5-15: MAXIMUM FORCE MEASURED AT EACH HYSTERETIC LOOP WAS PLOTTED AGAINST THE ELAPSED TIME.....	124
FIGURE 5-16: SUPERIMPOSED PLOTS OF MAXIMUM FORCE PER CYCLE FOR LRB1300 AND NRB1300	127
FIGURE 5-17: SUPERIMPOSED PLOTS OF AVERAGE STIFFNESS PER CYCLE FOR LRB1300 AND NRB1300.....	128
FIGURE 5-18: SUPERIMPOSED PLOTS OF ENERGY DISSIPATED PER CYCLE FOR LRB1300 AND NRB1300.....	130
FIGURE 5-19: SCHEMATIC OF THE PLANAR SECTION VIEW OF A CYLINDRICAL BEARING ILLUSTRATING THE CONCLUSION WHICH WAS DRAWN ABOUT ORIGATION AND PATH OF DISTRIBUTION OF THERMAL ENERGY	131
FIGURE 5-20: SHEAR STRESS APPLIED TO EACH COMPONENT WAS CALCULATED AND PLOTTED VERSUS SHEAR STRAIN.....	132
FIGURE 5-21: RESTORING STIFFNESS VERSUS SHEAR STRAIN FOR LRB1300 AS AN ASSEMBLY AND ITS COMPONENTS INDIVIDUALLY. RUBBER EXHIBITED CONSTANT STIFFNESS WITHIN THE ENTIRE RANGE OF SHEAR STRAIN	133
FIGURE 5-22: LOOP 33 OF NRB1300, A DISPLACEMENT OF 400 MM WAS IMPOSED ..	135
FIGURE 5-23: LOOP 33 OF LRB1300, A DISPLACEMENT OF 400 MM WAS IMPOSED ...	136
FIGURE 5-24: SUPERIMPOSED PLOTS OF ALL 50 HYSTERETIC LOOPS OF NRB-1300 PERFORMED DURING EXPERIMENT-1	136
FIGURE 5-25: THE PROPOSED EMPIRICAL EQUATION FOR HEAT-FLUX OF THE ROBINSON BEARING. THE DATA FITTED IN A POWER FUNCTION	140

FIGURE 5-26: SUPERIMPOSED PLOTS OF HEAT-FLUX VERSUS PRODUCT OF SHEAR STRAIN RATE AND TOTAL TRAVELED DISTANCE FOR LRB1300 AND LRB700.....	141
FIGURE 5-27: ILLUSTRATION CHART OF INTERACTIONS BETWEEN THE VARIABLE INVOLVED IN PROPERTY DEGRADATION OF ELASTOMERIC BEARING WITH LEAD CORE	143
FIGURE 6-1: FLOW DIAGRAM OF STEPS TAKEN IN PRESENT CHAPTER IS HIGHLIGHTED IN RED	148
FIGURE 6-2: THERMOCOUPLE RODS USED IN AN ATTEMPT FOR MEASURING INTERNAL TEMPERATURE OF A BEARING	150
FIGURE 6-3: THERMOCOUPLES WERE INSERTED AT CERTAIN LOCATIONS INTO BODY OF LRB700. THE EXPERIMENT FAILED DUE TO FAILURE OF THE THERMOCOUPLES TO STAY IN PLACE.....	150
FIGURE 6-4: SCHEMATIC OF THE TEST BEARING USED IN EXPERIMENT-2.....	152
FIGURE 6-5: HEATING ELEMENT AND ITS SHIELD	152
FIGURE 6-6: THE INSTRUMENTATION OF THE TEST BEARING USED FOR EXPERIMENT-2	153
FIGURE 6-7: LOCATION OF THE THERMOCOUPLES AT THE MID-HEIGHT STEEL PLATE	154
FIGURE 6-8: TOP VIEW OF THE BEARING SHOWS LOCATIONS OF THE THERMOCOUPLES WITH RESPECT TO THE NORTH WALL OF THE BEARING.....	154
FIGURE 6-9: TEMPERATURE PROFILE ACROSS THE BEARING SHOWS NONLINEAR TREND ACROSS THE BODY OF THE BEARING, AMBIENT TEMPERATURE WAS 17.59°C	159
FIGURE 6-10: TEMPERATURE AT EACH THERMOCOUPLE, PLOTTED VERSUS VARIATION OF AMBIENT TEMPERATURE AT CONSTANT HEAT FLUX OF 65500 W/M ²	162
FIGURE 6-11: LINEAR RELATION WAS OBSERVED BETWEEN INPUT HEAT-FLUX AND THE INTERNAL TEMPERATURE OF THE BEARING WHEN AMBIENT TEMPERATURE REMAINED CONSTANT	165
FIGURE 6-12: PLOT OF TEMPERATURE AT THE CLOSEST THERMOCOUPLE TO THE CORE AS A FUNCTION OF AMBIENT TEMPERATURE AND INPUT HEAT-FLUX.....	167
FIGURE 6-13: SCHEMATIC OF THERMAL INTERACTION BETWEEN THE CONSTITUENTS IN A TYPICAL ELASTOMERIC BEARING WITH LEAD	170
FIGURE 6-14: A UNIT CELL OF DIMENSION $L \times D \times h$ IS SELECTED BY CONSIDERING A SINGLE STEEL SHIM SANDWICHED IN BETWEEN THE HALF THE HEIGHT OF EACH OF THE UPPER AND LOWER RUBBER LAYERS	171
FIGURE 6-15: CONFIGURATION OF THE UNIT CELL USED FOR DERIVING OF COEFFICIENT OF THERMAL CONDUCTIVITY IN LONGITUDINAL DIRECTION	172
FIGURE 6-16: CONFIGURATION OF THE UNIT CELL USED FOR DERIVING OF COEFFICIENT OF THERMAL CONDUCTIVITY IN TRANSVERSE DIRECTION	174
FIGURE 6-17: THE UNIT CELL USED FOR DERIVING EQUIVALENT MODULUS OF ELASTICITY IN LONGITUDINAL DIRECTION FOR LAMINATED RUBBER-STEEL	177
FIGURE 6-18: THE LAMINATED UNIT CELL USED FOR DERIVING MODULUS OF ELASTICITY IN TRANSVERSE DIRECTION FOR RUBBER-STEEL	179
FIGURE 6-19: THE LAMINATED UNIT CELL USED IN DERIVING EQUIVALENT SHEAR MODULUS OF LAMINATED RUBBER-STEEL	180
FIGURE 6-20: THE LAMINATED UNIT CELL DEFORMED IN SHEAR	181

FIGURE 6-21: A CUT FROM CORNER OF THE BEARING ALLOWED KNOWING THE ARRANGEMENT AND CONFIGURATION OF INTERNAL COMPONENTS.	187
FIGURE 6-22: A GENERIC SCHEMATIC OF HOW THE FINITE ELEMENT MODEL WAS ASSEMBLED	189
FIGURE 6-23: THE TYPES OF EXCITATIONS WHICH RESULT IN STEADY STATE AND TRANSIENT HEAT TRANSFERS ARE PRESENTED. THE TRANSIENT STAGE CHANGES DEPENDING ON HOW ABRUPTLY THE HEAT-FLUX IS APPLIED	191
FIGURE 6-24: AIR CIRCULATED AT MUCH HIGHER RATE IN VICINITY OF TOP END AND SIDE WALLS RELATIVE TO BOTTOM OF THE BEARING, NON-UNIFORM CONVECTION RESULTS UNEVEN HEAT DISTRIBUTION WITHIN BODY OF THE BEARING	192
FIGURE 6-25: FLOW OF HEAT WAVES IS BI-DIRECTIONAL AT THE UPPER END OF THE BEARING AND GRADUALLY BECOMES UNIDIRECTIONAL TOWARD ITS LOWER END, THIS IS DUE TO INEQUALITY OF AIR VOLUME PASSING OVER TOP AND BENEATH THE BEARING.....	194
FIGURE 6-26: TEMPERATURE MAP ACROSS SECTION A-A.....	196
FIGURE 6-27: THE OUTER RUBBER-LAYER THAT IS WRAPPED AROUND THE BEARING ACTS LIKE AN INSULATOR THAT PRESERVES THE THERMAL ENERGY WITHIN THE BEARING FOR A LONG TIME, THIS RESULTED IN RISING THE BEARING'S BODY TEMPERATURE	197
FIGURE 6-28: TOP AND BOTTOM VIEW OF THE BEARING SHOWS TEMPERATURE DIFFERENCE, IT IS DUE TO LIMITED AIR CIRCULATION BENEATH THE BEARING.....	199
FIGURE 6-29: RISE OF TEMPERATURE WITHIN 45 MINUTES AT EACH THERMOCOUPLE, NEAR 95 % OF THERMAL STEADY STATES IS ESTABLISHED WITHIN THE FIRST HOUR OF THE HEAT TRANSFER PROCESS	202
FIGURE 6-30: TEMPERATURE PROFILE ALONG PATH "A" OBTAINED FROM THE DIRECT F.E. MODEL AND EXPERIMENT-2. HEAT-FLUX = 16300 W/m^2 , AMBIENT TEMPERATURE = 17.59°C . THE DIFFERENCE AT HIGHEST WAS $\sim 8\%$	204
FIGURE 6-31: SECTION VIEWS OF THE FINITE ELEMENT MODELS SHOW SIMILAR PATTERN OF HEAT DISTRIBUTIONS. TOP: DIRECT MODELING. BOTTOM: MODELING BY MEANS OF EQUIVALENT SUBSTITUTE MATERIAL SUBSTITUTION.....	210
FIGURE 6-32: TEMPERATURE PROFILE ALONG PATH "A" FOR THE DIRECT AND INDIRECT F.E.M. TOGETHER WITH THE RESULTS OF EXPERIMENT-2, SUPERIMPOSED ON A SINGLE COORDINATE SYSTEM, AT 16300 W/m^2	212
FIGURE 6-33: RESULT FORM PARAMETRIC STUDY OF HEAT TRANSFER SUGGESTED A MODEL THAT ACCURATELY MATCHED THE EXPERIMENTAL RESULTS. THE MODEL CORRELATED THE TEMPERATURE AT EACH POINT TO THE AMBIENT TEMPERATURE AND INPUT HEAT- FLUX	215
FIGURE 6-34: THE STEPS FOLLOWED TO VALIDATE TRANSIENT HEAT TRANSFER MODEL	217
FIGURE 6-35: TRANSIENT HEAT TRANSFER MODEL WAS CALIBRATED AND EXAMINED BY APPLYING A HEAT-FLUX OVER CERTAIN LENGTH OF TIME (10 MINUTES)	218
FIGURE 6-36: SCHEMATIC OF CONFINING PRESSURE APPLIED BY RUBBER ON LEAD PLUG. THE PRESSURE IS HIGH ENOUGH TO DISTORT THE SECTION GEOMETRY OF THE PLUG	220
FIGURE 6-37: STRESS-STRAIN BEHAVIOR OF LEAD AND RUBBER OBTAINED BY SUBTRACTING EXPERIMENTAL DATA OF NRB1300 FROM LRB1300	223

FIGURE 6-38: VARIATION OF MAXIMUM TENSILE STRAINS AT UPPER AND LOWER PLASTIC HINGES OF THE LEAD PLUG	224
FIGURE 6-39: 3-D VISUALIZATION OF INTERNAL COMPONENTS SHOWS LOCATIONS WITH HIGH STRAINS AND DEFORMATION AT CRITICAL POINTS, (DEVICE: LRB1300)	226
FIGURE 6-40: AT THE MID-SECTION VIEW PRESENTED ON THIS FIGURE, STRAIN AT UPPER AND LOWER PLASTIC HINGES ARE SHOWN WHEN DISPLACEMENT OF 400MM WAS APPLIED TO LRB1300.....	227
FIGURE 6-41: QUALITATIVE ASSESSMENT PERFORMED ON MIDDLE SECTION IS SHOWN. STRAIN VECTORS ARE HIGHEST AT THE ENDS OF LEAD PLUG RELATIVE TO THE REST OF THE BEARING	228
FIGURE 6-42: PERMANENT DEGRADATION DUE TO SLIPPAGE OF THE LEAD PLUG IN ITS HOUSING	229
FIGURE 6-43: FAILURE OF A BEARING DUE TO SHEAR FAILURE ALONG THE AXIS. (SOURCE: REPORT NO. 289, S.M BUILT, DEPT. OF CIVIL ENGINEERING, UNIVERSITY OF AUCKLAND, NEW ZEALAND)	229
FIGURE 7-1: THE SECTIONS HIGHLIGHTED IN RED ARE THE STEPS TAKEN AT THE PRESENT CHAPTER.....	232
FIGURE 7-2: SECTION VIEW OF LRB1300 PROVIDED BY THE FINITE ELEMENT MODELING SHOWS THE LEAD PLUG EXPERIENCED HIGH TENSILE STRAIN AT LOCATIONS OF THE PLASTIC HINGES	233
FIGURE 7-3: ULTIMATE TENSILE STRENGTH OF LEAD AS A FUNCTION OF TIME AT TWO STRAINING RATES OF 0.25 SEC^{-1} AND 0.0075 SEC^{-1}	235
FIGURE 7-4: THE ROBINSON BEARING EXPERIENCED SIGNIFICANT PER-CYCLE DECREASE IN DISSIPATED ENERGY BUT ALSO RAPID LOSS RECOVERY	239
FIGURE 7-5: STRAIN CONTOUR ON ONE OF THE FOUR LEAD PLUGS SHOWS THE LOCATION WHERE THE MAGNITUDE OF STRAIN IS AT MAXIMUM.....	240
FIGURE 7-6: PLUGS EXPERIENCED DIFFERENT STRAIN AT LOCATION OF PLASTIC HINGES .	242
FIGURE 7-7: THERMOGRAPHY IMAGING PERFORMED ON THE ROBINSON BEARING. THE IMAGES FROM TOP LEFT TO BOTTOM RIGHT SHOW THE SURFACE TEMPERATURE AT 60 SECONDS INTERVALS AFTER THE TEST WAS PERFORMED	244
FIGURE 7-8: INFRARED THERMOGRAPHY CONFIRMED LEAD PLUG STRAINED SIGNIFICANTLY AT THE LOCATION OF PLASTIC HINGES. HOWEVER, STRAIN IS HIGHER AT THE LOWER PLASTIC HINGE.....	245
FIGURE 7-9: SCHEMATIC REPRESENTATION OF THERMAL TRANSIENT AND STEADY STATES	246
FIGURE 7-10: USING FEM, A TEMPERATURE INCREASE OF $\Delta T = 23^{\circ}\text{C}$ AT THE CORE OF THE ROBINSON BEARING WAS PREDICTED FOR THE FIRST HYSTERESIS LOOP	248
FIGURE 7-11: ELEVATION OF TEMPERATURE AT EXPERIMENT-1 PERFORMED ON THE ROBINSON BEARING REPRODUCED BY FEM	249
FIGURE 7-12: COMPARISON OF DEGRADATION PREDICTED BY ANALYSIS THAT OF	251
FIGURE 7-13: PER-CYCLE DEGRADATION OF EQUIVALENT DAMPING, OBTAINED BOTH ANALYTICALLY AND EXPERIMENTALLY	253

FIGURE 7-14: PREDICTION OF DEGRADATION EQUIVALENT DAMPING WITHIN 10 CYCLES	254
FIGURE 7-15: CONTINUOUS APPLICATION OF HIGH AMPLITUDE SHEAR AT HIGH RATE RESULTS IN LOCAL ACCUMULATION OF THERMAL ENERGY WHICH CAUSES LEAD TO MELT.....	254
FIGURE 8-1: PREDICTION OF RUBBER HARDENING BY OVER-VULCANIZATION USING ARRHENIUS EQUATION, [10]	256

List of Tables

TABLE 2-1: SUMMARY OF THE APPLICATION AND OPERATION MECHANISM.....	41
TABLE 2-2: OPERATION BASIS AND COMPONENTS USED IN COMMONLY EMPLOYED SRMDs	42
TABLE 2-3: HYSTERETIC LOOP OF SOME COMMON SRMDs	43
TABLE 3-1: A SUMMARY OF THE HIGHLIGHTED PROPERTIES OF POLYMERS	52
TABLE 3-2: COMPARISON OF SOME IMPORTANT PHYSICAL PROPERTIES OF DIFFERENT ELASTOMERS	55
TABLE 3-3: INGREDIENTS AND THEIR PERCENTAGE USED IN A TYPICAL RUBBER COMPOUND	56
TABLE 3-4: ENGINEERING PROPERTIES OF HARD, NORMAL AND SOFT RUBBER. THE MODULI ARE OBTAINED FROM CYLINDRICAL TEST SAMPLES WITH SHAPE FACTOR OF 0.5 LOADED TO 50% STRAIN AT RATE OF 0.5Hz.	70
TABLE 3-5: MATERIALS USED IN MANUFACTURING COMMON TYPES OF SEISMIC RESPONSE MODIFICATION DEVICES	78
TABLE 4-1: PROMINENT MATERIALS USED IN MANUFACTURING ELASTOMERIC BEARING AND POSSIBLE DEGRADATION MODES.....	94
TABLE 4-2: AVAILABLE MODELS USED FOR QUANTIFICATION OF PROPERTY LOSSES IN ELASTOMERIC BEARINGS	95
TABLE 5-1: SPECIFICATIONS OF THE TEST BEARING OF EXPERIMENT-1	109
TABLE 5-2: PROTOCOL AND THE RESULTS OF THE EXPERIMENT-1 , PERFORMED ON LRB1300	114
TABLE 5-3: PROTOCOL AND THE RESULTS OF THE TEST PERFORMED ON THE ROBINSON BEARING	116
TABLE 5-4: REARRANGEMENT OF DATA INTO TWO NEW SETS OF VARIABLES	139
TABLE 6-1: RESULT OF EXPERIMENT-2, TEMPERATURE READING AT EACH THERMOCOUPLE AFTER 45 MINUTES OF TIME WAS ELAPSED	157
TABLE 6-2: REARRANGEMENT OF RECORDED DATA, VARIATION OF TEMPERATURE WITH RESPECT TO VARIATION OF AMBIENT TEMPERATURE	161
TABLE 6-3: REARRANGEMENT OF DATA OF EXPERIMENT-2	164
TABLE 6-4: TEMPERATURE AT THERMOCOUPLE #9 PRESENTED IN MATRIX FORM.....	166
TABLE 6-5: EQUATIONS DERIVED FOR MECHANICAL CHARACTERISTICS OF LAMINATED RUBBER	186
TABLE 6-6: CALIBRATED MATERIAL PROPERTIES	188
TABLE 6-7: SIDE-BY-SIDE COMPARISON OF RESULT OBTAINED FORM EXPERIMENT-2 TO THAT OF THE FINITE ELEMENT ANALYSIS. COMPARISON WAS MADE ON 5 TESTS WHICH WERE PERFORMED AT VARIOUS INPUT HEAT-FLUX BUT CONSTANT AMBIENT TEMPERATURE OF 17.95 °C	200
TABLE 6-8: SIDE-BY-SIDE COMPARISON OF RESULTS OBTAINED FROM EXPERIMENT, DIRECT AND INDIRECT FINITE ELEMENT MODELING	208

TABLE 6-9: INDIVIDUAL STRESS-STRAIN BEHAVIOR OF LEAD AND RUBBER IS OBTAINED BY SUBTRACTING TEST-DATA OF NRB1300 FROM LRB1300.	222
TABLE 7-1: EXPERIMENTAL AND PREDICTED VALUES FOR EDC AND PARAMETERS USED THROUGH THE ANALYSIS.....	250

Vita

2005	Bachelor of Science, University of California, San Diego
2005-2007	Research Assistant, Department of Structural Engineering, University of California, San Diego
2007	Master of Science, University of California, San Diego
2007-2010	Research Assistant, Department of Structural Engineering, University of California, San Diego
2010	Doctor of Philosophy, University of California, San Diego

FIELD OF STUDY

Major Field: Structural Engineering, Seismic Response Modification
Devices
Dr. Gianmario Benzoni

Studies in Seismic Design of Concrete Frame Structures
Professors Engelkirk, Shing, Restrepo

Studies in Seismic Design of Steel Frame Structures
Professor Uang

Studies in Mechanical Engineering, Structural Health Monitoring
Using Infrared Thermography

ABSTRACT OF THE DISSERTATION

**Thermal Degradation of the Performance of Elastomeric Bearings for
Seismic Isolation**

by

Ali Shirazi

Doctor of Philosophy in Structural Engineering

University of San Diego, California, 2010

Professor Chia-Ming Uang, Chair

Concern about reliability of elastomeric bearings is increasing along with the rapid development in application of such devices. Studies on experimental and in-service bearings have revealed the occurrence of permanent and transient changes in engineering

properties of these devices. This property loss, however, varies in quality and magnitude, depending on service or environmental conditions at which bearings are employed.

Knowledge about the magnitude of the lost property and the rate of degradation is critical for the safe performance of the isolated structure. Availability of such measures helps avoid unnecessary cost and service interruptions of bridge structures by optimizing monitoring and maintenance activities. It is necessary to identify the service and environmental conditions contributing in such degradation phenomenon. A literature review does not indicate the availability of complete and comprehensive studies on this topic. The focus of this research study is to identify and quantify property loss of elastomeric bearings, particularly due to heat, when they are subjected to cyclic lateral load under different environmental conditions. This research also proposes a methodology for a precise and accurate prediction of the temperature profile within the body of an elastomeric bearing. This methodology can be incorporated with the existing numerical models to assess the adequacy of performance of such bearings through seismic events.

The reversible changes in characteristics of lead plugs, which take place mainly due to heat, were found to represent the main

sources of transient changes in characteristics of an elastomeric bearing. Elastomeric bearings are also subjected to irreversible degradations such as stiffening of bearings as a result of hardening of rubber as when they are exposed to high temperature. High temperature is the result of generation of heat through hysteresis action of lead plugs.

1

Seismic Isolation and Seismic Response

Modification Devices, an Introduction

The Seismic Response Modification Device refers to a large family of mechanical devices that can modify the dynamic characteristics of a structure in order to improve its response and energy dissipation properties during seismic events. In terms of functioning technique they are divided in two main categories. The first category includes devices that improve structural dynamic performance by adding supplementary stiffness and/or damping properties to help structure gain more stability and energy dissipation property. Viscous Fluid Dampers and Tuned Mass Devices are two well recognized devices of this category. The second category includes devices that modify structural response by enforcing discontinuity on the path through which seismic perturbation travels through the structure. These devices are particularly called “Seismic Isolation Devices”.

1.1 Seismic Isolation, Principle and Primary Objective

Seismic Isolation is the principle of design methodology in which a structure is “separated” from the source of excitation. The technique

takes the name of “Base Isolation” when implemented in buildings where the separation happens between the elevated structure and the foundation system, (Figure 1-1).

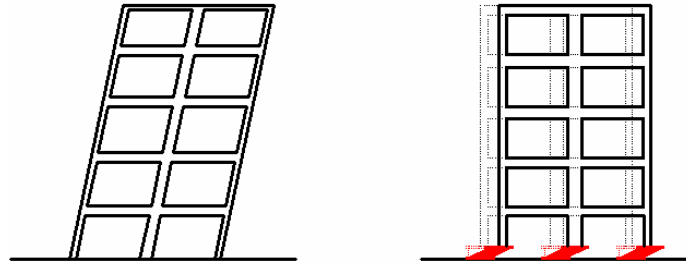


Figure 1-1: Schematic of comparison of deformation of a fixed-base and a base isolated structure

The decoupling has been also implemented in elevation and not only at the base in order to allow addition of several floors on top of an existing structure. In the case of bridges, isolation is most often applied by decompiling the superstructure from the bridge piers.

The technique is, in fact, particularly effective when the superstructure that attracts the majority of inertia forces during an earthquake event is separated by the weak components of the structure that are the bridge piers, Figure 1-2.

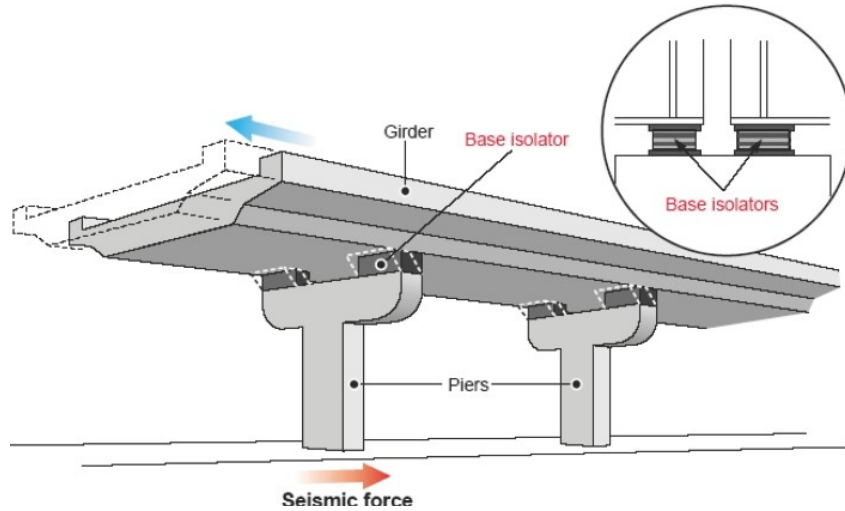


Figure 1-2: Application of base isolation on bridges

The introduction of isolation thus can be seen as the creation of an interface between the overall structure and the source of seismic excitation as well as between the components of the same structure. In both cases the primary objective of this approach is to shift the period of the entire structure to the regions of reduced amplification of seismic input. The isolation devices can also provide a significant contribution to dissipation of the seismic energy through their hysteretic performance. The principle of Seismic Isolation can be described through the equation of transmissibility, Equation 1-1.

$$T = \frac{X}{Y} = \frac{\sqrt{1 + \left(2\zeta \frac{\omega^2}{\omega_n}\right)^2}}{\sqrt{\left(1 - \left(\frac{\omega}{\omega_n}\right)^2\right)^2 + \left(2\zeta \frac{\omega^2}{\omega_n}\right)^2}} \quad \text{(Equation 1-1)}$$

where:

T = Amplification

X = Amplitude of total movement of the structure

Y = Amplitude of the ground motion

ω = Frequency of excitation

ω_n = Natural frequency of the structure

ζ = Damping ratio

When the period of the structural assembly is elongated by use of such devices, according to equation of transmissibility (Equation 1-1), less perturbation is transferred to the structure. As a result the spectral accelerations (pseudo-accelerations) of the isolated structure are significantly lower than that of an identical structure with fixed-base. Thus, the resultant forces acting on structural and nonstructural elements of the structure are significantly reduced compared to a conventional fixed-base structure, (Figure 1-3).

It must be noted that the technique implies that most of the non-linearity of the system are concentrated in limited components like the isolating devices, allowing the reduction in ductility demand of the structure when compared to a conventional fixed-base solution. Increased damping ratio is also often achieved, if needed, through usage of special energy dissipating elements such as high damping rubber or lead plugs in laminated rubber.

In Figure 1-3, the amplification factor $\frac{X}{Y}$ is plotted versus ratio of natural frequency to frequency of excitation, $\left(\frac{\omega}{\omega_n}\right)$.

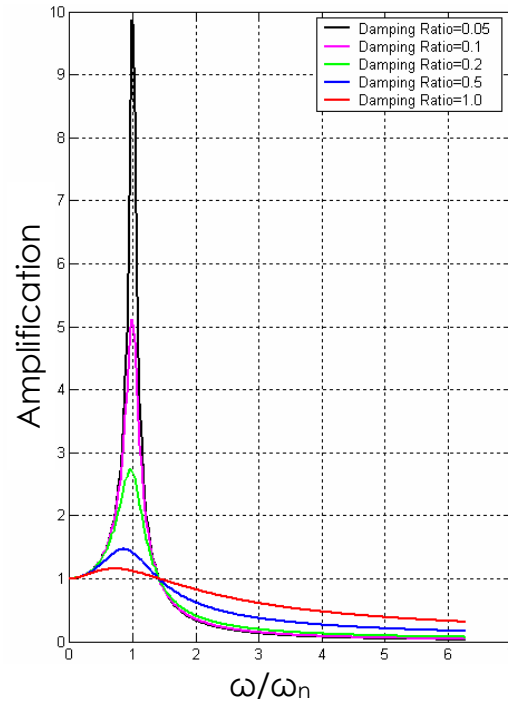


Figure 1-3: Dynamic response of a structure for different values of damping ratio

According to the equation of transmissibility, decrease in ω_n which causes increase in $\frac{\omega}{\omega_n}$ ratio, results in decrease $\left(\frac{X}{Y}\right)$ ratio, meaning higher attenuation is achieved. Thus, per equation of natural frequency, $\omega_n = \frac{2\pi}{T_n}$, a less stiff structure would have a longer period and takes advantage of higher attenuation.

1.2 Seismic Response Modification Devices

The design concept introduced by Seismic Isolation needs to refer to mechanical devices for practical implementation. Due to principles of the approach, these devices represent the most important (if not the only) resource for seismic protection of structure. The implication of excessive seismic capacity into the structure represents a contradiction to the isolation design approach, introducing excessive costs as well as possible degradation of seismic performance. That justifies the attention that designers dedicate to the quality and performance characteristics of these devices. The devices are often indicated as "Anti-Seismic" devices, Protection Devices, or more appropriately as "Seismic Response Modification Devices", (SRMD).

It must be noted that the classification does not take into account multifunctional aspects of some device performances. For instance, a common lead core rubber bearing device provides a discontinuity between the ground and the structure (isolation device), it can also serve as a source of significant energy dissipation by yielding of lead plugs during a motion (energy dissipater). A descriptive presentation of common SRMDs is included in Chapter 2 of this dissertation. The SRMDs are devices introduced to endure harsh environmental and service conditions, and virtually not expected to be

replaced due to their nature (design and materials). They are also typically subjected to limited maintenance services. The inspections of their general conditions and the assessment of their general performance variation is, however, becoming an important aspect to guarantee their full potential availability at the moment of a seismic event. This activity needs to be integrated with an accurate knowledge of the parameters potentially responsible for material degradation and with validated models of the impact of these changes to the device performance.

1.3 History and Application

The fundamental concept of Seismic Isolation is certainly not new. The temple of Diana in Ephesus (550 B.C.) was separated from the soil by a layer of coal and wool fleeces. However, it wasn't until the development and use of elastomeric bearings in New Zealand in the mid 1970s that the Seismic Isolation became a valuable design and construction alternative. Seismic Isolation has been widely used in existing and new buildings as well as on bridges and industrial structures. It is largely applied in Europe and Asia as well as in United States. In the United States, this technology is, however, implementation in smaller scale than, for instance, in Japan. Isolated structures are essentially historical structures like the Salt Lake City and County

buildings, the Utah State Capitol, the Oakland, San Francisco and Pasadena City Halls etc. Other buildings equipped with anti-seismic devices are essential facilities, structures that are extremely crucial to remain fully operational during and after an earthquake event. Examples of these installations are the Emergency Communication Center in San Francisco, Caltrans Traffic Center in San Diego and others. The limited application of isolation principles to new residential buildings is by many authors attributed to the existing building codes that heavily penalize the use of isolation, making the technique less cost effective than traditional fixed base structures.

The application of Seismic Isolation and energy dissipation to bridge structures in the U.S is instead very adequate both for retrofit of existing bridges as well as for new constructions. Application of Seismic Isolation in different types of structures, such as hospitals, power stations, fire departments, supercomputer buildings etc. is shown in Figure 1-4.



Figure 1-4: Application of Seismic Isolation in different types of structures. Hospitals, fire departments, power stations and bridges are the types of structures which are critical to remain operational during and after seismic events

In Japan immediately after the 1995 Haushin-Awaji earthquake, due to excellent performance of isolated buildings during the event, a significant increase in the confidence level about the performances of devices used for implementation of this technique was provided by the construction of the Caltrans SRMD Testing Facility of UCSD. The facility in fact is specially designed to perform tasks on full scale devices and allowed the California Department of Transportation to implement with confidence the Seismic Isolation approach on complex existing bridge structures such as the San Francisco-Oakland bay bridge, Coronado, Vincent Thomas, Benicia-Martinez. New Caltrans bridge project also includes the use of Seismic Isolation principles.

1.4 Problem Statement

In specialized seminars and conferences on the field of Seismic Isolation [31] engineers and researchers agreed on the critical need for the development of an understanding of the reliability and durability of SRMDs in service. Large experimental programs of prototype and proof tests of devices indicated the general quality of products presently installed in applications around the world. It is a common option that used products meet now a high level of quality and functionality that will appear evident in case of seismic event. This scale of investment, however, needs to be protected providing the reasonable level of monitoring and maintenance of the quality baseline of these critical components. It is well known for instance, the prohibitive cost associated with the replacement of damaged devices from a bridge structure, due to the need of interruption or limit the bridge operation. While standard testing programs are paramount for the performance characterization phase of device as well as for quality control, they are, however, not oriented to collect information about the possible response variation due to changing material conditions (time-dependent) and material degradation in service conditions among the different types of SRMDs. The attention is allocated to the largely most common device, the elastomeric bearings which are presented in

detail, in Chapter 2. On bridge applications their lives in service is now extended long enough to raise questions about their deviation of properties compared to the pristine conditions at the time installation. For instance, the California Department of Transportation initiated a research study for a comprehensive verification of the performance characteristics of the devices installed on their bridges finalized to the application of a plan for maintenance.

The definition of factors, contributing in the degradation process of the materials used for in service elastomeric SRMDs, is required in order to initiate a systematic reliability analysis of the performance of these devices. A literature review does not indicate the availability of complete and comprehensive studies on this topic. This is partially due to lack of sufficient experimental data in this area for drawing firm conclusions.

1.5 The State of Art

In many of existing investigations, conclusions are supported by the data obtained from tests performed on scaled-down bearing models [1],[3]. The interactions between elements of a real-size bearing can rarely be represented with sufficient accuracy by a scaled bearing model. For instance, the thickness of the steel shims of common full size bearings is in the order of 2 mm. Manufacturing a scaled-down replica

of such a thin member is a challenge which is likely associated with scaling error.

Heat is known to be the key factor in property loss of bearings, affecting components made by both rubber and lead. Prediction of thermal-degradation of rubber, which occurs over life span of a bearing, requires relatively precise estimation of temperature to which the internal parts of a bearing are exposed. In a test sample, ultimate temperature at thermal steady state condition and the time required for a bearing to reach this state is highly depended on volume of the bearing. Hence, a thermal phenomenon predicted on scaled-down samples can not be sufficiently accurate for a study of their related degradation effects. Studies are available in literature review about the aging of rubber due to thermal effect [14],[15],[16],[17]. Most of the available resources are, however, generated by experimental activities bases on acceleration aging of rubber in oven [17].

Rubber and lead, the primary constituents of elastomeric bearing, both exhibit properties which vary with variation of rate and amplitude of cyclic load. Hence, a complete set of experimental data is required in the case of modeling lead and rubber for dynamic analysis. In order to take the shape and size factors into account the

data must also be obtained from experiments performed on actual real-sized bearings.

This accelerated aging is then correlated to an equivalent real-time aging using Arrhenius equation [10],[15],[17]. Thermal exposure in oven is uniform where as, in a real bearing heat is generated in lead plugs by hysteretic action, and distributed in an elliptical fashion through the body of the bearing. For this reason, a temperature gradient exists across the bearing which can cause the occurrence of a non-uniform degradation phenomenon.

1.6 Goal of This Research

The goal of this research is to propose a series of experimentally supported methodologies to predict the transient and permanent degradations of lead core elastomeric bearing. Three requirements were identified for a comprehensive thermal degradation analysis. The proposed model has to be capable of precisely predicting the energy dissipated per cycle (EDC) under certain loading and environmental conditions. The predicted EDC must be used to assess the temperature to which the lead plug of a bearing is exposed, at both “Steady State” and “Transient State” thermal conditions. The analytically obtained temperature should finally be used toward assessment of transient

property loss of the lead plug as well as of the rate of vulcanization of rubber which results in irreversible hardening of rubber.

1.7 Outline

This research was conducted in 4 main steps. The ultimate goal of Step-1 was to verify the occurrence of degradation as well as to find a relation between the input load characteristics and energy dissipated per hysteretic loop. At Step-2, the knowledge conveyed from Step-1 is used to estimate temperature at any point of a test bearing at transient and steady state conditions. In Step-3, knowing the temperature at the core of a bearing, the property loss of the lead plug is estimated. The importation of all three preceding steps will together as model that interpret the results in scale by which the degradation of the bearing assembly is measured. In Figure 1-5, the major steps are outlined and the detail of each step is discussed in the following three sections.

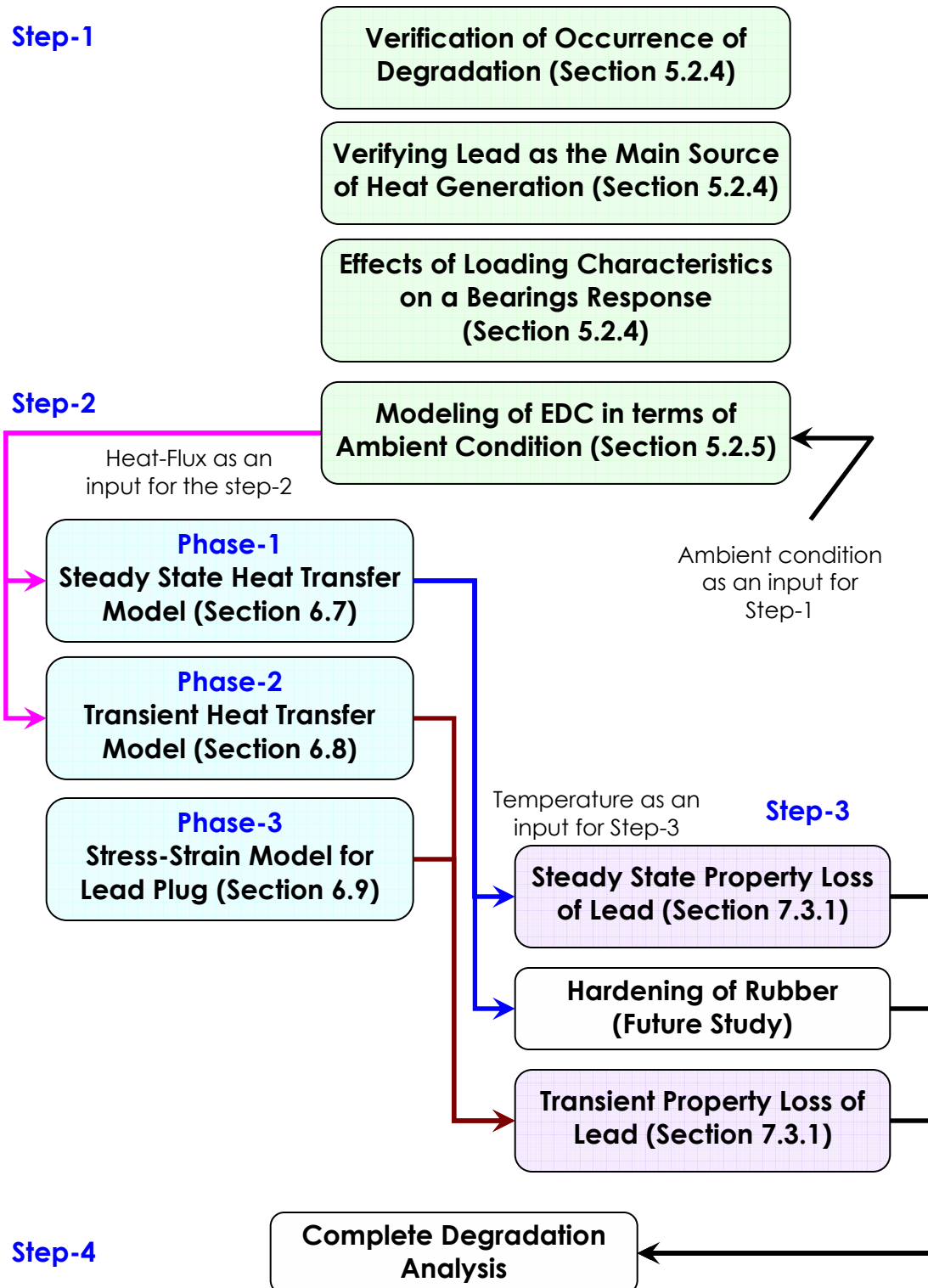


Figure 1-5: Outline of the program presented in this research for degradation analysis of elastomeric bearings

1.7.1 Step-1, Test of Full Scale Devices

The phase indicating in Figure 1-5 included full scale testing of four different type elastomeric bearings to study and verify the occurrence of property degradation due to cyclic loading, (Figure 1-6, S 1-1). In particular, the variation of essential response parameters like the energy dissipated per cycle, the horizontal stiffness as well as the peak horizontal force was monitored. The second outcome of the experimental analysis was the separation of responses, (Figure 1-6, S 1-2). The results, obtained from experiment, were the responses of the bearings as assemblies, however, for the purpose a finite element modeling, it was necessary to define the engineering properties of constituent materials individually. This task was performed by subtracting the responses of two identical bearings of which only one had lead plug.

The third focus of Step-1 was the identification of the performance characteristics of the device mostly affected by the loading conditions. In particular the effects of applied axial load, displacement amplitude and loading frequency were investigated, (Figure 1-6, S 1-3).

Finally the experimental results were analyzed in order to obtain a relationship between EDC and loading variables, such as displacement amplitude and frequency of loading (Figure 1-6, S 1-4).

Heat-flux, (HF), as the output of this step was used as the input for thermal analysis models (Step-3).

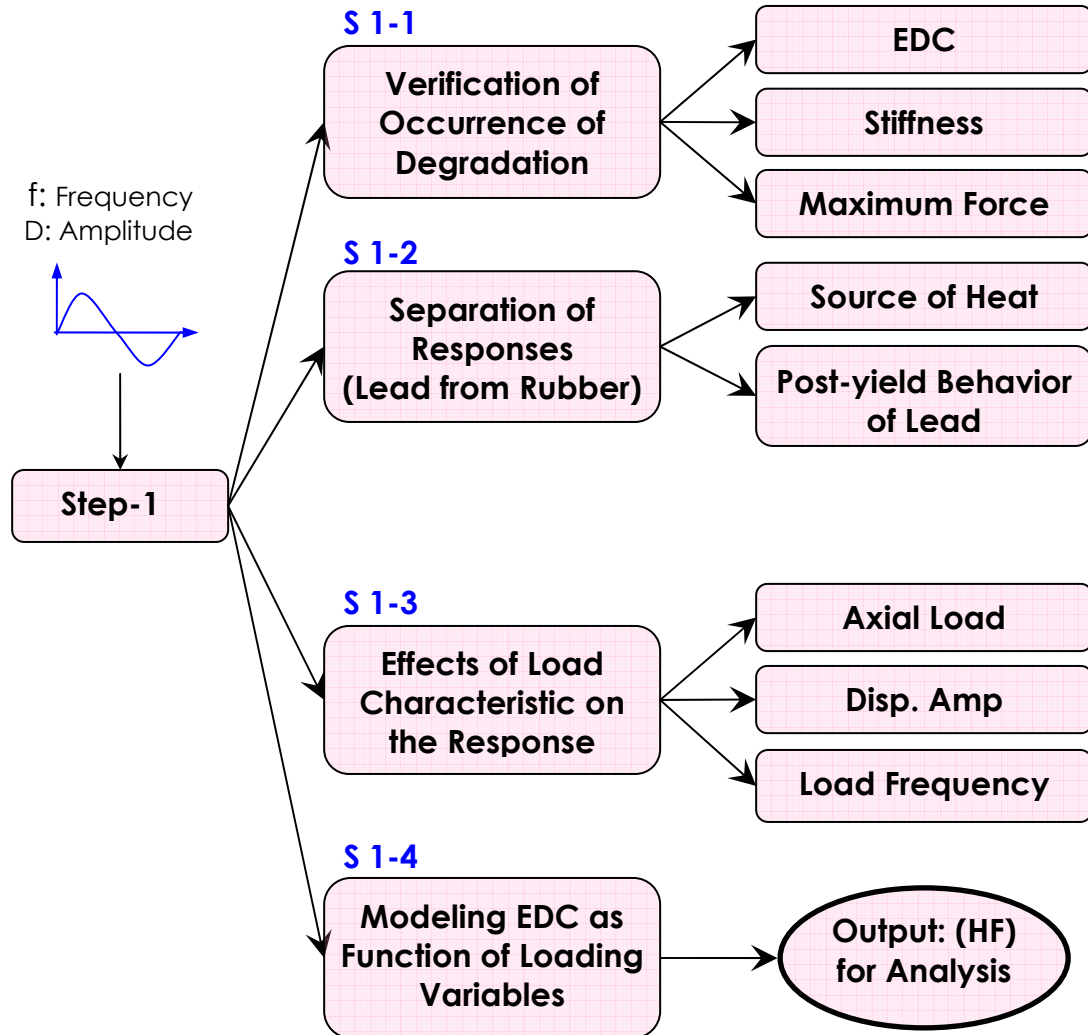


Figure 1-6: Objectives pursued in Step-1

1.7.2 Step-2, Thermal Behavior of Laminated Rubber Bearing

An initial attempt to instrument a test bearing with thermocouples installed on it was unsuccessful due to failure of thermocouples to stay in place during cyclic loading of the device. It was decided that the

study of thermal behavior had to be done in absence of dynamic actions and to obtain necessary information from a real size bearing under controlled laboratory conditions. As a result, the thermal stimulation had to be done in absence of dynamic actions. For this reason, on Experiment-2 a series of stationary thermal tests was performed on a real size bearing which was heated through its aluminum core by means of an electrical heating element.

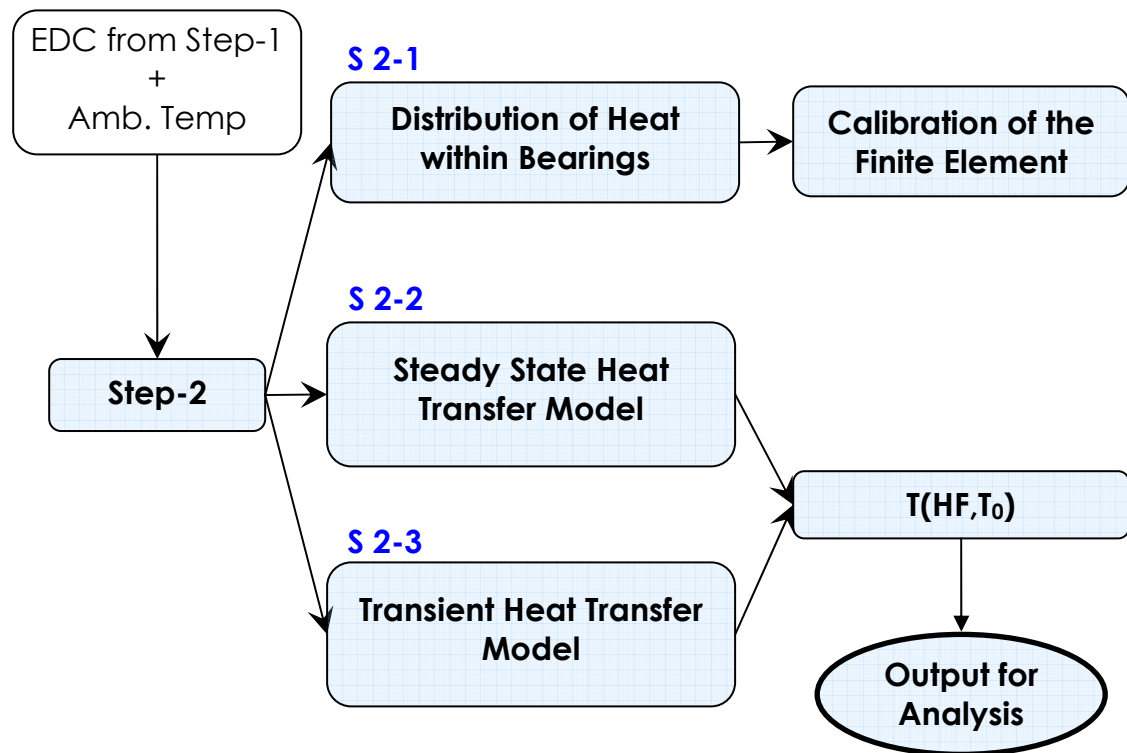


Figure 1-7: Objectives pursued in Step-2

The experiment was used to calibrate material properties in two finite element models, steady state and transient heat transfer models.

1.7.3 Step-3, Assessment of Tensile Strength of Lead

The F.E. model, created at Step-2 provided information about the locations of plastic hinges and the post-yield behavior of lead plugs. This information, together with information about temperature variation at core, resulted, from heat transfer models, was used as an input data for an existing equation. The existing equation [32] determined variation in tensile strength associated with the given temperature variation. The reduction in the tensile strength of lead can be interpreted as transient degradation of the assembly of a lead core bearing.

2

Types of Seismic Response Modification

Devices

Reasonable classification of Seismic Response Modification Devices can be difficult to organize due to their multifunctional performance characteristics. As mentioned before the category of seismic isolators mainly creates a discontinuation between structures foundation system or between components of overall structure assembly. They can also contribute as a component of additional dissipation of energy to the structure. It is mostly due to the mechanism they utilize to provide dissipation of energy that they can be classified. In this term, Figure 2-1, shows the families of elastomeric and sliding bearings the three most popular subcategories of elastomeric bearings are the Natural Rubber, Lead Core Rubber and High Damping devices. It must be noted that often the word bearing and devices is used in interchangeable way. More appropriately "bearing", should refer to devices able to support also vertical load. The family of sliding bearings includes devices that utilize friction as mechanism of energy dissipation. In Figure 2-1, as part of this family are reported also hybrid bearings that

could employ the characteristic of sliding device as well as additional functions obtained with different materials and conduction techniques. The two additional groups of SRMDs of Figure 2-1 could be classified as energy dissipation devices as the viscous fluid dampers can provide a contribution of stiffness to structure and dissipate significant amount of energy but they don't provide isolation effect as described before.

Basic performance of the most common devices is described in what follows with particular attention dedicated to elastomeric bearings for this research, Figure 2-1.

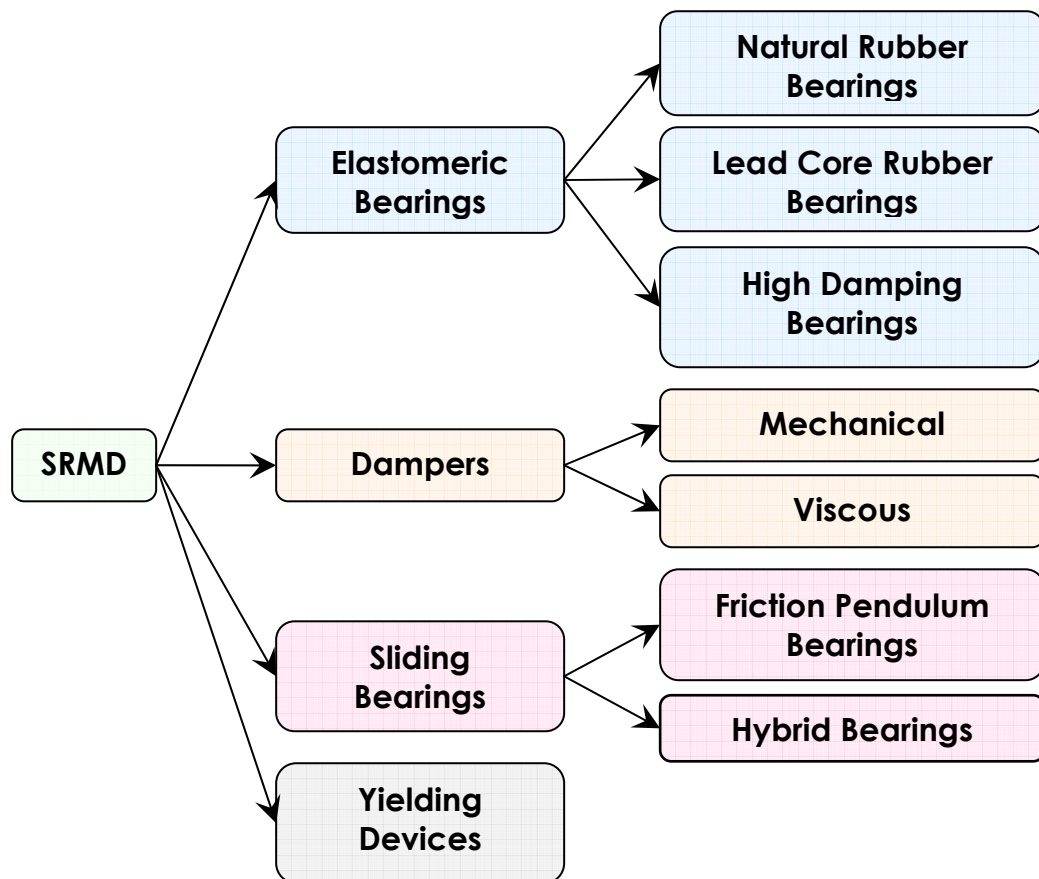


Figure 2-1: Different types of Seismic Response Modification Devices

2.1 Elastomeric Bearings

Rubber, as a material exhibits excellent resiliency. It can accommodate very high deformation, up to 900% in tension. Rubber is the least expensive and most widely available material with such a high resiliency. Resiliency is the key property for the elastomeric bearings. These devices are meant to accommodate large displacements imposed to the structure due to seismic activities or ambient vibrations. Also rubber is a nearly incompressible material.

2.1.1 Laminated Rubber Bearings

The simplest form of base isolation device is the Laminated Rubber device. It can accommodate shear strain of 100 % or higher with a damping ratio in the order of 10-15 %. It is manufactured by stacking rubber layers with steel shim. The use of steel shims improves axial load capacity and stability of the bearing.

Figure 2-2, presents the section views of two common types of rubber bearings, one with circular section and no lead plug and the other with square section and lead plug inserted. Lead plugs, as discussed in Section 2.1.2, provide additional damping.

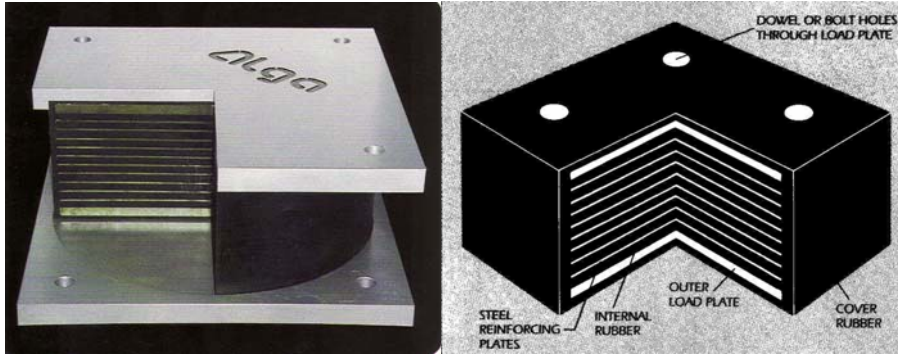


Figure 2-2: Section view of a typical laminated rubber bearing

Key parameters in the design of laminated rubber bearings are introduced below.

The maximum allowable vertical load that can be carried by a bearing, W_{\max} can be approximated by the following semi-empirical equation:

$$W_{\max} = A'GS\gamma_w \quad \text{Equation 2-1}$$

where:

A' =overlap area between the displaced top and bottom of bearings, (Figure 2.6).

G =shear modulus of rubber $\cong 1$ Mpa

S =shape factor of each rubber layer equal to the loaded area of the bearing divided by the shear force-free area of the bearing.

γ_w =allowable shear strain due to gravity load.

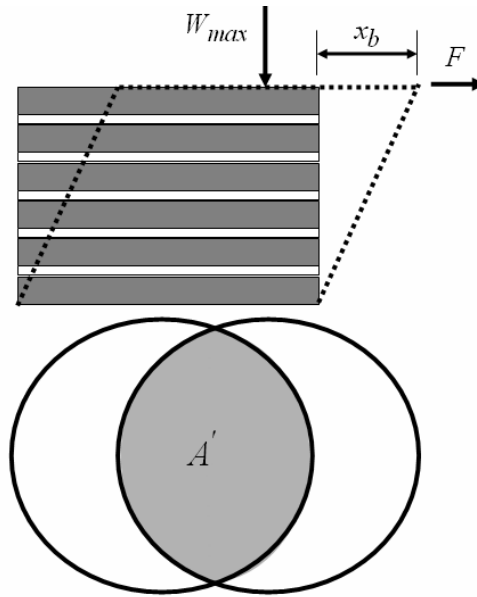
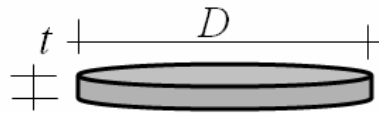


Figure 2-3: Effective cross section that resists compressive stress

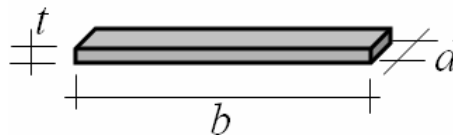
Cylindrical bearing:



$$S = \frac{\text{Loaded Area}}{\text{Force Free Area}} = \frac{\pi D^2/4}{\pi D t} \frac{D}{4t}$$

Equation 2-2

Rectangular bearing:



$$S = \frac{\text{Loaded Area}}{\text{Force Free Area}} = \frac{bd}{2t(b+d)}$$

Equation 2-3

γ_w = allowable shear strain due to gravity load. It is estimated as a ratio of the short-term failure strain of the rubber in pure tension (Bridge Engineering Standards, 1976)

$$\gamma_w = 0.2\epsilon_v$$

$$\gamma_w \approx 0.4 \text{ For design earthquake}$$

$$\gamma_w \approx 0.7 \text{ For extreme earthquake}$$

Laminated rubber bearings have a finite vertical stiffness that affects the vertical response of the isolated structure. The total vertical stiffness (k_v) of a laminated rubber bearing is the in-series sum of the vertical stiffness due to the rubber shear strain without volume change stiffness ($k_{v\gamma}$) and the vertical stiffness caused by the volume change of the rubber without shear, (k_{vV}).

$$k_v = \frac{k_{v\gamma}k_{vV}}{k_{v\gamma} + k_{vV}} \quad \text{Equation 2-4}$$

The component of vertical stiffness without volume change is given by:

$$k_{v\gamma} = \frac{6GS^2A}{h} \quad \text{Equation 2-5}$$

where,

A, the area of a layer of rubber

h, is the total height of rubber

G, is the shear modulus of rubber

S, is the shape factor of the bearing

The component of vertical stiffness due to volume change can be calculated as:

$$k_v = \frac{kA}{h} \quad \text{Equation 2-6}$$

where

$k_v = \frac{kA}{h}$ is the rubber compression modulus $\cong 2000 \text{ MPa}$.

The definition of the total vertical stiffness can then be written as:

$$k_v = 6GS^2 Ak / (6GS^2 + k)h \quad \text{Equation 2-7}$$

A small shape factor (S) gives a moderate vertical stiffness which is controlled by shear strain, while a sufficiently large value of S gives a very high vertical stiffness which is control by volume change. Contributions of shear strain and volume change are practically equal for $S \cong 18$. It is neglected the small reduction in k_v due to a pressure redistribution in the layers, when rubber compressibility is introduced.

A laminated rubber bearing may be approximated as a vertical shear beam, since the steel laminations severely inhibit flexural

deformations while providing no impediment to shear deformations. It can be assumed that pure shear deformations occur in the rubber only. The lateral stiffness of a laminated rubber bearing k_b can be approximated as:

$$k_b = \frac{GA}{h} \quad \text{Equation 2-8}$$

where:

A, is section area of the bearing

G, is shear modulus of rubber

h, total height of rubber

Some reduction in lateral stiffness at large displacements could be experienced, partly due to flexural beam action and partly due to increased compression of the reduced overlap area. This effect is negligible for shape factor S in the order of 10 to 20.

Rubber is a viscoelastic material. Damping in rubber, which is predominantly velocity dependent, is provided by deforming rubber layers. The high damping rubber was initially developed by Tun Abdul Razak Research Center (TARRC), UK. Rubber bearings are made from two major types of rubber, low and high damping rubbers. Low and high damping rubber bearing can provide ~10% and in excess of 15% damping respectively, [13], [14], [20]. This property is modified by

tweaking the amount of silica and carbon black used in rubber compound. Although damping property of the rubber can be improved by adjusting the two components some other useful properties can be deteriorated too. For instance, carbon blacking makes the rubber stiffer and reduces its elongation-to-break capacity.

2.1.2 Lead Core Rubber Bearings (LRB)

The lead plugs are introduced in laminated rubber bearings to improve energy dissipation through hysteretic action. The laminated rubber bearing used for this purpose is usually made of low damping rubbers. The use of lead is justified by property of this metal to yield in shear at a relative low stress of 8-10 (MPa) at normal temperature. The unique property of lead is that it can recrystallize at room temperature, which translates to the fact that lead regains its crystalline structure after yielding and continues to dissipate significant amount of energy. Lead is "hot-worked" when plastically deformed at ambient temperature. Ductility of lead at 20° C is equivalent to ductility of steel at more than 400 °C. Lead also has good fatigue properties during cycling at plastic strain. This material is readily available at high purity of 99.9%, required for its mechanical properties to be predictable. Figure 2-4, shows a typical configuration of a rubber bearing with a central core of lead.

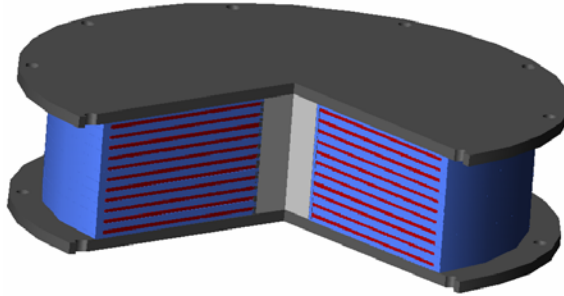


Figure 2-4: Sectional view of a lead core rubber bearing

Lead core bearings are typically made in square or cylindrical shapes, with top and bottom plates used to connect the device to the mating surfaces of the structure.

The simplest form of a lead core bearing is comprised of (1) lead that serves as energy dissipating component (2) rubber, the component that provides restoring force to bring the structure back to the point of static equilibrium. (3) steel shims that serve as reinforcing elements for rubber to improve stability and compressive load capacity.

The initial elastic stiffness, k_u , is defined as sum rubber and lead contribution, (Figure 2-5):

$$k_u = \frac{1}{h} (G_p A_p + G_r A_r) \quad \text{Equation 2-9}$$

where:

A_p = Total area of the lead plug

G_p = Shear modulus of the lead plug $\cong 5.6 \text{ GPa}$

A_r = Area of the rubber

G_r = Shear modulus of the rubber $\cong 0.8$ MPa

h = Total height of the bearing

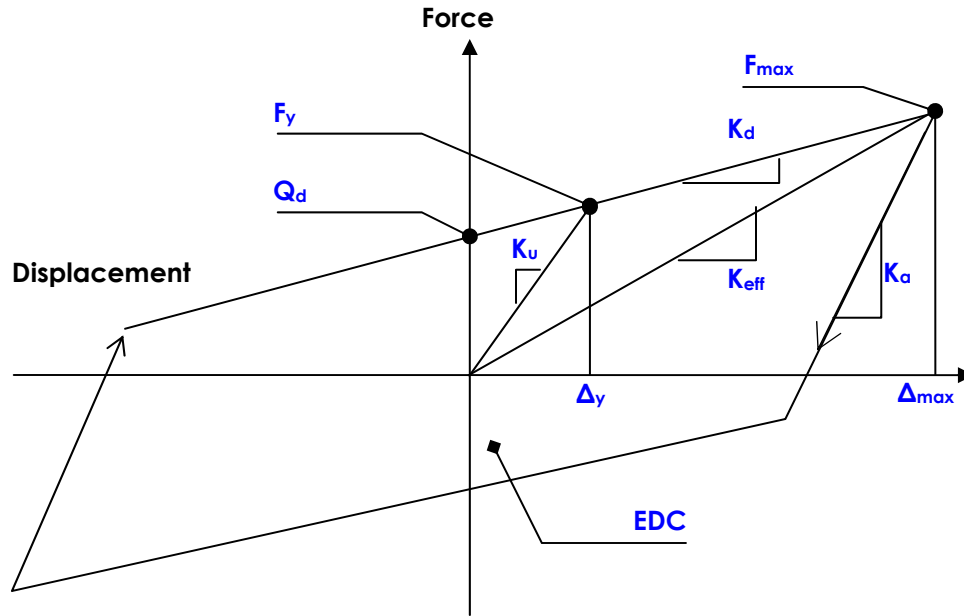


Figure 2-5: An idealized force-displacement loop of an isolation bearing

The post elastic stiffness, k_d , is mainly dominated by contribution rubber and can be approximated as:

$$k_d = \frac{G_r A_r f_c}{h} \quad \text{Equation 2-10}$$

where, f_c is a coefficient that accounts for lead at post-yield. For current types of LRB's the elastic stiffness k_u ranges between 6.5 to 10 times post-yield stiffness, k_d .

The enclosed area of a hysteresis loop is the measure of energy dissipated per cycle of motion (EDC). In the idealized system (Figure 2-

5) the resisting or damping force of the system is replaced by an equivalent viscous damping. This equivalent damping is determined in such a manner as to produce the same dissipation per cycle as that produced by the actual damping force. The relationship is defined as:

$$\beta = \frac{EDC}{2\pi k_{eff} \Delta_{max}^2} \quad \text{Equation 2-11}$$

where:

β = Critical damping

EDC = Energy dissipated per Cycle

k_{eff} = Effective stiffness

Δ_{max} = Maximum bearing displacement during a single cycle of testing

The yield force can be defined as the force required for yielding of the lead plus the elastic force carried by the rubber at the corresponding yield displacement:

$$F_y = \tau_{py} A_p \left(1 + \frac{G_r A_r}{G_p A_p} \right) \quad \text{Equation 2-12}$$

τ_{py} = shear yield strength of lead $\cong 10.5 \text{ MPa}$

The characteristic strength represents the shear force at zero displacement and is generally associated to the yield strength of the lead core:

$$Q \equiv \tau_{py} A_p \quad \text{Equation 2-13}$$

2.2 Sliding Bearings

Sliding bearings include all devices that accommodate large displacements by sliding rather than stretching, shearing or compressing. In this type of bearings, energy is dissipated by friction caused by sliding of the surfaces.

2.2.1 Friction Pendulum

The friction pendulum bearing is a member of the sliding devices category. It was officially developed by the Earthquake Protection System in California.

The friction pendulum device is illustrated in Figure 2-6. The bottom portion (concave plate) is typically constructed as a spherical dish with a stainless steel overlaying. An articulated slider is free to move over the concave plate and inside the bearing plate. The bottom of the slider and the inside of the cup part of the bearing plate are lined with self lubricating low friction composite. The device use the characteristics of a pendulum to lengthen period of the isolated

structure. The period imposed to the structure could be easily obtained as:

$$T = 2\pi \sqrt{\frac{R}{g}} \quad \text{Equation 2-14}$$

where, R is the radius of curvature of the concave plate. The isolator period is so controlled by the selected radius R and is independent of the mass of the supported structure. The second important mechanism in the respect of this device is the dissipation of energy through friction. Choices of bearing, material composite, mating surface properties can define the amount of friction of the isolator and therefore the amount of energy dissipation per cycle during seismic movements. The lateral stiffness and friction force is directly proportional to the supported weight of the bearing. Very recently the original concept of the device was extended to bearings with 2 and 3 sliding surface.

Figure 2-6, illustrates the components of a typical friction pendulum bearing.

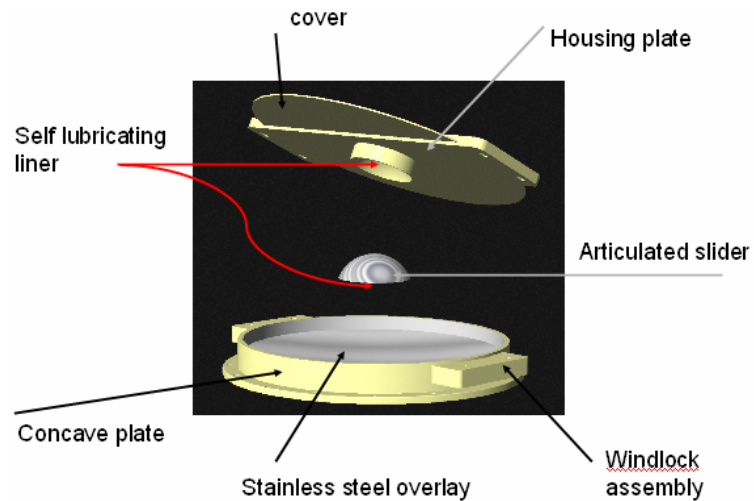


Figure 2-6: General components of a friction pendulum. Not shown in the image is a sealing system that rest between the two circular edges when the bearing is assembled, this helps in preventing dirt and debris from getting into the sliding zone

Figure 2-7, shows a friction pendulum bearing with only one sliding direction, installed on the Seahawk Stadium.

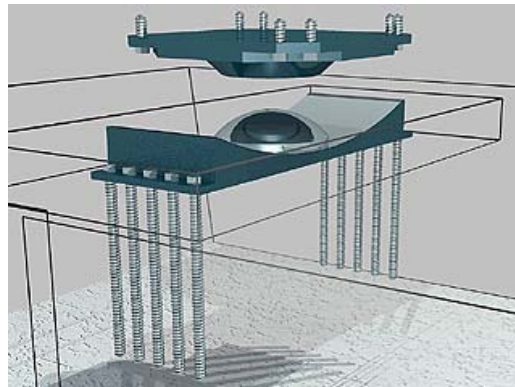


Figure 2-7: A friction pendulum damper system installed on Seahawks Stadium. It decouples the roof which attains the highest acceleration at a seismic event from the rest of the structure. Source: <http://www.djc.com/news/co/11134804.html>

In Figure 2-8 is presented the typical force-displacement curve of a friction pendulum device. The intersection of the curve with the Y-axis (zero displacement) is obtained as product of the friction coefficient (μ), times the supported load (W), the stiffness (k) is defined as:

$$k = \frac{W}{R}$$

Equation 2-15

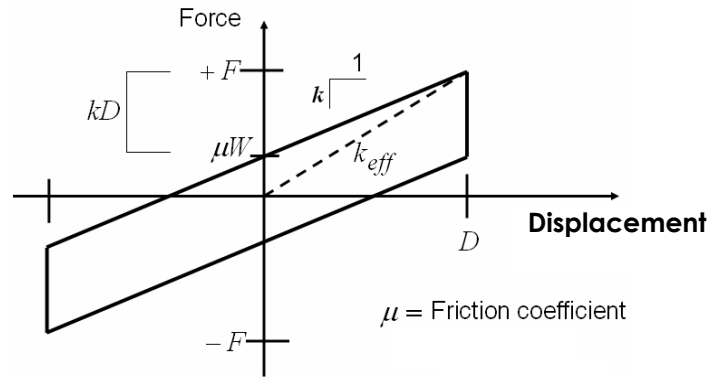


Figure 2-8: Schematic of hysteresis loop of a single concave Friction Pendulum bearing

Simpler sliding devices are available with flat sliding surfaces. Their behavior is simply associated to the friction as source of energy dissipation.

2.3 Hybrid Bearings

In principle hybrid bearing incorporate the functions of multiple types of bearings in one device. One example, presented in Figure 2-9 combines a laminated rubber bearing and a sliding bearing. Application of rubber and having a flat friction surface reduces the jerking of the motion caused by debris or wrinkled surface.

The sliding effect can be designed to provide the required energy dissipation (EDC). The possibility of high force due to static coefficient of friction as well as possible effect due to the static-slip

phenomenon could be mitigated by inserting an additional service of flexibility in the system, like a laminated rubber bearing. Figure 2-10 shows an experimental force-displacement curve for the bearing of Figure 2-9.

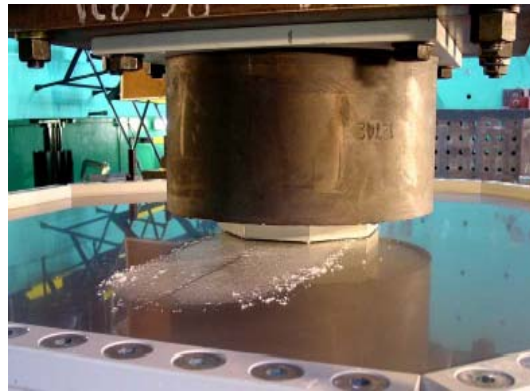


Figure 2-9: A common type of Hybrid bearing consisting of a laminated rubber bearing and a sliding bearing

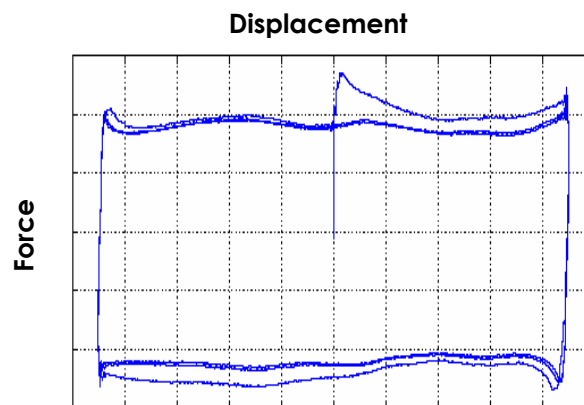


Figure 2-10: Hysteretic loop of a hybrid bearing comprised of elastomer and sliding surface

2.4 Yielding Bearings

Yielding dampers take advantage of the hysteretic behavior of metals when deformed into the post-elastic range. A large variety of

different types of devices have been developed that utilize flexural, shear or axial deformation modes into the plastic range, Figure 2-11.

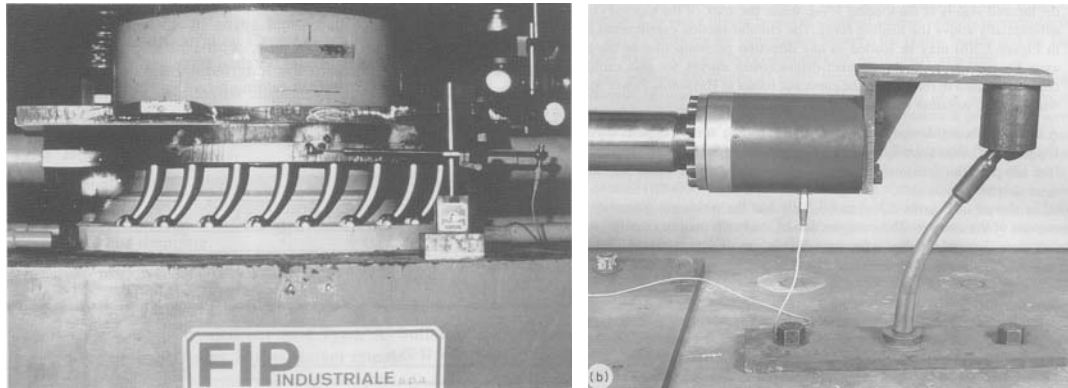


Figure 2-11: Flexural yielding bearings

In Figure 2-12, is presented the idealized force-displacement curve of a yielding device. The introduced amount of damping is related to the area bounded by the loop.

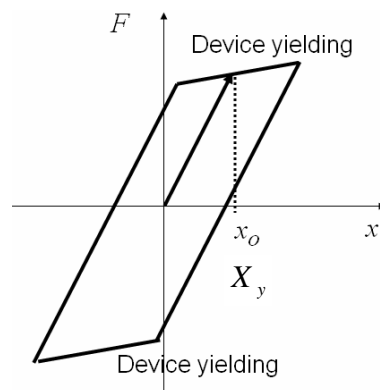


Figure 2-12: Idealized (perfectly bilinear) hysteresis loop of a yielding Device

2.5 Viscous Dampers (VDs)

The large majority of viscous dampers utilize a silicon fluid viscous material. In viscous fluids, dissipation refers to a process in which the viscous fluid absorbs energy from the imposed motion (kinetic energy)

and, transforms it into internal thermal energy of the fluid. In other word viscous dissipation is the work done by the velocity against the viscous stresses. The energy transferred to heat will raise the temperature of the fluid. Viscous dissipation is an irreversible process. The viscous damper device takes advantage of this principle to consume the seismic energy. That generates effective displacement between the device ends. Viscous dampers not only provides damping of up to 40 % but also used for reduction of structural drift.



Figure 2-13: Viscous damper tested at the Caltrans SRMD Test Facilities at UCSD



Figure 2-14: A typical viscous damper

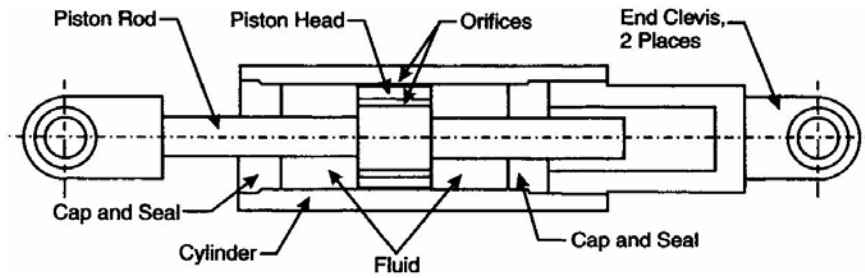


Figure 2-15: Section view of a typical viscous damper and its major components

The viscous damper is a cylindrical container (Figures 2-13, 2-14, 2-15) that accommodates a piston rod that extends outside the cylinder. The rod is also connected a piston which can move inside the cylinder. The piston moves together with the rod in close contact with internal surface of the cylinder. Fluid is inserted into the cylinder and forced to move from one side of the piston head to the other side by the motion of the head and the existence of openings (orifices) on the piston head. The reaction force that opposes the relative motion across the damper is generated by a pressure differential across the piston head.

The orifices are designed to produce a specific output force in the form:

$$f_D = c_\alpha \operatorname{sgn}(\dot{u}) |\dot{u}|^\alpha \quad \text{Equation 2-16}$$

where c_α is the experimentally determined damping coefficient with unit of force per velocity raised to the power α . The value of α , for standard devices ranges from 0.15 to 1. At the value of $\alpha = 1$ the device

behaves as a linear device otherwise the device exhibits non-linear behavior $\alpha \neq 1$.

In the following tables a summary of the fundamental performance characteristics, mechanism of operation, material components and the performance parameters presented for commonly used SRMD. In particular Table 2-1, is a summary of the typical functions and performance principles of the devices mentioned above.

In Table 2-2 the mechanical components and fundamental parameters describing the device performance are reported. An example of hysteretic response for devices tested at the Caltrans SRMD labs are reported in Table 2- 3.

Table 2-1: Summary of the application and operation mechanism

Type	Bearing Action	Operation Mechanism
Laminated Rubber Bearing	Provides Isolation Accommodates Torsion	Displacement is accommodated through high elasticity of rubber materials. Some degree of energy dissipation is expected through hysteretic action rubber
Lead Core Rubber Bearing	Provides Isolation Accommodates Torsion Dissipated energy up to 30%	Displacement is accommodated through high elasticity of rubber materials. Energy is dissipated mainly by yielding of lead plugs.
Sliding Bearing	Provides Isolation Accommodates Torsion Dissipated energy	Displacement is accommodated through decoupling joint system. Energy is dissipated through friction.
Hybrid Bearing	Provides Isolation Accommodates Torsion Dissipated energy	Displacement is accommodated by decoupling joint system and elasticity of rubber. Energy is dissipated through friction and yielding of lead plug
Dampers	Restrict drift of the structure Dissipates energy for up to 50%	The restricting force is generated by pressure differential. The resistance force is a function of velocity of load application.

Table 2-2: Operation basis and components used in commonly employed SRMDs


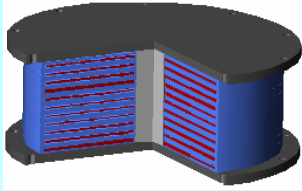
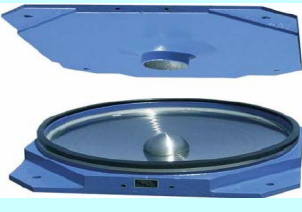
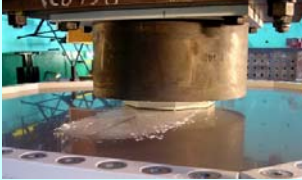

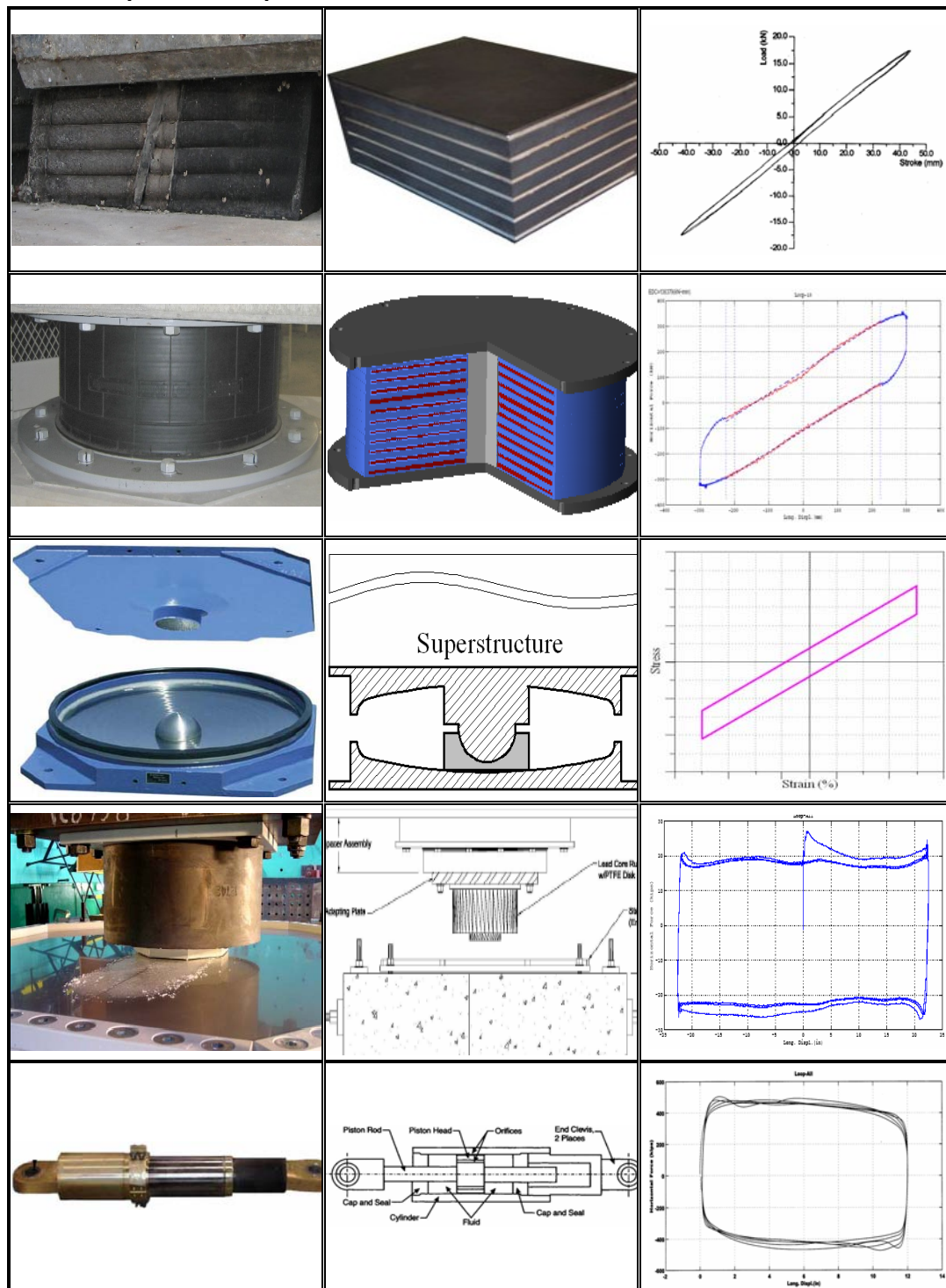
Device	Image	Components	Device Performance Parameters
Laminated Rubber Bearings		<ul style="list-style-type: none"> • Low or high damp Elastomer • Reinforcing Metal Shims • Interface Connector Discs (not shown on the image) • Fasteners (Bolts, washers and nuts) 	<ul style="list-style-type: none"> • Damping Ratio, ζ • Stiffness, K • Natural Period, T
Lead Core Rubber Bearings		<ul style="list-style-type: none"> • Elastomer • Lead plug • Reinforcing Shims • Interface Connector • Fasteners (Bolts, washers and nuts) 	<ul style="list-style-type: none"> • Damping Ratio, ζ • Stiffness, K • Natural Period, T • EDC
Sliding Bearings e.g. Friction Pendulum		<ul style="list-style-type: none"> • Slider • Cover • Housing Plate • Seal & Fasteners • Wind-lock • Concave Plate • Stainless Steel Overlay • Low Friction Material 	<ul style="list-style-type: none"> • Radius of Curvature of Bearing Surface, R • Coefficient of friction, μ • Durability of low friction material • Weight
Hybrids		<ul style="list-style-type: none"> • Elastomer • Lead Core • Connector Interface • Low friction material • Sliding Surface • Fasteners (Bolts, washers and nuts) 	<ul style="list-style-type: none"> • Damping Ratio, ζ • Stiffness, K • Coefficient of friction, μ
Viscous Dampers		<ul style="list-style-type: none"> • Piston and Cylinder • Orifices • Piston Rod • Viscous Fluid • Gasket and Sealers • Fasteners 	<ul style="list-style-type: none"> • Nonlinear coefficient, α • Force Constant, C

Table 2-3: Hysteretic loop of some common SRMDs



3

Materials Used in Manufacturing Elastomeric Bearings

Maintaining consistent physical and engineering properties during a seismic event and through out the lifespan of a device is the critical key for a successful performance of a Seismic Response Modification Device. Due to the nature of the functions of such devices, and exposure to various environmental conditions, materials from different mechanical and chemical categories have to work together to make a device perform as intended. Materials must be chosen meticulously in order for the device to function optimally and consistently over time.

3.1 Introduction to Polymers

Polymers are classified into three main groups of thermoplastics, thermosets, and elastomers. Studying each category individually makes it possible to understand the rational beyond choosing rubber as the provider of restoring force in elastomeric bearings. The thermoplastic materials, themselves, are also divided into two subcategories, Crystalline and Amorphous thermoplastic polymers. The following

sections introduce the three major members of the polymer family and their highlighted physical and mechanical properties. The types of elastomers available for civil structure applications, together with advantage and disadvantage of each one, will also be discussed in full detail.

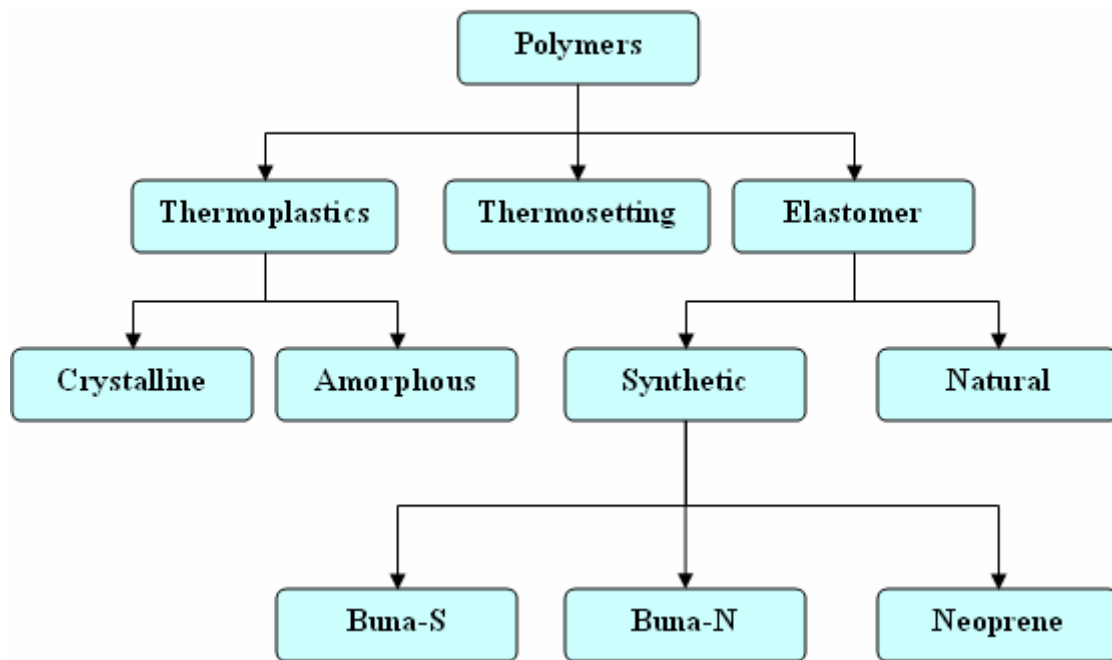


Figure 3-1: General classification of polymer family

3.1.1 Thermoplastic Polymers

The word “plastic” has many different physical and mechanical definitions. In physics the word plastic refers to a group of polymers that can be repeatedly softened by heating and then solidified by cooling, a process similar to the repeated melting and cooling of metals. Most linear and slightly branched polymers are thermoplastic. In mechanics

of materials the word plastic is an attribute to the group materials capable of experiencing noticeable permanent elongation without being ruptured.

Molecules in a thermoplastic are held together by relatively weak intermolecular forces so that the material softens when exposed to heat and then returns to its original condition when cooled. All the major thermoplastics are produced by chain polymerization. Thermoplastics have a wide range of applications because they can be formed and reformed in so many shapes. Characteristics of plastics materials can be changed by mixing or combining different types of polymers and by adding nonplastics materials. Particulate fillers such as wood, flour, silica, sand, ceramic, carbon powder, tiny glass balls, and powdered metal are added to increase modulus and electrical conductivity, to improve resistance to heat or ultraviolet light and to reduce cost. Plasticizers are added to decrease modulus and increase flexibility. Other additives may be used to increase resistance to ultraviolet light and heat or to prevent oxidation.

Highly crystalline polymers are rigid, high melting, and less affected by solvent penetration. Crystallinity makes a polymer strong, but also lowers their impact resistance. As an example, samples of polyethylene prepared under high pressure (5000 atm) have high

crystallinities (95 – 99 %) but are extremely brittle. Small molecules and ions form a three-dimensional lattice with an extended regular structure that makes large crystals possible. A small portion of the NaCl lattice is shown on (Figure 3-4). Such lattices with a unit cell are usually described as the smallest repeating unit in the lattice. In the case of NaCl, the unit cell is termed face-centered cubic, FCC.

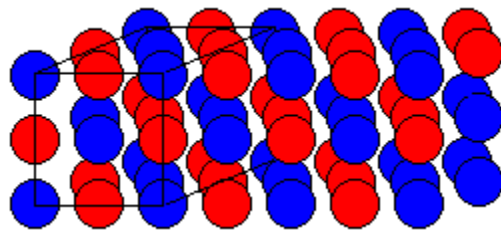


Figure 3-2: Schematic of FCC crystalline structure

Polymer molecules are very large, so it might seem that they could not pack together regularly and form a crystal. Regular polymers may form lamellar (plate-like) crystals with a thickness of 10 to 20 nm in which the parallel chains are perpendicular to the face of the crystals. Delrin, an example of crystalline polymers, is a lightweight, low-friction, and wear-resistant thermoplastic with good physical and processing properties and capable of operating in temperatures in excess of 90 degrees Celsius (approximately 200 degrees Fahrenheit). Polymer chains with branches or irregular pendant groups cannot pack together regularly enough to form crystals. These polymers are called amorphous. Amorphous regions of a polymer are made up of a

randomly coiled and entangled chain. They have been compared to a bucket containing a large number of entangled worms, each one 20 feet long and of 1/4-inch thickness.

Amorphous polymers are softer, have lower melting points, and are penetrated more by solvents than are their crystalline counterparts. Nylon is a well-known amorphous thermoplastic polymer.

To summarize, Thermoplastic have the advantage of having low density good energy absorption properties.

3.1.2 Thermoset Polymers

A thermosetting plastic, or thermoset, solidifies or "sets" irreversibly when heated. Thermosets cannot be reshaped by heating. Thermosets usually are three-dimensional networked polymers in which there is a high degree of cross-linking between polymer chains. The cross-linking restricts the motion of the chains and leads to a rigid material. In general the main advantage of thermoset polymers can be summarized as:

- High thermal stability
- High rigidity
- High dimensional stability
- Resistance to creep and deformation under load
- Light weight

- High electrical and thermal insulating properties

Thermosets are strong and durable. They are primarily used in automobiles and construction. They also are used to make toys, varnishes, boat hulls, and glues.

3.1.3 Elastomeric Polymers

Elastomers helped in revolutionary advancements in a wide spectrum of applications from heavy industrial machineries to medical and bioengineering fields. Rubbers are so crucial in everyday life that without them human's life would face serious challenges. A very simple example is their applications in manufacturing of tires. Elastomers comprise about 90% of ingredients of tires.

Elastomers are rubbery polymers that can be stretched easily to several times their original length and which rapidly return to their original dimensions when the applied stress is released, this property is called "Resiliency". Elastomers are cross-linked, but have a low cross-link density. The polymer chains still have some freedom to move, but unlike plastic materials, are prevented from permanently moving relative to each other by the cross-links. To stretch, the polymer chains must not be part of a rigid solid, either a glass or a crystal. An elastomer must be above its glass transition temperature, T_g , and have a low degree of

crystallinity. Rubber band is the most common example of application of elastomers.

Perhaps the most pronounced property of elastomeric material that differentiates them from other polymers is their unique strain-stress characteristics. Elastomers are nonlinear elastic polymers. A number of elastomers are, however, not perfectly elastic and associated with some plastic deformation depending on degree of strain to which they are subjected.

Since the elastic recovery is due to the action of inter-atomic and intermolecular forces, the values of elastic modulus will vary directly with the magnitude and the rate of application of these forces

Elastomers are a category of pliable plastic materials that are good at insulating, withstanding deformation, and molding into different shapes. As a particular kind of polymer, elastomers include natural and synthetic rubber. Elastomers are useful and diverse substances that easily form various rubbery shapes. Some advantages of elastomers are:

- Elastomers are resilient
- Elastomers are strong when struck
- Elastomers get hard when they are stretched
- Elastomers are scratch resistant

- Elastomers are resistant to corrosion from various chemicals
- Elastomers are good electrical insulators

Another beneficial property of elastomers is that they can be "compounded" or joined with other materials to strengthen certain characteristics. Admixture with additives helps to become more durable in extreme environmental conditions. Elastomers can easily be bonded to various other materials, such as metal, hard plastic or different kinds of rubber, with excellent adherence. The reason that elastomers can deform and return to their previous shape is their "cross-linked" property. The Cross-linking, graphically presented in Figure 3-3 means that different chains of polymer molecules have all been linked together so that the object can uniformly stretch but always returns to its pre-stretching configuration.

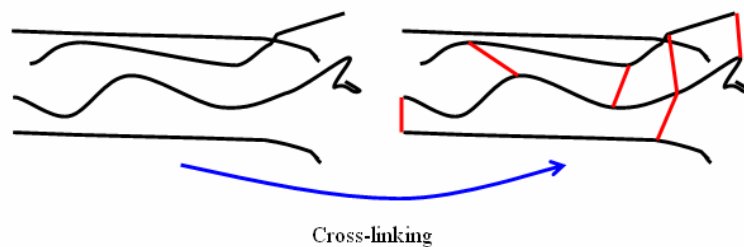


Figure 3-3: Schematic of crosslinking phenomenon

One negative aspect of this category of materials is that they are difficult to recycle, but luckily they last a long time without wearing down. A summary of the peculiar properties of polymers is reported in Table 3-1.

Table 3-1: A summary of the highlighted properties of polymers

	Example	Toughness	Brittleness	Plasticity	Resiliency
Elastomeric Polymers	Natural Rubber	Very High	None	None	High
Thermoplastic Polymers	Nylon Delrin	Low High	Low	Low to very high	None to Low (at elastic regime)
Thermoset Polymers	Epoxy	Low	High	Almost none	Almost none

3.1.4 Strain-Stress Curves of Common Polymers

In Figure 3-4 are presented strain-stress behavior of common polymers. Materials “a” and “b” show typical engineering behavior of thermoplastic materials. They exhibit distinguishable elastic to plastic transformation with a very pronounced yielding point.

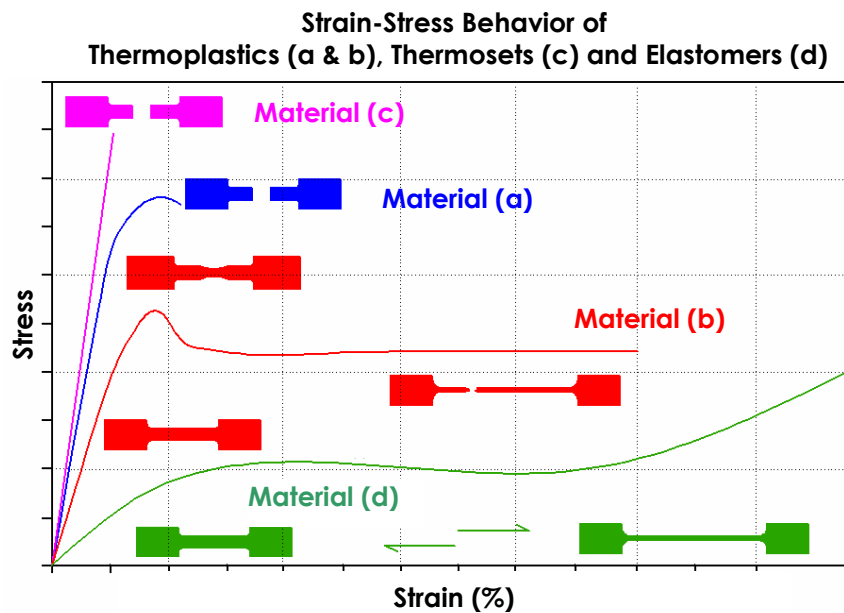


Figure 3-4: Strain-stress behavior of different types of polymers

3.2 Rubber

The unique and excellent properties existed in rubber makes it ideal choice for manufacturing of elastomeric bearings. Like in any other family of polymers ingredients of elastomers can be tweaked to optimize the properties that are demanded the most for specific applications. Polymerizations of a few major monomers result in major types of elastomers. Each of these polymers possesses improves specific properties suitable for particular application. Properties such as resistance to chemicals and petroleum, operation in wider range of temperature, ozone resistance etc are improved by optimization of the polymerization process. Some of well known monomers are isoprene, chloroprene, acrylonitrile and styrene.

1. Natural Rubber

Natural rubber has been known for centuries. It is obtained primarily from the latex of the rubber tree, which is native to South America. Latex is a gummy white liquid full of minute globules. It consists of a mixture of water, hydrocarbons, resins, oils, proteins, acids, salts, sugar and caoutchouc, the substance used as the source of rubber. Natural rubber has tensile strength of 15 MPa , strain capacity of 750 to 850 percent and density of $0.93\text{ (gr/cm}^3\text{)}$. It has a operating recommended temperature range of -50 to 82 degrees Celceous.

2. Synthetic Rubber, Neoprene Rubbers

One of the first successful synthetic rubbers resulting from numerous researches was neoprene. Neoprene is the polymer of the monomer chloroprene. The raw materials of chloroprene are acetylene and hydrochloric acid. Neoprene has high resistance to heat and such chemicals as oils and gasoline and is used in hose for conveying gasoline and as an insulating material for cables and in machinery. Neoprene is similar to isoprene except that the methyl group attached to the double carbon bond is replaced by a chlorine atom. The presence of the chlorine atom increases the resistance of the unsaturated double bonds to attack by oxygen, ozone, heat, light and weather.

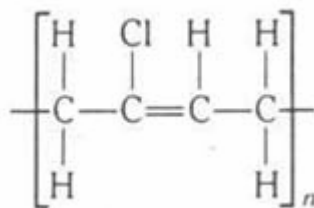


Figure 3-5: Chemical structure of neoprene rubber

Material "c" represents a thermoset material and material "d" the represents a typical elastomeric behavior. General properties and fundamental chemical properties of the above mentioned elastomers are summarized in Table 3-2

Table 3-2: Comparison of some important physical properties of different elastomers

General Properties		General Chemical Resistance	
		Resistant to:	Attacked by:
Neoprene	Good Weathering Resistance. Flame retarding. Moderate resistance to petroleum-based fluids.	Moderate chemicals and acids, ozone, oils, fats, greases, many oils, and solvents.	Strong oxidizing acids, esters, ketones, chlorinated, aromatic and nitro hydrocarbons.
Natural Rubber	Excellent physical properties including abrasion and low temperature resistance. Poor resistance to petroleum-based fluids.	Most moderate chemicals, wet or dry, organic acids, alcohols, ketones, aldehydes.	Ozone, strong acids, fats, oils, greases, most hydrocarbons.

3.2.1 Rubber Compounding Ingredients

To make rubber a more suitable material for manufacturing purposes, the raw material has to be admixed with particular ingredients through a process that is called compounding.

A brief Presentation of the rubber compounding ingredients is included in this chapter. The typical percentage and basic ingredients of rubber captured are listed in Table 3-3.

The notation “phr” stands for “parts per hundred rubber,” which means the parts, by weight, of an ingredient per hundred parts, by weight, of rubber. For example, 40 phr of carbon black means 40 parts, of carbon black per hundred parts, of rubber.

Table 3-3: Ingredients and their percentage used in a typical rubber compound

Ingredient	Phr (part per 100 rubber)
1. Base Rubber	100.0
2. Vulcanizing Agent (Sulfur)	0.5-40.0
3. Accelerator	0.5-5.0
4. Activator	1.0-5.0
5. Antioxidant	0.5-2.0
6. Reinforcing Fillers, Carbon Blacks and Minerals	25.0-200.0
7. Processing Oils	0.0-25.0
8. Inert Fillers	25.0-200.0
9. Coloring Additives	1.0-5.0

The ingredients used for compounding are classified into accelerators, activators, antioxidants, coloring agents, fillers and reinforcing agents, retardants, rubber process oils, softeners, and vulcanizing agents.

1. Vulcanizer

Although rubber, on its original, untreated form, was found to be the best material of choice to a broad range of applications, there were problems associated to its use. Rubber froze rock hard in the winter and melted in the summer. A piece of rubber with free polymer chains tends to show inelastic behavior, and permanent deformations. A process called Vulcanization was introduced to cure the natural rubber by forming crosslinks between the polymer chains of the rubber, this way they will no longer move independently. The vulcanization process makes rubber more resistant to changes in temperature. The

process is performed in presence of sulfur in combined with other additives. Some of these additives include activators like zinc oxide and stearic acid and also retarding agents to control the vulcanization rate. These additives also include anti degradant agents used to balance the effect of environmental accelerating factors like heat, oxygen and ozone.

In the process of vulcanization, the added sulfur allows some carbohydrate (C-H) bonds to be broken and replaced by carbon sulfur (C-S) bonds. The cross-linked molecules create a three-dimensional network of rubber. Each cross-link is a chain of about eight sulfur atoms between two long chains of polyisoprene. This process, vulcanization is accelerated in presence of heat.

While the formation of crosslinks helps natural rubber to improve its elastic behavior, the cross-link of the sulfur atoms between the polymer chains increases the strength of the rubber but reduces its strain capabilities. The process also adds stability to the material and decreases its nonlinear characteristic as documented in the stress-strain curves of Figure 3-6.

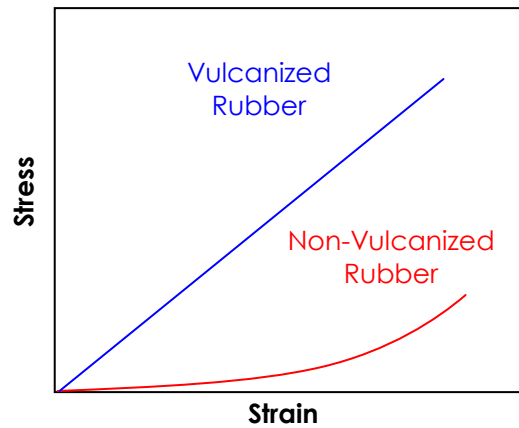


Figure 3-6: Comparison between stress-strain curves of natural and the chemical process of vulcanized rubber

The process of vulcanization from molecular point of view is presented in Figure 3-7

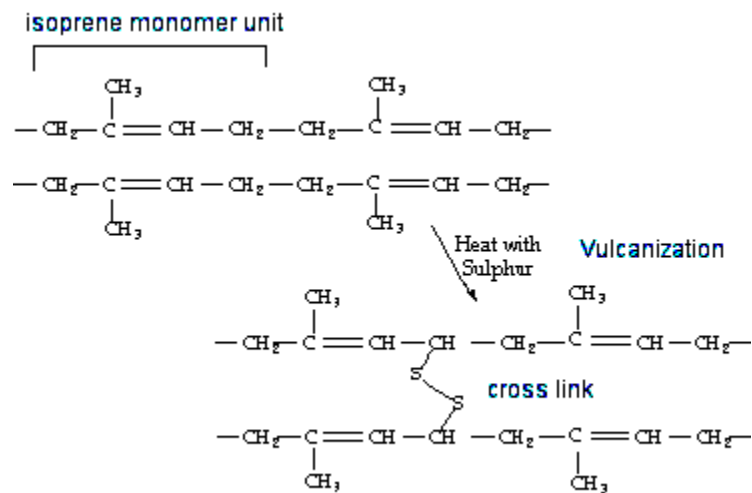


Figure 3-7: Vulcanization of natural rubber.

Vulcanization is a continuous process that results in stiffening the natural rubber. It happens due to presence of sulfur from initial vulcanization and a long action of heat. Excessive stiffening reforms the natural rubber to a brittle material which no longer possesses useful

properties of the natural rubber such as high strain capacity. As mentioned Sulfur is predominant vulcanizing agent. It is easily available in and vastly improves the properties of raw rubber which is sticky and soluble in solvents. With the addition of sulfur, rubber is converted into a non-sticky, tough, and elastic product.

2. Accelerators

Accelerators reduce the time required for vulcanization. The benefits of using accelerators are economy of heat, greater uniformity of finished goods, improved physical properties, improved appearance, and better resistance to deterioration. Organic accelerators are known to the rubber industry for over a century. Their use in rubber compounding has become universal. Some examples of organic accelerators are hexamine, mercapto-N-cyclohexyl benzothiazole sulfenamide, sodium diethyl dithiocarbamate, tetramethylthiuram disulfide, tetramethylthiuram monosulfide, etc. Inorganic accelerators such as lime and litharge are also used in slow curing products like rubber lining.

3. Activators

Activators help accelerators in the vulcanization process. Zinc oxide and zinc stearates are the most popular activators. Zinc oxide is also reinforcing filler.

4. Antioxidants

Rubber is degraded by oxidation. In order to prevent this, inhibitors are used during rubber compounding. These inhibitors are called antioxidants. The commercially available antioxidants are grouped into amine types and phenolic types. Products derived from amines, mostly aniline or diphenylamine, are called staining antioxidants because they tend to discolor non-black vulcanized rubber under exposure to light, and products derived from phenol are referred to as non-staining antioxidants.

5. Fillers and Reinforcing Agents

Fillers are classified into reinforcing and inert fillers. They can be either black or non-black fillers. Carbon black is a product resulting from the partial combustion or thermal decomposition of hydrocarbons manufactured under controlled conditions. Carbon black has numerous uses within the rubber industry and accounts for the consumption of approximately 90 % of all production. It is used primarily as reinforcing filler. In the tire industry, the modulus, hysteresis, and wear and tear resistance of the final product can be controlled by careful selection of the carbon black. Fillers that have significant effects on physical properties of rubbers, such as tensile strength, abrasion resistance, tear resistance, and fatigue resistance, are called

reinforcing fillers. Examples are carbon blacks, zinc oxide, magnesium carbonate, china clay, etc. Fillers that do not have an influence on these properties are called inert fillers (e.g. ebonite dust, graphite powder). Nevertheless, they perform a number of useful functions such as increasing chemical resistance, heat resistance, and ease of processing, providing rigidity or hardness to products, and most important of all reducing the cost of the compound. Examples of inert fillers are whiting, barytes, lithopone, talc, etc., apart from ebonite dust and graphite powder.

6. Retardants

Retardants are used to prevent premature vulcanization, called scorching of compounds, during processing and storing. During mixing and further processing in a colander, extruder, or molding press, the rubber compound is continuously subjected to heat which results in premature curing or pre-curing. To prevent this retardants are admixed with the compound. Salicylic acid is well-known retardants for natural rubber compounds, but it activates curing of neoprene compounds. Excessive use of retardants results in porosity in compounds. Many commercial grades of retardants are available.

7. Process Oils/Softeners

These additives help in mixing and extruding process. They are used along with fillers to reduce the cost of the compound. Peptizing agents are also softeners which increase the mastication efficiency and reduce the Mooney viscosity level to the desired processibility. Paraffin waxes with a melting point of approximately 55 °C are used as plasticizers. They bloom to the surface and protect ozone sensitive rubbers against cracking under static stress. Various kinds of resins are used as plasticizers; for example, coumarone resins, petroleum resins, high styrene resins, and phenolic resins to name a few. They give excellent flow characteristics to rubber compounds during extruding and molding.

3.2.2 Mechanical Characteristic of Rubbers

Static properties refers to the characteristics of an elastomer subjected to either a steady state loading, or a slowly applied dynamic load. Static engineering properties of elastomeric materials are obtained in completely different technique from other types of solids. Some static characteristics of the most commonly used rubbers are:

1. Hardness

Rubber is specified by its hardness which is its most important property. This is because hardness can be measured easily by

experiment, and it remains constant if environmental conditions don't change. It must be noted that modulus of elasticity for nonlinear elastic materials varies with variation of enforced deformation. Hardness is a term, refers to resistance of a solid object to indentations. Hardness is not one of the fundamental properties which directly enter into the design of a bearing. It is also important to differentiate between hardness and stiffness, Hardness is a measure of an elastomeric response to a small surface stress. Stiffness and compressive moduli measure the response to large stresses of the entire elastomeric part, however, shear and compressive moduli are correlated to hardness through mathematical equations. In engineering applications, the hardness of rubber compounds is measured by International Rubber Hardness Degree (IRHD) which ranges from 20 to 100. A durometer gage measures the depth of surface penetration for a pin of a predetermined geometry. The device is essentially a machine shop dial indicator measuring deflections between 0 and 0.100 inches, the gage reads 0 at 0.100 inches penetration and 100 at 0 inches penetration. A spring with a known stiffness is used. International Rubber Hardness Degrees (IRHD) and durometer are used interchangeably, since the test methods and theory are basically the same. However, durometer and IRHD will not necessarily be numerically equal. Typical rubber

compounds used in bearings made of rubber have hardness values of 50 to 60 IRHD, [NCHRP 449]. Schematic of Durometer testing is presented in Figure 3-8.

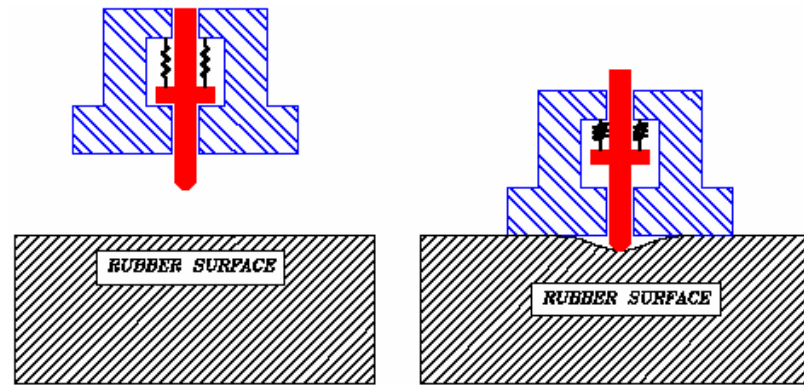


Figure 3-8: Durometer testing method

2. Elongation to Tear (Ultimate Strain)

Elastomers, unlike metals or plastic materials, do not experience yielding or pronounced plastic transformations. The only failure mode for a rubber sample in tension is when it tears apart. Elongation to tear (ET), is a unique limit state defined for elastomeric materials. They can be loaded up to the point where they are torn apart. Strain at the onset of tearing is called elongation to tear. Elongation to break like strain is measured by percentage.

3. Modulus of Resiliency (Bulk Modulus)

Elastomers are often treated as incompressible materials for analytical convenience. However, in many instances the compressive response of elastomers is very important. The bulk modulus is a property

of a material which defines its resistance to a volume change when compressed. It can be expressed as $k = P / \varepsilon_v$, where P is the hydrostatic pressure, ε_v is the volumetric strain and k is the bulk modulus. In practice, a positive volumetric strain is defined as a decrease in volume. Measuring a material's strain response to an applied pressure is a simple test for bulk modulus. The bulk modulus can be expressed as the derivative (slope) of the pressure-strain curve. The Young's and Bulk moduli are related to each other through equation:

$$E = 3k - (1 - 2\nu) \quad \text{Equation 3-1}$$

4. Tensile Strength

The tensile strength is the stress associated with strain at ET. It is expressed in "Pascal" or "psi". Elastomers possess tensile strengths from 2 to 3 MPa depending on their manufacturing processes and types of reinforcing fillers, [14].

5. Modulus of Tension

The plot of stress as a function of tensile stress is nonlinear, meaning that Hook's law is not valid within a wide range of strain for elastomeric materials. For this reason it is not possible to derive a definitive modulus of elasticity except in regions within small strains. Tension modulus obtained this way is called "Secant Tension Modulus". Plot of tensile behavior of an elastomer traces a wide "S" profile. The

tensile modulus of rubber is not usually calculated directly, it is rather done using modulus of shear that itself obtained experimentally, Figure 3-14.

6. Modulus of Shear

Obtaining elastic moduli of elastomeric materials is very delicate task. It is due to dependency of elastic behavior of rubber on many variables such as the strain level, strain rate and shape factor. No reliable model has yet been developed capable of accounting for all variables precisely. Empirical equation is obtained through experimental efforts. The experimental set up is formed by an assembly consisting of two identical cylindrical rubber samples glued to loading arms that connect the samples to load actuator. The samples are loaded to 50% shear strain and lateral displacement is measured. The shear modulus is obtained to be:

$$G = \frac{K h_{r0}}{A_0} \quad \text{Equation 3-2}$$

where, K is stiffness of each bearing obtained by dividing the force H by lateral displacement, d , of each rubber when 50 % shear strain is imposed, h_r is the height of each rubber disk and A_0 is the section area of each rubber disk when it is not loaded. The schematic of testing set up suggested by NCHRP is presented in Figure 3-9.

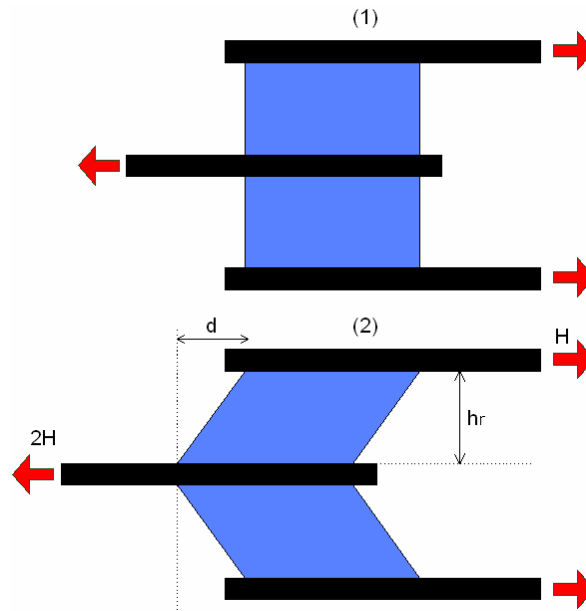


Figure 3-9: Schematic of the assembly used to obtain modulus of shear for elastomeric materials. A shear strain of 50% is sustained while modulus of shear is calculated (NCHRP 449)

7. Toughness

Toughness is a measure of the energy a sample of elastomeric material can consume before it tears apart. Toughness must not be mistaken by Resilience Toughness. Resilience Toughness is a dynamic characteristic of elastomers which refers to the area enclosed by a full hysteresis loop. It is more commonly known as damped energy, E_D .

8. Dynamic Properties of Rubber

The stiffening effect is caused by the natural hysteresis (internal damping) present in rubber materials, and low hysteresis rubbers like natural rubber exhibit relatively low dynamic stiffening. The degree of stiffening is dependent on the rubber properties, but for natural rubber the dynamic stiffness coefficient lies between 1.1 and 1.3 for rubbers

between 35 and 65 shore, [14]. In cyclic dynamic applications, the viscoelastic properties of elastomers are important. Dissipated energy, in the form of heat, arises from molecular friction as a result of applied load. When the loading and unloading cycle continues, the shape and position of the hysteresis curve changes. The response of a specimen to a sinusoidal deformation can best exhibit the dynamic properties of an elastomer. Engineering properties of a viscous material is proportional to the rate of deformation while properties an elastic material is proportional to the amount of deformation. Thereby, the property of rubber, which exhibits both viscous and nonlinear elastic behavior, is proportional to both rate and amount of deformation when it is subjected to dynamic loading.

3.2.3 High and Low Damping Rubbers

Damping property of natural and synthetic rubbers can be improved by compounding rubber gums with specific additives. Compounding can be done by adding substantial amounts of 1) Carbon black or 2) Additive of silanol group. There is, however, a trade off in each procedure for these improvements.

In structural engineering, high damping rubber bearings are ideal alternatives when a moderate level of energy dissipation is sufficient. This type of bearing can provide a damping of up to 10-15% of critical

($\xi=10-15$). This high damping capacity, however, is not achieved free, the trade off is losing elasticity of the rubber by increasing moduli of elasticity and lowering elongation to break capacity.

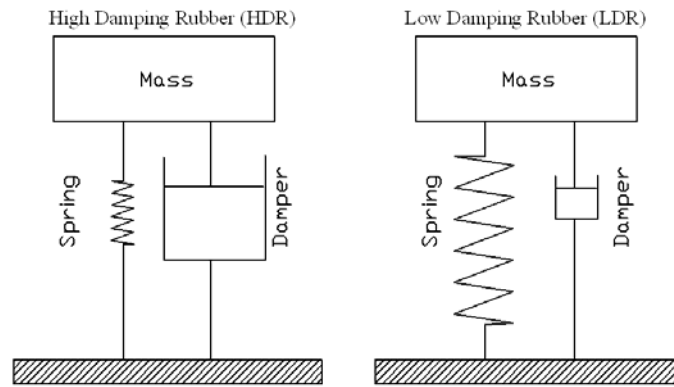


Figure 3-10: Spring-Dashpot example representing difference between high and low damping rubber

The compound of high damping rubbers usually contains a large amount of carbon black and some amount of a softening agent, a plasticizer and/or a resin in a large amount. Inclusion of a large amount of carbon black causes deterioration of workability upon kneading and molding. To reduce this effect, a polymer, having high glass transition point is used. The resulting rubber composition has a large dependence of elastic modulus on temperature and shows instable properties upon practical use. Also, Hitherto, a silicone rubber has been used as the main rubber component of rubber compositions having a high damping property and small dependence of elastic modulus on temperature. However, this rubber composition has a disadvantage in its fracture properties, it results in low tensile strength, low shear strength,

low shear elongation, etc. The comparison of some of the important characteristics of generic types of rubbers is listed In Table 3-4.

Table 3-4: Engineering properties of hard, normal and soft rubber. The moduli are obtained from cylindrical test samples with shape factor of 0.5 loaded to 50% strain at rate of 0.5Hz.

	Hardness	Tensile Strength (MPa)	ET (%)	G Modulus (MPa)
Hard	75±3	18	500	1.4
Normal	60±3	20	600	0.8
Soft	40±3	20	750	0.4

3.3 Lead

The damping characteristic of rubber is a function of frequency and amplitude of cyclic load. In many elastomeric bearings, rubber alone can not provide sufficient energy dissipation properties for seismic purposes. Though application of high damping rubber may help to some degree, long term durability of the end product might be sacrificed. Additional damping effect must be provided auxiliary elements. Lead plug is the major component in an elastomeric bearing which is considered to serve as the energy dissipating element. The enforced displacement results in yielding of the built-in lead plug, a process which is associated with consumption of energy. The plug is made of lead with 99% purity. Lead has been used to dissipate the energy associated with earthquake motion since 1970 [29]. It has been

used as a mechanical energy damper in many countries around the world.

The low melting temperature of lead (327°C), and its consequential malleability at room temperature, has made it an important material for technical investigation, modeling and some high deformation applications. The high energy dissipating capacity of lead and its good heat diffusivity, make it ideal for damping applications. Its tendency to recrystallize during deformation, and anneal at room temperature, make it a maintenance-free damping material, with limited susceptibility to fatigue during high cycle plastic deformation.

3.3.1 Damping Mechanism of Lead

This pressure, in the form of shear stress, distorts the shape of the crystals of the lead from coarse to fine in structure. This adds strength to the metal and thereby rigidity to the lead sample. However, in this instance, the added rigidity is a temporary phenomenon due to recrystallization. When lead is deformed at room temperature, the process of annealing recovery and recrystallization can begin during deformation. These mechanisms involve motion of point defects, dislocations and sub-grain boundaries. The recrystallization process requires nucleation and growth, and is very different to the recovery process and is extremely time and temperature dependent. The

material must be held at a temperature for a specific time to complete the process. Activation energy refers to the amount of energy required to initiate nucleation and subsequent recrystallization. This is considered an empirical constant, although it does not remain constant throughout a process, and instead changes constantly as the driving force resulting from cold working, is gradually depleted as the strain energy is invested in realignment of lattice discontinuities. Nucleation and growth occur together and the rate of recrystallization is dependent on the rate at which the nuclei form. Re-crystallization or relaxation of the lead occurs between 50% and 100% of the absolute melting temperature (the melting temperature of specimen measured in Kelvin degrees). The melting point of lead is 327 °C. This translates to 600 °K, also referred to as the absolute melting temperature of lead. A room temperature of around 23 °C or 296 °K is nearly 50 % of the absolute melting temperature of lead, and re-crystallization will begin as soon as the stretching of the lead is complete.

3.3.2 Mechanical Properties of Lead

Lead has a low modulus of elasticity, a low modulus of rigidity, and is a soft metal that is very malleable (easy to form). When lead is distorted (shape change due to temporary strain) it does not snap back to its original shape the way steel does. When subjected to loads,

lead exhibits a high degree of creep at room temperature since its melting temperature is relatively low. Creep can occur at low stresses, leading eventually to failure well below the nominal tensile strength of lead. If a weight is hung from a lead rod, the lead rod will elongate over time. When the weight is removed, the lead will not return to its original length because it has been permanently deformed. If the weight is not removed, the lead may eventually break. All materials expand or contract with an increase or decrease in temperature. The amount of this expansion or contraction is dependent on the coefficient of linear expansion. This coefficient is very rarely linear for a material, however, in most calculations a good average coefficient works well. Lead has a high coefficient of linear expansion. This means that a given length of a lead rod will exhibit a relatively large elongation for each degree of temperature it gains.

The tensile strength of pure lead is much lower than that of the other common metals (mild steel is about 15 times stronger; copper 10 times stronger). As with other metals, the tensile strength of lead can be considerably improved by small additions of alloying elements. Antimony, tin and copper are commonly used.

A discontinuity in the stacking order of the close packed plane in a lattice is a high energy region referred to as a "stacking fault". In

materials of high stacking fault energy, recovery is most pronounced and does not readily occur in low stacking fault materials, such as lead, Dynamic recrystallization is peculiar only to a few metals, in particular low stacking fault energy materials.

The stretching process will result in increased rigidity of the lead, but due to the phenomenon of re-crystallization this effect is temporary and will soon be lost at room temperature. A given piece of lead can only stretch a fixed amount before it will break. The continued deformation and following relaxation of the lead will form areas subject to cracking that will encourage corrosion and ultimate fracturing or failure of the lead.

Shear Modulus, $G(\text{Pa}) = 5.6 \times 10^9$

Young's Modulus, $E(\text{Pa}) = 16.0 \times 10^9$

Tensile Strength, $T_{\text{ult}} = 12 \times 10^6$

Density, $(\text{Kg}/\text{m}^3) = 11300$

Poisson's Ratio = 0.44

3.4 Steel

Non-reinforced rubber bearing can not resist high compression stress because of low modulus of elasticity and deflects significantly. This is because of high strain capacity. This not only results high poisson's ratio and excessive deflection but also results in instability of the bearing and

the isolated structure. The bulging of the elastomer is restrained by the steel reinforcement. Across the body of a bearing steel shims apply restraining shear stresses on the elastomer. It must be noted that low modulus of elasticity is desirable only at lateral deformation and not at vertical displacements. In addition to that, non-reinforced rubber bearing tends to slip when undergoes cyclic shear deformation (Stanton and Roeder, 1982). Figure 3-11 schematically show how addition of steel shims improves stability of a rubber bearing.

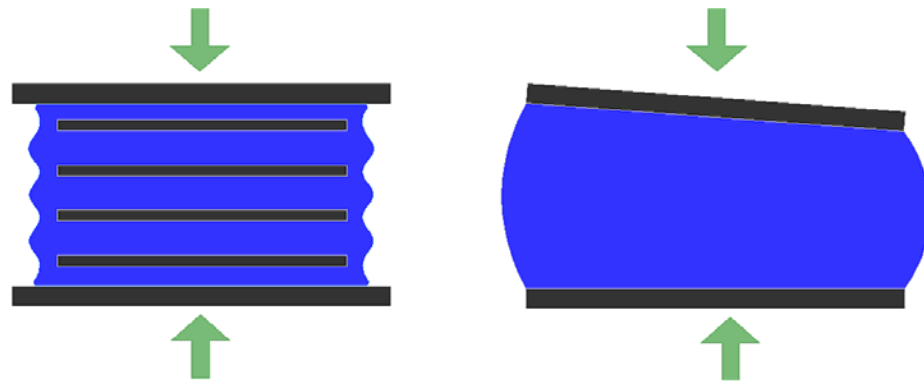


Figure 3-11: Using steel shims laminated with rubber improves stability of elastomeric bearings significantly

Another very important aspect of using steel plate is shear rigidity. Energy is dissipated primarily by yielding of lead plugs and formation of plastic hinges on it. The quality and length of these plastic hinges within the lead plug are highly depended on confining force applied to the lead plug. In a lead core elastomeric bearing since rubber has very low rigidity compare to the lead it can not force the lead plug to yield effectively, and as it gets farther from end rims toward the mid-height of

a bearing the effect becomes more significant. Presence of steel plates provides enough shear rigidity for application of more effective confining force.

Steel is a form of iron mixed with a percentage of carbon to reach desirable levels of strength and stiffness. The amount carbon varies with It is also alloyed with a group of other metals, like chromium, cobalt, columbium [niobium], molybdenum, nickel, titanium, tungsten, vanadium and zirconium, to improve its physical and chemical properties such as capabilities of being be machined, welded, and forged, all to varying degrees, depending on the type of steel. Steel contains less carbon than cast iron, but considerably more than wrought iron (0.04 percent carbon). The carbon content of mild steel which is universally used for ornamental iron work has up to about 0.25 percent. Structural steel contains carbon from 0.3 to 2.1 percent. Basic structural carbon steels are alloyed with chromium and nickel. Steel is often heat treated to improve/alter the mechanical properties such as ductility, hardness, yield strength, or impact resistance.

The heat treatment of carbon steels is typically done in two methods of "Normalizing" and "Quenching and Tempering". Normalizing involves air-cooling and produces essentially the same microstructure as that of hot-rolled carbon steel, except that the heat

treatment produces a finer grain size. This grain refinement makes steel stronger, tougher, and more uniform throughout. Quenching and Tempering, which is heating to about 900 °C, water quenching, and tempering at temperatures of 480 to 600 °C or higher, can provide a tempered microstructure that results in better combinations of strength and toughness.

The highlighted properties of structural steel that need to be considered for analysis of bearings are:

Young's Modulus, $E = 200 \times 10^9 \text{ Pa}$


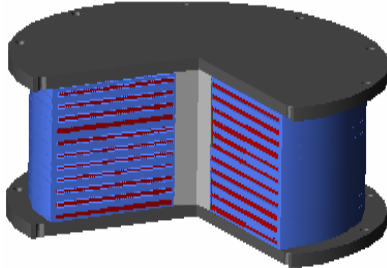

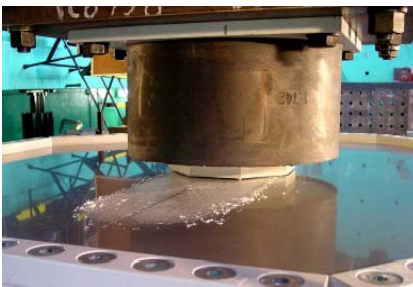

Tensile Strength, $T_{ult} = 400 \times 10^6 - 500 \times 10^6 \text{ Pa}$

Density $= 7900 \text{ Kg/m}^3$

Poisson's Ratio $= 0.33$

Major materials used in manufacturing common types of Seismic Response Modification Devices are listed in Table 3-5.

Table 3-5: materials used in manufacturing common types of Seismic Response Modification Devices

Device		Major Constituent Materials
Laminated Rubber Bearings		<ul style="list-style-type: none"> • High Damping Natural Rubber (HDNR) High Damping Natural Rubber (LDNR) • Synthetic Rubber (Neoprene) • Steel
Lead Core Rubber Bearings		<ul style="list-style-type: none"> • High Damping Natural Rubber (HDNR) • Low Damping Natural Rubber (LDNR) • Synthetic Rubber (Neoprene) • Steel • Lead
Sliding Bearings		<ul style="list-style-type: none"> • Austenitic Stainless Steel • Self-lubricating Material • Natural or synthetic rubber (for seals) • Steel • Elastic Polymer (for seals)
Hybrids		<ul style="list-style-type: none"> • High Damping Natural Rubber (HDNR) • High Damping Natural Rubber (LDNR) • Synthetic Rubber (Neoprene) • Steel • Lead • Austenitic Stainless Steel • Teflon
Viscous Dampers		<ul style="list-style-type: none"> • Viscous Fluid (Silicon Fluid) • Bronze • Stainless Steel • Rubber • Elastic Polymers (for seals and O-Rings)

4

Deterioration of Elastomeric Bearings from Material Point of View

In order to make a thorough investigation, this research was focused on only one family of the Seismic Response Modification Devices, which was selected to be elastomeric bearing. The selection was made based on the wide range of application and increasing popularity of these devices. Due to existence of a complex mode of degradation, a methodology is necessary to assess reliability of performance at any point of services life of such devices. The conducted studies and the proposed methodology in this research study is tailored for elastomeric bearings, however, the general approach can be applied to other types of SRMDs.

Natural or synthetic rubber, steel, and lead are prominent materials used in manufacturing the most common types of elastomeric bearings. Elastomeric bearings have excellent seismic performance capabilities, ease of installation, and relatively moderate cost. In addition to benefits offered by elastomeric bearing at the time seismic events, these devices are capable of accommodating odd

displacements such as in and out of plane torsions. Elastomeric bearings, though function effectively in mitigating damage caused by earthquakes, are vulnerable to property degradation. This could initiate from degradation of constituent materials.

4.1 Deterioration of Rubber

Degradation of mechanical properties of many types of rubbers is a function of factors such as temperature, oxygen, time etc. The significance of each influencing factor varies widely with respect to the application and loading and environmental conditions at which the rubber is used. For instance, oxidation may not be a matter of concern if the rubber is used in areas where the ambient temperature is above freezing point, or relaxation which is another mode of degradation for rubber products could have notable role only if the rubber sustain a strain of 100% or greater for long period of time.

Typically the degree of degradation is measured by studying the change of mechanical properties such tensile strength, modulus of shear and tension, elongation to break and hardness. Aging of rubber components is typically associated with oxidation or vulcanization. Oxygen levels in rubber components can significantly change with time. Laboratory simulated aging of rubber samples using accelerated exposure conditions, may also produce significant changes in oxygen

content. Recently, there has been significant interest in expanding the understanding of the aging process of parts made of rubber.

4.1.1 Hardening of Rubber and the Effect of Temperature

Hardening is widely known to be the primary mode of degradation for rubber products. Hardening of rubber is the unfavorable sub-result of vulcanization process. Formation of Covalent Bond between left over sulfurs from initial vulcanization process and polymer chains increases hardness of rubber.

Figure 4-1 show the polymer chains and formation of Covalent cross bonds, technically termed as crosslink, as a result of vulcanization process.

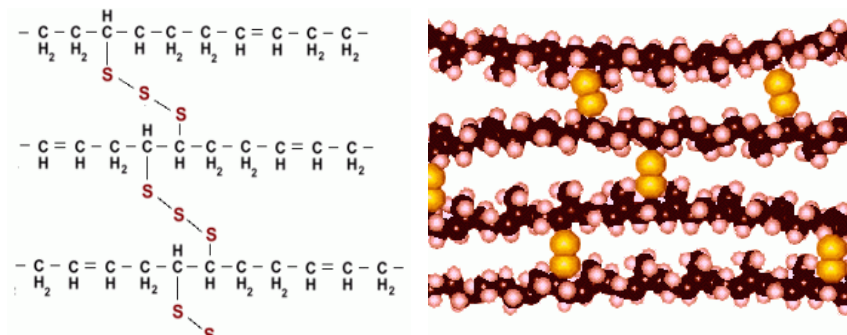


Figure 4-1: Formation of Covalent Bond through out vulcanization process

Variation of hardness itself affects many other properties including both modulus of elasticity and damping of rubber. This is a continuous process taking place through out the life span of rubber. The hardening effects at some point make the rubber too hard to function as an elastic material. Plot in (Figure 4-2) shows some

engineering properties of rubber affected by rubber hardening. As it can be seen in the figure, the tear and tensile strengths which are the most valuable properties of rubbers drop sharply as crosslink density increases.

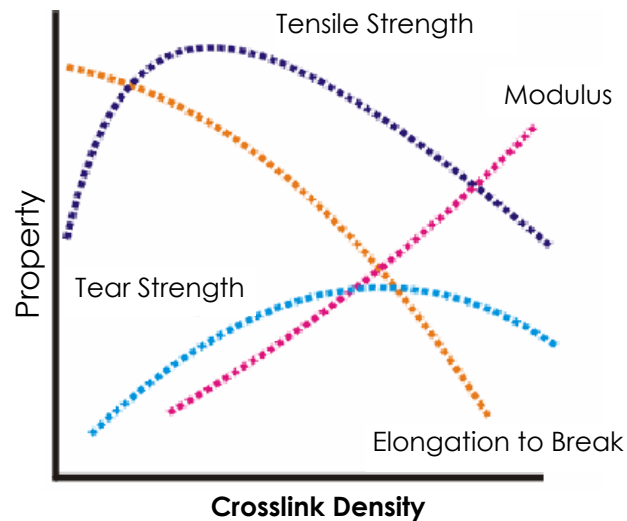


Figure 4-2: Change in engineering properties of rubber as cross link density increases

The rate at which this hardening or over-vulcanization process takes place is mainly subjected to the amount of sulfur added to the rubber compound and the temperature to which the rubber is exposed to during its service life.

Temperature affects the performance of rubber bearing in more than one way. As mentioned earlier, modulus of elasticity and damping ratio of the entire body of a rubber sample changes as it is exposed to higher degrees of temperature [10].

Plots in Figure 4-3 show the effects of over vulcanization by heat on damping properties and lateral stiffness of rubber samples. These rubber samples were artificially aged by placing into an oven [10].

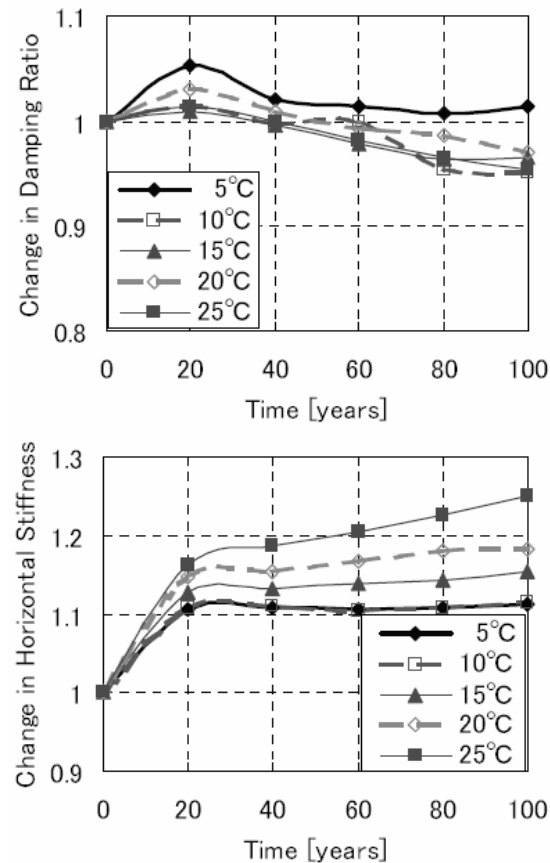


Figure 4-3: Variation of modulus of elasticity and damping ratio of rubber samples when exposed to various degrees of temperature [10]

4.1.2 Cracking and Debond

Formation of a unique temperature profile within an elastomeric bearing provides a situation through which temperature may contribute in degradation of rubber bearings. The rubber at vicinity of the lead plugs and steel shims is exposed to higher temperature. It

suggests the existence of a non-uniform temperature profile within the body of bearing which can lead to a non-uniform vulcanization rate.

Figure 4-4 shows the schematic of internal view of a lead core bearing. It shows how the rubber exposed to higher temperature at the interface with steel plated and lead plug.

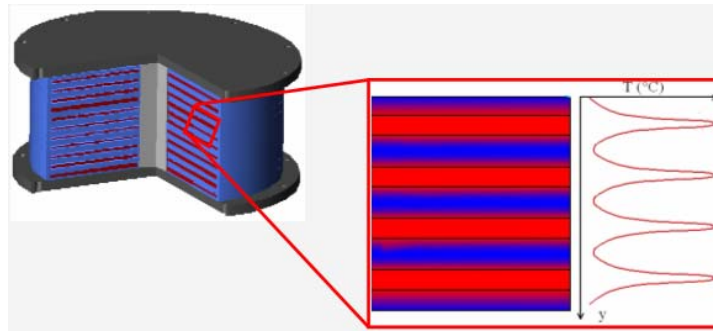


Figure 4-4: Rubber at vicinity of steel shims is exposed to higher temperature i.e. hardening happens at higher rate

As a result of exposure to high temperature, at location with high concentrated shear stress, rubber is not adequately elastic and cracks.

The stress distribution phenomenon and the situation that leads to cracking of rubber is shown in Figure 4-5.

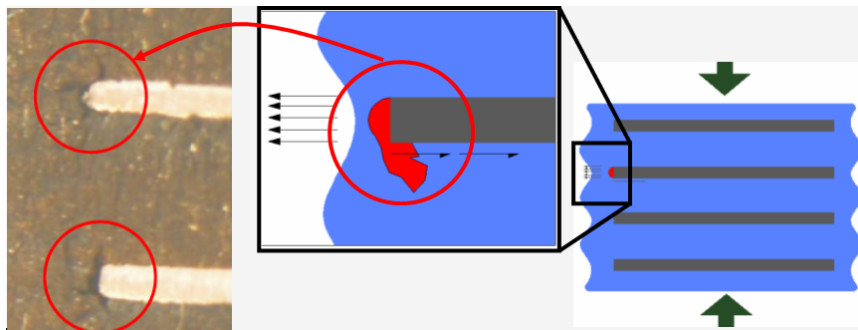


Figure 4-5: High rate of vulcanization makes rubber lose its elasticity and become more vulnerable to cracking and debonding at the areas around steel shims

Figure 4-6 shows the real examples of rubber degradation that resulted in cracking rubber at corners of steel plates. The bulges on sides of the bearing indicate the bond was lost between rubber and shims.

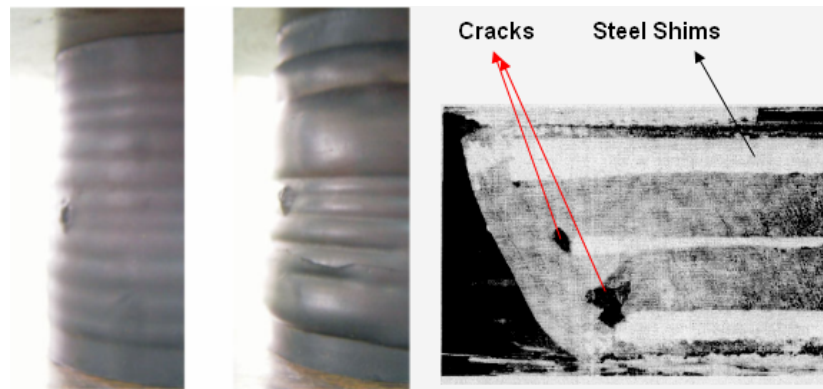


Figure 4-6: High rate of vulcanization make rubber lose its elasticity and more vulnerable to cracking and debonding. This phenomenon eventually results in complete failure of the bearing. Source: Yoshito Itoh, Dept of Civil Eng., Nagoya University, Japan [1]

However, nowadays, because of the advancement in techniques used in manufacturing the elastomeric bearings, which resulted in improvement in rubber compounds and their bonding to steel shims, disbond of this nature is no longer a matter of concern.

4.1.3 Fatigue of Rubber

Rubber is subjected to fatigue degradation. According to the result of experiments performed by Hsoun-Wei Chou, Jong-Shin Huang [3] on scaled bearing samples stiffness of laminated rubber dropped about 30% in after about 30 million cycles at 50% strain Figure 4-7.

Normalizes Stiffness versus Cycle Number

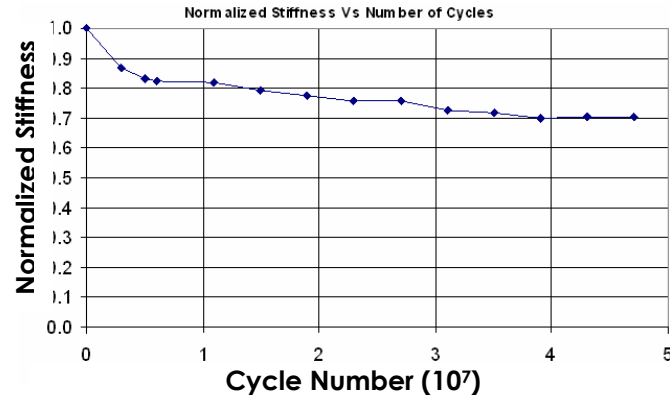


Figure 4-7: Variation of normalized stiffness as a function of number of cycles load applied to a rubber sample at velocity of 5mm/sec and 50% shear strain

4.1.4 Scragging

Scragging is a process at which an elastomeric bearing is subjected to one or more cycles of large amplitude displacement. The scragging process distorts the molecular structure of the elastomer and results in more stable hysteresis at strain levels lower than that to which the elastomer was scragged.

Figure 4-8 shows the scragging effect on a bearing at low frequency of 0.2 in/sec load cycles on 4 sequential cycles. It is observed that after the first cycle the effect becomes negligible at low frequency loading.

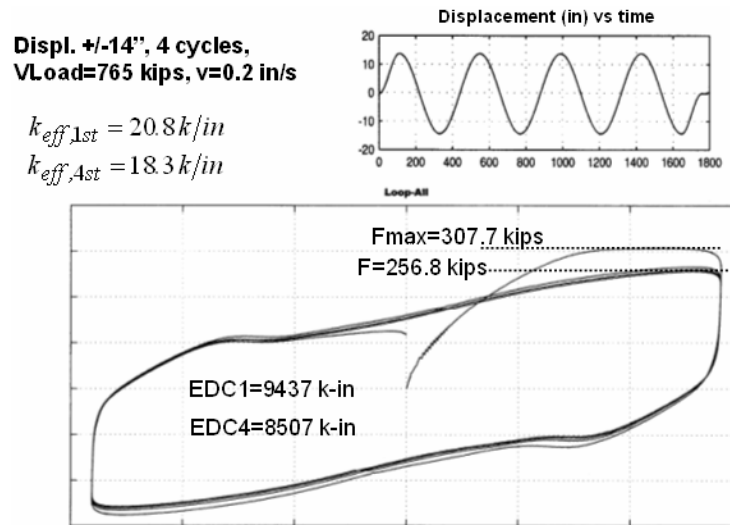


Figure 4-8: Hysteresis loops showing scragging effect at low frequency cyclic load

Although it is usually assumed that the scragged properties of an elastomer remain unchanged with time, recent studies suggest likelihood of partial recovery of unscragged properties. The extent of this recovery depends on the quality of elastomer compound.

It is also observed that the scragging is more pronounced at high frequency loadings. Figure 4-9 shows the scragging effect on a bearing loaded at frequency of 42.5 (in/sec).

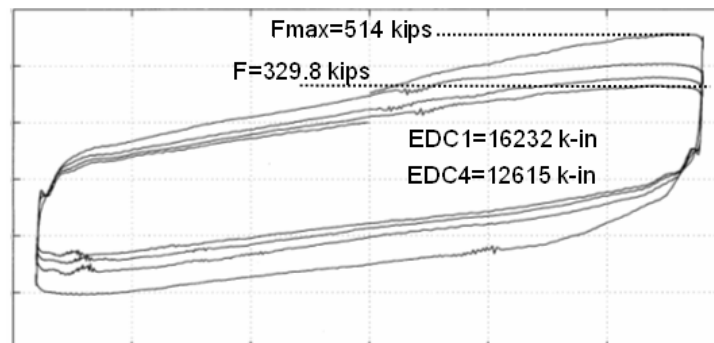


Figure 4-9: Hysteresis loops showing scragging effect at high frequency cyclic load

4.2 Deterioration of Lead

Lead is subjected to deterioration. But, unlike many other metals, it is not vulnerable to degradation due chemical changes such as oxidation or corrosion and so forth. Degradation of lead is mainly due to the quality of physical disturbance that is applied to it. Physical disturbance are such as stretching which makes the lead to behave plastic, or sustaining load that results in creeping. Thermal disturbance makes lead to soften rapidly and loses its strength and rigidity.

The common failure mechanism for lead in tension is microvoid coalescence. It is postulated that hydrostatic pressure will reduce the tensile stresses in the specimen neck, thus extending the strain to failure of the material. It has been observed that the relative fracture area failing by void coalescence decreases with pressure, whilst the relative area of shear fracture increases. At a transition temperature the fracture mechanism has been observed to change from void coalescence to fracture via highly localized bands of intense shear deformation.

4.2.1 Oxidation of Lead

Unlike steel lead is not vulnerable to detrimental oxidation. Lead like copper and aluminum forms a protective passive film by reaction with oxygen. This passive film protects the metal from further oxidation in

similar atmospheric conditions and the structural strength is retained. The film has two layers, a very thin, tightly adhering inner barrier layer and a much thicker outer porous layer, which are integral to each other and to the base material, i.e. the film is not a coating and in normal conditions will restore itself if damaged.

4.2.2 Fatigue of Lead

Lead is subject to fatigue deteriorations. This phenomenon is the failure of metals, after repeated loading cycles, at stresses below the normal tensile strength of the material. It occurs because of the growth of tiny cracks within the material - stresses at the crack tip are much higher than across the bulk of the specimen. It can be caused by mechanical loading and even cycles of thermal expansion. The shear test of 100% strain for 20 cycles at a frequency of 1 Hz is a standard method of testing for unconstrained lead introduced by ASTM. The results of such experiments show that during unconstrained cyclic deformation to very high strains, lead samples provided damping consistently within 20 % of the initial cycle. Failure was by cracking induced by geometric breakdown.

Constrained samples under pressure subjected to 144,000 cycles, producing consistent damping. The damping capacity of lead is 47 MJ/m³ per cycle of strain of +/-1. From the characteristic features

observed in the stress-strain diagram and the features of the microstructure of lead it has been seen that pure lead recrystallizes at room temperature. Also, from the investigations conducted on this area by of other researchers it appears that recrystallization occurs statically and dynamically. Specimens under confinement fail in a semi-ductile manner as opposed to the high ductility failure prevalent in unconfined lead.

4.2.3 Distortion of Lead Plug

Lead is mainly used as auxiliary energy dissipating element in the form of cylindrical shape in lead core elastomeric bearings. The geometry of lead plugs can be severely distorted when bearings are pushed beyond their limits. The possibility of failure is higher if lead plugs of inappropriate size are used. Based on the model suggested by Kelly and Koh the core dissipates energy by formation plastic hinges at the ends where it is subjected to flexural stresses due to lateral motion and, by shear resistance at the midsection when it undergoes almost pure shear stress. The quality of this process depends on how well the core is gripped and confined by the rubber-shim assembly.

Figure 4-10 shows analytical spring model of elastomeric bearing suggested by Kelly and Koh,

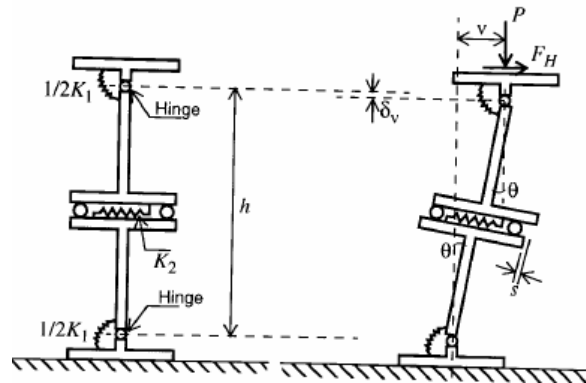


Figure 4-10: Analytical spring model of elastomeric bearing suggested by Kelly and Koh

The size of the lead plug and its proportionality with the bearing's diameter is the key factor in optimizing the performance of a lead core elastomeric bearing. As the core becomes wider in radius shear force along the axis increases this could end in tearing the plug along its axis. In these rare situations, depending on the rate of applied load or ambient temperature the shear force imposed to the lead plug may result in catastrophic shear failure of the lead plug along its axis.

Figure 4-11 show the situation which may result in shear failure. At left, is an actual lead plug failed in shear along its axis.

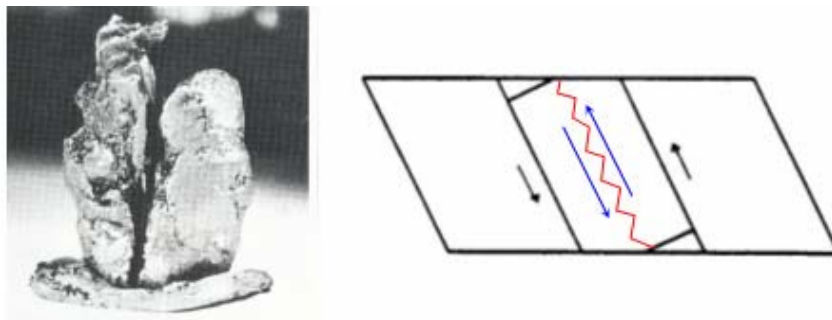


Figure 4-11: Failure of a bearing due to shear failure along the axis. (Source: Report No. 289, S.M Built, Dept. of Civil Engineering, University of Auckland, New Zealand)

4.3 Degradation of Steel

Steel, in terms of degradation is opposite of lead. Steel is very resistant to physical disturbance but very susceptible to degradations due chemical reaction. The chemical reactions are such as, oxidation, corrosion, reaction with acids etc.

4.3.1 Corrosion

In saline environment, due to permeability of rubber (capability of absorption of liquids) electrolyte is accumulated in the cracks and debonded regions with in the rubber and the rubber-shims interface. This electrolyte, together with presence of carbon black used in rubber compound and also presence of lead in the core, forms a strong corrosive system. Corrosion is the main cause of debonding between rubber and steel shims. The carbon black used in rubber compound as additional filler though may improve damping properties of rubber product it serves as cathode electrode that contributes in formation of corrosion system.

Figure 4-12 shows the schematic of cracking of rubber due to hardening and formation of corrosion environment.

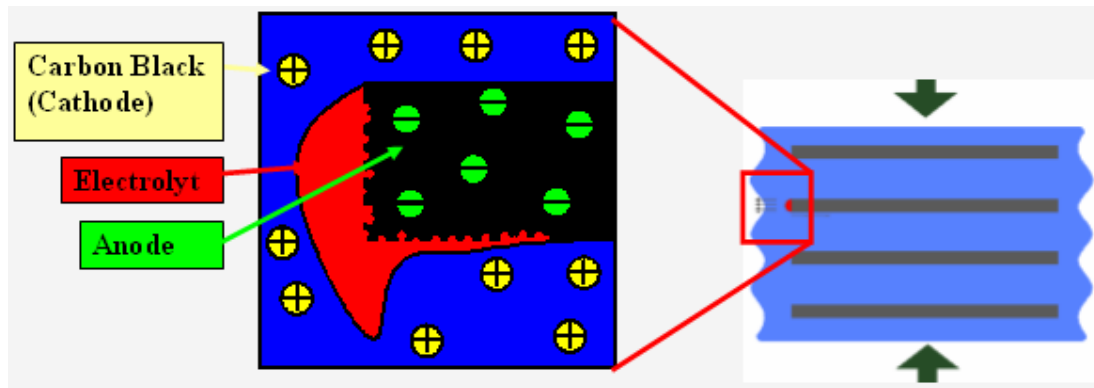


Figure 4-12: Formation of corrosion system in saline environment

Corrosion of steel shims is not an independent effect and is highly depended on quality and rate of crack formation within rubber and the condition and factors that may contribute on the phenomenon.

4.4 Highlight of the Chapter

The major engineering characteristics that are subjected to degradation and the conditions in which degradation might take place were introduced and discussed in this chapter. For instance, in an elastomeric bearing, damping characteristics and energy dissipated per cycle is defined by the stiffness and maximum force at each hysteretic loop. Hence, these are the two characteristics on which the response of a bearing is depended.

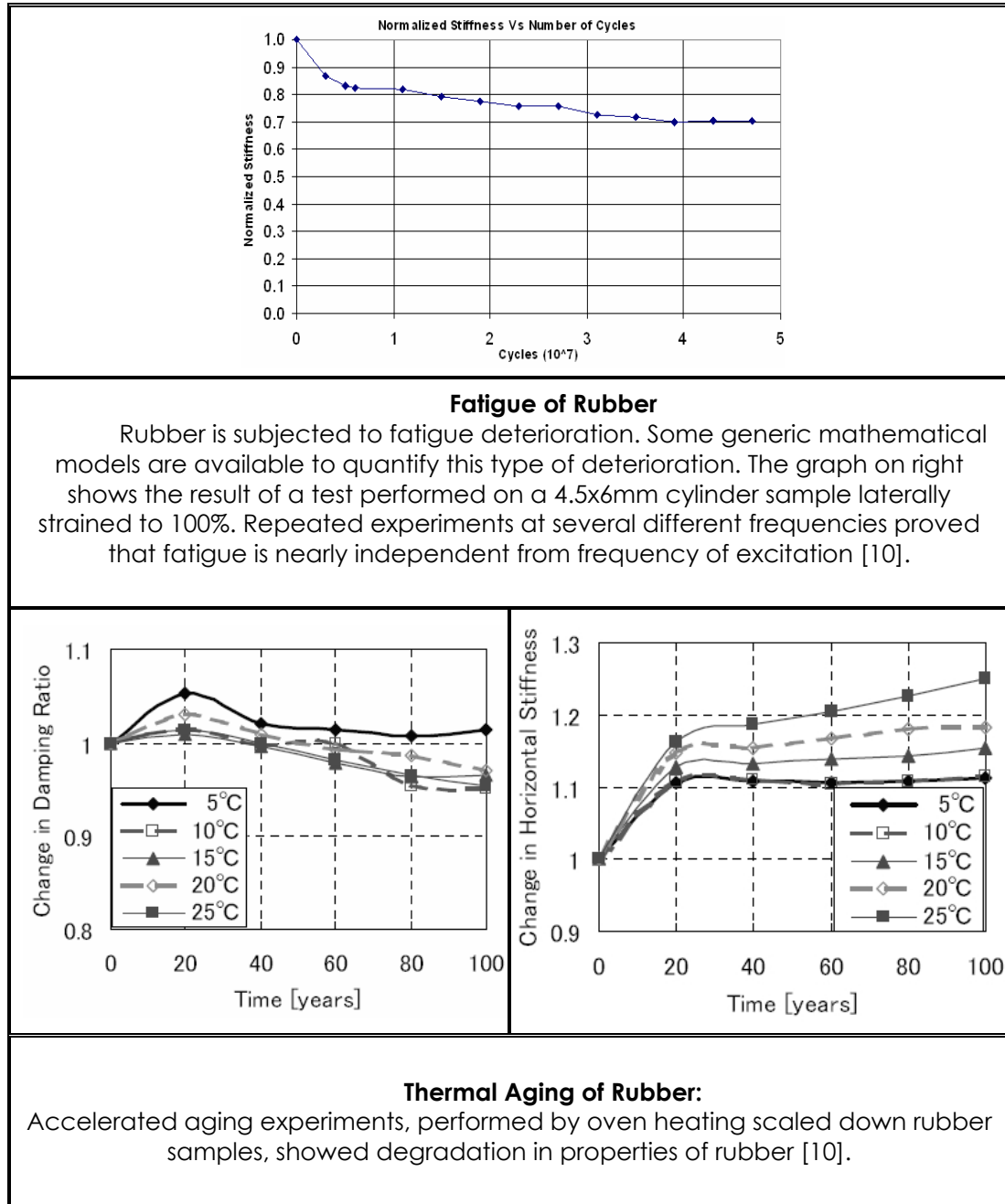
In literature, there is insufficient information available about the degradation phenomenon in elastomeric bearings. A brief summary of what was discussed in this chapter about the types of degradation and situation in which the phenomenon takes place is presented in Table 4-

1. Also, in the table the primary materials, used in manufacturing elastomeric bearings, are also briefly introduced.

Table 4-1: Prominent materials used in manufacturing elastomeric bearing and possible degradation modes

Category		Predominant degradations		Affected Properties
Elastomeric Bearings	Natural Rubber	<ul style="list-style-type: none"> • Thermal aging (over vulcanization) • Low temperature crystallization 	<ul style="list-style-type: none"> • Strong acids, fats, oils, greases, most hydrocarbons • Ozone attack 	<ul style="list-style-type: none"> • Stiffness (and natural period as a result) • Damping ratio
	Synthetic Rubber	<ul style="list-style-type: none"> • Oxidation • UV attack • Fatigue of rubber • Scragging 	<ul style="list-style-type: none"> • Strong oxidizing acids, esters, ketones, chlorinated, aromatic and nitro hydrocarbons 	
	Steel	<ul style="list-style-type: none"> • Corrosion (attacked by saline, acidic and alkaline chemicals) • Oxidation 		Tensile and Shear Strength
	Lead	<ul style="list-style-type: none"> • Formation of microvoid coalescence when enduring cyclic tensile-compressive load. • Severe distortion at high strain. During unconstrained cyclic deformation to very high strains lead starts cracking. 		<ul style="list-style-type: none"> • Shear modulus • Hysteretic Stiffness • Damping Ratio

Table 4-2: Available models used for quantification of property losses in elastomeric bearings



5

Degradation Phenomenon in Elastomeric Bearings and the Contributing Factors

Ambient vibration is the resultant of some forces applied to a structure simultaneously. Ambient vibration is activated by forces such as wind load, friction forces due to stop-and-go action of on going traffic on a bridge and also thermal expansion and contractions. It is documented [3], [15], [27], [28] that a number of mechanical characteristics of elastomeric bearings in service are changed as a result of exposure to certain load and environmental conditions. Relatively complete set of information about degradation of constituents of elastomeric bearing is available [1], [3], [6], [8]. However, there is a lack for methodologies to quantify and assess the degradation phenomenon and to predict residual life of elastomeric bearings.

Figure 5-1 presents the typical environmental elements contributing in formation of "Ambient Condition".

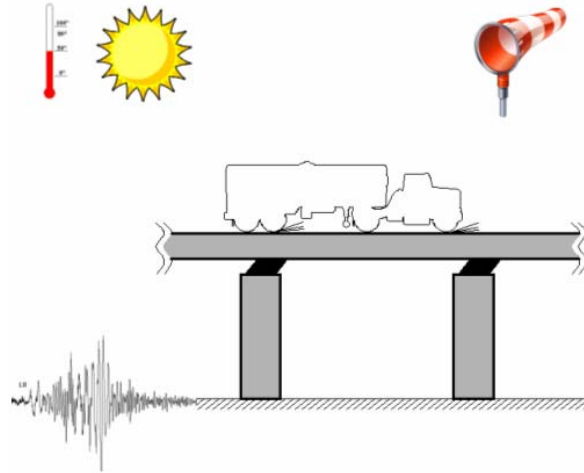


Figure 5-1: Loading and environmental conditions create transient and steady state motion to in-service elastomeric bearings

Despite all the effort in literature, placed to quantify the property variation of bearings, no realistic measuring criteria for degradation of elastomeric bearings has yet been developed. It is partially due to:

1. Complexity in aging behavior of rubber and lack of a comprehensive knowledge about contributing factors in this phenomenon
2. Lack of a reliable and cost effective methodology to acquire information about the internal temperature of elastomeric bearings when they are dynamically loaded

5.1 Property Deterioration and Connection with Heat

It is postulated that a significant amount of thermal energy is generated within the body of the bearing through hysteretic action. Hence from the material point of view, heat is likely responsible for a

wide range of property losses in elastomeric bearings. The above statements are yet to be validated and quantified through different experimental and theoretical studies. Also, for criticality analysis, it is necessary to determine a degree to which each engineering characteristic is affected.

In Figure 5-2, the subjects of the present chapter are highlighted in red. The specific goal of this step will be the validation of the occurrence of property changes due to cyclic loading of the bearings. In particular, the focus was to address the variations of performance characteristics of the bearing as a function of lead and rubber contribution. The energy dissipated per cycle (EDC) was then associated to variation and distribution of temperature inside the bearing.

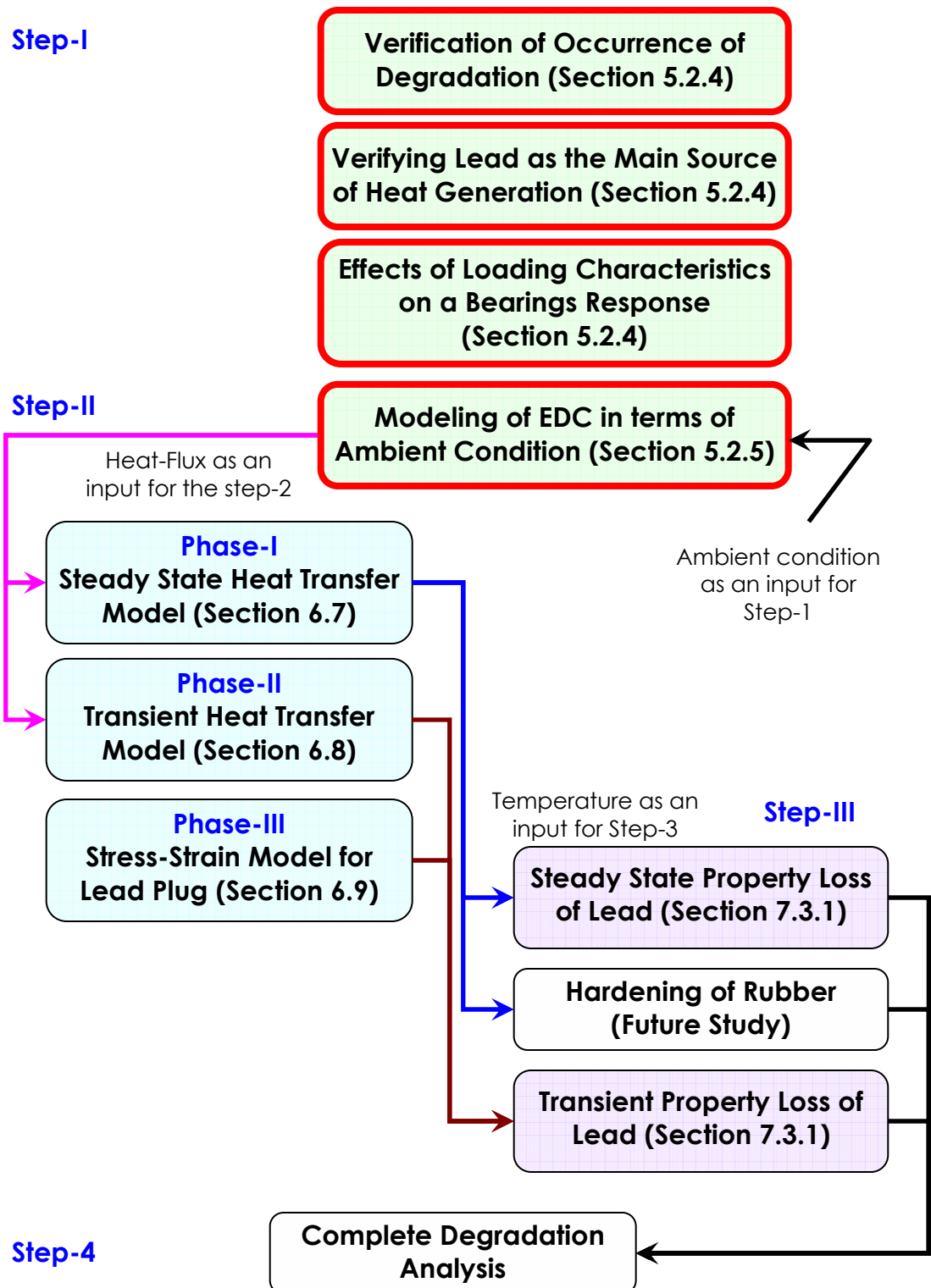


Figure 5-2: Complete flow diagram of steps taken for degradation analysis

5.2 Experiment-1

The objectives discussed in the introduction of the present chapter were pursued through Experiment-1.

For this experiment, four bearings of different sizes were selected. Exact detail of the test bearings is given in Figure 5-5 to Figure 5-8. Two cylindrical lead core laminated bearings, one cylindrical laminated rubber bearing with no lead plug and a square bearing included in the selection. This careful selection of the test bearings and the divers loading protocols made it possible to investigate the effects of:

1. The size and shape of a bearing on its response by comparison between cylindrical and square bearings
2. The existence of lead plug by comparison of responses to identical bearings, one with lead plug and one without it, and applying identical load protocol to both
3. The loading characteristics on the response of a bearing by applying divers load protocols that included various amplitudes and velocities.

The bearings were laterally loaded with sinusoidal cyclic load of various rates. Each load case was specified by five characteristics:

- Type of load. Harmonic loads in the form of sinusoidal were applied to all test bearings during Experiment-1, (Figure 5-3).

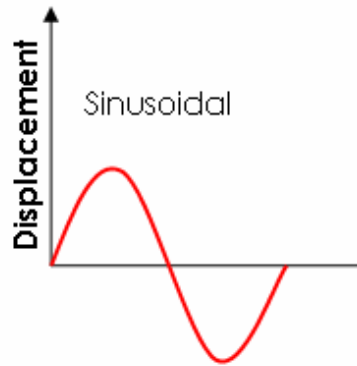


Figure 5-3: Harmonic sinusoidal was the type excitation applied to all of the bearings through the Experiment-1

- Direction. Unidirectional, East-West, symmetrical load was applied.
- Displacement amplitude, measured in mm. Various displacement amplitude applied within each test protocol
- Velocity amplitude measured in mm/sec. Different values of displacement amplitude applied within each test protocol

A schematic overview of testing set up and loading configuration is presented in Figure 5-4. As indicated in the figure, shear force is applied to the bottom end plate while upper plate is fixed.

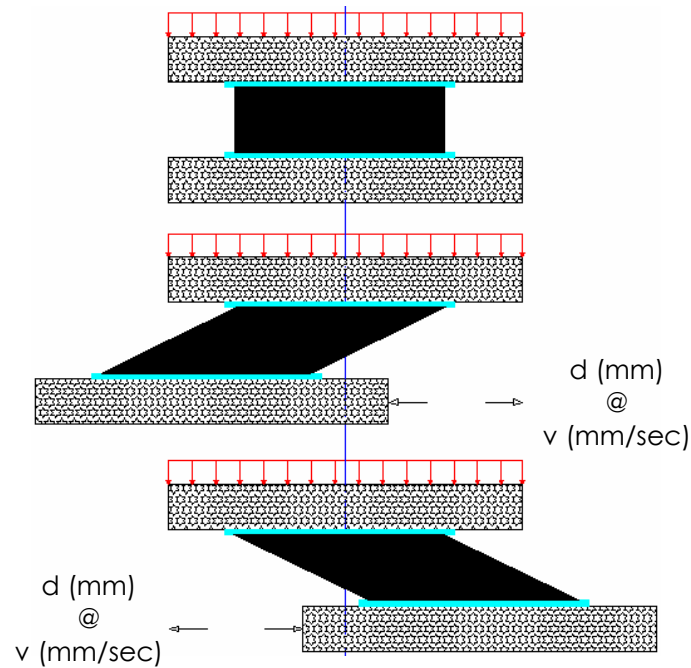


Figure 5-4: Schematic of Testing set up

5.2.1 Specification of Test Bearings

1. Takinaka LRB700 Bearing

LRB700, one of the three cylindrical bearings, is made by lamination of soft rubber layer of 4.7 mm thick with steel plates of 3.1 mm thick in between. A lamination of total of 30 rubber layers and 29 steel plates formed the body of the bearing to reach an effective height of 230.9 mm and together with the end plates a total height of 286.9 mm was reached. A cylindrical lead plug of 140 mm in diameter and height of 258.9 mm was placed coaxially inside the bearing. Figure 5.5 shows the schematic of cross section view and notations of bearing LRB700.

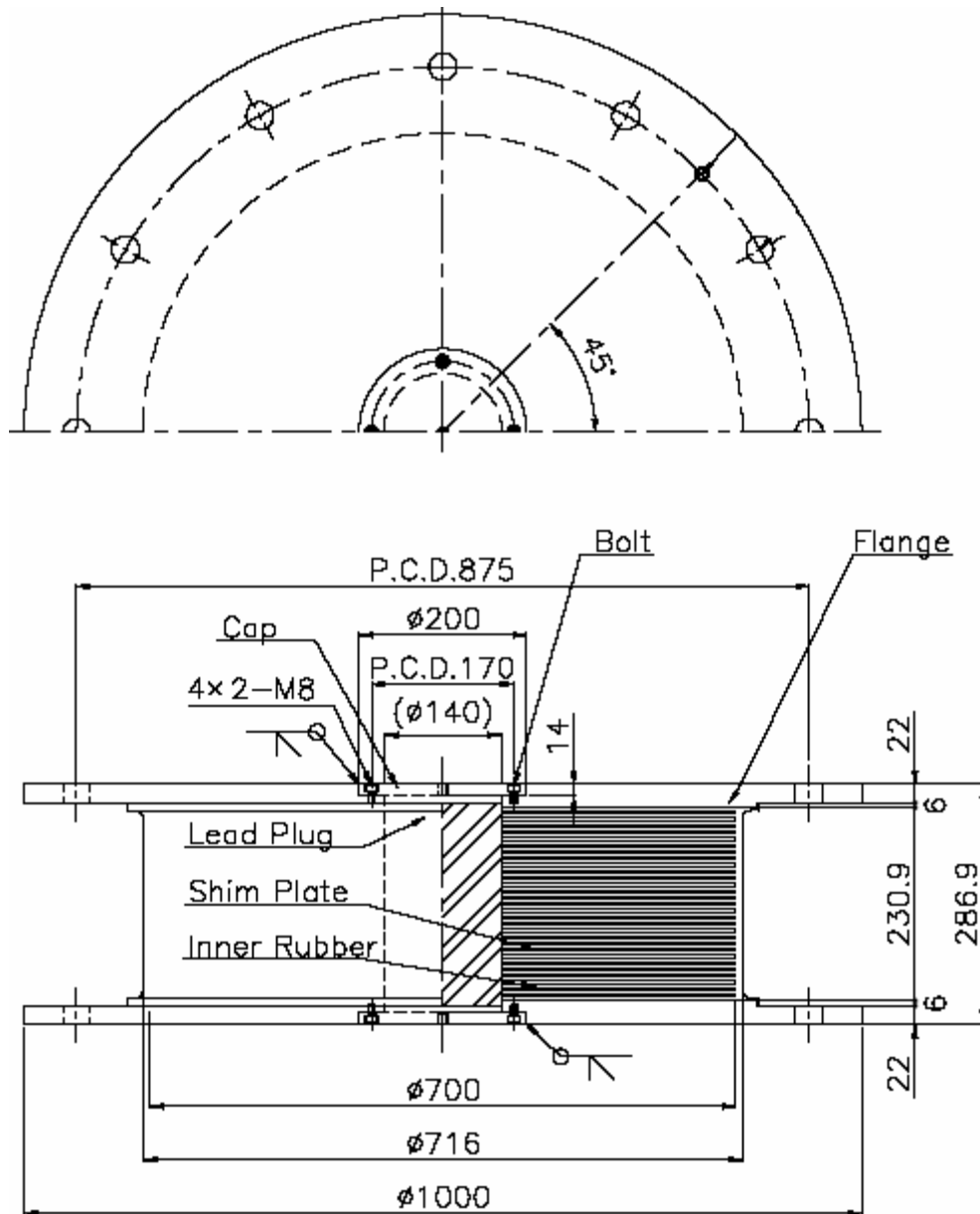


Figure 5-5: Drawing of section view of LRB700

2. Takinaka LRB1300 Bearing

The other cylindrical bearing, LRB1300 is made by lamination of soft rubber layers of 8.7 mm thick with steel plates of 4.4 mm thick in

between. Like in LRB700, lamination of total number of 30 rubber layers and 29 steel plates used to reach an effective height of 388.6 mm, and together with the end plates a total height of 468.6 mm was reached. A lead plug of 260 mm in diameter and height of 432.6 mm was coaxially built in the assembly. Both cylindrical bearings have the lead-to-rubber volume ratios of nearly 0.065.

Figure 5.6 shows the schematic of cross section view and detail of the bearing LRB1300.

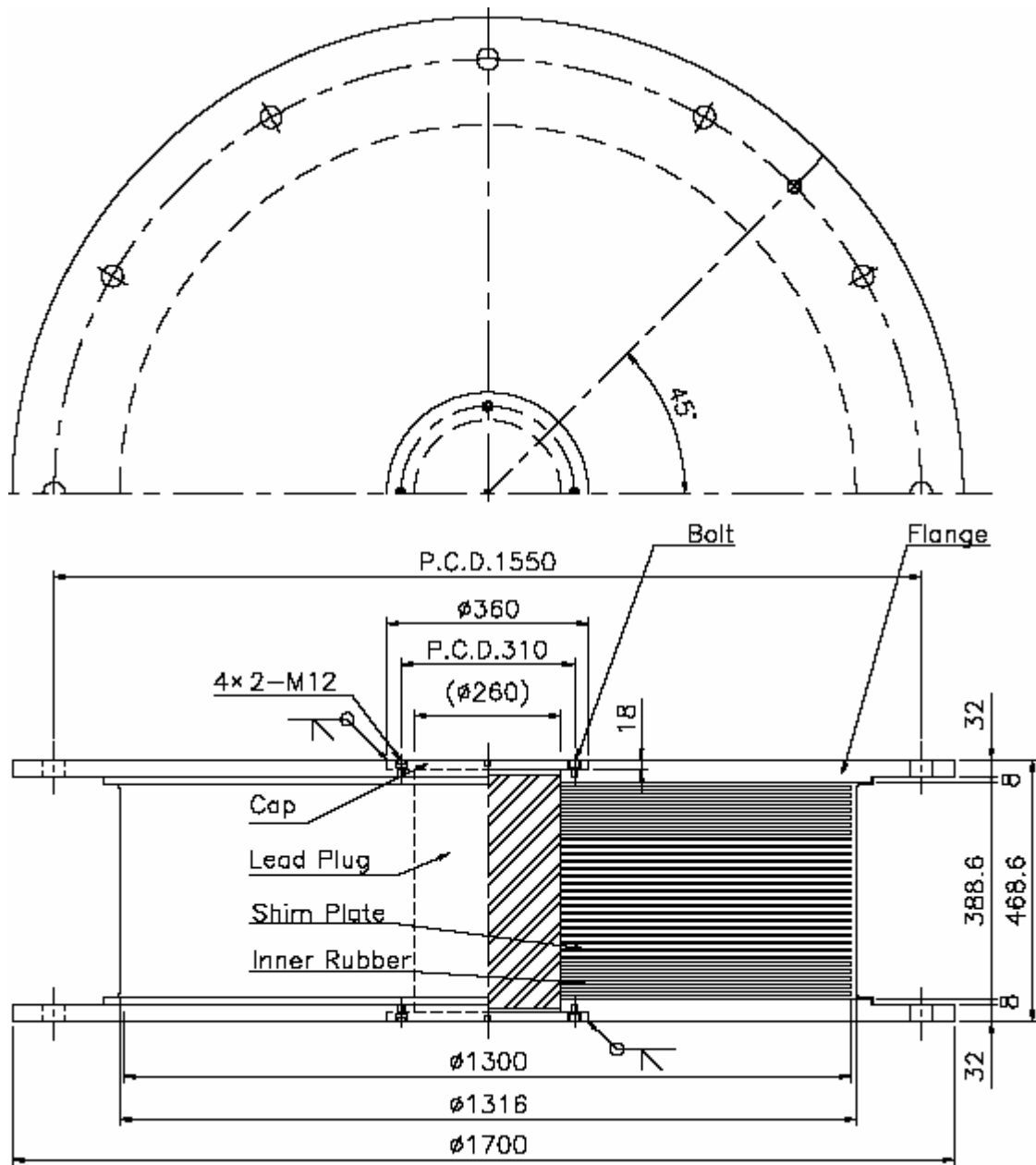


Figure 5-6: Drawing of section view of LRB1300

3. Takinaka NRB1300 Bearing

The other cylindrical bearing, NRB1300 had exact dimension and lamination detail as LRB1300 and made of the same type of rubber.

However, it had no lead plug installed. Figure 5.7 shows the schematic of cross section view and detail of the bearing NRB1300.

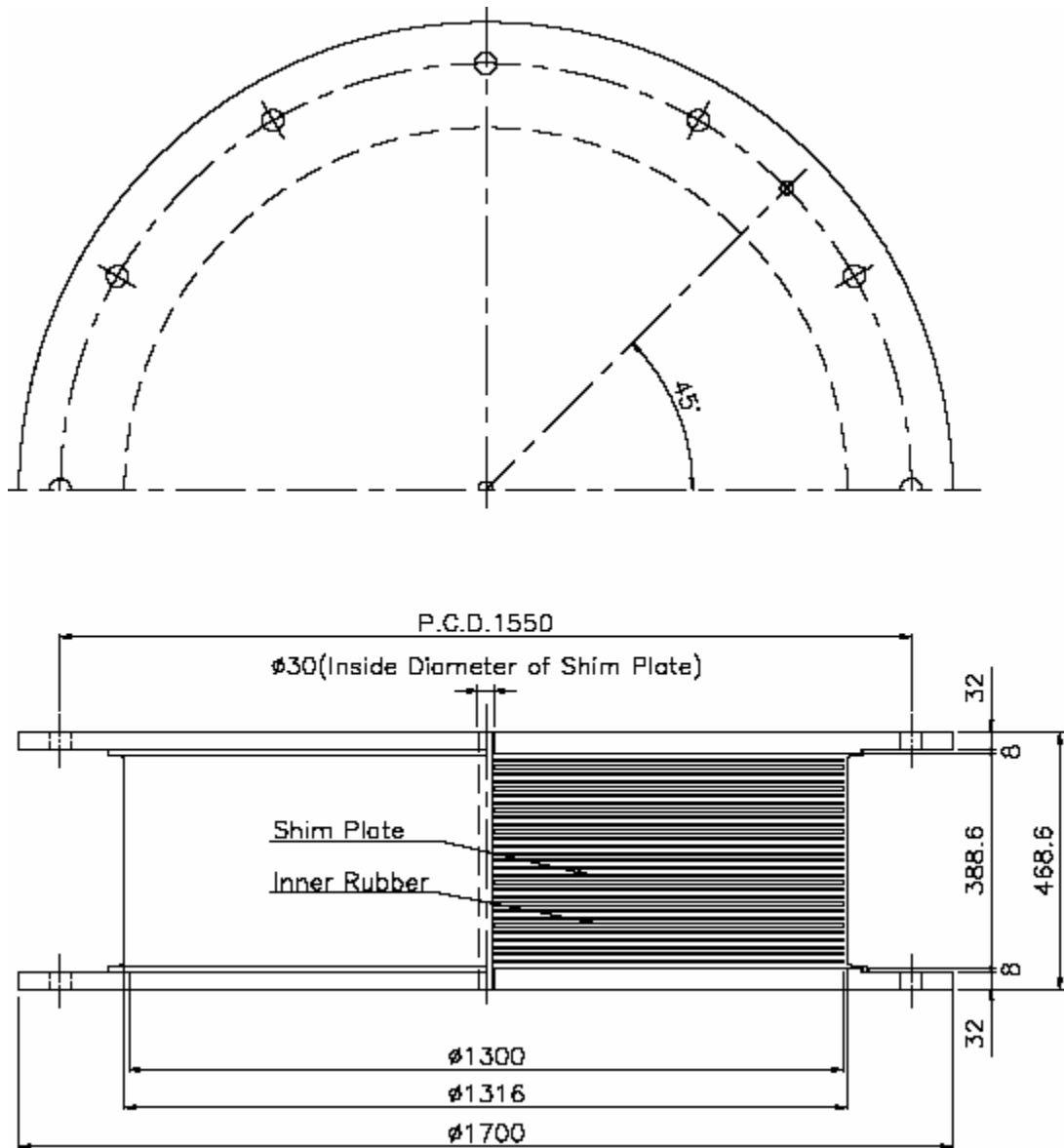


Figure 5-7: Drawing of section view of NRB1300

4. Robinson Square Bearing

The Robinson bearing with square section was made by lamination of 27 soft rubber layers of 10 mm thick and 26 steel plates of 2.5 mm thick. The effective and total heights were 335 mm and 435 mm respectively. This square-base bearing, denoted as Robinson bearing, had 4 cylindrical lead plugs each of which was 125 mm in diameter and 385 mm in height. The lead to rubber volume ratio for Robinson bearing was 0.078.

Detail of the geometry for the Robinson bearing is presented on Figures 5-8.

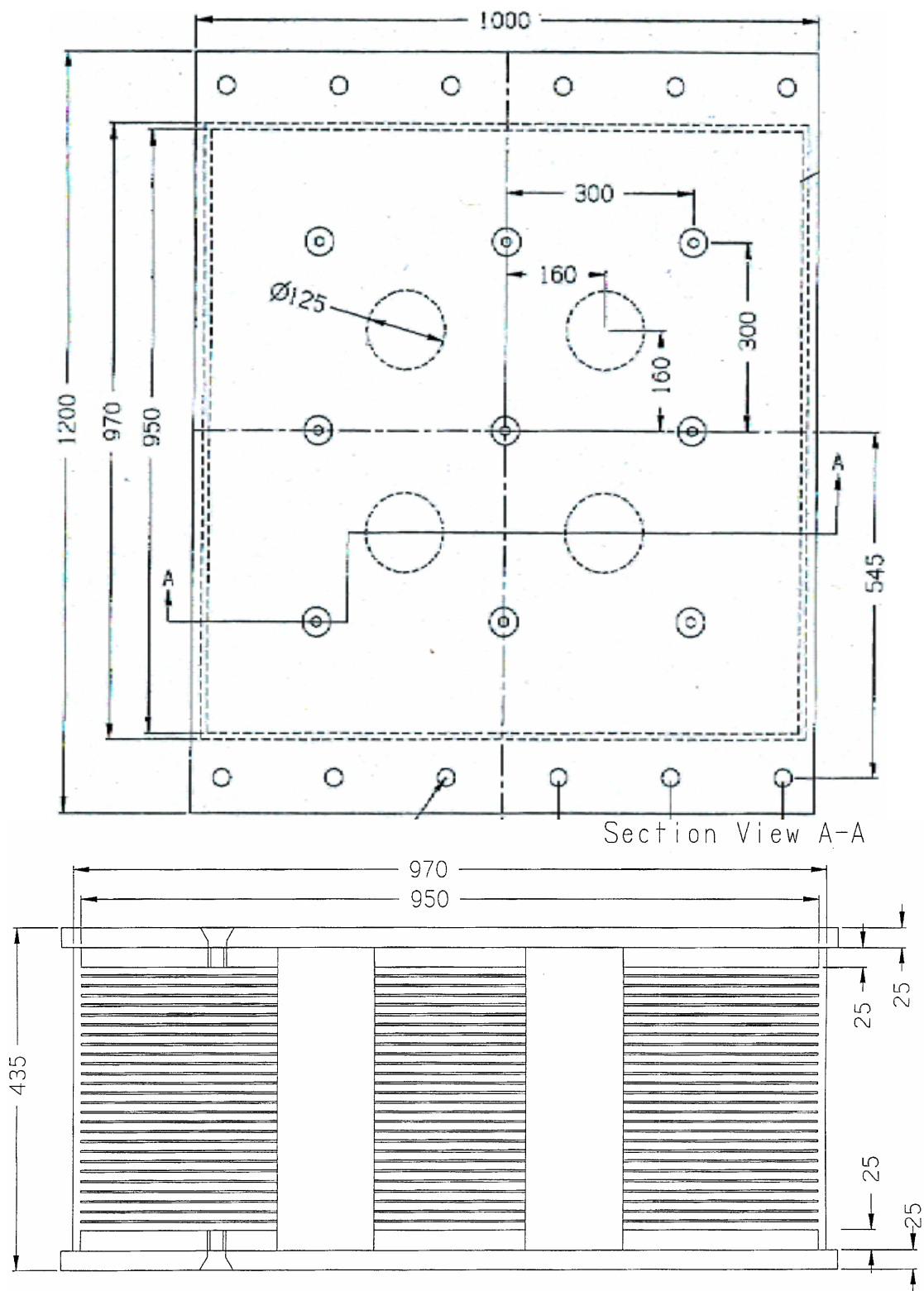


Figure 5-8: Drawing of section view of the Robinson bearing

The highlighted specifications of the four bearings of Experiment-1 are listed in Table 5-1.

Table 5-1: Specifications of the test bearing of Experiment-1

Device Name	Section Geometry and Effective Dimension	Number of Lead Plugs	Total Height of Rubber mm	Total Volume of Lead (mm ³)	Lead/Rubber Ratio
LRB 700	Circle d=700 mm h=230.9	1 Cylindrical Coaxial d=140 mm h=231 mm	141	3.556×10^6	0.068
LRB 1300	Circle d= 1300 mm h=388.6	1 Cylindrical Coaxial d=260 mm h=400 mm	261	2.124×10^7	0.065
NRB 1300	Circle d= 1300 mm h=388.6	None	261	0	0
Robinson bearing	Square 970x970x435	4 at Corners d=125 mm h=389 mm	270	1.89×10^7	0.078

5.2.2 Test Set Up

On the two sides of the rubber bearings (North and South) displacement transducers were placed as indicated in Figure 5-9. Specifically, the additional sensors were installed to monitor the vertical relative displacements between the top and the bottom plates of the bearings. Two types of devices were used for this task. The first one consists of wire potentiometers installed with a pulley/swivel mechanism (two per side of the bearings). The second type consists of spring

loaded potentiometers with round tip, able to translate solidly with the bearing. The configuration of transducers is shown in Figure 5-9.

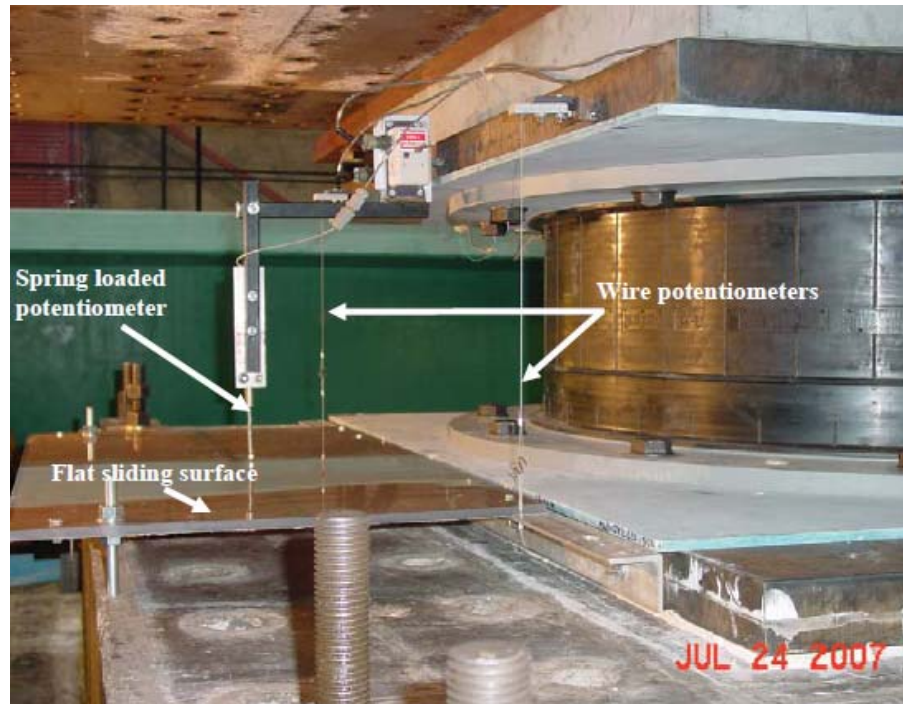


Figure 5-9: Displacement transducer configuration

5.2.3 Test Protocols and Results

In terms of loading protocols the bearings were divided into two groups, each of which was assigned a specific loading protocol. The three cylindrical bearings LRB700, LRB1300 and NRB1300 were loaded with 50 continuous sinusoidal cycles. The Robinson bearing was tested through a completely different protocol including tests of various amplitudes and velocities.

The obtained result from data acquisition system includes the following characteristics for each hysteretic loop:

- Maximum velocity relative to the specific loop
- Time frame for the loop under consideration
- Maximum horizontal force
- Minimum horizontal force
- Maximum lateral displacement
- Minimum lateral displacement
- Average restoring stiffness (K_{ra}), as obtained from the best-fit straight lines K_{ru} (upper line) and K_{rl} (lower line).
- Effective Stiffness, defined as:

$$k_{eff} = \frac{F_{max} - F_{min}}{D_{max} - D_{min}} \quad \text{Equation 5-1}$$

where: D_{max} and F_{min} are the maximum and minimum displacements, and F_{max} and F_{min} are the peak forces recorded after the 75 % of peak displacement.

- Energy dissipated per cycle (EDC), the area bounded by hysteresis loop.
- Equivalent viscous damping (β_{eq}), calculated per Equation

$$2-11: \beta_{eq} = \frac{EDC}{2\pi k_{eff} D_{av}^2}$$

Where: k_{eff} is the effective stiffness of each hysteretic loop and D_{av} is the average of absolute values of amplitudes

within each cycle (only if the cycle is not symmetric with respect to initial point, otherwise $D_{av} = D_{max} = |D_{min}|$)

The main characteristics of a hysteresis loop, by which the response of a bearing is defined, are illustrated in Figure 5-10.

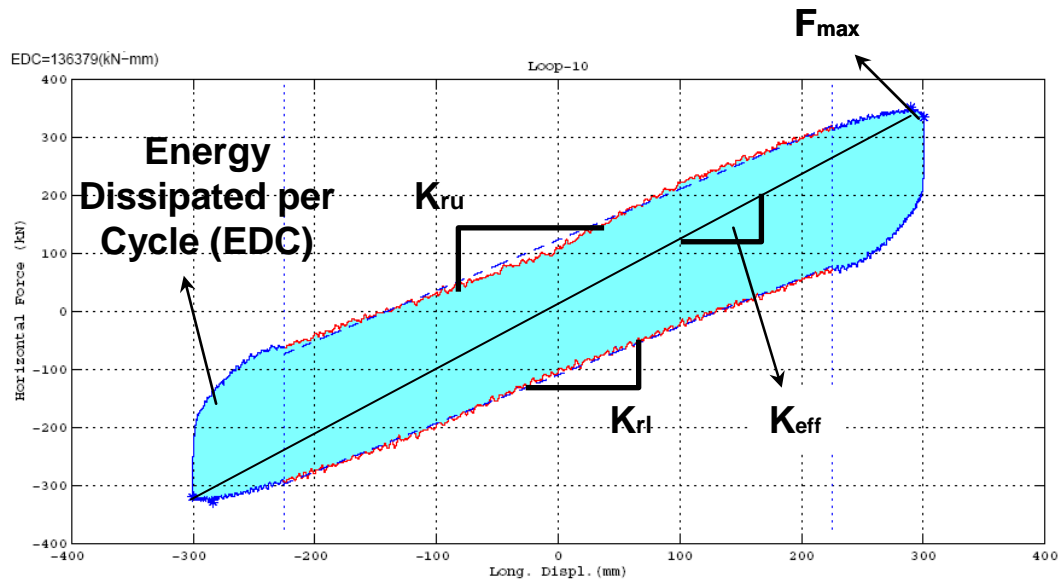


Figure 5-10: Characteristic of a hysteresis loop used for analysis

The experiments on cylindrical bearings included several tests at various displacement amplitudes. A total of 50 continuous sinusoidal excitations, at 5 groups of various displacement amplitudes, were given within 10 tests. All 10 tests were performed at a constant loading rate of 13 mm/sec and constant axial load of 5400 kN. The rational behind using such a wide range of displacement amplitudes was to learn about the response behaviors of the bearings, affected by variation of amplitude. Figure 5-11, shows test protocol used for experiment performed on NRB1300, LRB1300 and LRB700.

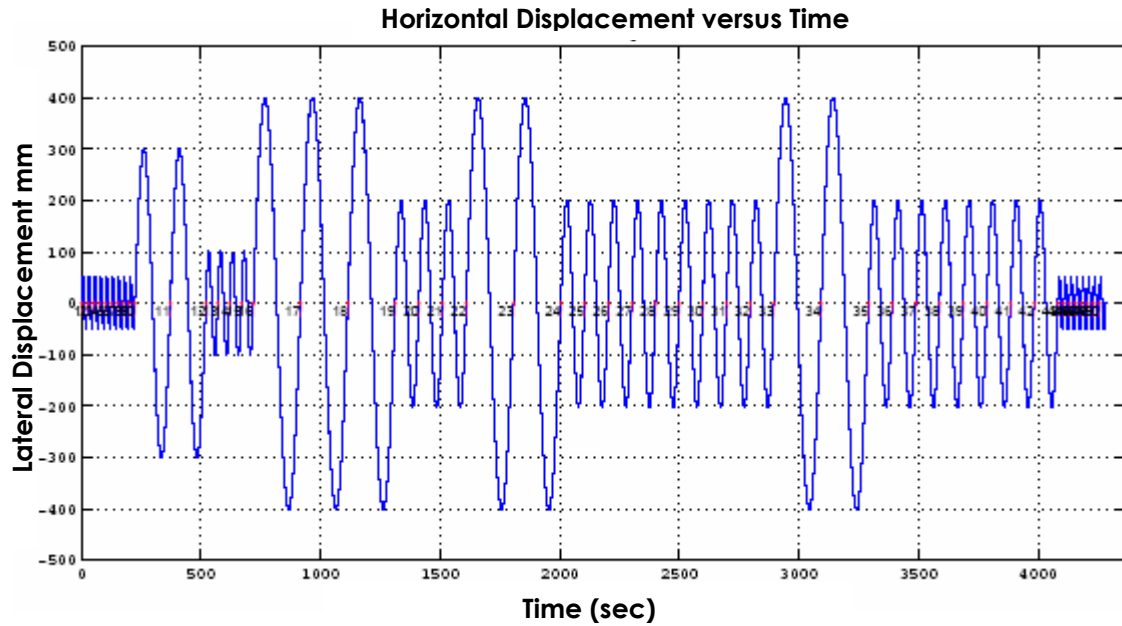


Figure 5-11: Plot of displacement versus time of the load protocol applied to NRB1300, LRB1300 and LRB700

Also, the rational behind keeping the velocity constant was to isolate the effect of only one variable, which selected to be displacement amplitude, on dynamic characteristics of the bearings. The protocol and results of the tests performed on LRB1300 is shown in Table 5-2, however, a complete set of tables for the other test bearings of Experiment-1 is available in Appendix A.

Table 5-2: Protocol and the results of the Experiment-1, performed on LRB1300

LRB1300			Input Data			Output Data		
Test	Cyl # (total)	Cycle	Disp. Amp. (mm)	Max Vel. (mm/sec)	Ver. load (kN)	EDC (kN-mm)	Fmax (kN)	Kra (kN/mm)
A	1	1	50	13	17800	53793	418.9	2.74
	2	2	50	13	17800	55408	424.8	4.11
	3	3	50	13	17800	53594	407.7	4.03
	4	4	50	13	17800	52713	401.5	4.02
	5	5	50	13	17800	52125	397.9	4.00
	6	6	50	13	17800	51912	391.3	3.95
	7	7	50	13	17800	51813	389.7	3.92
	8	8	50	13	17800	51493	390.5	3.94
B	9	9	50	13	17800	51183	384.9	3.91
	10	1	300	13	17800	372871	780.1	1.85
C	11	2	300	13	17800	355692	760.7	1.82
	12	1	100	13	17800	105279	407.6	2.05
	13	2	100	13	17800	105710	411.4	2.10
	14	3	100	13	17800	105054	408.6	2.09
D	15	4	100	13	17800	104676	409.8	2.08
	16	1	400	13	17800	468008	917.9	1.80
	17	2	400	13	17800	458438	903.8	1.79
E	18	3	400	13	17800	453267	900.7	1.78
	19	1	200	13	17800	212766	569.2	1.79
	20	2	200	13	17800	210630	567.4	1.80
F	21	3	200	13	17800	210708	568.1	1.80
	22	1	400	13	17800	445703	903.3	1.79
G	23	2	400	13	17800	442536	895.1	1.79
	24	1	200	13	17800	209100	568.9	1.80
	25	2	200	13	17800	208110	567.0	1.81
	26	3	200	13	17800	207739	567.9	1.81
	27	4	200	13	17800	207362	567.1	1.81
	28	5	200	13	17800	207267	565.5	1.82
	29	6	200	13	17800	207087	565.8	1.82
	30	7	200	13	17800	206744	565.8	1.82
H	31	8	200	13	17800	206621	565.3	1.83
	32	9	200	13	17800	205899	566.6	1.83
I	33	1	400	13	17800	435818	900.0	1.80
	34	2	400	13	17800	434592	893.9	1.80
J	35	1	200	13	17800	205714	565.3	1.82
	36	2	200	13	17800	204516	562.7	1.82
	37	3	200	13	17800	203856	563.9	1.82
	38	4	200	13	17800	204126	563.9	1.83
	39	5	200	13	17800	203544	564.1	1.83
	40	6	200	13	17800	203518	564.9	1.84
	41	7	200	13	17800	203323	564.7	1.84
	42	8	200	13	17800	202994	564.6	1.84
J	43	1	50	13	17800	43904	304.7	3.11
	44	2	50	13	17800	44044	314.3	3.29
	45	3	50	13	17800	43838	309.5	3.29
	46	4	50	13	17800	44029	310.9	3.32
	47	5	50	13	17800	43941	309.3	3.32
	48	6	50	13	17800	44049	308.6	3.32
	49	7	50	13	17800	43757	306.5	3.33
	50	8	50	13	17800	43705	309.4	3.38

The second test protocol which was applied on the Robinson bearing comprised of 14 sets of tests. Some of these tests were set at constant amplitudes and varying velocities, (tests 1, 2 and 4). These three tests were set for maximum displacement amplitude of 150 mm and maximum velocities of 345 mm/sec, 0.65 mm/sec and 13 mm/sec respectively. The purpose of such a set up was to investigate the effects of variation of velocity on hysteretic characteristic of the bearing.

While the experiment was being conducted Infrared thermography was performed on the Robinson. There was an interest to investigate whether or not the surface temperature can be treated as a means for screening the internal temperature of a bearing.

The protocol and results of the tests performed on the Robinson is shown in Table 5-3, however, a complete set of tables is available in Appendix A.

Table 5-3: Protocol and the results of the test performed on the Robinson bearing

Robinson 970			Input Data			Output Data		
Test	Cyl # (total)	Cycle	Disp. Amp. (mm)	Max Vel. (mm/sec)	Ver. load (kN)	EDC (kN-mm)	Fmax (kN)	Kra (kN/mm)
1	1	1	142.92	345	7882	218457	877.77	3.33
	2	2	142.82	345	7882	202086	834.07	3.17
	3	3	142.77	345	7882	188470	772.65	2.95
2	4	1	150.09	0.65	9617	127789	576.06	1.83
	5	2	150.09	0.65	9617	130423	571.44	1.85
	6	3	150.06	0.65	9617	129554	571.06	1.84
3a	7	1	5.85	15	9617	2434	257.50	17.48
	8	2	5.84	15	9617	2485	262.55	18.17
	9	3	5.82	15	9617	2493	263.48	18.40
	10	4	5.81	15	9617	2510	265.69	18.51
	11	5	5.79	15	9617	2492	270.74	18.65
	12	6	5.80	15	9617	2522	264.57	18.63
	13	7	5.79	15	9617	2517	263.52	18.77
	14	8	5.79	15	9617	2506	267.45	18.86
	15	9	5.81	15	9617	2534	267.97	18.80
	16	10	5.82	15	9617	2524	268.47	18.89
	17	11	5.82	15	9617	2531	266.67	18.91
	18	12	5.83	15	9617	2541	265.09	19.00
	19	13	5.86	15	9617	2540	263.14	18.70
	20	14	5.86	15	9617	2534	265.71	18.83
	21	15	5.86	15	9617	2540	264.24	18.86
	22	16	5.86	15	9617	2549	263.96	18.77
	23	17	5.86	15	9617	2550	262.18	18.76
	24	18	5.84	15	9617	2536	261.45	18.81
	25	19	5.84	15	9617	2546	261.33	18.66
	26	20	5.84	15	9617	2505	261.58	18.19
4	27	1	142.49	13	7882	164274	697.30	2.52
	28	2	142.55	13	7882	162059	643.24	2.50
	29	3	142.59	13	7882	157370	624.85	2.41
5a	30	1	143.15	345	7882	213577	878.45	3.31
	31	2	143.05	345	7882	197780	817.76	3.12
	32	3	142.79	345	7882	185326	757.63	2.92
5b	33	1	35.82	88	7882	27562	390.56	5.69
	34	2	35.78	88	7882	28278	415.87	6.31
	35	3	35.73	88	7882	28166	422.07	6.46
5c	36	1	71.66	175	7882	73977	580.78	4.48
	37	2	71.60	175	7882	73051	587.27	4.61
	38	3	71.59	175	7882	70843	580.06	4.53
5d	39	1	107.42	260	7882	134481	738.98	3.87
	40	2	107.36	260	7882	128837	729.63	3.85
	41	3	107.33	260	7882	123473	705.85	3.71
5e	42	1	143.24	345	7882	210740	878.01	3.34
	43	2	143.17	345	7882	196738	829.91	3.19
	44	3	142.99	345	7882	185123	768.87	2.98
5f	45	1	178.96	433	7882	296644	992.79	2.97
	46	2	178.82	433	7882	267309	888.08	2.72
	47	3	178.62	433	7882	245981	812.22	2.52

Table 5-3 Continue								
Test	Cyl # (total)	Cycle	Disp. Amp. (mm)	Max Vel. (mm/sec)	Ver. load (kN)	EDC (kN-mm)	Fmax (kN)	Kra (kN/mm)
6a	48	1	143.38	345	7882	226738	1036.00	3.04
	49	2	143.33	345	7882	209466	980.90	2.93
	50	3	143.26	345	7882	194756	912.40	2.73
	51	4	142.98	345	7882	184119	862.10	2.58
	52	5	142.85	345	7882	175361	825.70	2.47
	53	6	142.81	345	7882	168536	796.00	2.38
	54	7	142.72	345	7882	162233	771.50	2.31
6b	55	1	143.30	345	7882	225395	1017.50	2.99
	56	2	143.24	345	7882	209690	972.80	2.91
	57	3	143.19	345	7882	194298	905.50	2.72
	58	4	142.93	345	7882	182746	852.70	2.57
	59	5	142.84	345	7882	174412	813.90	2.46
	60	6	142.82	345	7882	166643	783.40	2.37
	61	7	142.69	345	7882	160171	758.60	2.30
6c	62	1	143.21	345	7882	222473	1001.60	2.94
	63	2	143.15	345	7882	207729	960.90	2.87
	64	3	143.05	345	7882	191724	894.80	2.70
	65	4	142.82	345	7882	180564	842.90	2.55
	66	5	142.75	345	7882	171707	804.80	2.45
	67	6	142.73	345	7882	164454	774.60	2.36
7a	68	1	5.88	15	9617	2184	194.27	17.67
	69	2	5.82	15	9617	2225	197.19	17.92
	70	3	5.78	15	9617	2202	203.68	17.78

5.2.4 Observations and Remarks

Data was rearranged a multiple times in order to isolate the effects of variables, one at a time. It was also necessary to identify the engineering characteristics of the bearings affected by changes of these variables. The plots of the energy dissipated per cycle, EDC, the maximum horizontal force of each loop, F_{max} , and the average restoring stiffness of each loop, K_{ra} were prepared for all experiments.

In an elastomeric bearing, heat is generated through hysteretic action when the bearing is subjected to lateral cyclic load. This is called

Energy Dissipated per Cycle, EDC. The EDC causes temperature of a bearing to rise. The EDC is assumed to take place primarily within the lead plug, however, some relatively small amount of heat is also generated by damping effect of rubber. Contribution of rubber in the heat generation is often neglected because of low damping characteristic of the type of rubber often used in manufacturing lead core elastomeric bearings. This claim, however, must be validated experimentally.

1. Loss of Mechanical Properties of the Bearings During the Tests

For bearings LRB700 and LRB1300, noticeable per-cycle change in EDCs was observed only on the tests with high amplitudes, (Figures 5-13 and 5-12, Tests D, F, and H). These three tests were performed at constant shear strains of 1.028 mm/mm and 1.7 mm/mm and constant shear strain rates of 0.033 sec^{-1} and 0.056 sec^{-1} for LRB1300 for LRB700 respectively. However, a steady state reduction in EDC was observed from one test to another among these three tests (indicated by red arrow in Figure 5-12). Variation in responses to the identical loadings is justified by the steady state property loss of lead, occurred in LRB700 and LRB1300. Plots of EDC versus time for bearings LRB1300 and LRB700 are presented in Figures 5-12 and 5-13.

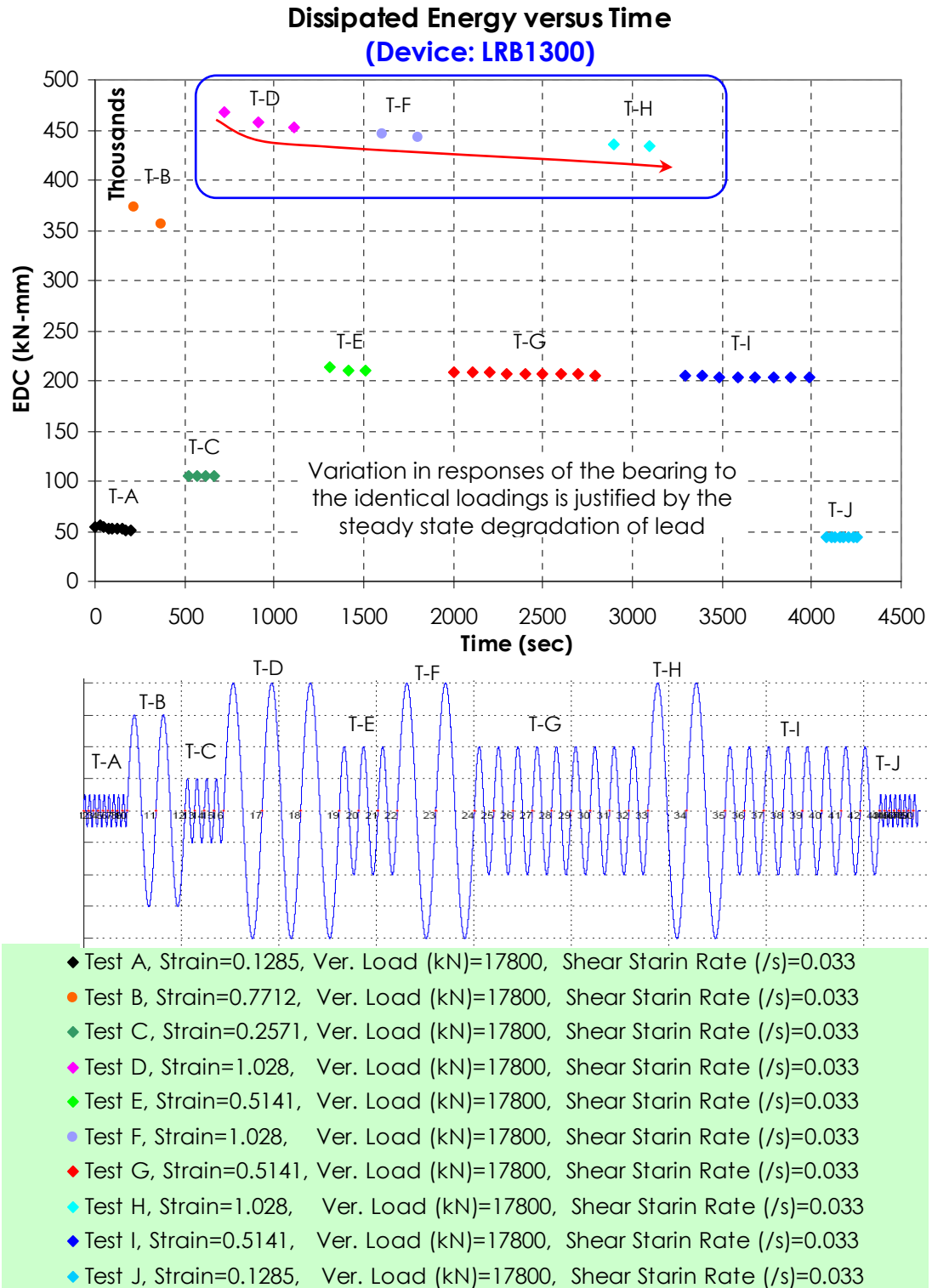


Figure 5-12: Energy Dissipated per Cycle for LRB1300

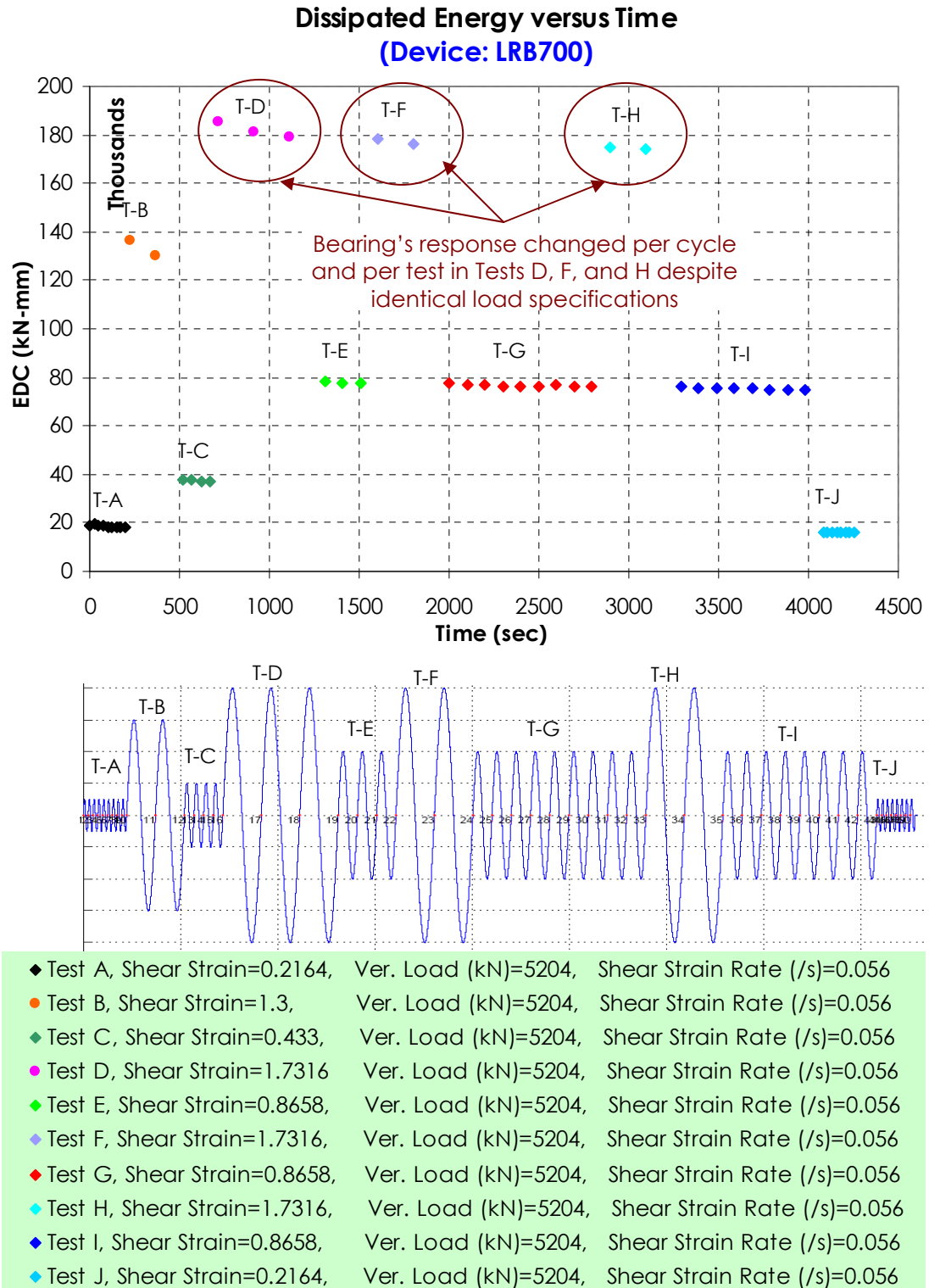


Figure 5-13: Energy Dissipated per Cycle for LRB700

The Robinson bearing responded completely different compared to the other two bearings discussed earlier. It showed significant reduction per cycle in all of its response characteristics at each test. This could be as a result of high straining rates, used in the experiment performed on Robinson bearing, compared to the other three bearings.

In Figure 5-14 the results of test T1, T5a and T5e indicated a consistent reduction-per-cycle in EDC in the order of nearly 10% (indicated by red arrows in the Figure 5-14). It has to be noted that these tests were performed in identical manner. It was observed that an almost perfect recovery took place within 20 minutes after completion of each test, (see tests T1, T5a, T5e, in Figure 5-14). The recovery from subsequent tests in terms of EDC is indicated by the blue arrows in Figure 5-14. Lead is characterized by its unique capability of recrystallization which can take place at room temperature. Therefore, upon interruption between each two tests the lost properties were expected to be recovered. This justifies the relatively fast recovery of the bearing.

Tests T6a, T6b and T6c were also identical in loading characteristics. They exhibited the similar behavior as the previous tests

in terms of dropping in EDC values. However, recovery was less complete due to short time interval between each two tests.

It was postulated that there could be a link between property loss and the temperature of the lead plug which is raised by EDC.

At each hysteretic loop, EDC is a function of two variables of stiffness and maximum horizontal force. At this experiment, the EDC was observed to be mainly affected by the maximum force at each hysteretic loop. This conclusion was made by investigating and comparing the effects of cyclic loads on all three characteristics of the test bearings. Figures 5-14 and 5-15 shows EDC and F_{\max} plotted versus time for the Robinson bearing.

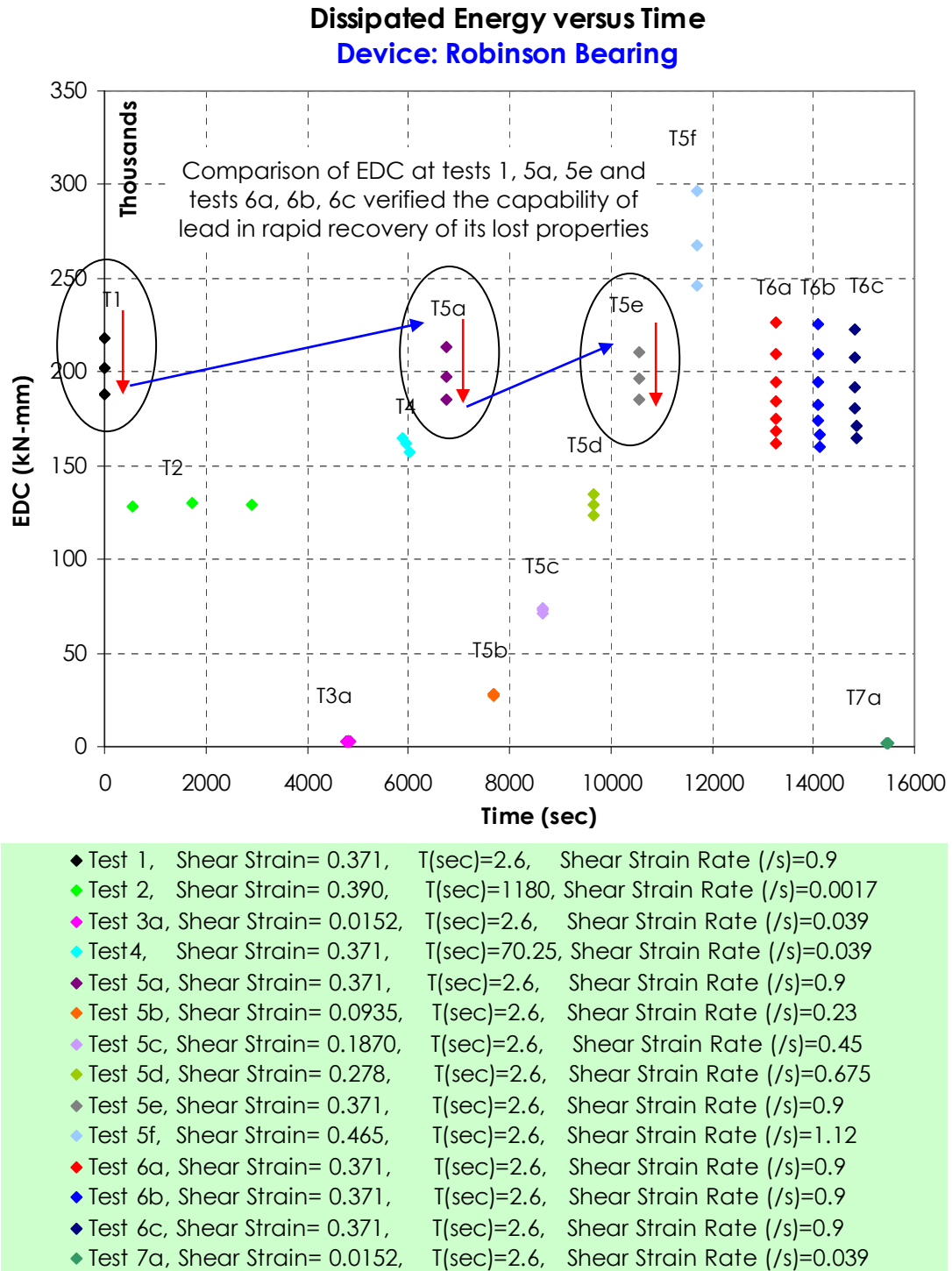
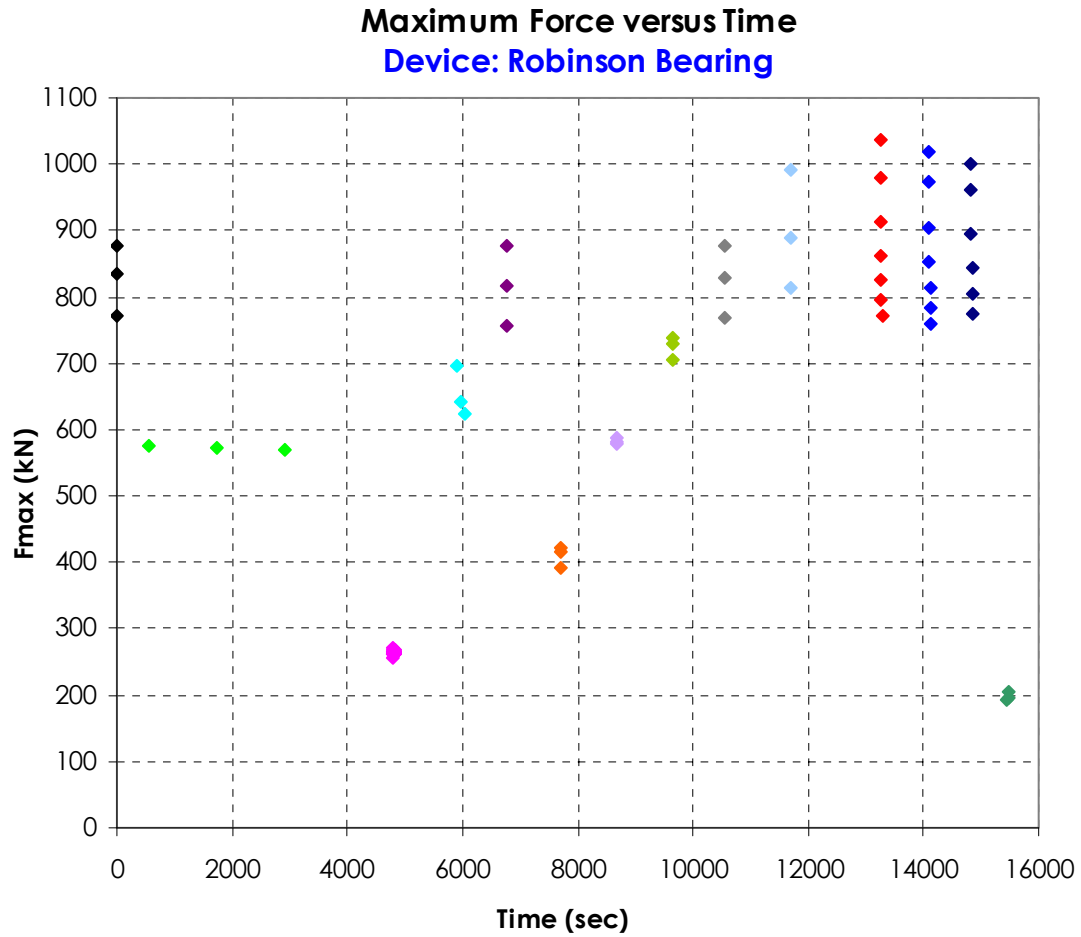


Figure 5-14: Energy dissipated per cycle as a function of time for the Robinson bearing



◆ Test 1,	Shear Strain= 0.371,	T(sec)=2.6,	Shear Strain Rate (/s)=0.9
◆ Test 2,	Shear Strain= 0.390,	T(sec)=1180,	Shear Strain Rate (/s)=0.0017
◆ Test 3a,	Shear Strain= 0.0152,	T(sec)=2.6,	Shear Strain Rate (/s)=0.039
◆ Test 4,	Shear Strain= 0.371,	T(sec)=70.25,	Shear Strain Rate (/s)=0.039
◆ Test 5a,	Shear Strain= 0.371,	T(sec)=2.6,	Shear Strain Rate (/s)=0.9
◆ Test 5b,	Shear Strain= 0.0935,	T(sec)=2.6,	Shear Strain Rate (/s)=0.23
◆ Test 5c,	Shear Strain= 0.1870,	T(sec)=2.6,	Shear Strain Rate (/s)=0.45
◆ Test 5d,	Shear Strain= 0.278,	T(sec)=2.6,	Shear Strain Rate (/s)=0.675
◆ Test 5e,	Shear Strain= 0.371,	T(sec)=2.6,	Shear Strain Rate (/s)=0.9
◆ Test 5f,	Shear Strain= 0.465,	T(sec)=2.6,	Shear Strain Rate (/s)=1.12
◆ Test 6a,	Shear Strain= 0.371,	T(sec)=2.6,	Shear Strain Rate (/s)=0.9
◆ Test 6b,	Shear Strain= 0.371,	T(sec)=2.6,	Shear Strain Rate (/s)=0.9
◆ Test 6c,	Shear Strain= 0.371,	T(sec)=2.6,	Shear Strain Rate (/s)=0.9
◆ Test 7a,	Shear Strain= 0.0152,	T(sec)=2.6,	Shear Strain Rate (/s)=0.039

Figure 5-15: Maximum force measured at each hysteresis loop was plotted against the elapsed time

2. Property Degradations and Relation with Specification of Input load

Observation on the two Takinaka bearings LRB700 and LRB1300 indicated very slight per-cycle degradations only to high amplitude loads cycles. These two bearings tested on constant rate of 13 mm/sec. However, the Robinson bearing was largely affected by accumulation of thermal energy only on tests within which cyclic load at a rate of 100 mm/sec or greater was applied. Hence, a direct link was observed to exist between the EDC and the velocity of cyclic load. It was also observed that a direct link existed between the property loss and the rate of EDC in an elastomeric bearing.

The experiment showed that the EDC is affected in large by variation of load characteristics such as displacement amplitude and frequency of cyclic load.

3. Source of the Heat Generation in Elastomeric Bearings with Lead Core

Energy is dissipated in the form of heat through hysteretic action of a lead core elastomeric bearing. It was presumed that energy is mainly dissipated through hysteretic action of lead plugs, and only a negligible amount of energy is dissipated by rubber. This claim, however, had to be supported by experiments.

The results of Experiment-1 on bearings LRB1300 and NRB1300 were considered for this part of analysis. As pointed previously, these two bearing are identical in size, type and manufacturing process, except that, only LRB1300 had a lead plug. Figure 5-20 to Figure 5-22 shows the comparison of maximum force, stiffness and energy dissipated per cycle for the two bearing. This experiment allowed distinguishing the participation of each of the components in the two bearings.

In Figure 5-16, maximum forces at each loop obtained from LRB1300 and NRB1300 are superimposed on a single coordinate system.

In Figure 5-17, average restoring stiffness of each loop obtained from LRB1300 and NRB1300 are superimposed on a single coordinate system.

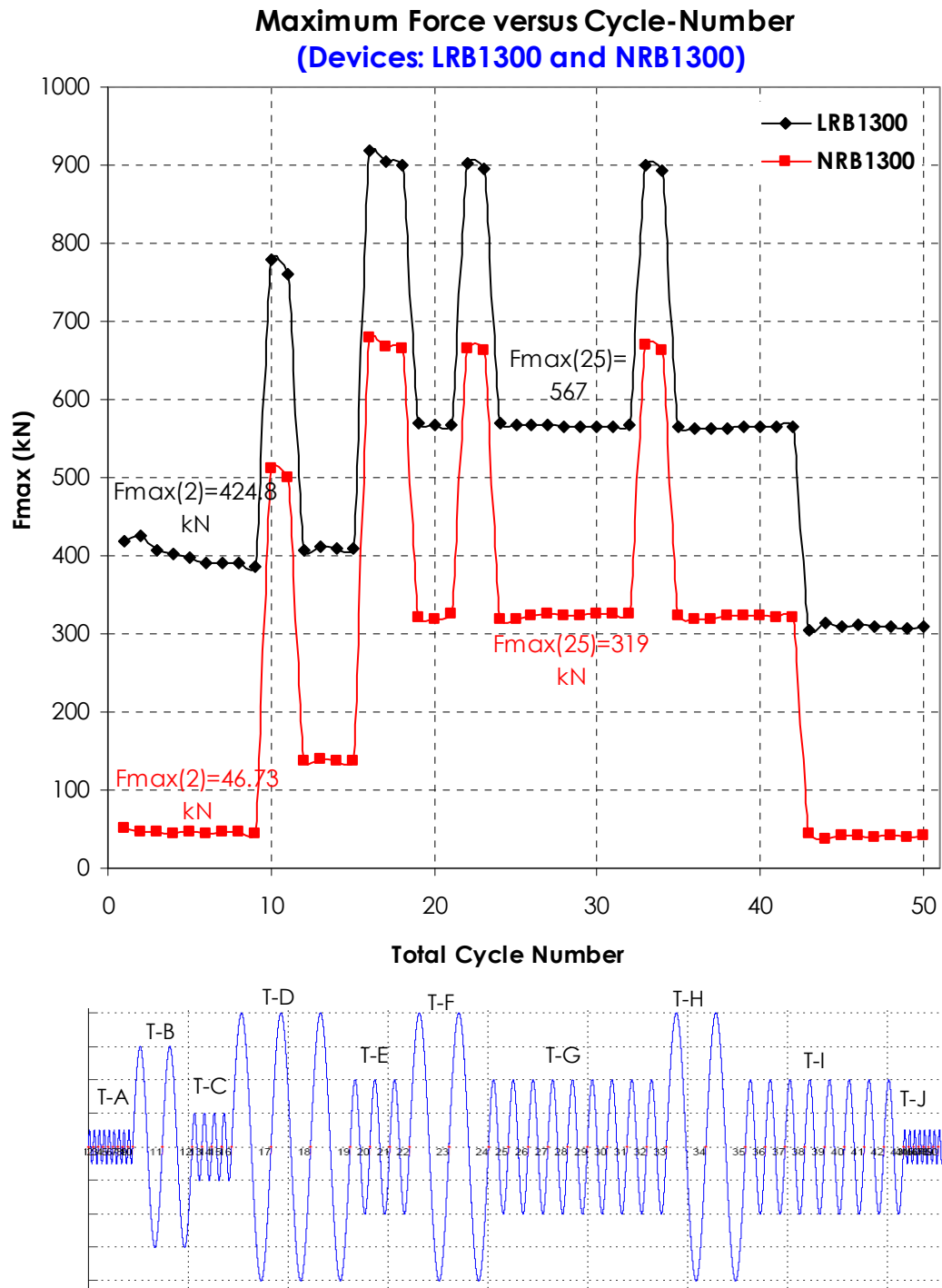


Figure 5-16: Superimposed plots of maximum force per cycle for LRB1300 and NRB1300

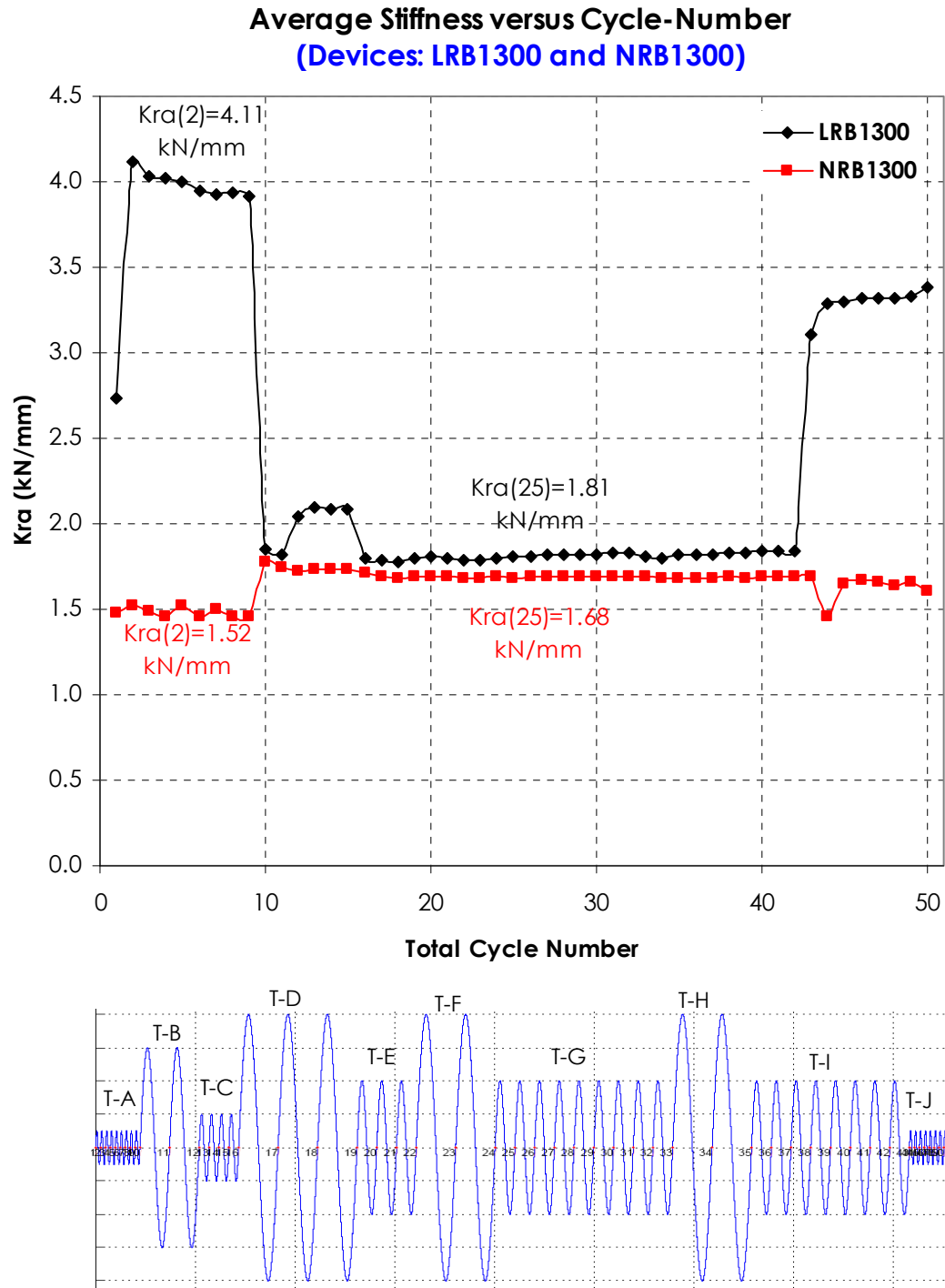


Figure 5-17: Superimposed plots of average stiffness per cycle for LRB1300 and NRB1300

The superimposed plot of EDC versus cycle number was prepared for LRB1300 and NRB1300 (Figure 5-18). At this plot, it was observed that energy dissipation ratio (EDC_{Lead}/EDC_{Rubber}) at a randomly picked cycle, for instance, cycle number 25, is $\frac{208110}{4250} = 48.96$,

stating this value by percentage:

$$\frac{208110 - 4250}{208110} \times 100 = 97.95 \%$$

Repeating the above computation for all of the loops resulted in a consistent lead-to-rubber energy dissipation ratio. Per the of above investigation it was concluded that, in a lead core rubber bearing, more than 95 % of energy is dissipated by hysteretic action of the lead plug.

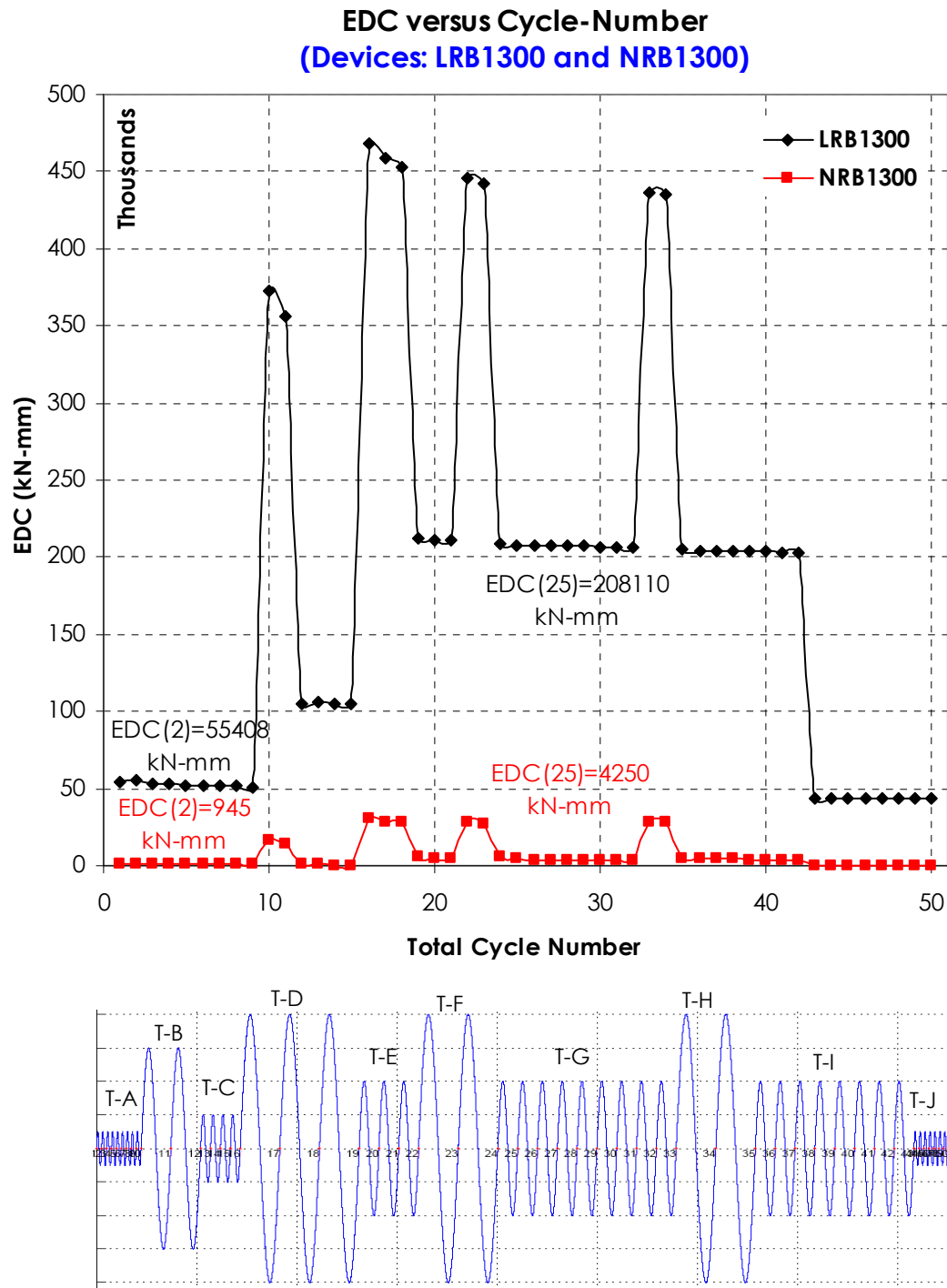


Figure 5-18: Superimposed plots of energy dissipated per cycle for LRB1300 and NRB1300

Thereby, in a lead core elastomeric bearing, heat is originated from the lead plug and spread radial through the body, as indicated in Figure 5-19. This assumption is an important basis on which the Experiment-2 (Chapter 6) is outlined.

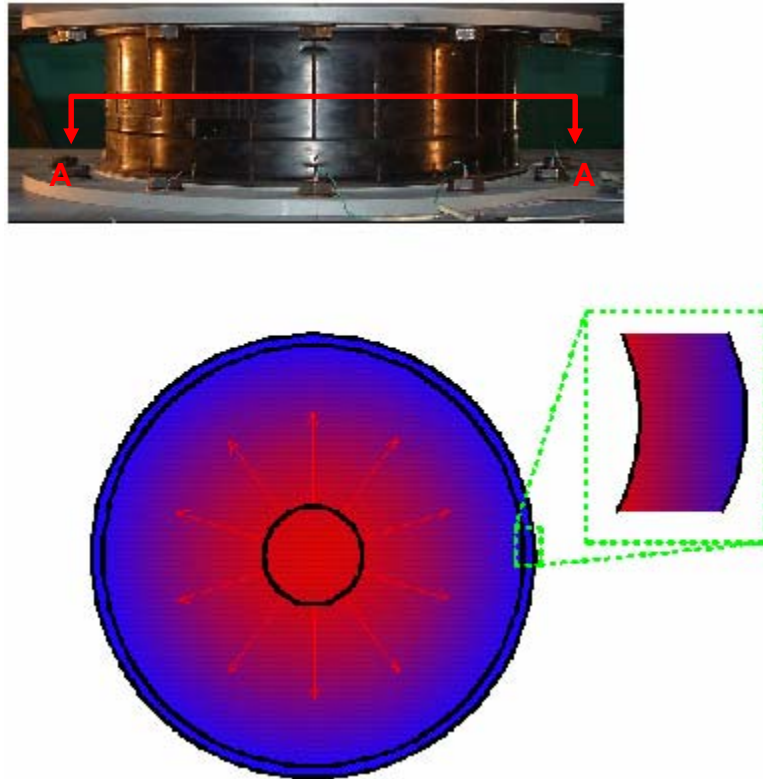


Figure 5-19: Schematic of the planar section view of a cylindrical bearing illustrating the conclusion which was drawn about origination and path of distribution of thermal energy

4. Post-yield Behavior of Lead

The response of a bearing as an assembly is the resultant of responses of its individual components, which In the case of elastomeric bearings are rubber and lead. In elastomeric bearings, sensitivity of each of these individual components to degrading agents is different,

and each is expected to experience a different level and quality of degradation. In the plot of Figure 5-20, it is indicated that lead shows nearly constant post-yield behavior for a wide range of strain (120 %). The assembly of rubber-shim remains almost completely elastic through that range of strain. Figure 5-20 is a representation of superimposed plots of shear stress verses shear strain for LRB1300 and its individual components.

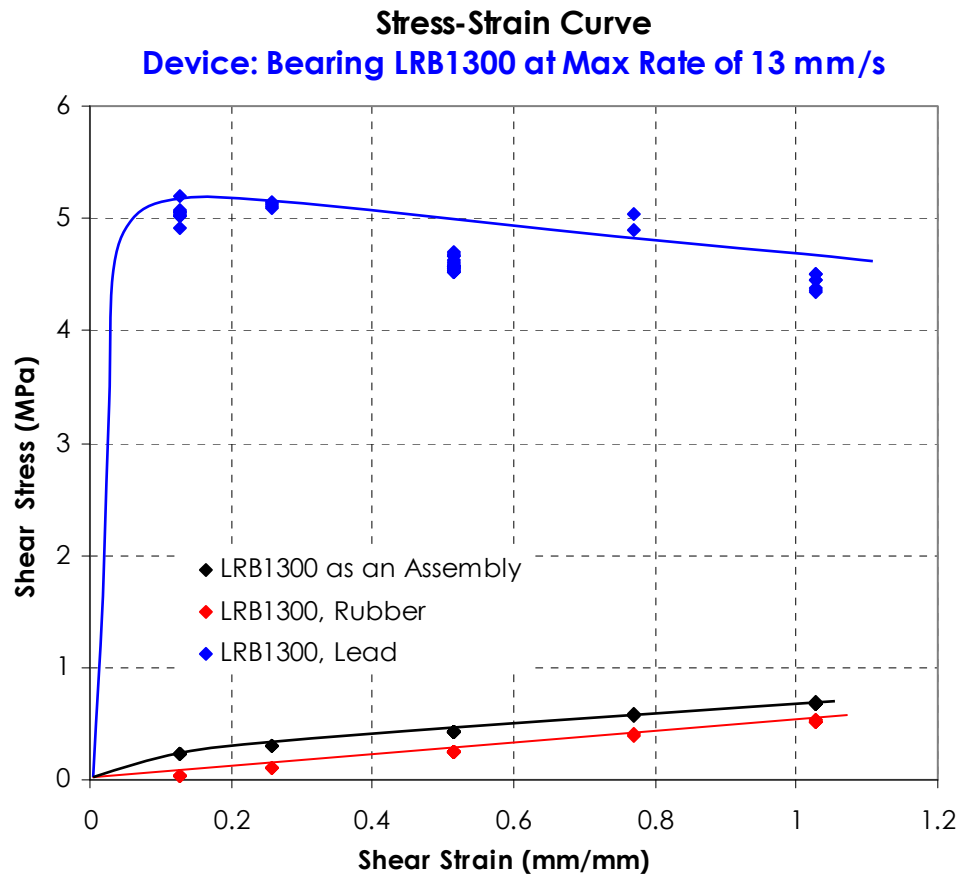


Figure 5-20: Shear stress applied to each component was calculated and plotted versus shear strain

In Figure 5-21, plots of restoring stiffness versus shear strain are presented for LRB1300 as an assembly and its components individually.

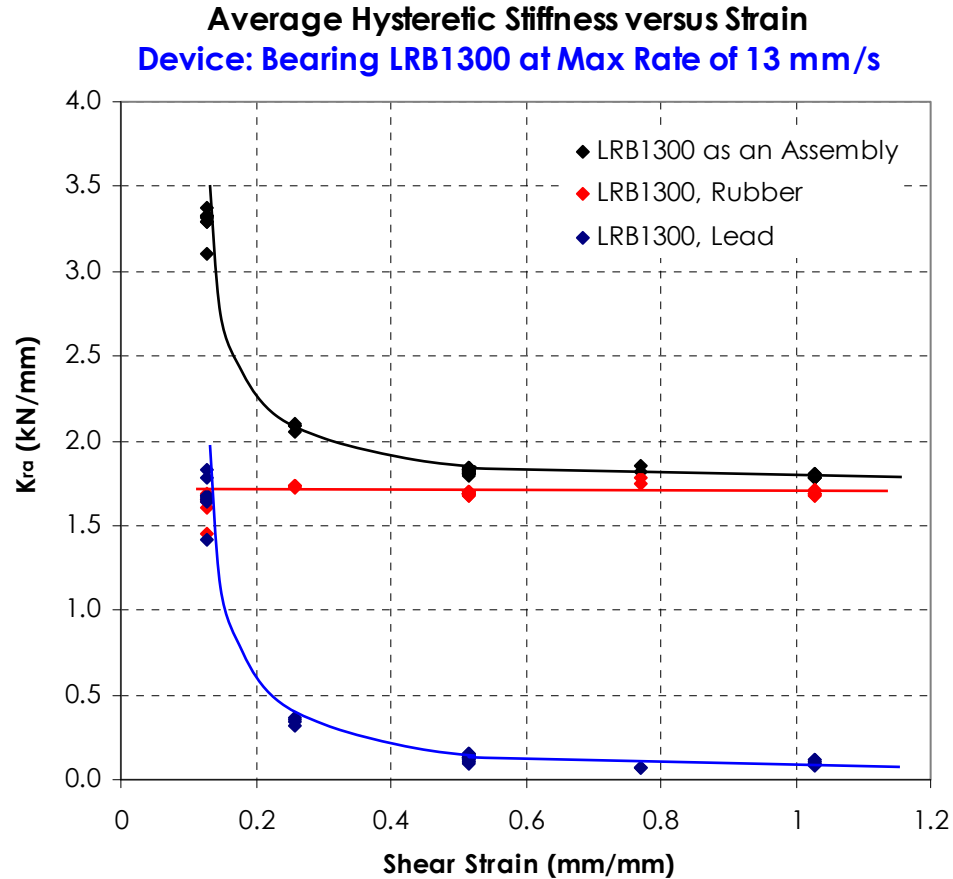


Figure 5-21: Restoring stiffness versus shear strain for LRB1300 as an assembly and its components individually. Rubber exhibited constant stiffness within the entire range of shear strain

5. Property Degradations and Relation with Heat

The results of Experiment-1 and the analysis performed on its data, revealed evidences of existing direct link between the generated heat and property losses of lead core elastomeric bearings. The thermal energy, generated within a lead plug, travels slowly toward the outer surface of a bearing. The reason for such a slow conduction is the

low thermal conductivity of rubber. Slow conduction does not allow the lead plug to expel this concentrated thermal energy fast enough, and causes the plug to heat up quickly. Because of the low melting point of lead, even small rise of temperature can significantly change its yielding strength and stiffness. This justifies the per-cycle property loss of the bearings used in this experiment when subjected to cyclic load.

6. Variation of Effective stiffness

Effective stiffness is one of the variables included in the equation for equivalent viscous damping of bearings, recalling Equation 2-11:

$$\beta = \frac{EDC}{2\pi k_{eff} \Delta_{max}^2}$$

In order to quantify the variation of effective damping with temperature, it was necessary to determine how the variation of temperature could affect K_{eff} . This was done by separation of the stiffness provided by lead from that of rubber, using data obtained from LRB1300 and NRB1300. Figure 5-22, presents loop 33 of Experiment-1 performed on the NRB1300. Per Equation 5-1, the effective stiffness of this hysteretic loop was computed to be:

$$K_{eff} = \frac{(670 + 743) (kN)}{800 (mm)} = 1.77 \text{ kN/mm}$$

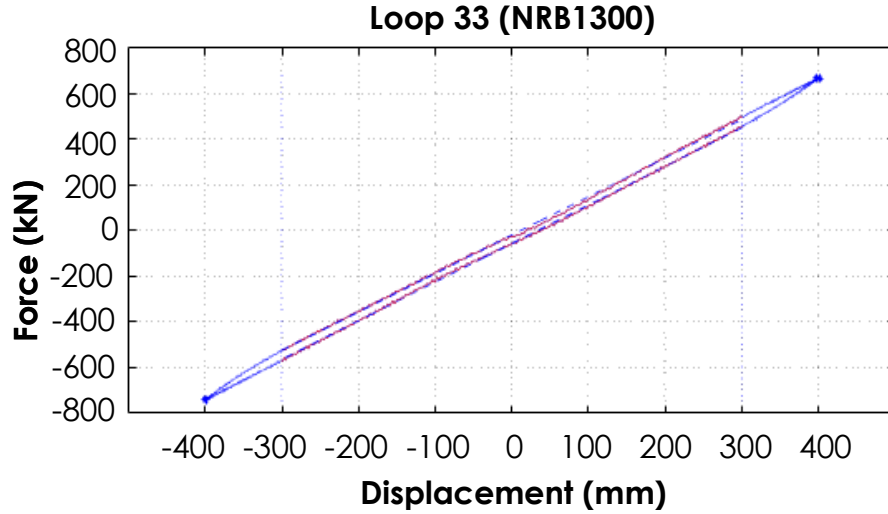


Figure 5-22: Loop 33 of NRB1300, a displacement of 400 mm was imposed

For the LRB1300 the hysteretic loop 33 is presented in Figure 5-23. In similar fashion, the effective stiffness for the loop 33 of LRB1300 was computed to be:

$$K_{eff} = \frac{(900 + 952) (kN)}{800 (mm)} = 2.32 \text{ kN/mm}$$

, and the contribution ratios are:

$$\frac{K_{eff}(Rubber)}{K_{eff}(Total)} = \frac{1.76}{2.32} \times 100 = 76 \%$$

$$\frac{K_{eff}(Lead)}{K_{eff}(Total)} = \frac{0.56}{2.32} \times 100 = 24 \%$$

The above results confirm the assumption that, in a standard size lead core elastomeric bearing, the effective stiffness is mainly (76 %) provided by rubber. According to this result, it can also be concluded that per-cycle variation of overall K_{eff} , due to slight per-cycle variation in K_{eff} of lead is negligible.

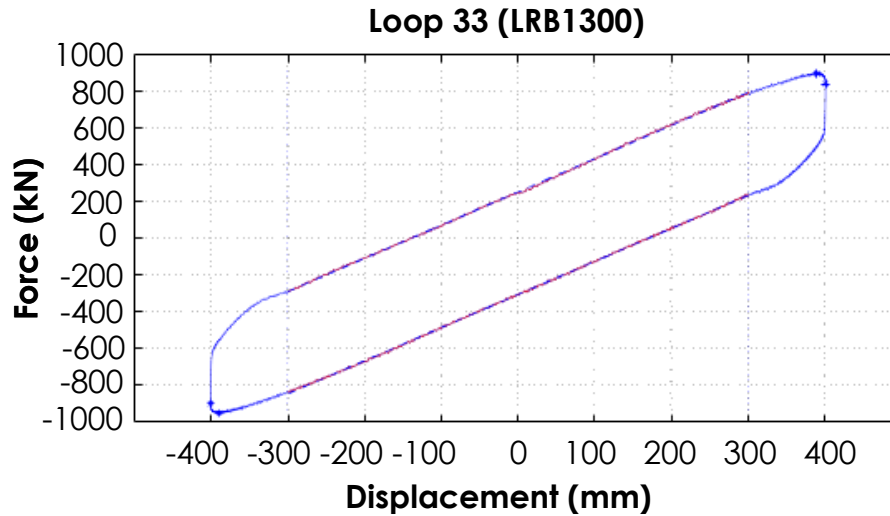


Figure 5-23: Loop 33 of LRB1300, a displacement of 400 mm was imposed

Superimposed plots of all 50 hysteretic loops are presented in Figure 5-24. The plot shows a constant effective stiffness through out all 50 cycles. This result states that, in an elastomeric bearing, the effective stiffness, provided by rubber, is constant.

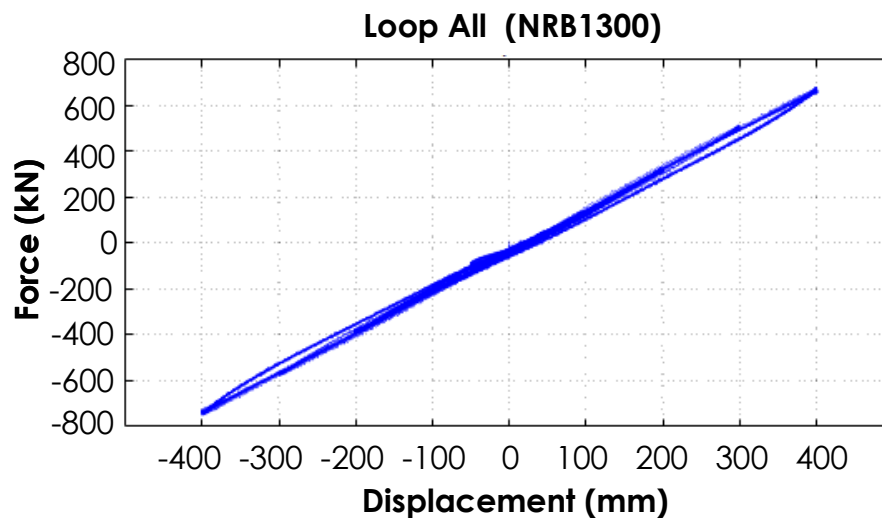


Figure 5-24: Superimposed plots of all 50 hysteretic loops of NRB-1300 performed during Experiment-1

5.2.5 Empirical Model for EDC in Terms of Input Characteristics

As the first step in assessment of durability, it was necessary to find an empirical equation for EDC in terms of the engineering characteristics of the bearing, environmental and loading conditions.

The EDC is not an independent variable. This quantity represents the area bounded by a hysteresis loop, and is determined by the maximum lateral force and the hysteretic stiffness of each cycle. However for parametric studies of this research, EDC as the combined effect of these two variables is considered for investigations. The plots of EDC versus cycle number of all 4 bearings indicated that the energy dissipated per cycle is largely affected by a series of variables such as the total traveled distance per cycle, shear strain rate and size of the lead plug. For instance, on the experiment performed on the Robinson bearing, Test-4 and Test-5e were performed at the same displacement amplitude (0.371 m) but different shear strain rates (0.9 sec^{-1}) at Test-5e compare to 0.039 sec^{-1} at Test-4, (Figure 5-14). This difference resulted in nearly 70 % higher energy dissipation of the bearing in Test-5e. However, the rate of displacement alone can not be used as an independent variable on which the EDC is depended. It must be transformed to a more detailed form to account for the height of the lead plugs. It is

done by dividing the displacement rate by the height of the plug, the term “shear strain rate” was used for this quantity.

Although, the sizes of lead plugs are constant for each bearing they must be taken into consideration for proposing a logical relation for EDC that accounts for all contributing variables. That relation can be applied to bearings of different size but same family (for instance, all cylindrical bearings with single coaxial lead plug). The entire set of variables was taken into account by creating two new sets of variables. The term, accounted for output data and the bearing characteristics, was set in the form of “EDC per unit of time per unit area of plugs”. It was computed by dividing EDC by period and by total area of the plugs. The input variable was formed of the product of square of strain rate and total distance traveled per cycle. The term “EDC per unit of time per unit area of plugs” has a unit of (Joule/sec/m²), which can be simplified into Watt/m². This is the unit for heat-flux, a quantity representing the amount of thermal energy passing through a unit of area per unit of time. The data of Experiment-1 was rearranged in a way that heat-flux could be plotted as a function of input variables. The rearranged data of all three experiments are given in Table 5-4.

Table 5-4: Rearrangement of data into two new sets of variables

	Strain Rate ² x Total Dist. Trv (m/sec ²)	EDC/ Unit Time / Unit Area (Watt/m ²)
Test	LRB1300	
A	0.000111683	6696
B	0.000670099	7732
C	0.000223366	6691
D	0.000893465	7318
E	0.000446732	6725
F	0.000893465	7066
G	0.000446732	6597
H	0.000893465	6925
I	0.000446732	6490
J	0.000111683	5384
	0	0
	LRB700	
A	0.000316711	7388
B	0.001900264	8845
C	0.000633421	7414
D	0.002533686	9044
E	0.001266843	7733
F	0.002533686	8813
G	0.001266843	7628
H	0.002533686	8684
I	0.001266843	7511
J	0.000316711	6186
	0	0
	Robinson970	
1	0.2312631	129043
2	8.6732E-07	180
3a	1.76471E-05	1579
4	0.000433621	3776
5a	0.231848163	126463
5b	0.003786222	17809
5c	0.029011446	46175
5d	0.097942289	81975
5e	0.232008543	125593
5f	0.448824822	171697
7	1.77116E-05	1248
	0	0

The heat-flux computed for the Robinson bearing, well fitted into a power function with relatively small residual (Figure 5-25). The

equation $y = 8204.9x^{0.5035}$, with residual of $R^2 = 0.9932$ governs the relation between heat-flux and input characteristics. Where x represents the term $[(\text{Strain Rate})^2 \times \text{Total Distance Traveled per Cycle}]$. According to the equation, heat-flux varies with respect to square of strain rate. This equation allows computing the heat-flux passing through the lead plugs of the Robinson bearing in terms of characteristics of the applied load. Plot of heat-flux as a function of load specification for the Robinson bearing is presented in Figure 5-25.

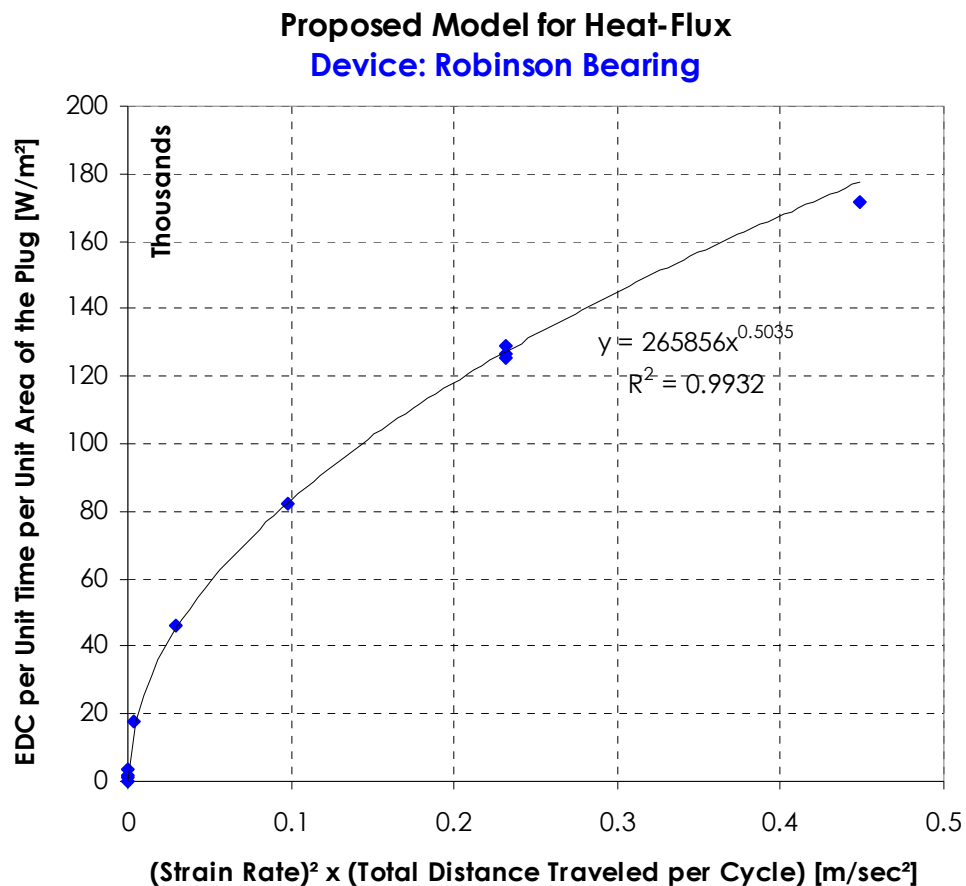


Figure 5-25: The proposed empirical equation for heat-flux of the Robinson bearing.
The data fitted in a power function

The plot of heat-flux for LRB1300 and LRB700 (Figure 5-26) also indicates a trend through which the prediction of heat-flux is possible. However, the result is not fitted as accurately as that of the Robinson bearing. It might be due to a number of reasons such as shape factor, location of lead plugs or even manufacturing quality. The plot for bearings LRB700 and LRB1300 is given in Figure 5-25.

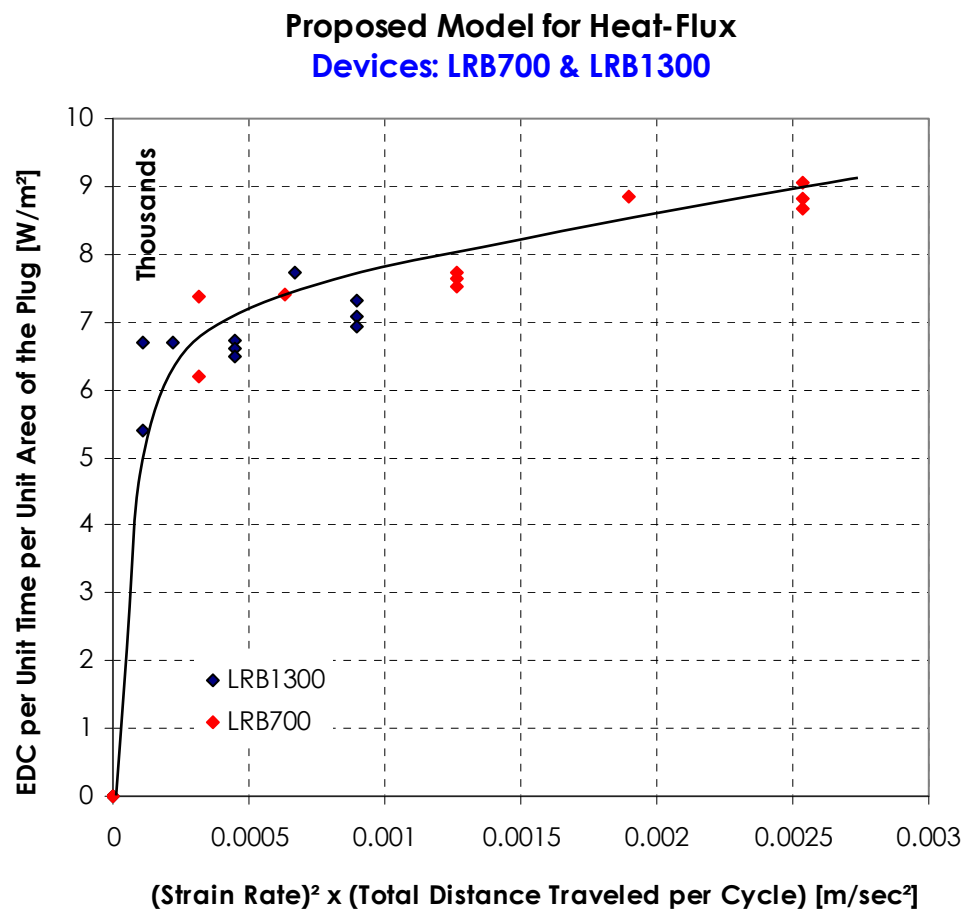


Figure 5-26: Superimposed plots of heat-flux versus product of shear strain rate and total traveled distance for LRB1300 and LRB700

5.2.6 Highlights of Experiment-1

Important conclusions were made through a direct qualitative assessments and analytical studies. The occurrence of thermal degradation was verified. It was also verified that lead plugs were the main source of generation of thermal energy. A pattern suggesting distribution of stress between components of elastomeric bearings was proposed by comparing the responses of NRB1300 and LRB1300. The post-yield behavior of lead in an elastomeric bearing was also studied.

The reversible changes in characteristics of lead plugs, which take place mainly due to heat, are the main sources of transient changes in characteristics of elastomeric bearings. Elastomeric bearings are also subjected to irreversible degradations such as stiffening of bearings, which are caused by hardening of rubber due to over-vulcanization as a result of being exposed to high temperature.

Goals pursued in this chapter of the research study were completed by proposing two models for bearings with both circular and rectangular sections. The models are proposed and discussed in Section (5.1.5). The proposed models compute the heat-flux generated at the lead plugs of elastomeric bearings. These models accounted for all involved variables such as loading amplitude and frequencies, size of lead plugs and total traveled distance at each loop.

Since both lead and rubber are nonlinear viscoelastic materials, the average stiffness and maximum force of a hysteretic loop is also affected by specification of input load. It was verified through a wide range of experiments that all of the factors; responsible for property degradation in elastomeric bearing bearings with lead core, are in interaction with each in an iterative fashion. This translates to the fact that degradation phenomenon is a function of several dependant variables, which are continuously changed with time.

The chart in Figure 5-24 illustrates how ambient temperature and loading characteristics together with the mechanical characteristics of a lead core elastomeric bearing, interact with each other in continuously affecting the response a bearing.

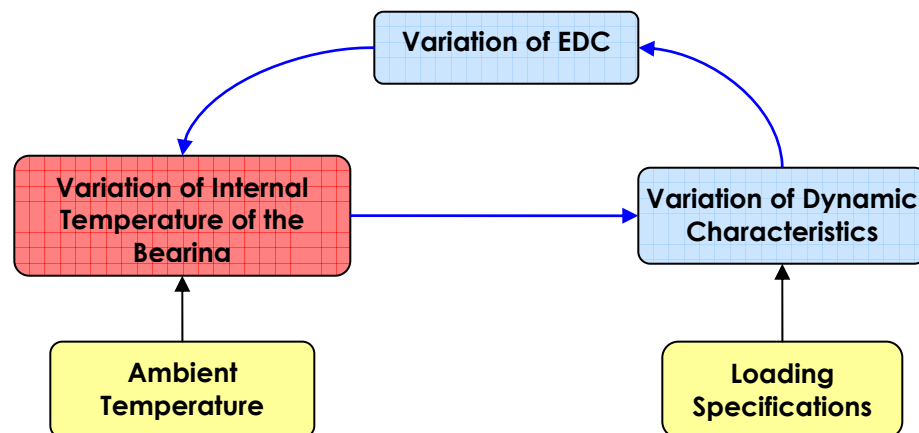


Figure 5-27: Illustration chart of interactions between the variable involved in property degradation of elastomeric bearing with lead core

From the result of experiment I, which was performed on 4 elastomeric devices through divers test protocols, it was confidently concluded that:

- Elastomeric bearings experience property degradations when they are subjected to cyclic load.
- Heat-flux, defined as $[EDC/Period/Area]$, must be considered for degradation analysis rather than EDC alone.
- In most elastomeric bearings with lead plug, heat is mainly (~95 %) generated in lead plug.
- The two characteristics, average stiffness and ultimate force (and consequently EDC), are the main properties of interest for degradation analysis.
- The property loss due to cyclic load is affected by a number of loading specifications such as the type of cyclic load, amplitude and frequency of loading.
- The property degradation of elastomeric bearings could also be a function of size and shape of the bearing.
- Lead can recover a notable portion of its lost property within a short interruption (less than 20 minutes) in loading.

6

Thermal Behavior and Modeling

Step-1 of this research, which was performed and discussed in Chapter 5, made it clear that elastomeric bearings experience progressive property loss, as cyclic load is continuously applied. Lead plugs are primarily targeted in such degrading conditions. However, other conditions may also contribute in property loss of lead plugs.

It was also discussed in Chapter 4 that rubber, as one of the two major components of elastomeric bearings is susceptible to thermal degradation, which itself is resulted by over-vulcanization process. Knowledge about the internal temperature of a bearing is a requirement for quantification of the property loss, when a bearing is subjected to a certain ambient and loading conditions.

For this reason, an experimentally supported F.E.M. was created in order to evaluate the internal heat status of an elastomeric bearing. Such model must be capable of representing the differentiation of temperature inside the bearing when only generic information such as ambient condition, thermal properties (thermal conductivity and specific heat) and geometries of the components of the bearing are available.

The numerical model must be supported with sufficient experimental and theoretical bases.

This chapter discusses the finite element modeling technique which was performed and, laid out a discussion foreground to analyze and correlate the obtained results of each development phase. The objectives pursued during this step of the research are addressed below.

1. Evaluation of the reliability of F.E. modeling by means of side-by-side comparison to the actual experiment data.
2. Implementation of a second approach to verify the reliability of F.E. modeling by further measures and different approaches. This task was performed by introducing in the F.E. model an equivalent substitute material for which the thermal properties are obtained theoretically.
3. Proposing a model to quantify steady state temperature of the lead plug inside a bearing with respect to the input heat-flux and ambient temperature.
4. Proposing a model to quantify transient temperature at the lead plug during application of load during a single cycle. This was to be used in quantifying per-cycle degradation of a bearing due to abrupt motions of earthquake.

5. Proposing a methodology to investigate the effects of dynamic interaction between internal components of a bearing on temperature distribution within the core.

In Figure 6-1, the subjects of the present chapter are highlighted in red. The specific goal of this step will be proposing a model to analytically calculate the internal temperature of the test bearings, used in Experiment-1, both in transient and steady state.

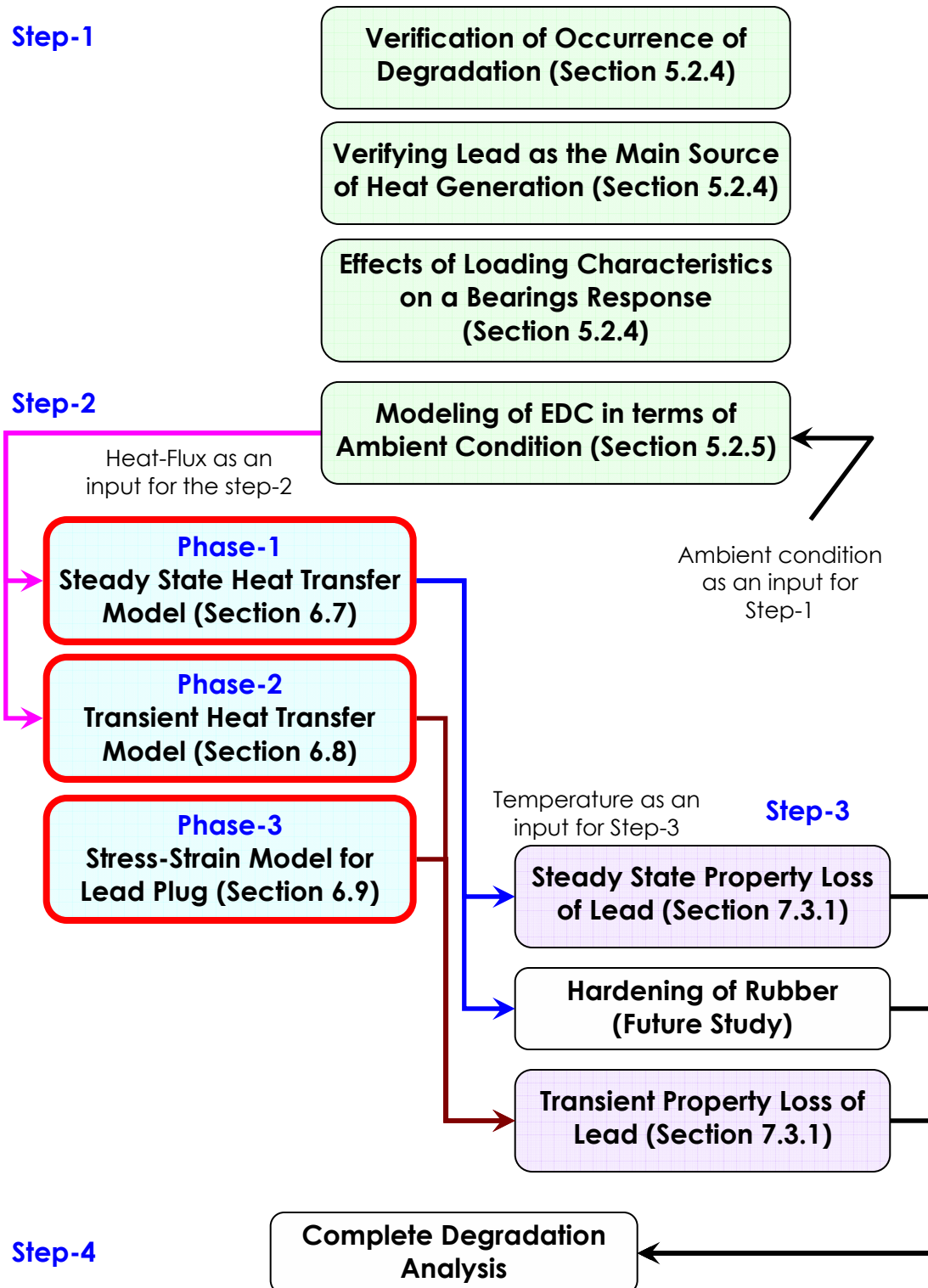


Figure 6-1: Flow diagram of steps taken in present chapter is highlighted in red

6.1 Study of the Thermal Behavior of Elastomeric Bearings

The result of Experiment-1 proved that an elastomeric bearing loses its engineering and physical properties transiently and permanently. This phenomenon happens particularly when a bearing is subjected to lateral cyclic load at certain loading condition. The rate and magnitude of this property loss is increased as the number of cycle increases or the load specifications changes. The temperature rise within the body of an elastomeric bearing is a result of heat generation within the lead plug through its hysteretic action.

Therefore, in order to predict and quantify the degradation of a bearing it is needed to know the magnitude of temperature at vicinity of the core as well as the body of the bearing.

The efforts at this part of the research were focused on finding a methodology through which measuring the internal temperature of elastomeric bearings was possible. Due to the fact that almost the entire (~95%) thermal energy is generated within the lead plugs, a non-uniform degradation is expected within the body of an elastomeric bearing. For that reason, it was necessary to have information about state of temperature within the core. Since the core is not accessible, a technique by which measuring the internal temperature becomes possible, must be proposed. For this purpose, thermocouples were

placed in certain depths of LRB700 and subjected the bearing to dynamic load. Figure 6-2 shows the type thermocouple used in an attempt to experimentally measure the internal temperature of a bearing. The test set up configuration is shown in Figure 6-3.

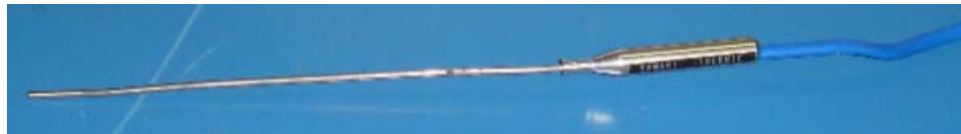


Figure 6-2: Thermocouple rods used in an attempt for measuring internal temperature of a bearing



Figure 6-3: Thermocouples were inserted at certain locations into body of LRB700. The experiment failed due to failure of the thermocouples to stay in place

The experiment was not successful due to failure of the thermocouples to stay in place when the bearing was dynamically loaded. To overcome this obstacle a different experiment was performed on a stationary bearing with heat generated by means of a

heating element. Functionality of thermocouples faced no difficulty through the application of this method.

6.2 Experiment-2

The goal of this experiment was to make a test bearing capable of generating thermal energy on which temperature measuring devices installed in specific locations. This provided information about heat distribution profile, also led to an understanding about the effects of ambient temperature and input energy on overall temperature of a bearing.

6.2.1 Instrumentation of the Test Bearing

The material and instruments for this experiment was carefully selected in order make the response of the bearing as close to a real bearing as possible.

The experiment was initiated by preparing a block of laminated rubber, manufactured with details similar to an actual bearing. A borehole with diameter of 140 mm was made at the center of the block and an aluminum shaft was tightly inserted in the borehole. The main body of this test bearing was a block of rubber with 17 embedded steel plates of 2.3 mm thick. Steel plates were equally spaced over the

height of the bearing. Schematic and major dimension of the test bearing is given in Figure 6-4.

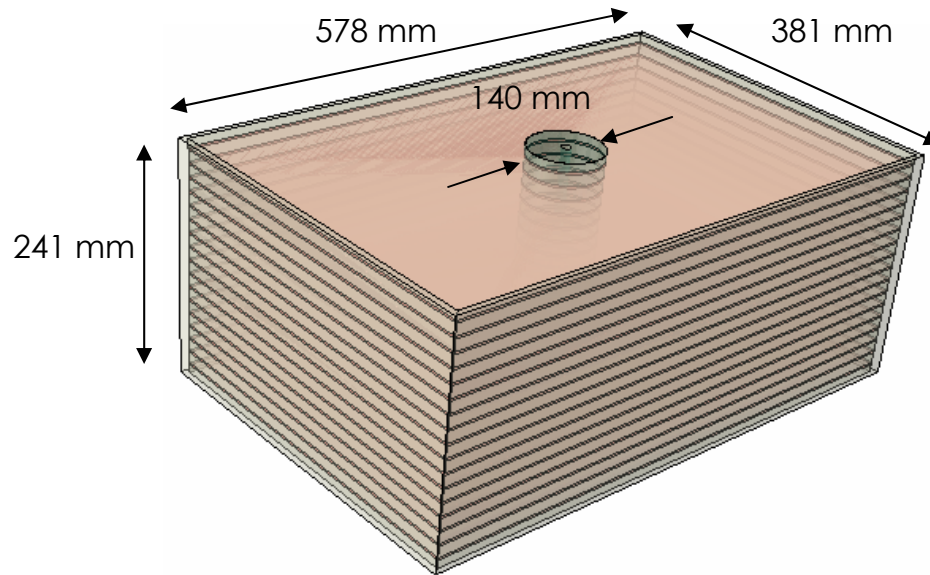


Figure 6-4: Schematic of the test bearing used in Experiment-2.

A heating element was placed by drilling a hole at the center of an aluminum shaft along its axis, Figure 6-5.



Figure 6-5: Heating element and its shield

This assembly served as the core of the bearing. There was no dynamic stimulation intended to be placed on this test bearing.

The bearing, with heating assembly installed on it, was connected to a voltage control device equipped with a thermostat system. The thermostat allowed a controlled steady flow of heat into the bearing. Figure 6-6 shows the test bearing with the heating assembly installed on it.

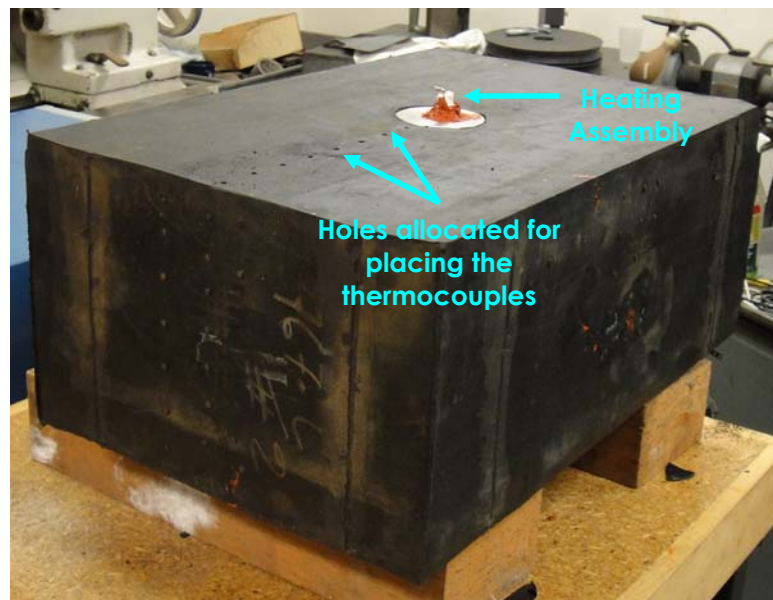


Figure 6-6: The instrumentation of the test bearing used for Experiment-2

Eight equally spaced holes were drilled on the bearing at locations shown in Figures 6-7 and 6-8. The holes stopped at the steel plate located at mid-height. Thermocouples were placed in holes and pushed firmly to have solid contacts with steel plate (Figure 6-6). They were then connected to a 12-channel data acquisition unit. The thermocouples denoted by TC 01 to TC 09 where TC 09 is the closest to the core.

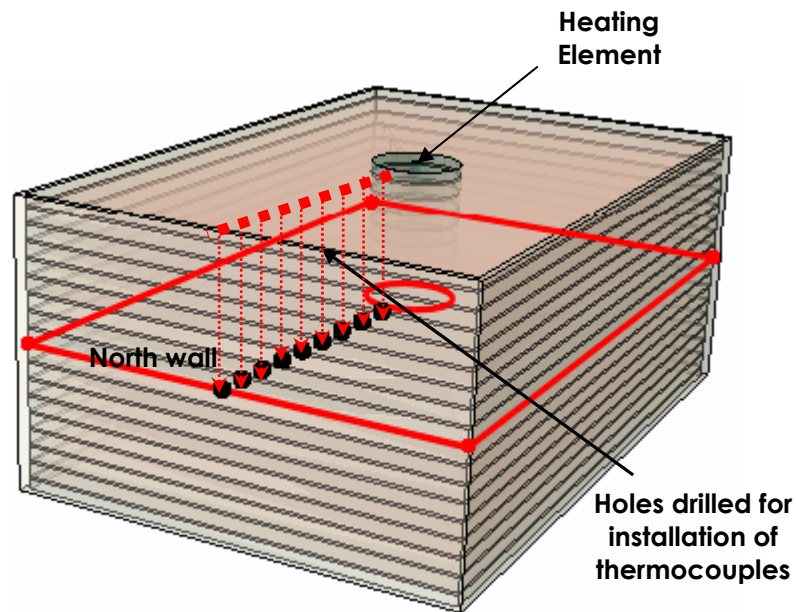


Figure 6-7: Location of the thermocouples at the mid-height steel plate

Figure 6-8 shows a schematic of top view of the bearing with location of thermocouples marked.

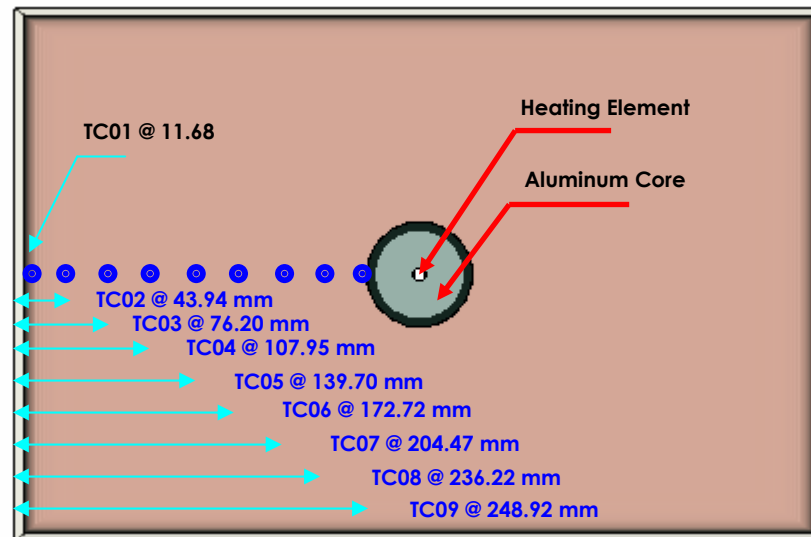


Figure 6-8: Top view of the bearing shows locations of the thermocouples with respect to the north wall of the bearing

6.2.2 Test Procedure and Result

The voltage control system was manually set to heat up the assembly to 5 different temperatures. In order to provide consistent initial conditions over the course of experimentation, only one test was performed per day and let the bearing cooled down to the ambient before the next test was performed. The temperature at TC09 (temperature at core) was used as the reference temperature. As one of the objectives of the experiment, it was necessary to acquire knowledge about the effect of preexisting and also the ambient temperatures on thermal conduction behavior of the bearing. For this reason, a number of tests were performed at various input heat-flux and ambient temperature but, only one set of variables was let free at each test. The task of keeping consistency in heat-flux was done by measuring the resistance at the end of the potentiometer that controlled the input voltage. The data acquisition unit was set to a sampling rate of 1 per 10 seconds. It took nearly 1 hour for the assembly to reach a temperature close to thermal steady state condition. Nearly 360 samples were collected at each test. The temperature of each thermocouple at thermal steady state condition is given on (Table 6-1). Test-A to Test-E refer to a series of tests at which heat flux varied from one test to another while temperature recorded at each

thermocouple. Heat flux is a measure of energy flow per unit of area per unit of time (Section 6.3.1). In SI units, it is measured in watt per meter square W/m^2 . Heat- flux was computed by measuring the resistance and potential difference of the heat element while it was connected to the power supply. According to the Joule's law, in an electrical system power " P " is equal to:

$$P = VI \quad \text{Equation 6-1}$$

where, V is the potential difference across, and I is the current passing through the heating element. Electrical current I , can be written as its equivalent in terms of voltage and resistance R ,

$$I = \frac{V}{R} \quad \text{Equation 6-2}$$

thus, power measured in watts, is re-written as

$$P = \frac{V^2}{R} \quad \text{Equation 6-3}$$

The amount of heat flux was kept unchanged over the course of each test. Total of 5 levels of heat flux (Tests A to E) were put into the bearing at 5 levels of ambient temperatures (T_{a1} to T_{a5}), hence, 225 readings were recorded for all 9 thermocouples. It was performed this way to investigate the simultaneous effects of variation of energy and ambient temperature on the internal body temperature of the bearing. The test data of the Experiment-2 is listed in Table 6-1.

Table 6-1: Result of Experiment-2, temperature reading at each thermocouple after 45 minutes of time was elapsed

Thermocouple	Distance (mm)	Test A 16300 W/m ²	Test B 25000 W/m ²	Test C 37000 W/m ²	Test D 51500 W/m ²	Test E 65500 W/m ²
Ambient		17.59	17.59	17.59	17.59	17.59
Surface	0	20.53	22.84	25.23	28.55	31.19
TC 01	11.68	21.58	24.21	27.94	31.90	36.56
TC 02	43.94	21.90	24.88	28.97	33.58	38.25
TC 03	76.20	22.94	25.93	30.31	35.61	40.62
TC 04	107.95	23.61	26.94	32.31	38.30	44.99
TC 05	139.70	25.03	28.67	35.12	41.48	50.25
TC 06	172.72	27.08	32.75	40.55	50.27	61.66
TC 07	204.47	30.14	37.83	47.34	60.34	73.73
TC 08	236.22	34.90	45.65	60.75	78.10	95.54
TC 09	248.92	39.20	51.30	67.00	87.50	107.00
Ambient		19.30	19.30	19.30	19.30	19.30
Surface	0	22.24	24.55	26.94	30.26	32.90
TC 01	11.68	23.30	25.94	29.67	33.61	38.30
TC 02	43.94	23.61	26.59	30.69	35.31	39.98
TC 03	76.20	24.65	27.67	32.05	37.33	42.34
TC 04	107.95	25.34	28.66	34.02	40.02	46.73
TC 05	139.70	26.77	30.40	36.86	43.19	51.96
TC 06	172.72	28.79	34.47	42.27	51.98	63.40
TC 07	204.47	31.86	39.55	49.08	62.07	75.46
TC 08	236.22	36.63	47.36	62.46	79.84	97.26
TC 09	248.92	40.94	53.02	68.73	89.21	108.72
Ambient		20.40	20.40	20.40	20.40	20.40
Surface	0	23.34	25.65	28.04	31.36	34.00
TC 01	11.68	24.40	27.04	30.77	34.71	39.40
TC 02	43.94	24.71	27.69	31.79	36.41	41.08
TC 03	76.20	25.75	28.77	33.15	38.43	43.44
TC 04	107.95	26.44	29.76	35.12	41.12	47.83
TC 05	139.70	27.87	31.50	37.96	44.29	53.06
TC 06	172.72	29.89	35.57	43.37	53.08	64.50
TC 07	204.47	32.96	40.65	50.18	63.17	76.56
TC 08	236.22	37.73	48.46	63.56	80.94	98.36
TC 09	248.92	42.04	54.12	69.83	90.31	109.82
Ambient		21.61	21.61	21.61	21.61	21.61
Surface	0	24.55	26.86	29.25	32.57	35.21
TC 01	11.68	25.61	28.25	31.98	35.92	40.62
TC 02	43.94	25.93	28.91	33.00	37.63	42.29
TC 03	76.20	26.97	29.98	34.36	39.64	44.65
TC 04	107.95	27.66	30.97	36.34	42.33	49.05
TC 05	139.70	29.09	32.71	39.18	45.50	54.27
TC 06	172.72	31.11	36.78	44.58	54.29	65.72
TC 07	204.47	34.17	41.86	51.39	64.38	77.77
TC 08	236.22	38.95	49.68	64.77	82.15	99.57
TC 09	248.92	43.26	55.33	71.04	91.52	111.03
Ambient		22.92	22.92	22.92	22.92	22.92
Surface	0	25.86	28.17	30.56	33.88	36.52
TC 01	11.68	26.92	29.57	33.29	37.23	41.93
TC 02	43.94	27.24	30.22	34.31	38.94	43.60
TC 03	76.20	28.28	31.29	35.67	40.95	45.96
TC 04	107.95	28.97	32.28	37.65	43.64	50.36
TC 05	139.70	30.40	34.03	40.49	46.81	55.58
TC 06	172.72	32.42	38.10	45.89	55.61	67.03
TC 07	204.47	35.48	43.17	52.70	65.69	79.08
TC 08	236.22	40.26	50.99	66.09	83.46	100.88
TC 09	248.92	44.57	56.64	72.35	92.83	112.34

6.2.3 Analysis and Conclusions

The conclusions and important observations, made during the parametric study by means of the finite element model, is discussed in the next 4 subsection. The highlights of these observations are:

1. Nonlinearity of heat distribution across the bearing
2. Linear relation between a bearing's internal temperature and variation of ambient temperature
3. Linear relation between a bearing's internal temperature and variation of input heat-flux
4. Empirical equation governing the relation between a bearing's internal temperature and the two variables of ambient temperature and input heat-flux

1. **Nonlinearity of Heat Distribution across the Bearing**

It was observed on all 25 tests that the temperature profile across the bearing is not linear, Figure 6-9. This result matched the anticipated behavior of heat across the bearing. Non-linearity was expected due to the non-isotropic nature of the bearing. Linear profile can only be expected for materials with equal thermal conductivity in all directions. Metals are examples of these type materials. Temperature at each thermocouple, plotted versus its location along path "A", is shown in

Figure 6-9. The Data was sampled after 45 minutes of times was elapsed and ambient temperature was 17.59 °C.

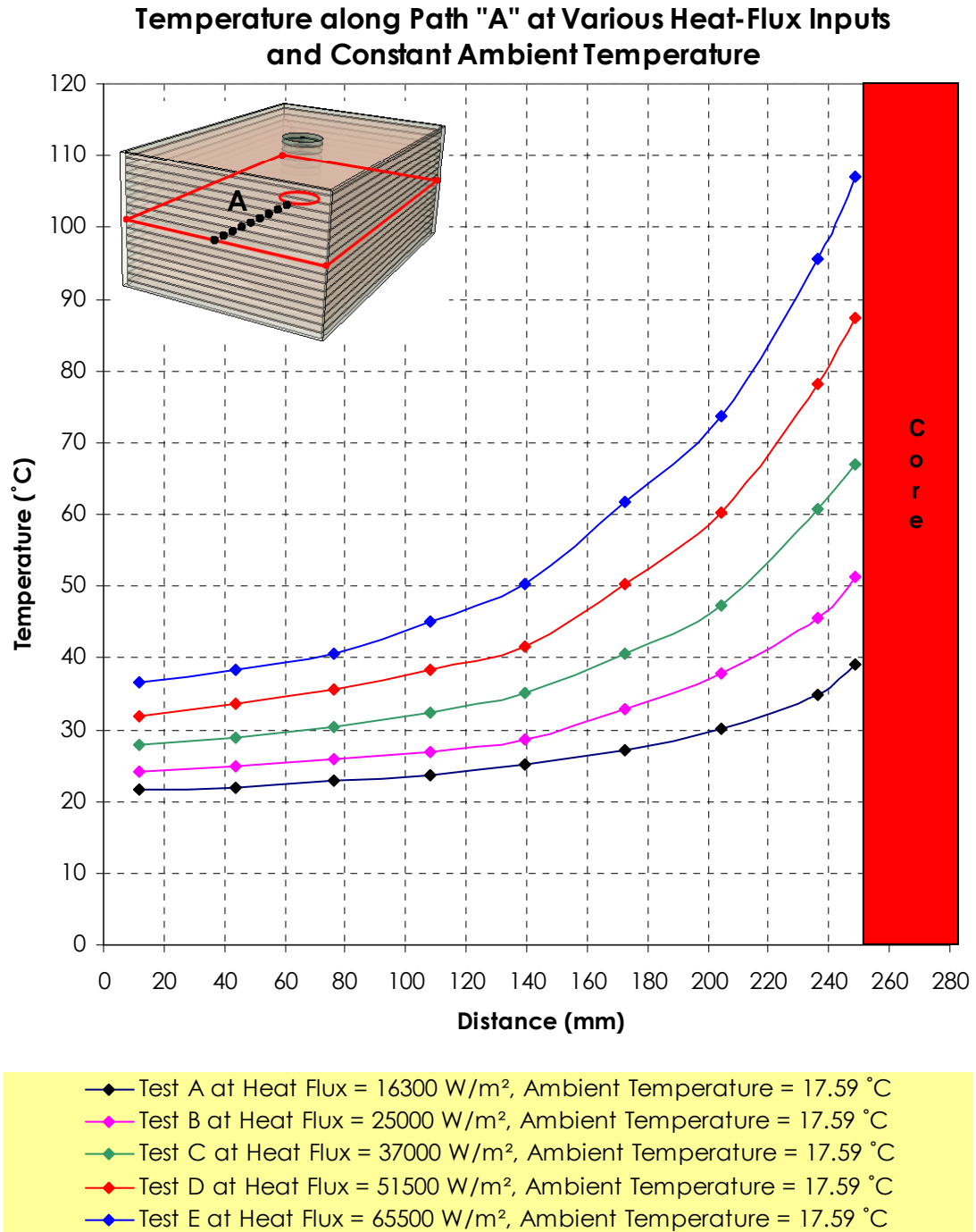


Figure 6-9: Temperature profile across the bearing shows nonlinear trend across the body of the bearing, ambient temperature was 17.59°C

2. Effect of Variation of Ambient Temperature

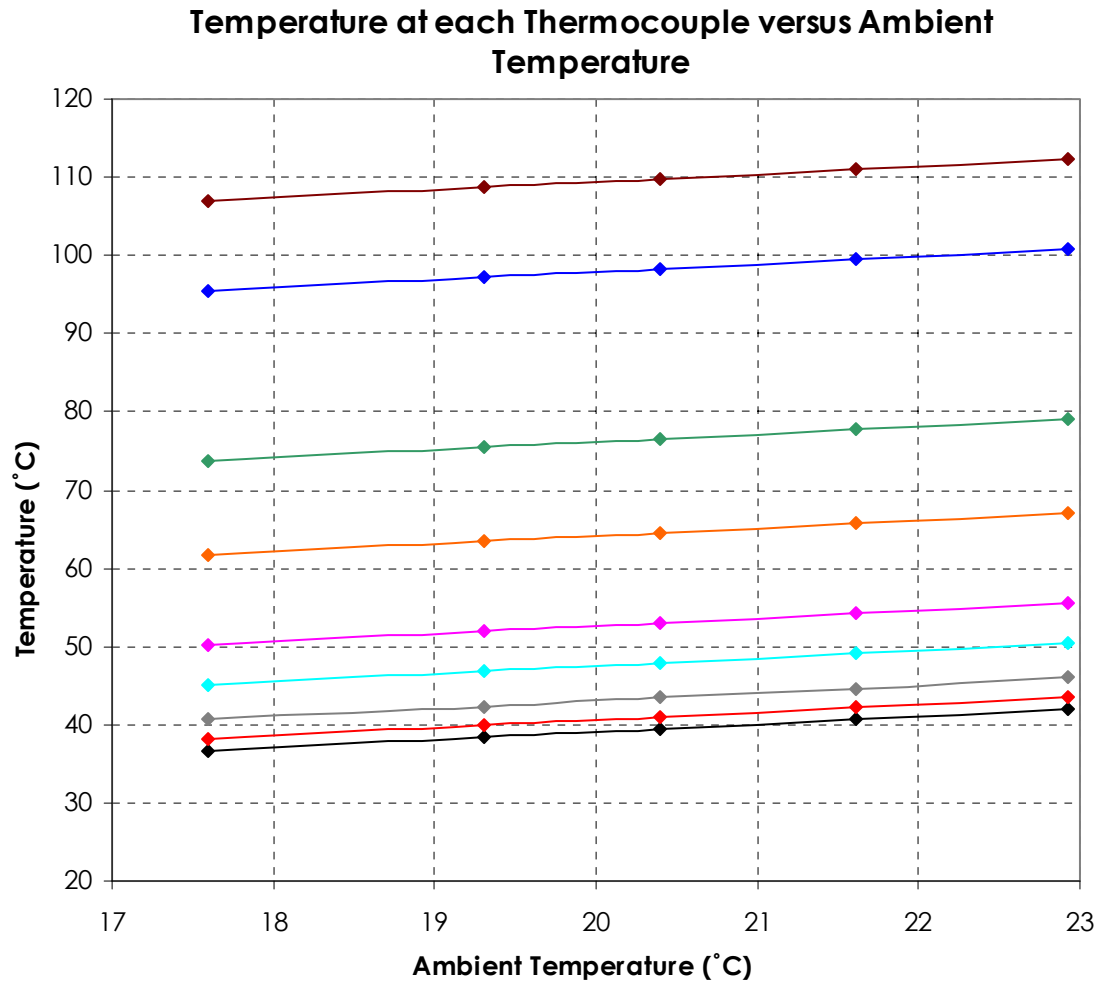
The data was rearranged in new sets in a way that the input heat-flux was kept constant at each set. Keeping this variable constant made it possible to investigate the effect of variation of ambient temperature on internal temperature of the bearing at each location. It was observed that temperature at each thermocouple varies linearly with variation of ambient temperature. This result was valid for all tests performed at various ambient temperatures.

In Table 6-2 the rearrange data are listed for each thermocouple. The table is color-coded based on the magnitude of heat flux given to the bearing at each test.

Table 6-2: Rearrangement of recorded data, variation of temperature with respect to variation of ambient temperature

Ambient (°C)	TC 01	TC 02	TC 03	TC 04	TC 05	TC 06	TC 07	TC 08	TC 09
Heat-Flux = 16300 W/m²									
17.59	21.58	21.90	22.94	23.61	25.03	27.08	30.14	34.90	39.20
19.30	23.30	23.61	24.65	25.34	26.77	28.79	31.86	36.63	40.94
20.40	24.40	24.71	25.75	26.44	27.87	29.89	32.96	37.73	42.04
21.61	25.61	25.93	26.97	27.66	29.09	31.11	34.17	38.95	43.26
22.92	26.92	27.24	28.28	28.97	30.40	32.42	35.48	40.26	44.57
Heat-Flux = 25000 W/m²									
17.59	24.21	24.88	25.93	26.94	28.67	32.75	37.83	45.65	51.30
19.30	25.94	26.59	27.67	28.66	30.40	34.47	39.55	47.36	53.02
20.40	27.04	27.69	28.77	29.76	31.50	35.57	40.65	48.46	54.12
21.61	28.25	28.91	29.98	30.97	32.71	36.78	41.86	49.68	55.33
22.92	29.57	30.22	31.29	32.28	34.03	38.10	43.17	50.99	56.64
Heat-Flux = 37000 W/m²									
17.59	27.94	28.97	30.31	32.31	35.12	40.55	47.34	60.75	67.00
19.30	29.67	30.69	32.05	34.02	36.86	42.27	49.08	62.46	68.73
20.40	30.77	31.79	33.15	35.12	37.96	43.37	50.18	63.56	69.83
21.61	31.98	33.00	34.36	36.34	39.18	44.58	51.39	64.77	71.04
22.92	33.29	34.31	35.67	37.65	40.49	45.89	52.70	66.09	72.35
Heat-Flux = 51500 W/m²									
17.59	31.90	33.58	35.61	38.30	41.48	50.27	60.34	78.10	87.50
19.30	33.61	35.31	37.33	40.02	43.19	51.98	62.07	79.84	89.21
20.40	34.71	36.41	38.43	41.12	44.29	53.08	63.17	80.94	90.31
21.61	35.92	37.63	39.64	42.33	45.50	54.29	64.38	82.15	91.52
22.92	37.23	38.94	40.95	43.64	46.81	55.61	65.69	83.46	92.83
Heat-Flux = 65500 W/m²									
17.59	36.56	38.25	40.62	44.99	50.25	61.66	73.73	95.54	107.00
19.30	38.30	39.98	42.34	46.73	51.96	63.40	75.46	97.26	108.72
20.40	39.40	41.08	43.44	47.83	53.06	64.50	76.56	98.36	109.82
21.61	40.62	42.29	44.65	49.05	54.27	65.72	77.77	99.57	111.03
22.92	41.93	43.60	45.96	50.36	55.58	67.03	79.08	100.88	112.34

The plot of temperature at each thermocouple as a function of variation of ambient temperature and constant heat flux of 65500 W/m² is shown in Figure 6-10. The rest of plots of this category are available in Appendix E.



- ◆— Thermocouple #1 at Distance = 11.68 mm, Heat-Flux = 65500 W/m²
- ◆— Thermocouple #2 at Distance = 43.94 mm, Heat-Flux = 65500 W/m²
- ◆— Thermocouple #3 at Distance = 76.20 mm, Heat-Flux = 65500 W/m²
- ◆— Thermocouple #4 at Distance = 107.95 mm, Heat-Flux = 65500 W/m²
- ◆— Thermocouple #5 at Distance = 139.70 mm, Heat-Flux = 65500 W/m²
- ◆— Thermocouple #6 at Distance = 172.72 mm, Heat-Flux = 65500 W/m²
- ◆— Thermocouple #7 at Distance = 204.47 mm, Heat-Flux = 65500 W/m²
- ◆— Thermocouple #8 at Distance = 236.22 mm, Heat-Flux = 65500 W/m²
- ◆— Thermocouple #9 at Distance = 248.92 mm, Heat-Flux = 65500 W/m²

Figure 6-10: Temperature at each thermocouple, plotted versus variation of ambient temperature at constant heat flux of 65500 W/m²

3. Linear Relation Between the Input Heat Flux and Internal Temperature

To isolate the effects of heat-flux on internal temperature of the bearing, the data obtained from Experiment-2 was rearranged in a way that ambient temperature was kept constant at each test. That allowed plotting variation of temperature at any point as a function of input heat flux. The rearranged data is tabulated in Table 6-2.

The plots of all 25 tests, which were performed at 5 levels of heat-flux within 5 different ambient temperatures, show existence of a linear relation between the amount of energy given to the system and the temperature at each point within the body of the bearing. The slope of the line, however, changed from one test to another depending on magnitude of the heat flux. This result is valid only when the thermal steady state condition is established.

Table 6-3: Rearrangement of data of Experiment-2

H-Flux (w/m ²)	TC 01	TC 02	TC 03	TC 04	TC 05	TC 06	TC 07	TC 08	TC 09
Ambient = 17.59 °C									
16300	21.58	21.90	22.94	23.61	25.03	27.08	30.14	34.90	39.20
25000	24.21	24.88	25.93	26.94	28.67	32.75	37.83	45.65	51.30
37000	27.94	28.97	30.31	32.31	35.12	40.55	47.34	60.75	67.00
51500	31.90	33.58	35.61	38.30	41.48	50.27	60.34	78.10	87.50
65500	36.56	38.25	40.62	44.99	50.25	61.66	73.73	95.54	107.00
Ambient = 19.30 °C									
16300	23.30	23.61	24.65	25.34	26.77	28.79	31.86	36.63	40.94
25000	25.94	26.59	27.67	28.66	30.40	34.47	39.55	47.36	53.02
37000	29.67	30.69	32.05	34.02	36.86	42.27	49.08	62.46	68.73
51500	33.61	35.31	37.33	40.02	43.19	51.98	62.07	79.84	89.21
65500	38.30	39.98	42.34	46.73	51.96	63.40	75.46	97.26	108.72
Ambient = 20.40 °C									
16300	24.40	24.71	25.75	26.44	27.87	29.89	32.96	37.73	42.04
25000	27.04	27.69	28.77	29.76	31.50	35.57	40.65	48.46	54.12
37000	30.77	31.79	33.15	35.12	37.96	43.37	50.18	63.56	69.83
51500	34.71	36.41	38.43	41.12	44.29	53.08	63.17	80.94	90.31
65500	39.40	41.08	43.44	47.83	53.06	64.50	76.56	98.36	109.82
Ambient = 21.61 °C									
16300	25.61	25.93	26.97	27.66	29.09	31.11	34.17	38.95	43.26
25000	28.25	28.91	29.98	30.97	32.71	36.78	41.86	49.68	55.33
37000	31.98	33.00	34.36	36.34	39.18	44.58	51.39	64.77	71.04
51500	35.92	37.63	39.64	42.33	45.50	54.29	64.38	82.15	91.52
65500	40.62	42.29	44.65	49.05	54.27	65.72	77.77	99.57	111.03
Ambient = 22.92 °C									
16300	26.92	27.24	28.28	28.97	30.40	32.42	35.48	40.26	44.57
25000	29.57	30.22	31.29	32.28	34.03	38.10	43.17	50.99	56.64
37000	33.29	34.31	35.67	37.65	40.49	45.89	52.70	66.09	72.35
51500	37.23	38.94	40.95	43.64	46.81	55.61	65.69	83.46	92.83
65500	41.93	43.60	45.96	50.36	55.58	67.03	79.08	100.89	112.34

Figure 6-11 shows plots of temperature at each thermocouple versus input heat-flux at constant ambient temperature of 22.92 °C. The rest of plots of this group for other tests are available in Appendix F.

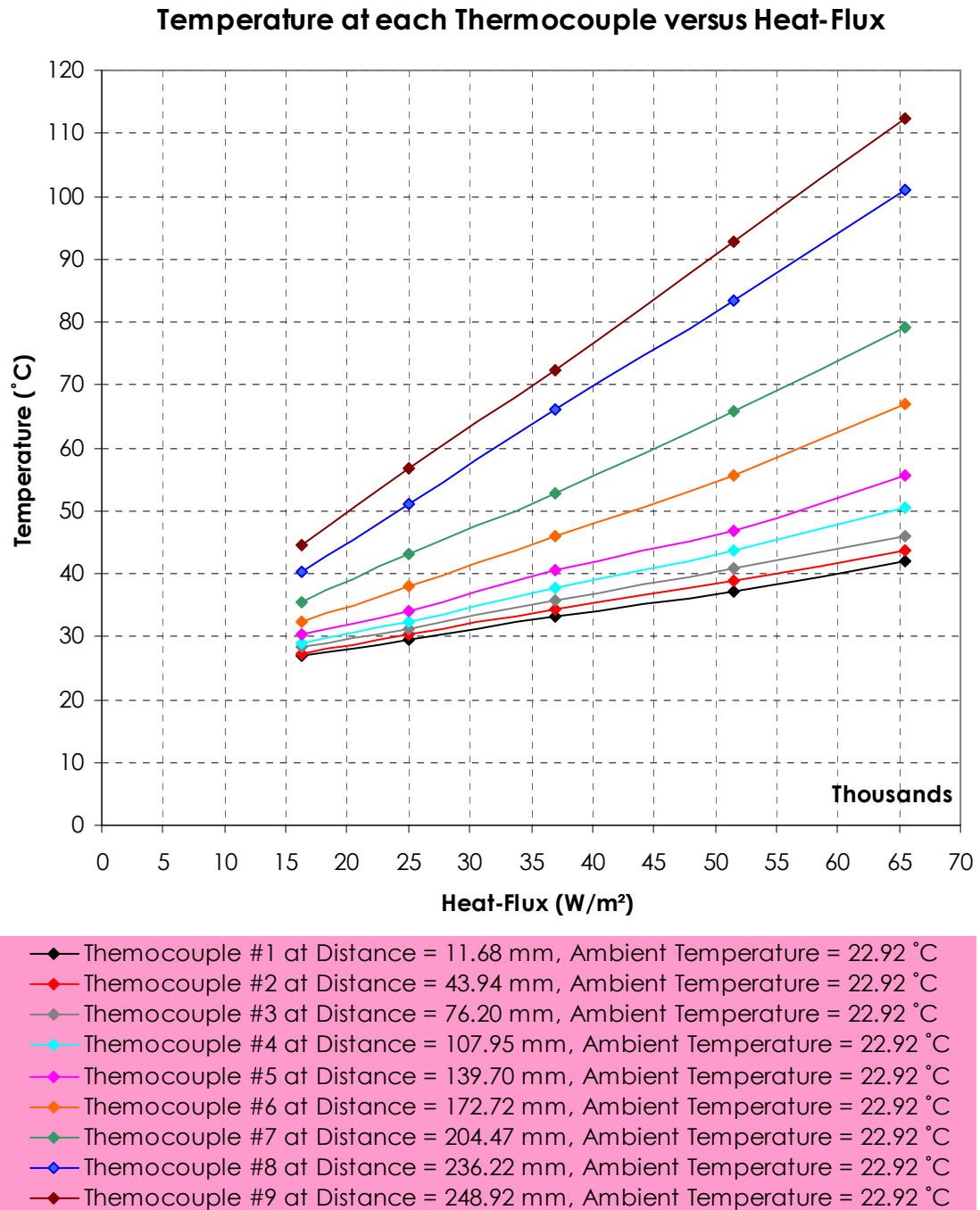


Figure 6-11: linear relation was observed between input heat-flux and the internal temperature of the bearing when ambient temperature remained constant

4. Variation of Temperature at the Core with Respect to Ambient Temperature and Input Heat-flux

From the analysis of the two previous sections it became known that temperature at each of the 9 thermocouples is in a linear relation with input heat-flux when the ambient temperature was constant. Similarly, the temperature showed to be in a linear relation with ambient temperature when the input heat-flux was kept constant. Letting the two variables free to change, it was expected to have the temperature of each thermocouple to shift as the ambient temperature changes. Collected data from thermocouple #9 at all 25 performed tests is given in (Table 6-4). Also, the plot in Figure 6-12 shows the temperature at thermocouple #9 as a function of input heat flux at various ambient temperatures.

Table 6-4: Temperature at thermocouple #9 presented in matrix form

	HF1=16300 W/m ²	HF2=25000 W/m ²	HF3=37000 W/m ²	HF4=51500 W/m ²	HF5=65500 W/m ²
T _{a1} =17.59 °C	T11=39.20	T12=51.30	T13=67.00	T14=87.50	T15=107.00
T _{a2} =19.30 °C	T21=40.94	T22=53.02	T23=68.73	T24=89.21	T25=108.72
T _{a3} =20.40 °C	T31=42.04	T32=54.12	T33=69.83	T34=90.31	T35=109.82
T _{a4} =21.61 °C	T41=43.26	T42=55.33	T43=71.04	T44=91.52	T45=111.03
T _{a5} =22.92 °C	T51=44.57	T52=56.64	T53=72.35	T54=92.83	T55=112.34

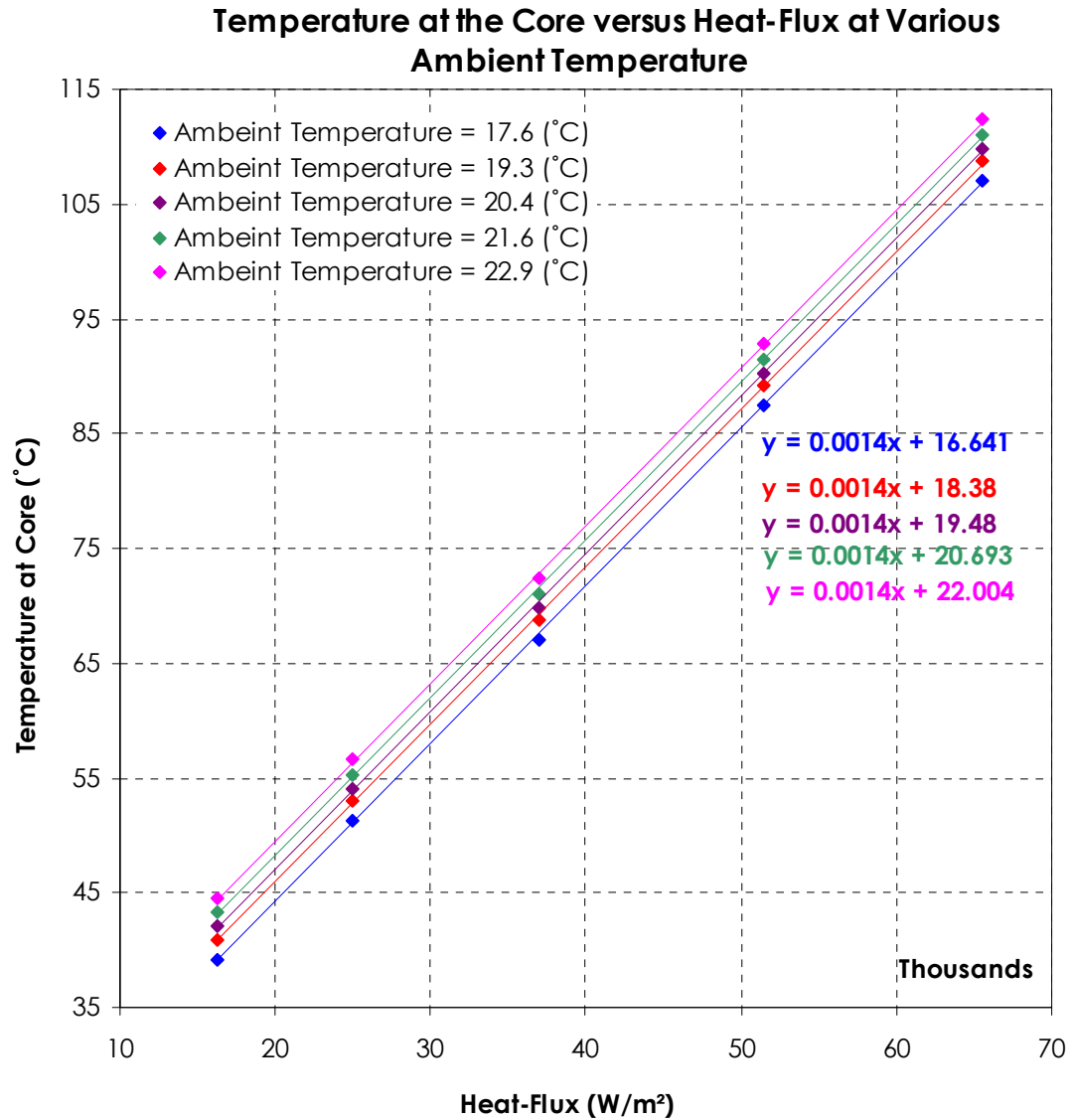


Figure 6-12: Plot of temperature at the closet thermocouple to the core as a function of ambient temperature and input heat-flux

6.2.4 Highlights of Experiment-2

The result obtained from Experiment-2 showed that:

- Heat distribution across the body of a bearing is nonlinear.

- Preexisting temperature of a bearing can only affect the time that it takes a bearing to reach its thermal steady state condition.
- Temperature at any point on or within a bearing is in linear relation with input heat flux.
- Temperature at any point on or within a bearing is in linear relation with ambient temperature.

6.3 Mechanical Properties of Laminated Rubber

The finite element modeling was verified with further measures by applying an additional approach. In this approach the laminated rubber was to be substituted with an equivalent material for which the mechanical properties were derived theoretically. This approach was termed the "Indirect Finite Element Modeling". The results of the three approaches (experiment, direct F.E.M and indirect F.E.M) were expected to converge.

Theory of laminated materials was used to derive effective mechanical properties of laminated rubber-steel. The equivalent properties needed to be assigned for the following characteristics:

Longitudinal coefficient of thermal conductivity, $K_{eff(L)}$.

Transverse coefficient of thermal conductivity, $K_{eff(T)}$.

Longitudinal Young's modulus, $E_{eff(L)}$.

Transverse Young's modulus, $E_{eff(T)}$.

Major Poisson's ratio, ν_{12}

In-plane Shear modulus, G_{12}

1. Coefficient of Thermal Conductivity in Longitudinal Direction,

$$k_{eff(L)}$$

Thermal energy is transferred between two points within a body, or bodies in contact, when temperature gradient exists. The term Conduction refers to the heat transfer occurring across a medium, solid or fluid, in presence of temperature gradient. The heat flux q_x'' [W/m²K] is the heat transfer rate in the X direction (X is any random direction) per unit area perpendicular to the direction of transfer, and is proportional to temperature gradient $\frac{dT}{dx}$ in this direction. Thermal conductivity refers to the proportionality constant k , which exists in relation $q_x'' = k \frac{dT}{dx}$. The unit of thermal conductivity is W/mK. In elastomeric bearings heat is initiated at the lead plug and reached the rubber and steel shims by conduction. Beside that, conduction takes place between rubber and steel shims.

Coefficient of thermal conductivity is available in literature for many common isotropic materials such as steel, aluminum, ceramic

and wood etc. However, for non-isotropic materials such as laminated materials, coefficient of thermal conductivity must be evaluated theoretically. It can be done if the lamination order and thermal characteristics of the constituents of the bearing are known. The energy distribution path shows that the generated energy is mainly transferred to the steel shim and distributed rapidly in longitudinal direction, on its path through steel shims. This energy is partially absorbed by layers of rubber which have relatively large area in contact with steel shims, i.e. transverse conduction takes place. It, however, happens in much lower rate compare to the longitudinal conduction. Hence, the effective coefficient of conduction is expected to be a function of thermal conductivity and volume fraction of the main constituents of a bearing which are lead, rubber and steel. Figure 6-13 presents a schematic of thermal interaction among the constituents in a typical elastomeric bearing with lead.

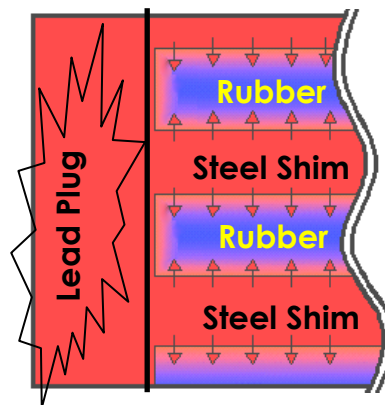


Figure 6-13: Schematic of thermal interaction between the constituents in a typical elastomeric bearing with lead

A unit cell of dimension $L \times D \times h$ is selected by considering a single steel shim laminated in between half of the height of each of the upper and lower rubber layers.

A few assumptions made for this derivation are such as:

- Steel and rubber are perfectly isotropic materials
- Thickness of each layer remains constant
- Rubber and steel shims are perfectly bonded together
- Thermal steady state is established

The configuration of the unit cell of laminated rubber-shim is given in Figure 6-14.

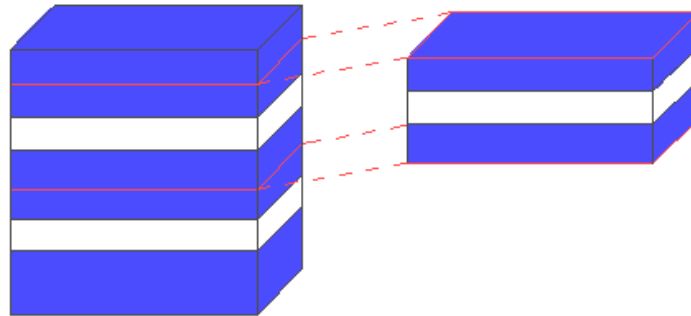


Figure 6-14: A unit cell of dimension $L \times D \times h$ is selected by considering a single steel shim sandwiched in between the half the height of each of the upper and lower rubber layers

Considering the unit cell of Figure 6-2 is subjected to a temperature difference $\Delta T = T_{out} - T_{in}$, the Fourier's law of conduction states:

$$q = -kA \frac{dT}{dx} = \frac{kA}{L} (T_{in} - T_{out}) \quad \text{(Equation 6-4)}$$

where:

q , k , A , $\frac{dT}{dx}$, L , $(T_{in} - T_{out})$ are the input energy, thermal conductivity, section area perpendicular to the flux, temperature gradient, length of the unit cell and temperature difference at the ends of the laminated unit cell respectively. Figure 6-15 shows the laminated unit cell and the notations used for deriving coefficient of thermal conductivity in longitudinal direction for laminated rubber-steel.

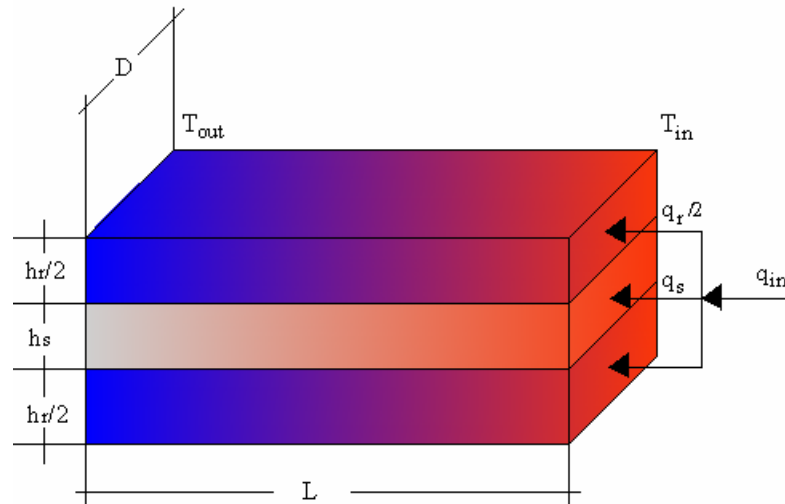


Figure 6-15: Configuration of the unit cell used for deriving of coefficient of thermal conductivity in longitudinal direction

The entering energy, q , is divided and distributed over the layers of the unit cell based on thermal conductivities of steel and rubber. Thus, the total entering energy can be expressed as:

$$q_{in} = q_R + q_S \quad \text{(Equation 6-5)}$$

where:

q_R and q_S are the energies passing through rubber and steel layers respectively.

Plugging Equation 6-1 into Equation 6-2 gives:

$$\frac{k_{(L)eff} A}{L} (T_{in} - T_{out}) = \frac{k_R A_R}{L} (T_{in} - T_{out}) + \frac{k_S A_S}{L} (T_{in} - T_{out}) \quad \text{(Equation 6-6)}$$

where:

$k_{(L)eff}$, k_R , k_S are the longitudinal conductivities of the laminated unit cell, rubber and steel layers respectively and A_R , A_S are section areas of rubber layers and steel shims. Simplified form of the Equation 6-3 is:

$$k_{(L)eff} A = k_R A_R + k_S A_S \quad \text{(Equation 6-7)}$$

since all layers have the same length, the cross section areas can be substituted by volume of each layer.

$$k_{(L)eff} V = k_R V_R + k_S V_S \quad \text{(Equation 6-8)}$$

where:

V , V_R , V_S are the volumes of the laminated unit cell, rubber and steel layers respectively. Dividing both sides of Equation 6-5 by V , the equation can be simplified as:

$$k_{(L)eff} = k_R \frac{V_R}{V} + k_S \frac{V_S}{V} \quad \text{(Equation 6-9)}$$

$$k_{(L)eff} = k_R \lambda_R + k_S \lambda_S \quad \text{(Equation 6-10)}$$

Where:

λ_R and λ_s are the volume fractions of rubber and steel layers respectively.

2. Coefficient of Thermal Conductivity in Transverse Direction, $k_{eff(T)}$

To find the effective coefficient of thermal conductivity in transverse direction, the unit cell is considered to be subjected to a temperature difference on transverse direction. Variable, $\Delta T_{(C)}$, $\Delta T_{R(T)}$, $\Delta T_{R(B)}$, ΔT_s are temperature differences across the entire cell, the upper rubber, the lower rubber and the steel plate respectively. The height of the upper and lower rubber layers are halves of a whole rubber layer.

Figure 6-16 shows the laminated unit cell and the notations used for deriving coefficient of thermal conductivity in transverse direction for laminated rubber-steel.

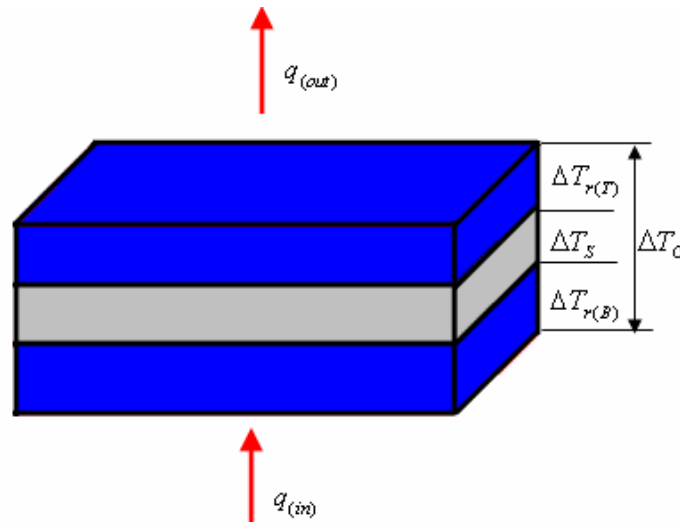


Figure 6-16: Configuration of the unit cell used for deriving of coefficient of thermal conductivity in transverse direction

Based on the law of conservation of energy, the amount of energy entering and leaving each layer is the same, therefore:

$$q_{(C)} = q_{R(T)} = q_S = q_{R(B)} \quad \text{(Equation 6-11)}$$

where:

$q_{(C)}$, $q_{R(T)}$, $q_{R(B)}$, q_S are the energies entering the unit cell, top rubber, bottom rubber and steel layers.

Temperature difference at the unit cell can be written as the summation of temperature differences across each layer:

$$\Delta T_{(C)} = \Delta T_{R(T)} + \Delta T_S + \Delta T_{R(B)} \quad \text{(Equation 6-12)}$$

however, using Equation 6-3, q , can be written in terms of temperature gradient and thermal conductivity:

$$q_{(in)} = \frac{k_{(T)eff} A}{t_C} \Delta T_{(C)} = \frac{k_R A}{t_{R(TOP)}} \Delta T_{R(T)} = \frac{k_R A}{t_{R(BOT)}} \Delta T_{R(BOT)} = \frac{k_S A}{t_S} \Delta T_S \quad \text{(Equation 6-13)}$$

where:

$\Delta T_{(C)}, t_C$, $\Delta T_{R(T)}, t_{R(TOP)}$, $\Delta T_{R(BOT)}, t_{R(BOT)}$, $\Delta T_S, t_S$ are the temperature differences and thicknesses of the laminated unit cell, upper rubber, lower rubber and steel layers. Equation 6-10 can be reformed by substituting ΔT of each layer by its equivalent in terms of k :

$$\frac{q_{(in)} t_C}{k_{(T)eff} A} = \frac{q_{(in)} t_{R(TOP)}}{k_R A} + \frac{q_{(in)} t_{R(BOT)}}{k_R A} + \frac{q_{(in)} t_S}{k_S A} \quad \text{Equation 6-14}$$

simplifying and dividing both sides by t_c :

$$\frac{1}{k_{(T)eff}} = \frac{\lambda_R}{k_R} + \frac{\lambda_S}{k_S} \quad \text{(Equation 6-15)}$$

Considering the coefficients of thermal conductivity of rubber and steel to be 0.10-1.5 W/mK and 35-45 W/mK respectively, for a bearing made by laminating steel shims of 2.5 mm and rubber layers of 10 mm thicknesses the values of effective coefficient of thermal conductivity in longitudinal and transverse direction roughly are:

$$\begin{aligned} k_{(L)eff} &= k_R \lambda_R + k_S \lambda_S = 0.10 * 0.8 + 40 * 0.2 = 8.08 \text{ W/mK} \\ \frac{1}{k_{(T)eff}} &= \frac{\lambda_R}{k_R} + \frac{\lambda_S}{k_S} = \frac{0.8}{0.1} + \frac{0.2}{40} = 8.05 \rightarrow k_{(T)eff} \approx 0.125 \text{ W/mK} \\ \frac{k_{(L)eff}}{k_{(T)eff}} &= \frac{8.08}{0.125} \approx 65 \end{aligned}$$

The computed coefficients show that in laminated rubber bearings conduction takes place in significantly higher rate in longitudinal direction compared to transverse direction.

3. Modulus of Elasticity in Longitudinal Direction

Considering stress σ_c is applied to the laminated unit cell in longitudinal direction. The force resulted by the stress applied to the unit cells is equal to summation of the force taken by each layer.

Figure 6-17 shows the laminated unit cell and the notations used for deriving longitudinal modulus of elasticity for laminated rubber-steel.

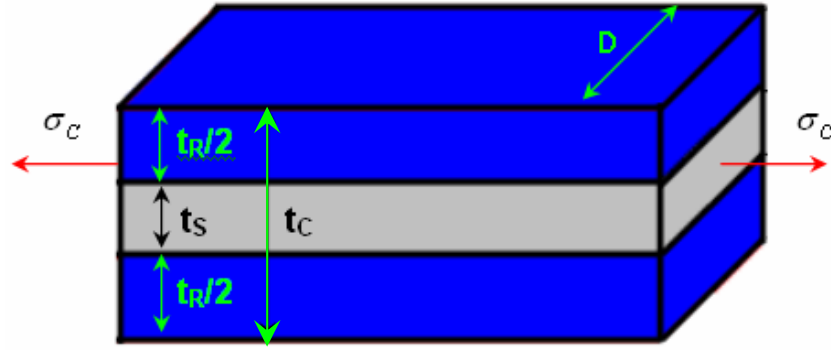


Figure 6-17: The unit cell used for deriving equivalent modulus of elasticity in longitudinal direction for laminated rubber-steel

The force applied to the unit cell can be written as summation of forces applied to each layer:

$$F_C = F_{R1} + F_S + F_{R2} \quad \text{(Equation 6-16)}$$

since $F_R = F_{R1} + F_{R2}$ then:

$$F_C = F_R + F_S \quad \text{(Equation 6-17)}$$

The forces taken by each layer can be rewritten as:

$$F_C = \sigma_C A_C, \quad F_R = \sigma_R A_R, \quad F_S = \sigma_S A_S \quad \text{(Equation 6-18)}$$

where:

$F_C, \sigma_C, A_C, F_R, \sigma_R, A_R, F_S, \sigma_S, A_S$ are the forces, stresses, and cross section areas of the unit cell, rubber and steel respectively. Stress can be written in terms of modulus elasticity and strain. Hence,

$$\sigma_C = E_C \epsilon_C, \quad \sigma_R = E_R \epsilon_R, \quad \sigma_S = E_S \epsilon_S \quad \text{(Equation 6-19)}$$

where:

$E_C, \epsilon_C, E_R, \epsilon_R, E_S, \epsilon_S$ are the moduli of elasticity and strains in the unit cell, rubber and steel layers. Substituting Equation 6-14 and Equation 6-15 into Equation 6-13:

$$E_C \epsilon_C A_C = E_R \epsilon_R A_R + E_S \epsilon_S A_S \quad \text{(Equation 6-20)}$$

and since a perfect bond is assumed between rubber and steel shims they strain equally when stretched, hence, $\epsilon_C = \epsilon_R = \epsilon_S$. By simplifying and dividing both sides of Equation 6-16 by section area of the unit cell, Equation 6-16 is modified to be Equation 6-17, which states the longitudinal modulus of elasticity in terms of moduli of rubber and steel and their volume fractions in the unit cell.

$$E_{eff(L)} = E_R \lambda_R + E_S \lambda_S \quad \text{(Equation 6-21)}$$

4. Modulus of Elasticity in Transverse Direction

Modulus of elasticity in transverse direction the most important characteristic needed for the finite element analysis of rubber bearings. To find the modulus of elasticity in transverse direction a deformation is applied to the unit cell in that direction.

Figure 6-18 shows the unit cell and the notations used for deriving modulus of elasticity in transverse direction for laminated rubber-steel.

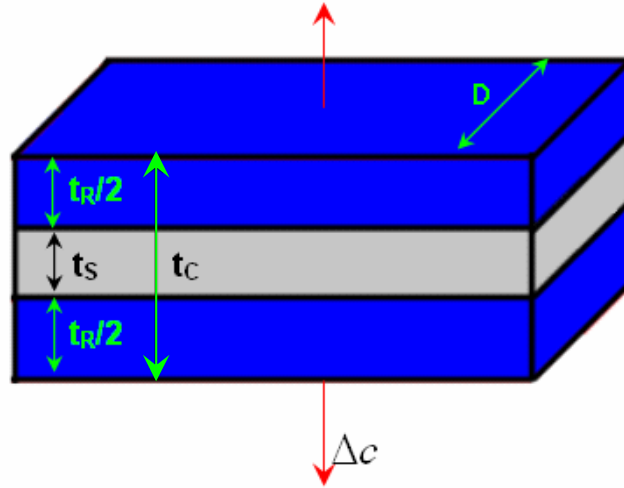


Figure 6-18: The laminated unit cell used for deriving modulus of elasticity in transverse direction for rubber-steel

The total elongation in transverse direction is the summation of elongations of individual layers:

$$\Delta c = \Delta_R + \Delta_S \quad \text{(Equation 6-22)}$$

and by definition of strain:

$$\Delta c = \varepsilon_C t_C, \quad \Delta_R = \varepsilon_R t_R, \quad \Delta_S = \varepsilon_S t_S \quad \text{(Equation 6-23)}$$

applying Hook's law:

$$\varepsilon_C = \frac{\sigma_C}{E_C}, \quad \varepsilon_R = \frac{\sigma_R}{E_R}, \quad \varepsilon_S = \frac{\sigma_S}{E_S} \quad \text{(Equation 6-24)}$$

Equation 6-21 is obtained by substituting Equation 6-19 and Equation 6-20 into Equation 6-18, which gives transverse modulus of elasticity of a laminated material in terms of moduli of its constituents:

$$\frac{1}{E_{eff(T)}} = \frac{\lambda_R}{E_R} + \frac{\lambda_S}{E_S} \quad \text{(Equation 6-25)}$$

5. In-Plane Shear Modulus, G_{12}

Shear deformation of the laminated unit cell can be written as the summation of shear deformations of rubber and steel.

Figure 6-19 shows the laminated unit cell and the notations used for deriving modulus of shear for laminated rubber-steel.

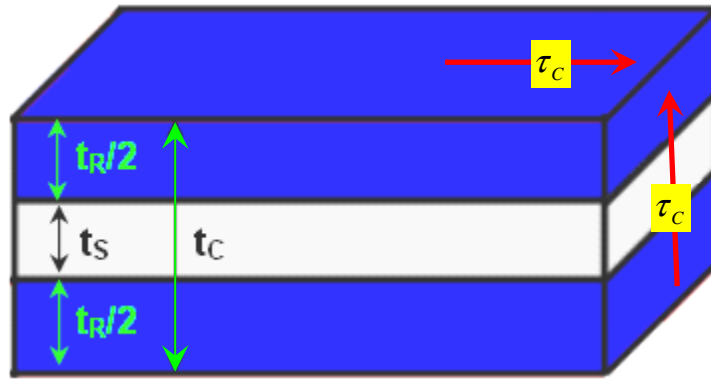


Figure 6-19: The laminated unit cell used in deriving equivalent shear modulus of laminated rubber-steel

A shear deformation to the laminated unit cell can be written as shear deformations of its individual components:

$$\delta_C = \delta_{R1} + \delta_S + \delta_{R2} \rightarrow \delta_C = \delta_R + \delta_S \quad \text{(Equation 6-26)}$$

where:

δ_C , δ_R , δ_S are the shear deformations of the unit cell, rubber and steel layers respectively.

Shear strain is defined as:

$$\gamma_C = \frac{\delta_C}{t_C}, \quad \gamma_R = \frac{\delta_R}{t_R}, \quad \gamma_S = \frac{\delta_S}{t_S} \quad \text{(Equation 6-27)}$$

from Hook's law:

$$\gamma_C = \frac{\tau_C}{G_{12C}}, \quad \gamma_R = \frac{\tau_R}{G_{12R}}, \quad \gamma_S = \frac{\tau_S}{G_{12S}} \quad \text{(Equation 6-28)}$$

where:

$(\tau_C, \gamma_C, G_{12C})$ $(\tau_R, \gamma_R, G_{12R})$ $(\tau_S, \gamma_S, G_{12S})$ are the applied shear stresses, shear strains and shear moduli of cell, rubber and steel respectively. Figure 6-20 shows the schematic of cross section of the unit cell when a shear deformation is applied.

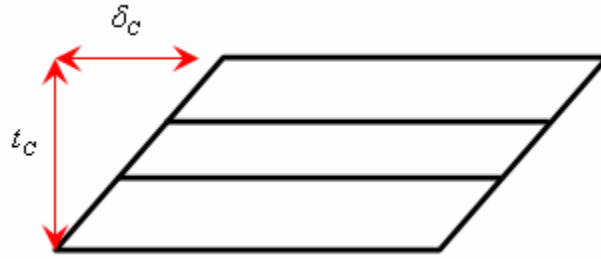


Figure 6-20: The laminated unit cell deformed in shear

Substituting Equation 6-23 and Equation 6-24 into Equation 6-22,

$$t_C \frac{\tau_C}{G_{12C}} = t_R \frac{\tau_R}{G_{12R}} + t_S \frac{\tau_S}{G_{12S}} \quad \text{(Equation 6-29)}$$

per assumption of perfect bonds shear at each layer is equal to shear applied to the unit cell, $\tau_C = \tau_R = \tau_S$

$$\frac{t_C}{G_{12C}} = \frac{t_R}{G_{12R}} + \frac{t_S}{G_{12S}} \quad \text{(Equation 6-30)}$$

since the layers have equal surface area, volume fractions are the same as ratios of thicknesses. Dividing both side of (Equation 6-31) by t_C :

$$\frac{1}{G_{12C}} = \frac{\lambda_R}{G_{12R}} + \frac{\lambda_S}{G_{12S}} \quad \text{(Equation 6-32)}$$

6. Major Poisson's Ratio

The ratio of normal strain on transverse direction to the normal strain in longitudinal direction when load is applied in longitudinal direction is defined as major Poisson's Ratio. If normal stress σ_C is applied in normal direction the deformation of the unit cell in transverse direction is the sum of the deformations of individual layers:

$$\delta_C^T = \delta_R^T + \delta_S^T \quad \text{(Equation 6-33)}$$

using definition of normal strain:

$$\epsilon_C^T = \frac{\delta_C^T}{t_C}, \quad \epsilon_R^T = \frac{\delta_R^T}{t_R}, \quad \epsilon_S^T = \frac{\delta_S^T}{t_S} \quad \text{(Equation 6-34)}$$

substituting (Equation 6-35) into (Equation 6-36):

$$\epsilon_C^T t_C = \epsilon_R^T t_R + \epsilon_S^T t_S \quad \text{(Equation 6-37)}$$

since rubber and steel are isotropic materials their Poisson's ratio is the same at every direction. By definition the Poisson's ratio for each component is,

$$\nu_{12C} = \frac{\epsilon_C^T}{\epsilon_C^L}, \quad \nu_R = \frac{\epsilon_R^T}{\epsilon_R^L}, \quad \nu_S = \frac{\epsilon_S^T}{\epsilon_S^L} \quad \text{(Equation 6-38)}$$

where:

ν_{12C} is the major poison's ratio of the unit cell and ν_R , ν_S are the poison's ratios of rubber and steel respectively. Substituting Equation 6-34 in Equation 6-39:

$$\nu_{12C} \epsilon_C^L t_C = \nu_R \epsilon_R^L t_R + \nu_S \epsilon_S^L t_S \quad \text{(Equation 6-40)}$$

however, because of strain compatibility in longitudinal direction,

$$\epsilon_C^L = \epsilon_R^L = \epsilon_S^L,$$

hence:

$$\nu_{12C} t_C = \nu_R t_R + \nu_S t_S$$

since the layers have equal surface area volume fraction is the same as

$$\text{ratios of thicknesses. Then, } \nu_{12C} t_C = \nu_R \frac{t_R}{t_C} + \nu_S \frac{t_S}{t_C}$$

$$\nu_{12C} = \lambda_R \nu_R + \lambda_S \nu_S \quad \text{(Equation 6-41)}$$

7. Density

Heat diffusivity of a material is a thermal characteristic on which transient heat transfer is depended. Heat diffusivity is a function of density, thermal conductivity and specific heat of a material (ρ , k , c_p). Density of a laminated material can be simply obtained through the following derivation.

Mass of the unit cell can be written as the summation of masses of individual components:

$$M_C = M_R + M_S \quad \text{(Equation 6-42)}$$

substituting the masses with their equivalents in terms of density and volume the Equation 6-38 is transformed to:

$$\rho_C V_C = \rho_R V_R + \rho_S V_S \quad \text{(Equation 6-43)}$$

dividing the both sides of Equation 6-39 by the total volume of the unit cell:

$$\rho_C \frac{V_C}{V_C} = \rho_R \frac{V_R}{V_C} + \rho_S \frac{V_S}{V_C}$$

this can be written in terms of volume fractions:

$$\rho_C = \rho_R \lambda_R + \rho_S \lambda_S \quad \text{(Equation 6-44)}$$

where, (ρ_C, M_C) , (ρ_R, M_R) , (ρ_S, M_S) are the densities and masses of the unit cell, rubber and steel layers respectively.

8. Specific Heat

Coefficient of Specific Heat is another thermal characteristic of a material which must be taken into account for transient heat transfer analysis. Specific Heat is defined as the amount of energy required to rise the temperature of a unit mass by 1 degree of measuring unit.

This quantity is used to analytically obtain the amount energy required for mass M at temperature T_1 to reach temperature T_2 through the equation,

$$E = MC(T_2 - T_1) \quad \text{(Equation 6-45)}$$

The energy, entering a laminated unit cell, is distributed between rubber and steel:

$$E_C = E_R + E_S \quad \text{(Equation 6-46)}$$

substituting (Equation 6-41) into (Equation 6-42):

$$M_C C_{PC} \Delta T_C = M_R C_{PR} \Delta T_R + M_S C_{PS} \Delta T_S \quad \text{(Equation 6-47)}$$

however, temperature difference, ΔT , is the same for all three components when steady state is established, $\Delta T_C = \Delta T_R = \Delta T_S$. Also $M = \rho V$ is substituted in (Equation 6-42) and simplified to be in the form of:

$$\rho_C V_C C_{PC} = \rho_R V_R C_{PR} + \rho_S V_S C_{PS} \quad \text{(Equation 6-48)}$$

$$C_{PC} = \lambda_R \frac{\rho_R}{\rho_C} C_{PR} + \lambda_S \frac{\rho_S}{\rho_C} C_{PS} \quad \text{(Equation 6-49)}$$

The summary of equivalent properties of laminated rubber is listed in Table 6-5.

Table 6-5: Equations derived for mechanical characteristics of laminated rubber

Coefficient of Thermal Conductivity	Longitudinal	$k_{(L)eff} = k_r \lambda_r + k_s \lambda_s$
	Transverse	$\frac{1}{k_{(T)eff}} = \frac{\lambda_r}{k_r} + \frac{\lambda_s}{k_s}$
Modulus of Elasticity	Longitudinal	$E_{eff(L)} = E_R \lambda_R + E_S \lambda_S$
	Transverse	$\frac{1}{E_{eff(T)}} = \frac{\lambda_R}{E_R} + \frac{\lambda_S}{E_S}$
Shear Modulus	$\frac{1}{G_{12C}} = \frac{\lambda_R}{G_{12R}} + \frac{\lambda_S}{G_{12S}}$	
Poisson's Ratio	$\nu_{12C} = \lambda_R \nu_R + \lambda_S \nu_S$	
Density	$\rho_C = \rho_R \lambda_R + \rho_S \lambda_R$	
Specific Heat	$C_{PC} = \lambda_R \frac{\rho_R}{\rho_C} C_{PR} + \lambda_S \frac{\rho_S}{\rho_C} C_{PS}$	

6.4 Finite Element Modeling

Reliability of F.E. modeling was evaluated by means of side-by-side comparison to the actual experiment data. The same sample which was used through Experiment-2 of Section 6.1 was selected for "Steady-State Heat Transfer Modeling". A complete set of thermal experiment data became available through Experiment-2, for that

reason this bearing was used for finite element modeling and evaluation of its precision and accuracy.

The model was made in part and assembled by observing the exact manufacturing order of the actual bearing. The physical and thermal properties of components were assigned individually. This technique, herein, denoted as Direct F.E. Modeling.

Modeling procedure started by making a small cut at the corner of the test bearing. That provides access for precise measurement of the internal components of the test bearing, Figure 6-21.



Figure 6-21: A cut from corner of the bearing allowed knowing the arrangement and configuration of internal components.

A material library was initially made by defining materials used in the bearing and assigning physical properties for each one of the materials. Appropriate material was selected for each part from the material library. The model was created by assembling the parts that were previously defined. All parts were properly constrained and,

appropriate interaction was defined for each pair. Assigning correct interactions is the most crucial step in F.E. modeling.

Thermal properties of materials used through the F.E. model are given in Table 6-6. Coefficient of thermal conduction of rubber for instance, falls in the range of 0.1-2.0 W/mK, depending on its compound ingredients. In a much similar way is the coefficient of convection of the air, which varies in a wide range of 1-100 W/m²K. This coefficient was expected to be significantly different in top and bottom ends of the test bearing of Experiment-2. For the reason mentioned above, the data of Experiment-2 was used to calibrate the material properties of the "Material Library" established for the model. The results of calibration are listed in Table 6-6.

Table 6-6: Calibrated material properties

	Thermal Conductivity (W / m. K)	Density (kg / m³)	Specific Heat (J / kg. K)	Convection Coefficient (W / m².K)
Aluminum	250	2700	900	N/A
Rubber	1.2	1100	2010	N/A
Steel	40	7900	477	N/A
Wood	0.12	500	2000	N/A
Air	N/A	N/A	N/A	4 (Lower end) 100 (Upper end)

The results and processing time of the virtual experiments, performed on the F.E. model were optimized by taking a number of considerations into account. The execution of a virtual experiment in a finite element model is an extremely labor intensive operation for the computation devices. The intensity of computation labor can be remarkably reduced by taking some considerations into account. This includes assembly and meshing procedure and, assignment of proper constraints and interaction properties between internal components of the model. Figure 6-22 indicates the procedure of assembling order observed in creation of the finite element model.

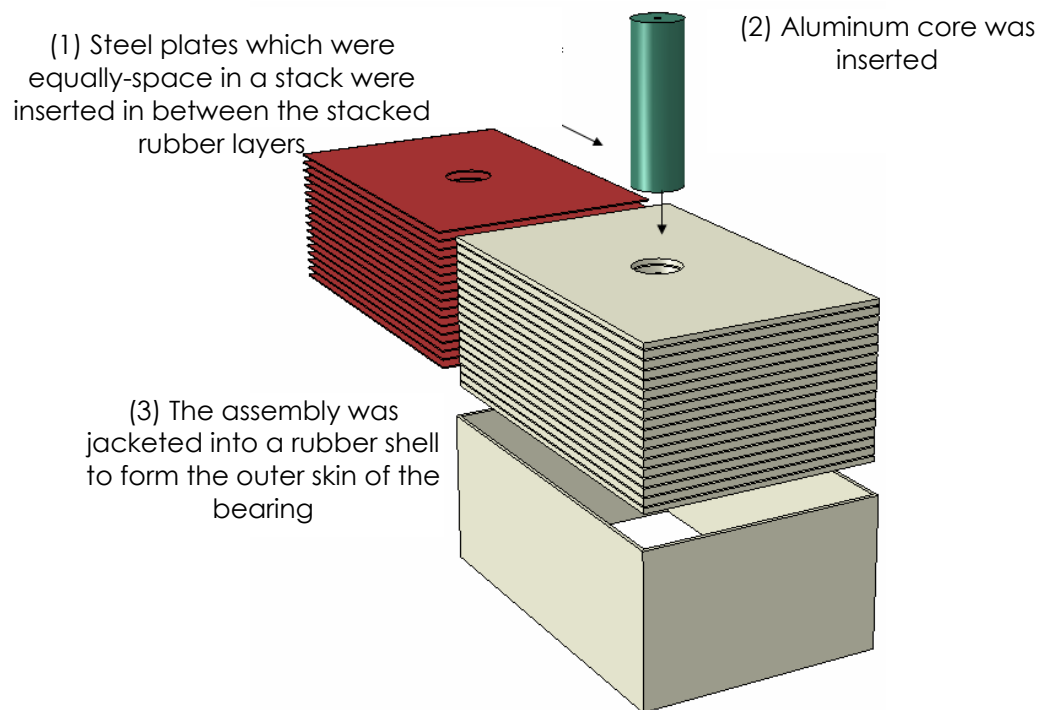


Figure 6-22: A generic schematic of how the finite element model was assembled

6.5 Steady State Heat Transfer

Energy enters a bearing system in the form of dynamic motion, and then is converted to heat through hysteretic action of the bearing. At presence of a temperature gradient within a body, thermal energy flows from high to low temperature zones.

The rate of this energy flow is governed by coefficient of thermal conductivity, k , through the Fourier's equation of thermal conductivity, $q'' = k\nabla T$ where q'' [W/m²] represents heat flux. Upon exposure to a constant heat generating source, an object of initial temperature T_0 starts warming up to the point where its temperature is stabilized. That point is called thermal steady state. Once the steady state is established the temperature is maintained so long as the heat source generates energy with the same constant rate.

The types of excitations which result in steady state and transient heat transfers are presented in Figure 6-23. Red and blue indicates transient and steady state conditions in input and response plots.

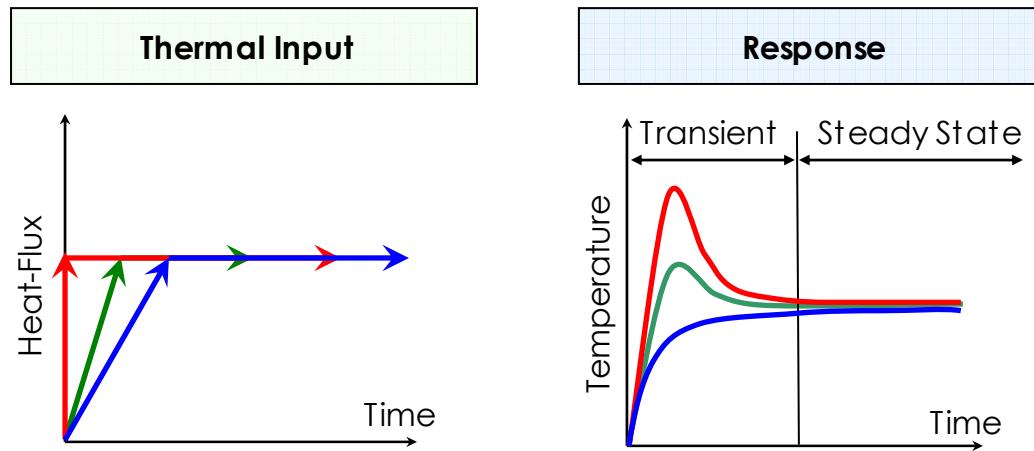


Figure 6-23: The types of excitations which result in steady state and transient heat transfers are presented. The transient stage changes depending on how abruptly the heat-flux is applied

Bridge structures are subjected to harmonic lateral motion. The magnitude and frequency of this harmonic motion is depended on geographical location and their service condition of the bridge. The harmonic motion of the bridge results in a steady rate of energy dissipation which causes the internal temperature to rise. The property of the bearing is affected by this temperature rise, hence, it must be quantified as the first step in property degradation analysis of the bearing.

At the first set of testing, the model was excited by a heat-flux of 16300 W/m^2 and ambient temperature was set to be 17.59°C (290.59 K), the coefficient of convection was set at $70 \text{ W/m}^2 \text{ K}$ for the top and side walls and $5 \text{ W/m}^2 \text{ K}$ for the bottom where a limited volume of air circulated compared to the other sides.

6.5.1 Qualitative Observation

From a qualitative point of view the performance of the F.E. model were in agreement with expectations from theoretical studies in terms of shapes and boundaries of the temperature contours.

From the analytically calculated thermal conductivities it was expected to see the density of heat-flow into the rubber be negligible compared to that of steel shims. This was observed and confirmed by comparing the heat-flow vectors in axial and radial directions, Figure 6-25.

The final stage of the interaction is when a portion of the thermal energy is escaped from the outer surface of the bearing to the air through convection phenomenon. The air circulation was limited through the spacing beneath the bearing relative to the other 5 sides. For that reason, a higher temperature was expected at lower-half of the bearing.

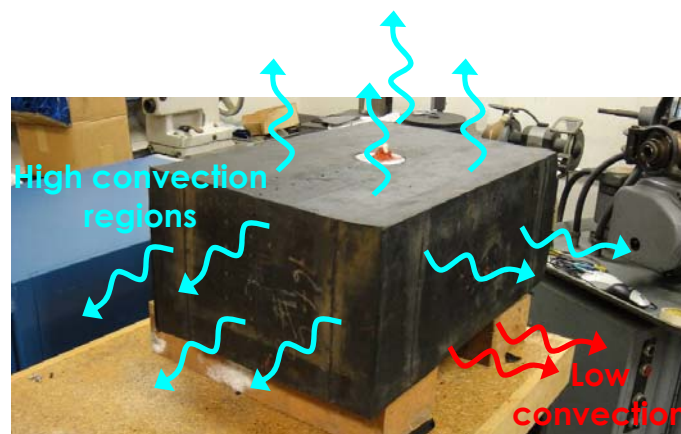


Figure 6-24: Air circulated at much higher rate in vicinity of top end and side walls relative to bottom of the bearing, non-uniform convection results uneven heat distribution within body of the bearing

In Figure 6-25, it was also observed that the heat-flow vectors have both horizontal and vertical components at the top end of core, but they gradually lose their vertical components and became more radial toward the bottom end. The reason for such a behavior was that, the air which acted like a heat sink through the convection phenomenon was not uniformly effective on all surfaces. It was due to the fact that a limited amount of air flow allowed through the passage beneath the bearing, Figure 6-24. Therefore, a thermal gradient formed along axis of the bearing.

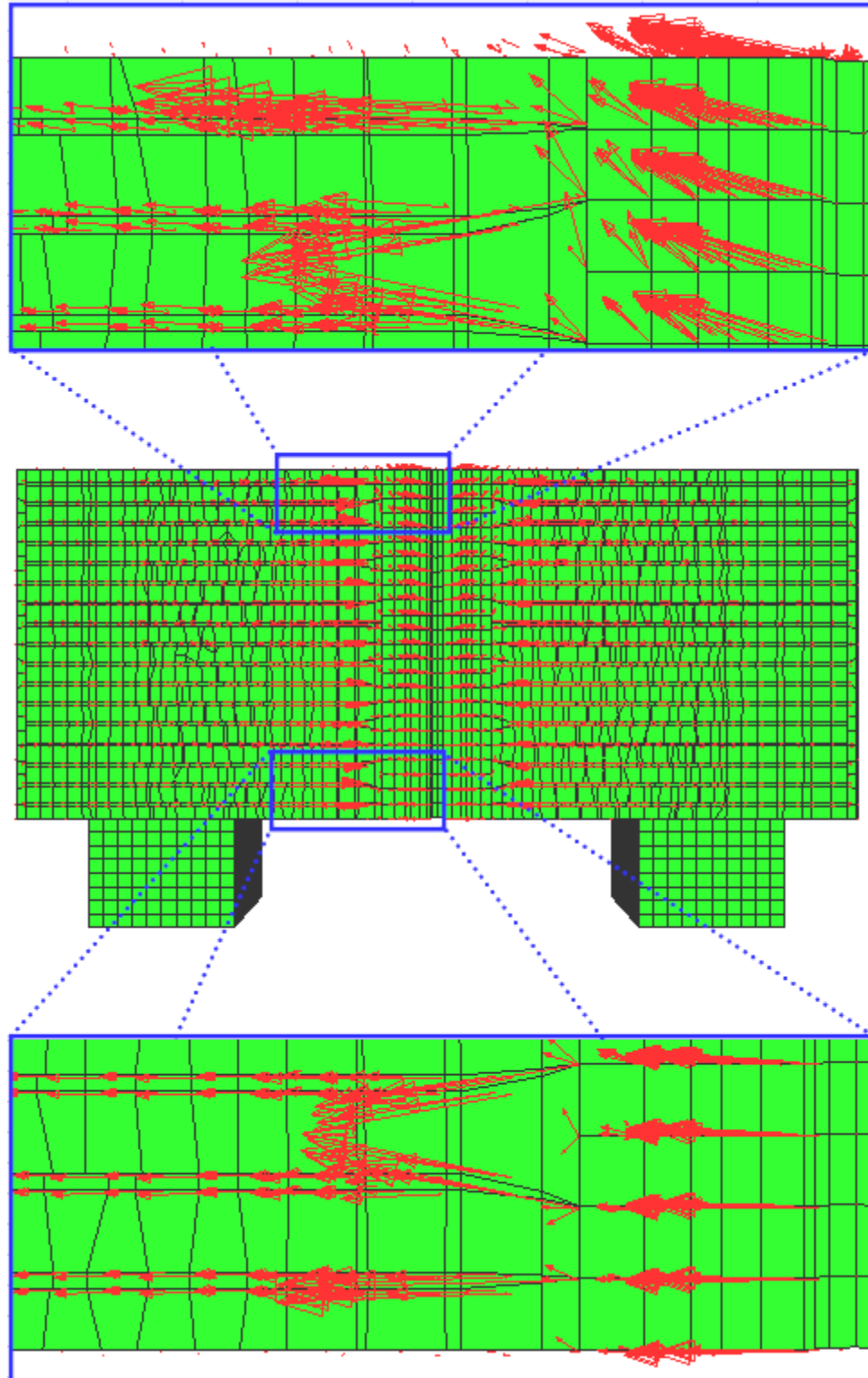


Figure 6-25: Flow of heat waves is bi-directional at the upper end of the bearing and gradually becomes unidirectional toward its lower end, this is due to inequality of air volume passing over top and beneath the bearing

The side-view of the bearing across section A-A shows the heat waves moving in elliptical shape contours, Figure 6-26. These contours divide the bearing's volume into sectors based on the temperature range to which each sector is exposed. The non-uniformity of internal temperature explains the incredibility of the experiments existed in literature, the experiments in which rubber bearings were placed in oven for accelerated aging.

In Experiment-2, it was also observed that the non-uniform thermal convection causes the lower half of the bearing to be hotter than the upper one, this fact was implemented into the F.E. model by assigning appropriate coefficients of convections for each side of the bearing.

The entire body of the laminated rubber is wrapped in a rubber cover of about 6.5 mm thick. Because of the low thermal conductivity of rubber this cover acted as a thermal insulator and made the temperature to increase, Figure 6-27.

Temperature (K)

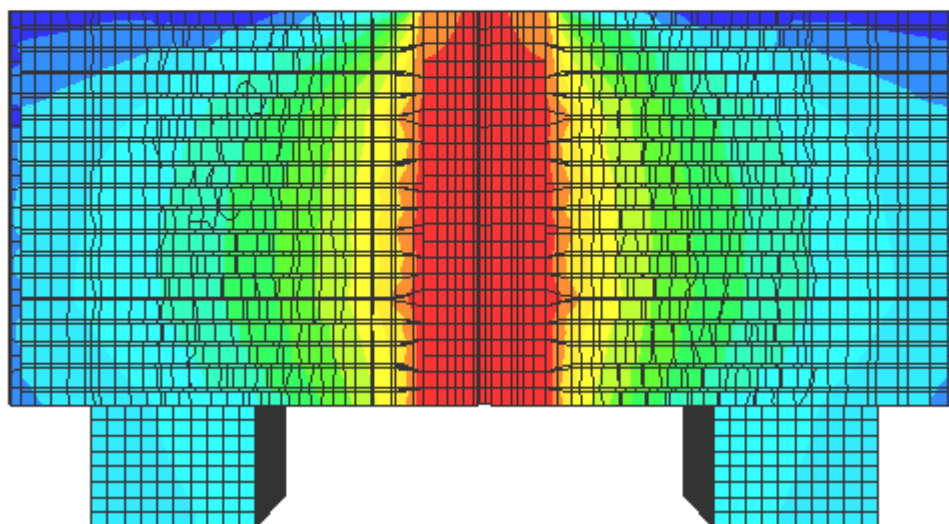
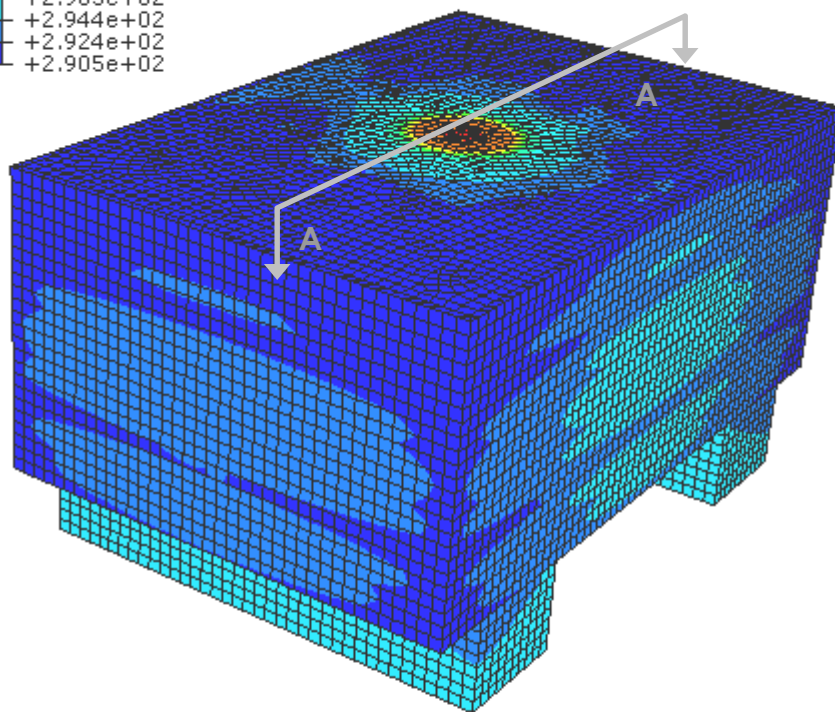
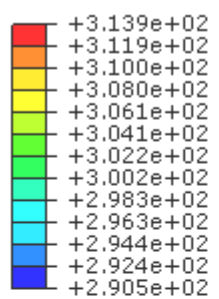


Figure 6-26: Temperature map across section A-A

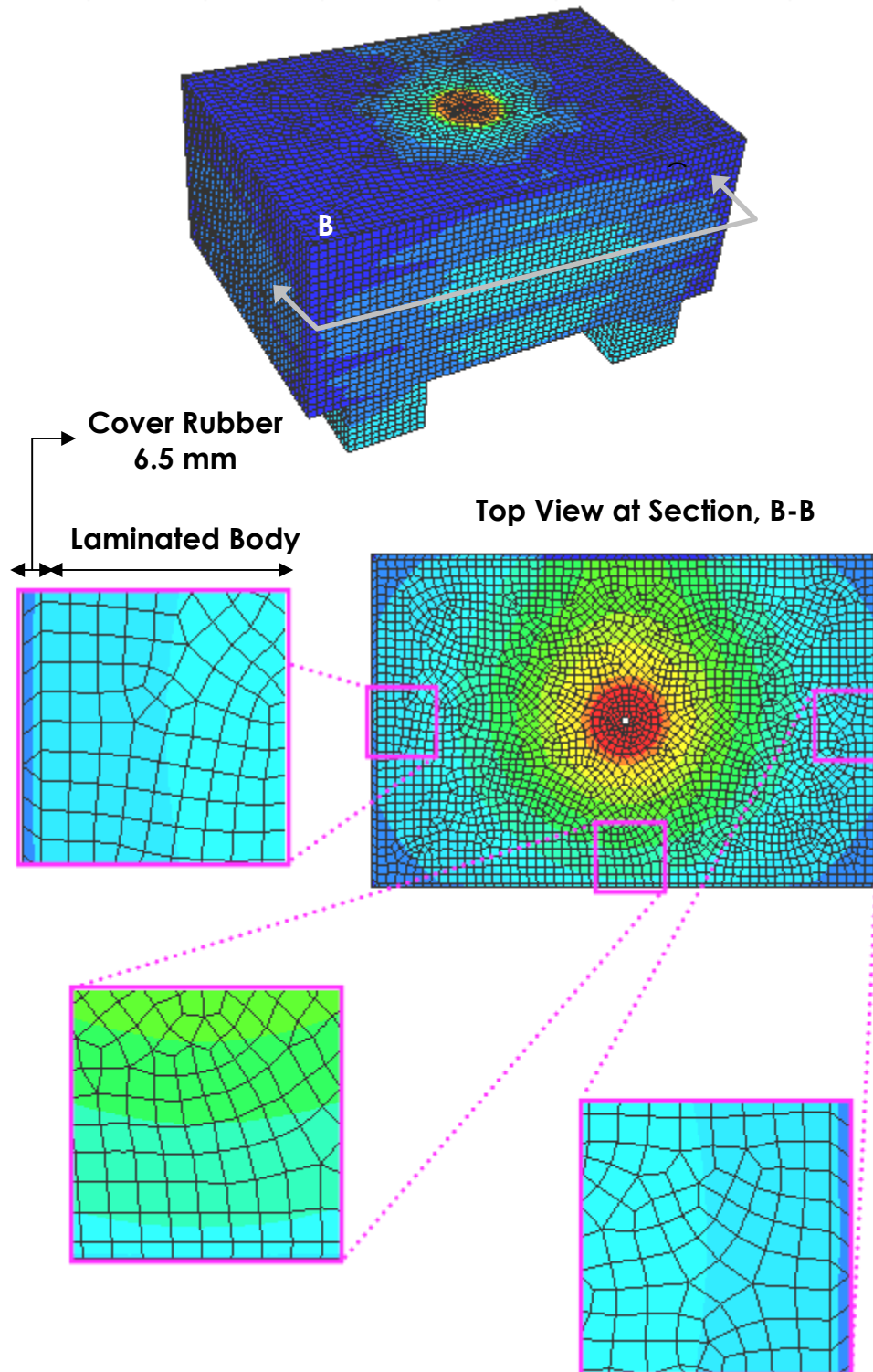


Figure 6-27: The outer rubber-layer that is wrapped around the bearing acts like an insulator that preserves the thermal energy within the bearing for a long time, this resulted in rising the bearing's body temperature

The situation where conduction or convection is not uniform at all contact points is very common in in-services bearings. A common situation of such uneven heat distribution is the applications of bearings in truss bridges with concrete piers. In situations like this, heat escape from top which connected to steel bridge easier and faster than the lower end which is seating on concrete. Another circumstance is when location of a structure allows more exposure of sunshine to one or a group of bearings compared to the rest of the bearings installed on that structure. In such conditions the bearings which are subjected to higher and longer sunshine exposure experience higher service temperature i.e. more rapid degradation. It is known that rate of degradation exponentially increases with rise of temperature [“Rubber Deterioration in an Air Oven”, ASTM, D573, (2007)]. Thus, more often monitoring and maintenance services are required for safety and assurance of adequate seismic performance of bridges in such conditions. Figure 6-28 shows the temperature difference at top and bottom of the FEM.

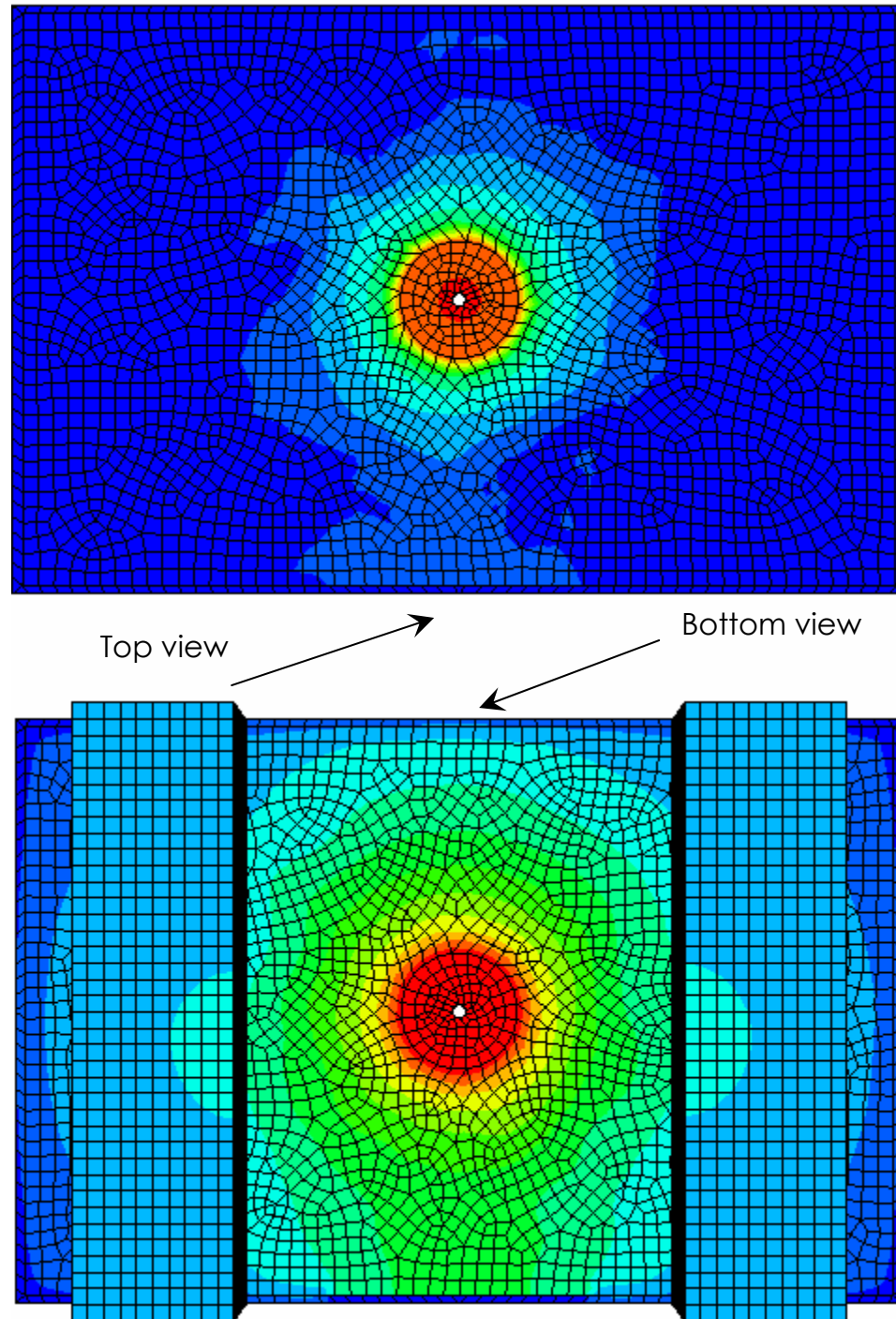


Figure 6-28: Top and bottom view of the bearing shows temperature difference, it is due to limited air circulation beneath the bearing

6.5.2 Quantitative Assessments and Conclusions

Thermocouples of Experiment-2 were installed on the 9th embedded steel shim. The data used for comparison purposes recorded from the exact corresponding locations at the finite element model.

A side-by-side comparison of result obtained from Experiment-2 to that of the finite element analysis is presented in Table 6-7. Comparison was made on 5 tests which were performed at various input heat-flux but constant ambient temperature of 17.95 °C.

Table 6-7: Side-by-side comparison of result obtained from Experiment-2 to that of the finite element analysis. Comparison was made on 5 tests which were performed at various input heat-flux but constant ambient temperature of 17.95 °C

Thermocouple		T1	T2	T3	T4	T5	T6	T7	T8	T9
D mm		11.68	40.50	76.20	107.95	139.70	171.60	204.47	236.22	248.92
Test A HF=16300 W/m ² K	EXP	21.58	21.90	22.94	23.61	25.03	27.08	30.14	34.90	39.20
	FEM	22.21	23.26	24.46	25.83	27.44	29.57	32.16	36.79	39.80
Test B HF=25000 W/m ² K	EXP	24.21	24.88	25.93	26.94	28.67	32.75	37.83	45.65	50.02
	FEM	24.49	26.05	27.83	29.87	32.26	35.42	39.25	46.12	50.60
Test C HF=37000 W/m ² K	EXP	27.94	28.97	30.31	32.31	35.12	40.55	47.34	60.75	66.34
	FEM	27.98	30.32	33.00	36.05	39.64	44.38	50.13	60.44	67.15
Test D HF=51500 W/m ² K	EXP	31.90	33.58	35.61	38.30	41.48	50.27	60.34	78.10	85.84
	FEM	32.30	35.60	39.40	43.70	48.77	55.46	63.59	78.15	87.63
Test E HF=65500 W/m ² K	EXP	36.56	38.25	40.62	44.99	50.25	61.66	73.73	95.54	105.70
	FEM	36.44	40.67	45.53	51.04	57.52	66.09	76.49	95.13	107.26

Temperatures of all 9 thermocouples were plotted versus their locations with respect to the north wall. Agreement was observed between data obtained experimentally and by the finite element modeling. Disagreements at locations with largest discrepancies were about 7 % - 8 %.

A perfect thermal steady state condition was assumed for the finite element modeling whereas, in the Experiment-2 data was obtained at constant elapsed time of 3000 sec at which steady state thermal condition was not completely established. For a normal operating situation, it took less than an hour for the bearing to reach up to about 95 % of its steady state temperature. Once the temperature get near to thermal steady state, from that point the rise of temperature became so gradual (less than half a degree per hour) that could be safely ignored, Figure 6-19. For this reason, in order to maintain consistency, sampling was performed at constant elapsed time. The above rational explains the small gap existed in between the data obtained in these two methods, Figure 6-30. The farther a thermocouple was from the heat source, the longer it took to reach the steady state condition. For instance, in Figure 6-29, the temperature at TC09 takes 10 minutes to reach from 23 °C to a temperature of 43 °C, but from that point it took 50 minutes for the temperature to increase by 3 °C.

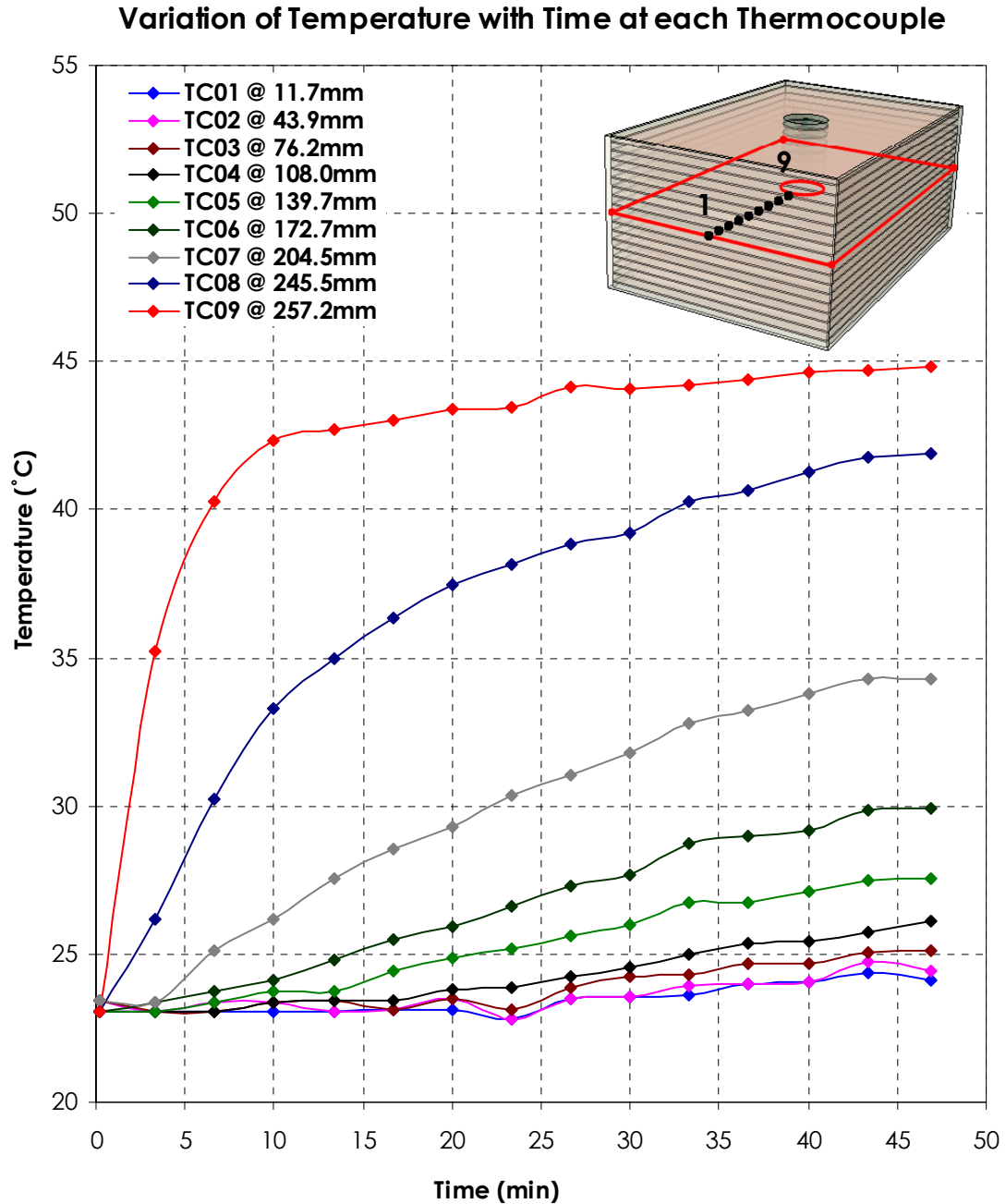


Figure 6-29: Rise of temperature within 45 minutes at each thermocouple, near 95 % of thermal steady states is established within the first hour of the heat transfer process

In addition to the reason explained above, another factor that could contribute in such slight differences is the manufacturing imperfection. The test sample was assumed to have perfect lamination

characteristic such as perfectly paralleled layers with uniform thickness and equally spaced. Any imperfection of this nature could result in discrepancies in results.

The plot of temperature at each thermocouple versus their locations along path “A” was given in Figure 6-30. The plot presents the data obtained from experiments, performed at an ambient temperature of 17.59 °C and a heat-flux of 16300 W/m². A complete set of graphs of this group is available in Appendix G

Careful observation of the plots indicates agreement between the data obtained experimentally and by the finite element modeling. This approves the credibility of the finite element model for parametric studies intended for further studies.

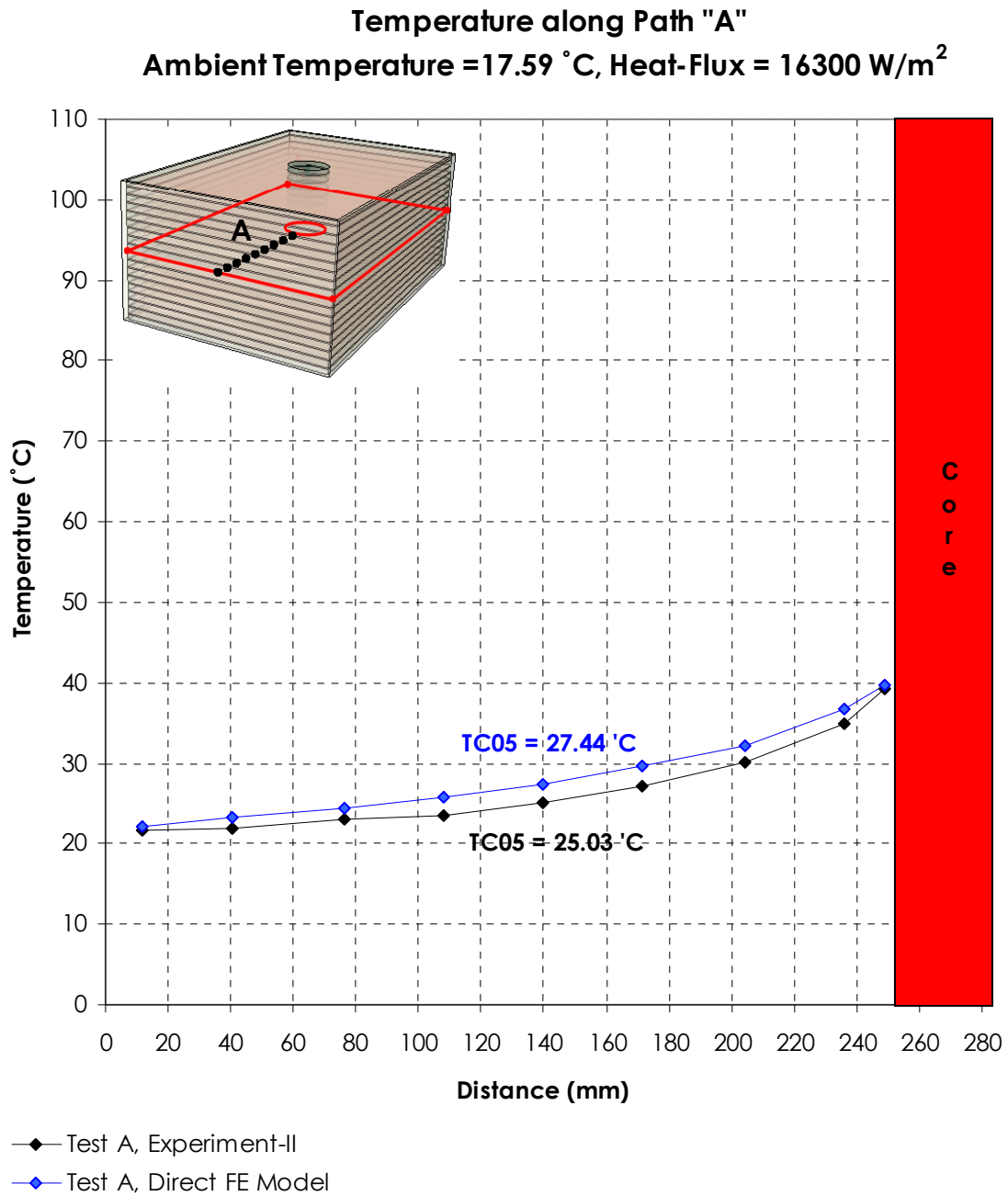


Figure 6-30: Temperature profile along path "A" obtained from the direct F.E. model and Experiment-2. Heat-Flux = 16300 W/m², Ambient temperature = 17.59 °C. The difference at highest was ~8 %

6.6 Validation of F.E.M. Using Theoretical Approach

The reliability of the finite element modeling approach was validated through the processes performed in Section 6.5. Also, the accuracy and precision of the model in simulating thermal conduction was investigated. This was done by applying the same test protocol which was applied to the test sample of Experiment-2 to F.E. model.

The goal of this section is to implement a second approach to verify the reliability of F.E. modeling by further measures and different approaches. This task was performed by introducing in the F.E. model an equivalent substitute material for which the thermal properties are obtained theoretically.

The body of the bearing can be treated as a bulk of laminated material made by lamination of rubber and steel layers. This hybrid material possesses a thermal-conduction property set by properties and volume of its primary constituents. The laminated body of the bearing can be substituted by an equivalent non-isotropic material. Procedure for deriving theoretical engineering properties of a lead core elastomeric bearing made from rubber-steel lamination was explained in Section 6.3 and the resulting equations are given in Table 6-5.

6.6.1 Results of Direct and Indirect FEM

Analytically calculating the internal temperature at any point on or within the bearing was made possible by using an equivalent laminated material to be substituted with the laminated body of the bearing. The knowledge about the thermal characteristic of the equivalent laminated material together with input heat-flux and ambient temperature can be used in the Fourier's Equation of Heat Transfer. The Fourier's Equation of Heat Transfer can be solved for the temperature at any point of a solid and any moment of time. However, due to tediousness of computation and intensity of required effort for solving differential equation of heat transfer the Abaqus software was used as a numerical equation solver. It was denoted as "Indirect" finite element modeling. Unlike the direct method in which the model was made by lamination, the body of bearing was replaced by an equivalent substitute material. And, rather than providing the model with thermal characteristics of individual constituents separately, the model was provided with a single set of properties for the equivalent substituted body of the bearing. There were two major benefits in using indirect F.E. modeling. First, convergence of the results of all three approaches validates the reliability of F.E.M. with further standards. Also, using the substitute material for laminated body of a bearing in F.E.M

saves a lot of memory and CPU volume for the computational device. As a result, large devices can be modeled and analyzed in shorter time. For instance, for the bearing used in Experiment-2, at a completely identical setting for meshing, It requires 26250 (36 %) more mesh cells if modeled straight without using equivalent substitute material.

6.6.2 Observations and Results

At Section 6.3, an equivalent substitute material theoretically calculated property was used as the substitute material for the body of the bearing. The reliability of model was verified by graphically comparing to the result obtained from Experiment-2 with those of the two F.E. models. A customized term, "Indirect F.E. Modeling" was defined and used for the second F.E. M. method.

Comparison of the results showed agreement among the methods of the three approaches. The result confidently proved that real experiments can be safely reproduced using finite element modeling techniques. Therefore, further investigation on how a bearing responds on certain conditions can be simulated through the finite element modeling. However, the method requires high capacity computational devices. Theoretical assumptions were verified by comparing the results of direct and indirect finite element modeling. In

Figure 6-31, section views of the F.E. models, qualitatively show very close similarity in the pattern of heat distributions in the two case of F.E. modeling.

The other benefit of using equivalent material is that it can optimize the F.E. modeling by degrading the intensity of computations, which allows larger devices to be modeled with better precision.

A Side-by-side comparison of results obtained from Experiment-2, direct and indirect finite element modeling is presented in Table 6-9.

Table 6-8: Side-by-side comparison of results obtained from experiment, direct and indirect finite element modeling

Thermocouple		T1	T2	T3	T4	T5	T6	T7	T8	T9
D (mm)		11.68	40.50	76.20	107.95	139.70	171.60	204.47	236.22	248.92
Test A HF=16300 W/m ² K	EXP	21.58	21.90	22.94	23.61	25.03	27.08	30.14	34.90	39.20
	FE (Dir)	22.21	23.26	24.46	25.83	27.44	29.57	32.16	36.79	39.80
	FE (Indir)	22.02	23.11	23.73	24.80	26.41	28.65	31.71	36.03	39.56
Test B HF=25000 W/m ² K	EXP	24.21	24.88	25.93	26.94	28.67	32.75	37.83	45.65	50.02
	FE (Dir)	24.49	26.05	27.83	29.87	32.26	35.42	39.25	46.12	50.60
	FE (Indir)	24.32	25.81	26.94	28.89	31.00	34.70	38.97	45.77	50.43
Test C HF=37000 W/m ² K	EXP	27.94	28.97	30.31	32.31	35.12	40.55	47.34	60.75	66.34
	FE (Dir)	27.98	30.32	33.00	36.05	39.64	44.38	50.13	60.44	67.15
	FE (Indir)	27.86	29.60	32.00	34.80	38.63	43.50	49.17	60.53	66.92
Test D HF=51500 W/m ² K	EXP	31.90	33.58	35.61	38.30	41.48	50.27	60.34	78.10	85.84
	FE (Dir)	32.30	35.60	39.40	43.70	48.77	55.46	63.59	78.15	87.63
	FE (Indir)	32.10	34.96	38.22	42.25	47.49	54.38	62.54	78.11	86.91
Test E HF=65500 W/m ² K	EXP	36.56	38.25	40.62	44.99	50.25	61.66	73.73	95.54	105.70
	FE (Dir)	36.44	40.67	45.53	51.04	57.52	66.09	76.49	95.13	107.26
	FE (Indir)	36.39	40.06	44.97	49.60	56.19	64.90	75.69	95.20	106.75

The heat distribution pattern across the sections of the two models is presented in Figure 6-31. The two patterns are qualitatively compared and close similarity was observed in both qualitative and quantitative measures.

The contour lines of the model, made by indirect method is, however, smoother than that of direct model because the equivalent substituted material is a one piece uniform material without internal discontinuity.

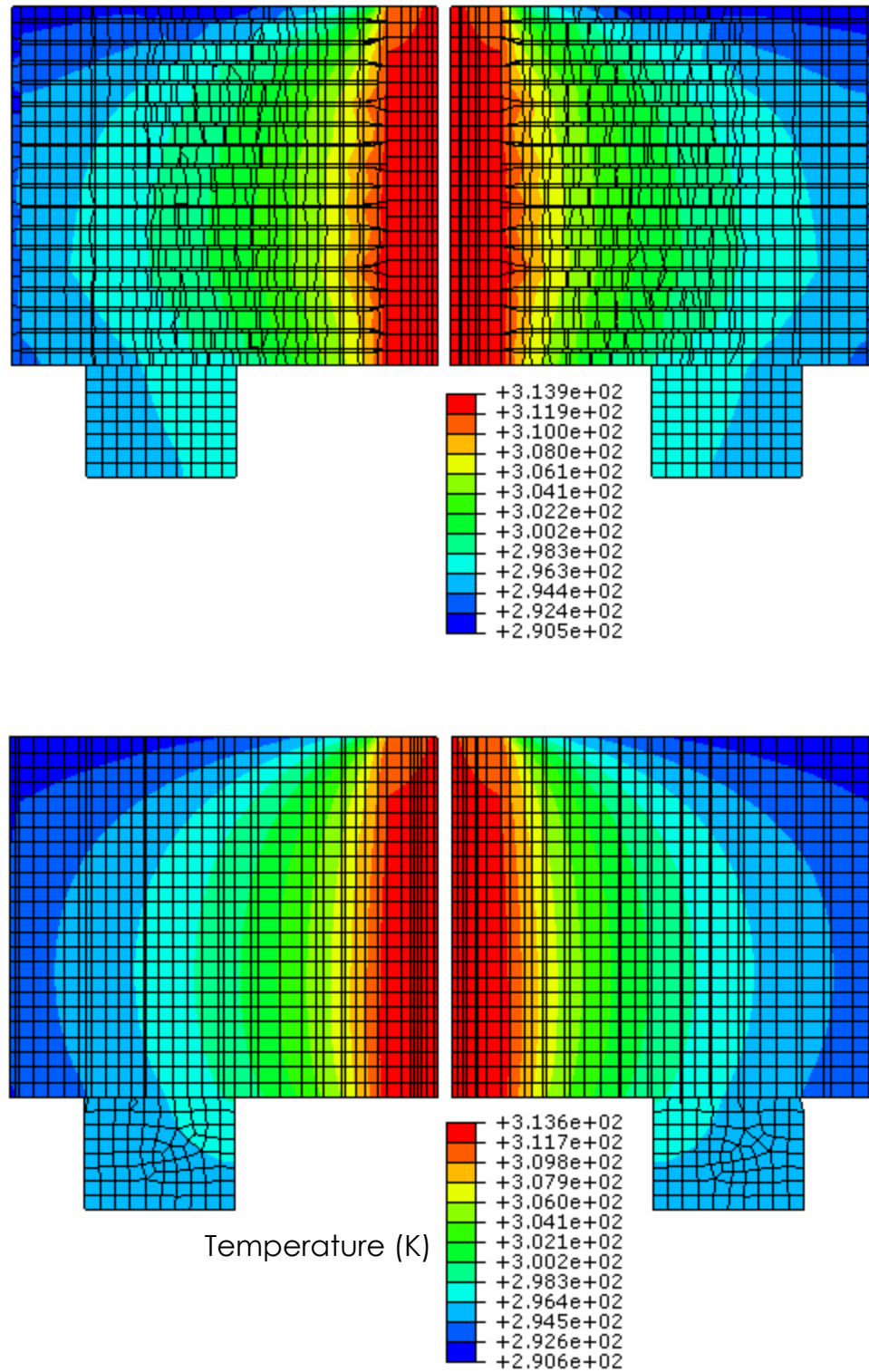


Figure 6-31: Section views of the finite element models show similar pattern of heat distributions. Top: direct modeling. Bottom: Modeling by means of equivalent substitute material substitution

The results obtained from Experiment-2 and the two finite element models were compared by superimposing the plots of temperature-distance of the three approaches. It was observed that all three sets of data are in agreement altogether (Figure 6-32). The data obtained from indirect model lied in between the other two sets of data. It is due to the fact that in direct modeling, the model is assumed to have perfect lamination characteristic such as perfectly parallel layers, layers with perfectly constant thickness and equally spaced. Any imperfection on manufacturing process could result in results.

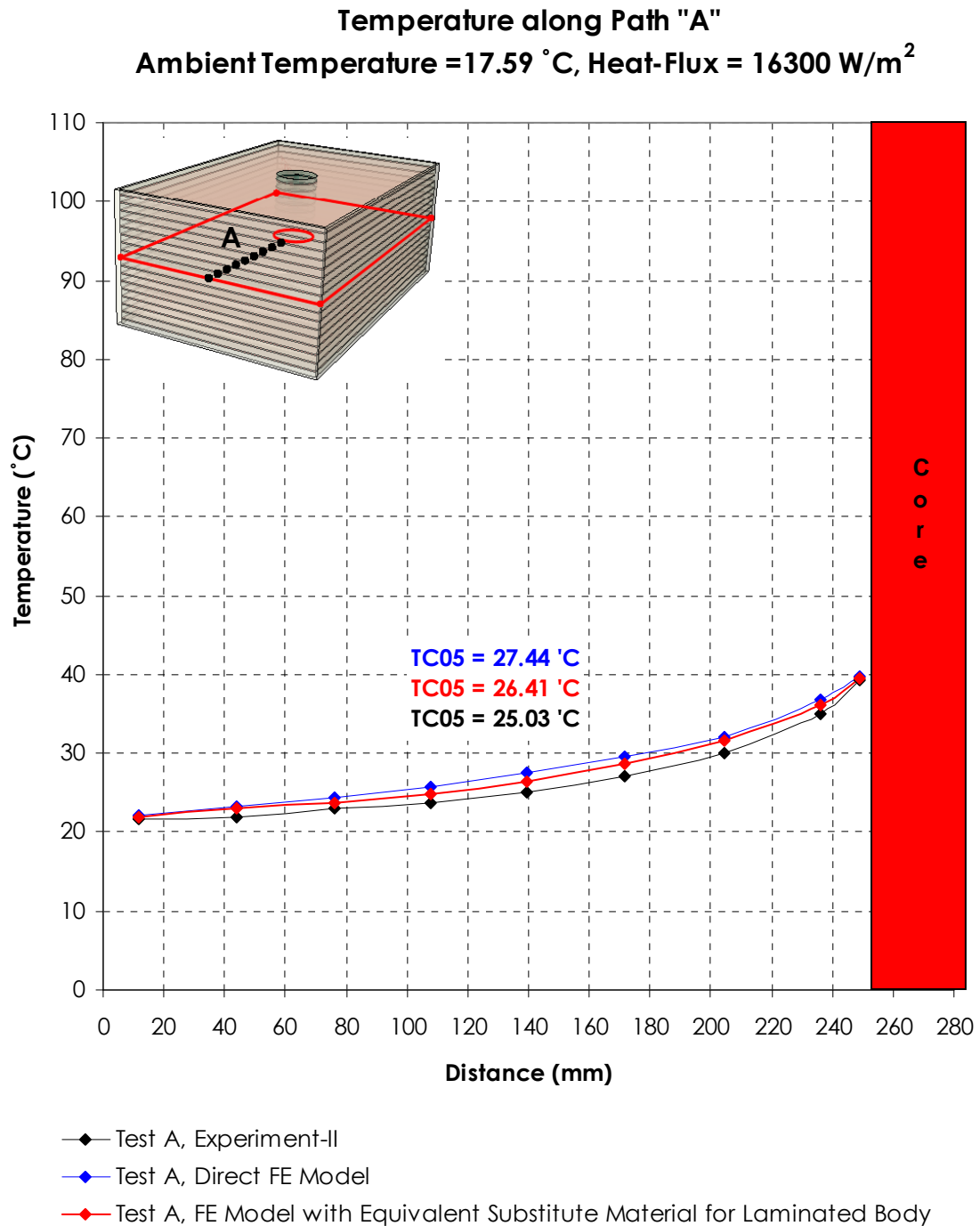


Figure 6-32: Temperature profile along path "A" for the direct and indirect F.E.M. together with the results of Experiment-2, superimposed on a single coordinate system, at 16300 W/m²

6.7 Phase-1, Steady State Heat Transfer Model

A parametric study was incorporated with the created finite element model to find a governing function, which correlates variables of ambient condition to the internal temperature of bearing. The F.E. model was used in simulating experiment at which ambient temperature and heat-flux, each varied to values. Therefore, a total of 36 pairs of input variables were prepared. T_{xy} , represents the temperature at vicinity of the lead plug of Experiment-2 at ambient temperature X °C and heat-flux Y [W/m²K]

The data of matrix T was fitted onto a linear plot by using the curve-fitting toolbox of Microsoft Excel.

$$T_{ambient} = \begin{bmatrix} 288 \\ 293 \\ 298 \\ 303 \\ 308 \\ 313 \end{bmatrix} (K), \quad HF = \begin{bmatrix} 10000 \\ 20000 \\ 30000 \\ 40000 \\ 50000 \\ 60000 \end{bmatrix} (W/m^2 K)$$

$$T_{xy} = \begin{bmatrix} 290.866 & 293.722 & 296.583 & 299.445 & 302.306 & 305.167 \\ 295.866 & 298.722 & 301.583 & 304.445 & 307.306 & 310.167 \\ 300.866 & 303.722 & 306.583 & 309.445 & 312.306 & 315.167 \\ 305.866 & 308.722 & 311.583 & 314.445 & 317.306 & 320.167 \\ 310.866 & 313.722 & 316.583 & 319.445 & 322.306 & 325.167 \\ 315.866 & 318.722 & 321.583 & 324.445 & 327.306 & 330.167 \end{bmatrix} (K)$$

$$T_{xy} = \begin{bmatrix} 17.866 & 20.722 & 23.583 & 26.445 & 29.306 & 32.167 \\ 22.866 & 25.722 & 28.583 & 31.445 & 34.306 & 37.167 \\ 27.866 & 30.722 & 33.583 & 36.445 & 39.306 & 42.167 \\ 32.866 & 35.722 & 38.583 & 41.445 & 44.306 & 47.167 \\ 37.866 & 40.722 & 43.583 & 46.445 & 49.306 & 52.167 \\ 42.866 & 45.722 & 48.583 & 51.445 & 54.306 & 57.167 \end{bmatrix} (^{\circ}C)$$

Linear relation of temperature with the two variables of ambient temperature and heat-flux was verified in Section 6.2.3 (Figures 6-10 and 6-11). Ultimately it became possible to predict the internal temperature of an elastomeric bearing by knowing the thermal properties of its constituents, ambient temperature and heat flux. The equation through which the temperature is obtained has the linear form of:

$$T_{(HF, T_o)} = C_1 \cdot HF + T_o \quad \text{Equation 6-50}$$

Which in the case of the bearing used in Experiment-2 coefficient $C_1=0.0003$

In Figure 6-33, the result form parametric study of heat transfer is plotted versus input heat-flux at different temperature.

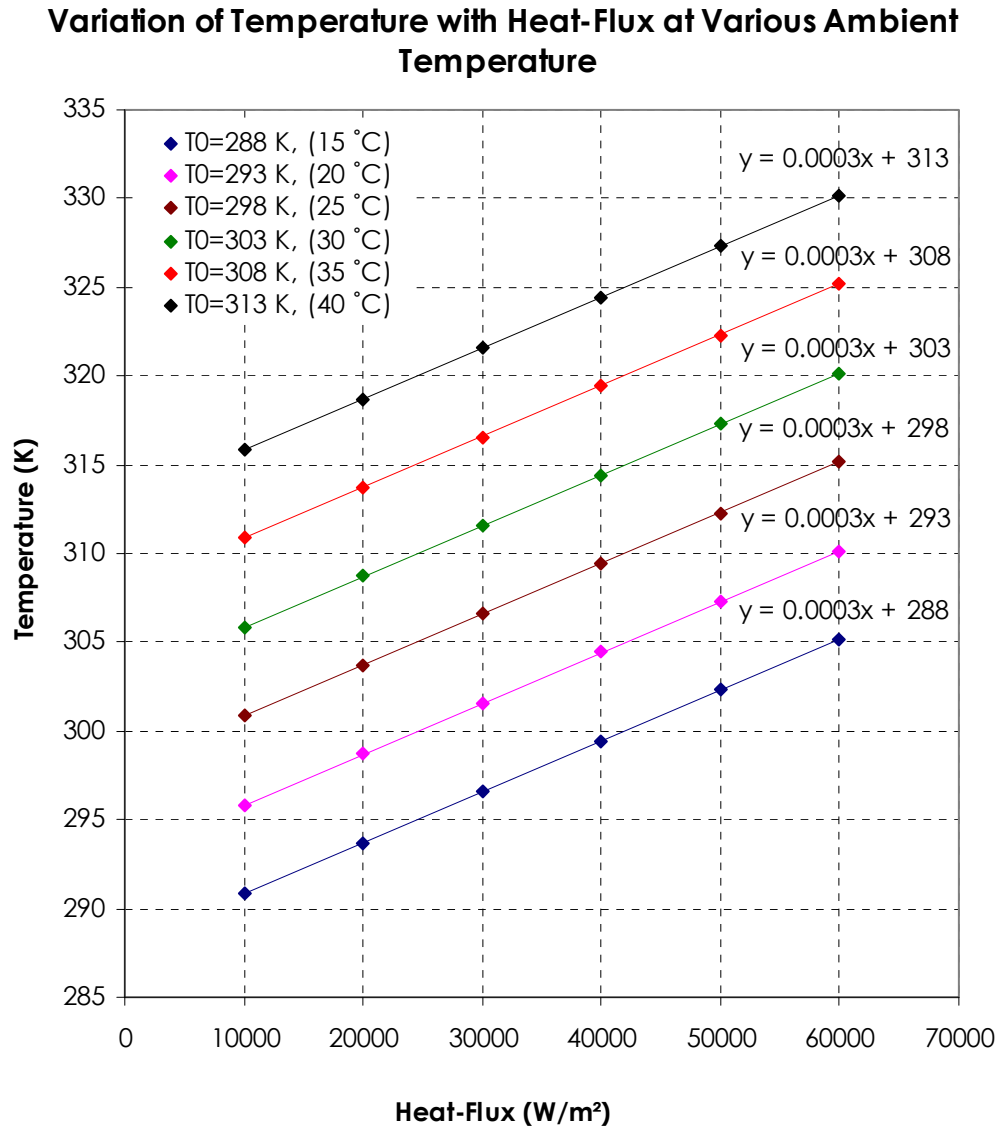


Figure 6-33: Result form parametric study of heat transfer suggested a model that accurately matched the experimental results. The model correlated the temperature at each point to the ambient temperature and input heat-flux

6.8 Phase-2, Transient Heat Transfer Analysis

Ambient vibration, as discussed in previous section causes the bearing to warm up gradually and steadily. During application of steady harmonic excitation, the final thermal stage where further variation of temperature with time is small and negligible, is called

Thermal Steady State. Steady state heat analysis is needed for prediction of a bearing's internal temperature when subjected to harmonic dynamic excitation at steady rates. Steady state heat transfer analysis was adequate because of the steady and gradual nature of temperature change.

There is, however, another situation where a significant amount of energy is abruptly enforced to a bearing which results in sudden elevation of temperature. Strike of an earthquake is the most common example of the aforementioned situation. If heat is generated at too much higher rate than is conducted, it causes concentration of heat i.e. very high local temperature, Figure 6-23.

The heat acts rapid enough to make notable changes in property of the lead plug before the next cycle strikes. Therefore, a crucial step in quantifying degradation is to quantify temperature at critical zones over split-second time intervals. Performing transient heat analysis is a straightforward task, because lead has known thermal characteristics which can be found in the literature. However, the model must be validated through experiment.

Since application of an abrupt uniform heat pulse of large magnitude required special devices, the validation was made by measuring temperature at certain times and locations, when a gradual

heating was applied. The program, used in performing a controlled excitation and sampling, is presented in the diagram shown in Figure 6-34. The F.E.M. was calibrated to reproduce the response when excited with the same loading specification.

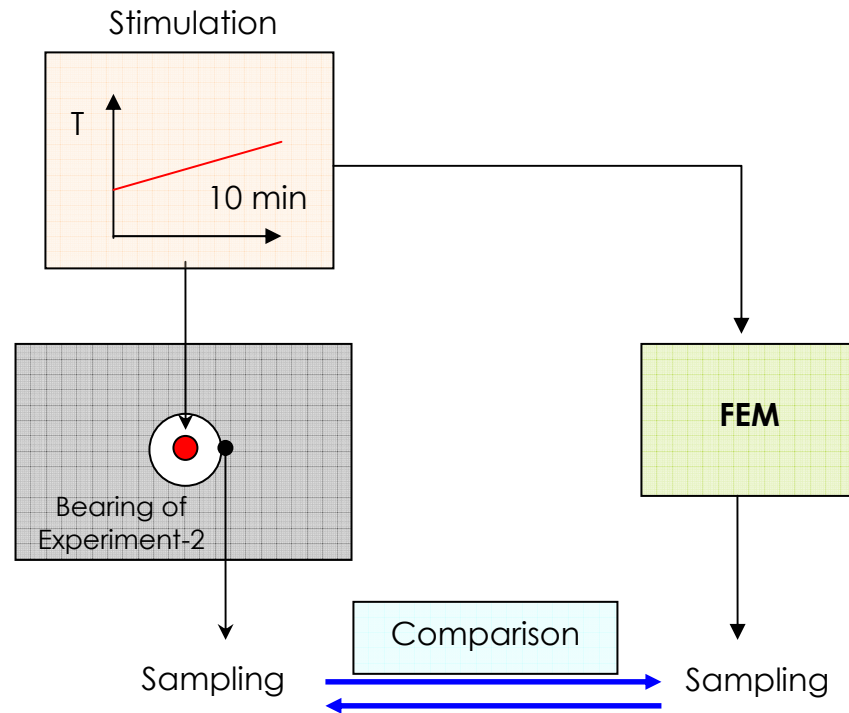


Figure 6-34: The steps followed to validate transient heat transfer model

Verification of the transient heat transfer was done by exposing the aluminum core of the test sample used for Experiment-2 to a temperature difference for 10 minutes. To make a loading profile for F.E.M., temperature was recorded from a point on aluminum core close to heating element. Sampling, however, was performed from a point on outer circumference of the aluminum core. The finite element model was executed with a customized ramp-load which was modeled using

recorded temperature at reference point (Figure 6-34). The accuracy of the finite element heat transfer model was examined through comparison with experimental results. In Figure 6-35 the temperature at a point on the core is plotted versus time for the actual experiment and F.E. model.

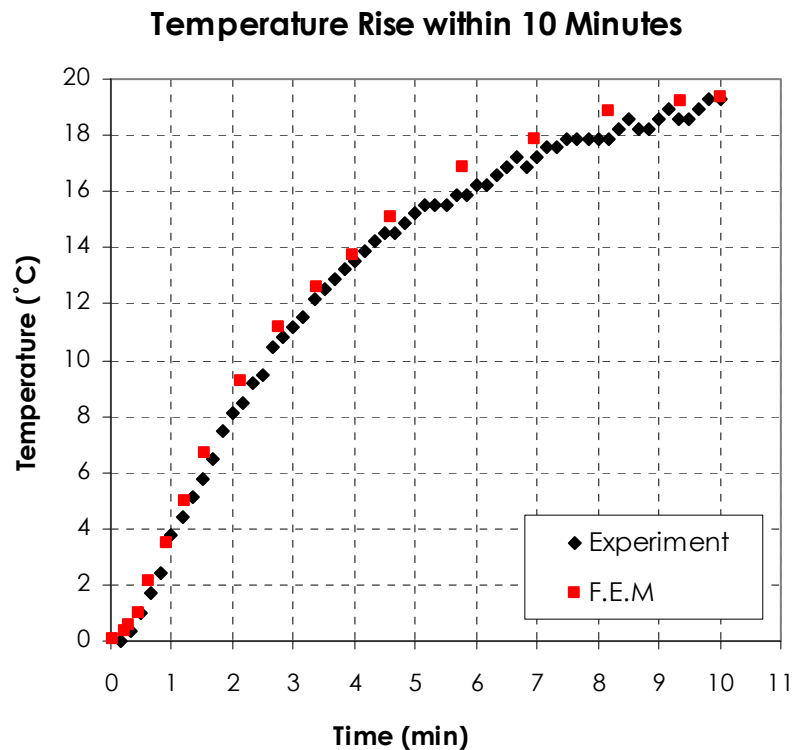


Figure 6-35: Transient heat transfer model was calibrated and examined by applying a heat-flux over certain length of time (10 minutes)

6.9 Phase-3, Stress Analysis (Post-yield behavior of Lead)

Formation of microcracks at high tensile strain is a situation at which lead loses its tensile strength. The deterioration in strength of lead is directly linked to the property losses of this element and must be quantified as a part of a degradation analysis. At this phase, the goal

was to perform a stress analysis on the bearings to acquire information about post-yield behavior of lead plugs as well as the distribution of stress over these elements. Post-yield behavior of the lead was also needed for a proper definition of this material when it was to be used in F.E. dynamic analysis. The result was verified by extracting the response of the lead plug by subtracting the total response of NRB1300 from that of LRB1300 bearings. These two bearings were used in Experiment-1.

6.9.1 Complexity of the Phenomenon

Elastomeric bearings are designed to accommodate large lateral displacements. The ratio of lateral displacement to the height of a bearing is expected to reach up 1.5 at normal service conditions. For instance, LRB700 reached to the ratio of 1.75 through Experiment-1 of this research.

Lead exhibits engineering properties which vary with the rate of application of a load. For this reason it can act ductile, semi-ductile or even brittle depending on the rate of applied load.

Rubber behaves different from many ordinary solids due to its high poisson's ratio and nonlinear elastic behavior, and that is another contributing factor in complexity of the phenomenon. In an elastomeric bearing the rubber's "Bulging" a "Necking" effects which happens in compression and tension causes the confining stress on the lead plug

varies in a wide range. Confining stress plays a significant role in adjusting yielding and ultimate stress of lead. The confining pressure experienced by lead plug inside a bearing is high enough to distort the section geometry of the plug, (Figure 6-36).

Due to the problem mentioned above, a theoretical stress-strain analysis can not be easily achieved for an elastomeric bearing. For this reason a finite element analysis could be an alternative method for this purpose. The engineering properties of the constituent materials of the bearing used for modeling were defined precisely in order to achieve a successful result from a finite element analysis. It was done by using the results of experiments performed on LRB1300 and NRB1300 bearings.

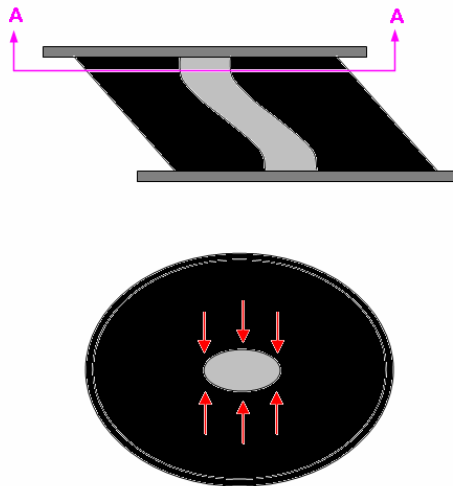


Figure 6-36: Schematic of confining pressure applied by rubber on lead plug. The pressure is high enough to distort the section geometry of the plug

6.9.2 Defining Engineering Properties of Constituent Materials

Defining engineering properties of constituent elements was the most delicate part of a finite element modeling. Properties such as modulus of elasticity, yielding stress, ultimate tensile strength etc. were all needed to be properly defined. These properties had to be obtained experimentally by performing tests on the assemblies and not on the elements individually.

The information about stress-strain behavior of steel and rubber was obtained by subtracting the test data of NRB1300 from that of LRB1300, these two bearing, used in Experiment-1 were identical in size and structure except, only one of them had lead plug. Also, they both subjected to identical test protocols consisting of 50 sinusoidal load of constant velocity of 13 mm/sec at various displacement amplitudes. This test allowed separation stress-strain behavior of each component. The result of individual contribution is given in Table 6-10.

Table 6-9: Individual Stress-Strain behavior of lead and rubber is obtained by subtracting Test-data of NRB1300 from LRB1300.

	Displ. Amp mm	50	100	200	200	200	300	400	400	400
	Shear Strain	0.1287	0.2573	0.5147	0.5147	0.5147	0.7720	1.0293	1.0293	1.0293
Lead	Avg. Force (kN)	267.89	271.58	243.13	246.56	242.57	263.53	230.86	235.50	237.21
	Avg. Kra (kN/mm)	1.67	0.35	0.13	0.11	0.15	0.07	0.12	0.10	0.09
	Avg EDC (kN-mm)	43777	104468	203219	206628	199663	348935	407220	416311	430733
	Section Area (mm²)	5.3093 x 10 ⁴								
	Shear (MPa)	5.00	5.10	4.60	4.60	4.60	5.00	4.30	4.40	4.50
Rubber	Avg. Force (kN)	41.26	137.78	323.52	321.67	321.70	506.86	666.11	663.71	670.24
	Avg. Kra (kN/mm)	1.63	1.73	1.69	1.69	1.69	1.76	1.68	1.68	1.70
	Avg. EDC (kN-mm)	132	712	4106	4740	4286	15347	27986	27809	29171
	Section Area (mm²)	1.3273 x 10 ⁶								
	Shear (MPa)	0.0310	0.1038	0.2437	0.2423	0.2423	0.3819	0.5018	0.5000	0.5050

Plot of the data obtained from subtraction of the results of the two bearings is shown in Figure 6-37. The assembly of rubber and steel shims remained linearly elastic within the entire range of shear strain

ratio. Shear stress experienced by lead remained nearly constant after yielding which happened in early stages of loading with an average of 5 (MPa).

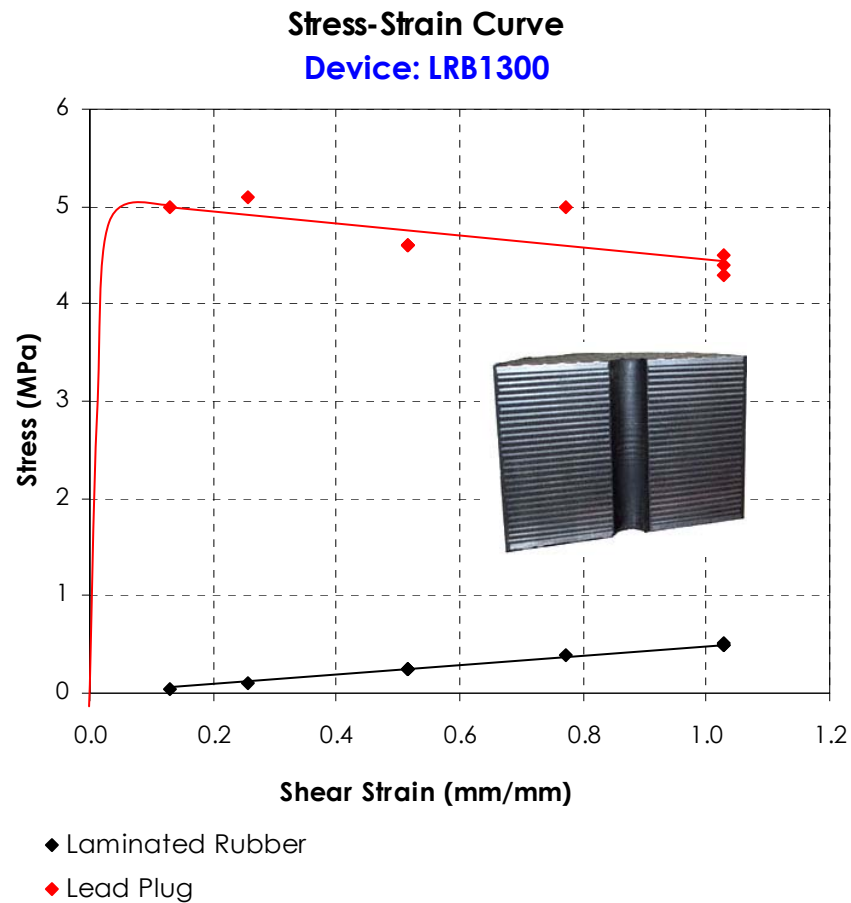


Figure 6-37: Stress-strain behavior of lead and rubber obtained by subtracting experimental data of NRB1300 from LRB1300

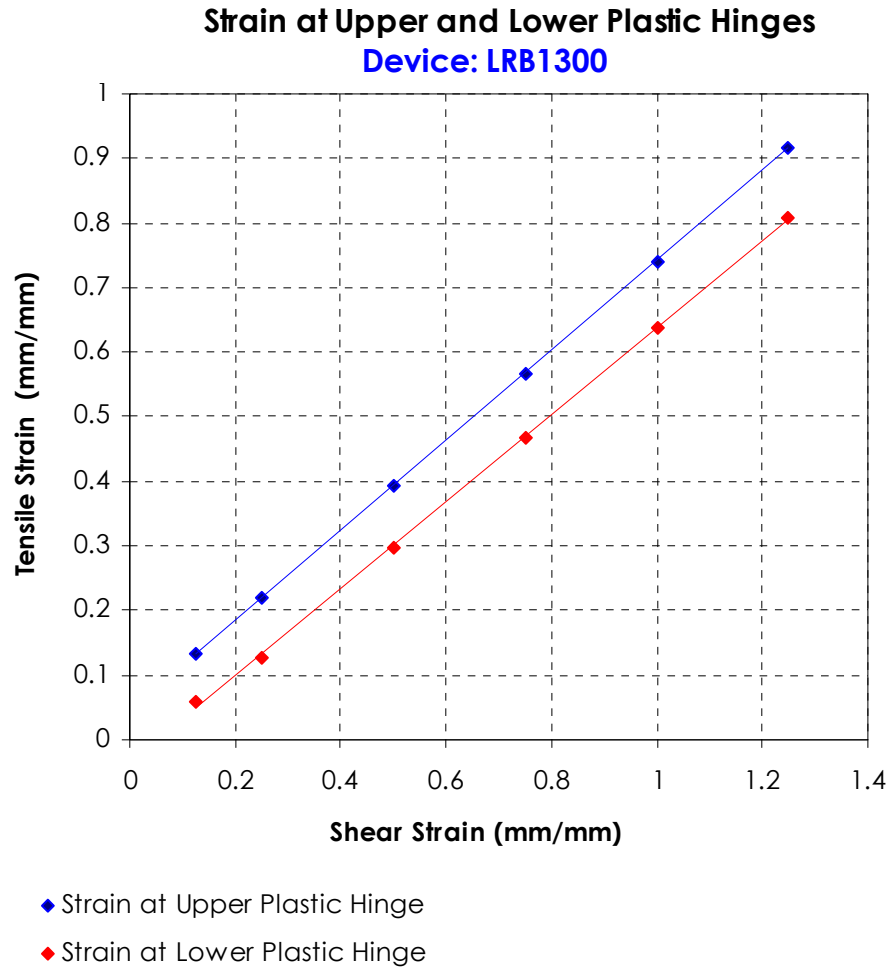


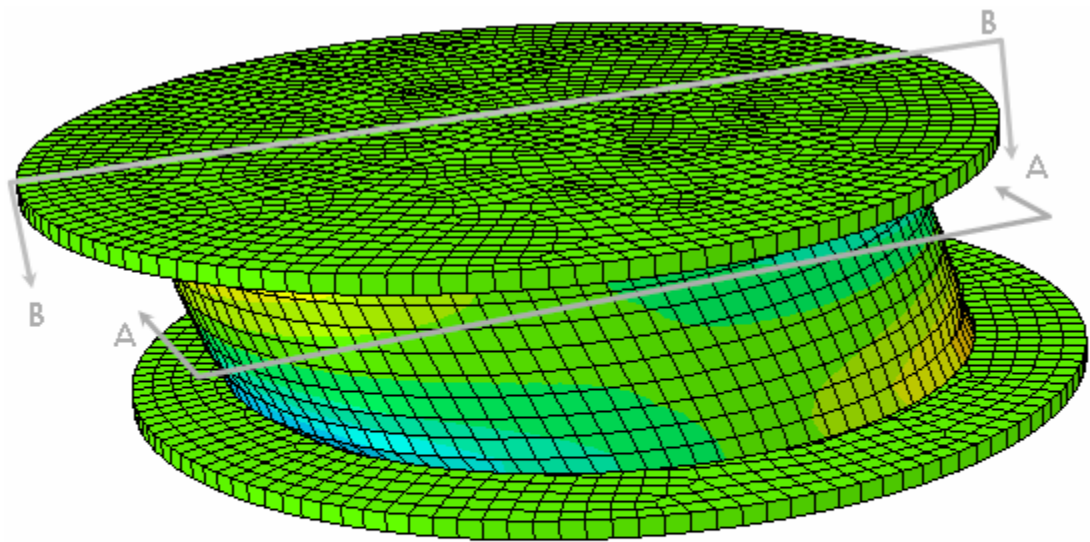
Figure 6-38: Variation of maximum tensile strains at upper and lower plastic hinges of the lead plug

The information about moduli of elasticity and plastic behavior of lead was extracted from plots of (Figure 6-37) and (Figure 6-38). The information was used in creation of the finite element model. The 3-D images, obtained from the finite element model, reflect the state of strain on internal components of LRB1300, Figures 6-39 and 6-40.

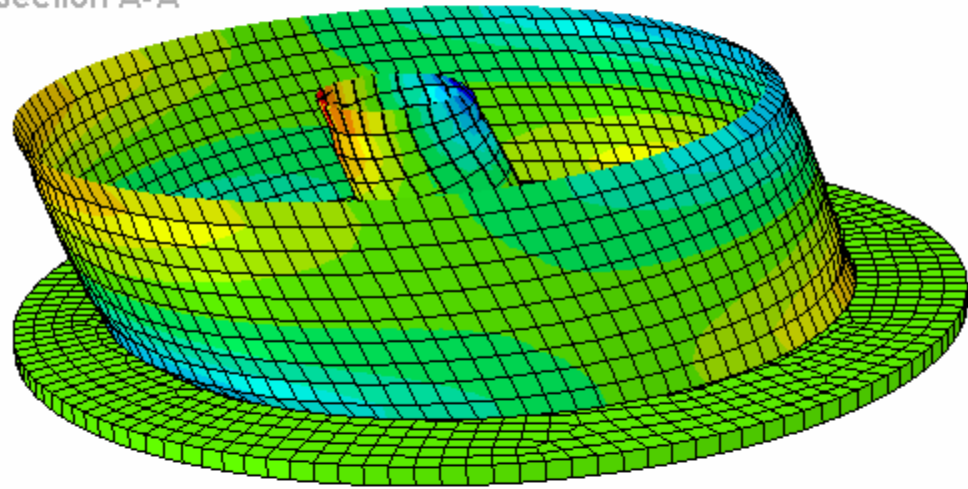
The lateral displacement of 400 mm, which was applied to LRB1300 during Experiment-1 was reproduced by the finite element

model. Different section views presented in Figure 6-39 shows the locations with stress concentration on critical points of the bearing.

It is also observed in Figure 6-40, from the two plastic hinges formed on the lead plug, the lower plastic hinge experienced higher strain level compared to the upper one. This was confirmed by infrared imaging operations performed on Robinson bearing during Experiment-1, Figure 7-7.



Section A-A



Section B-B

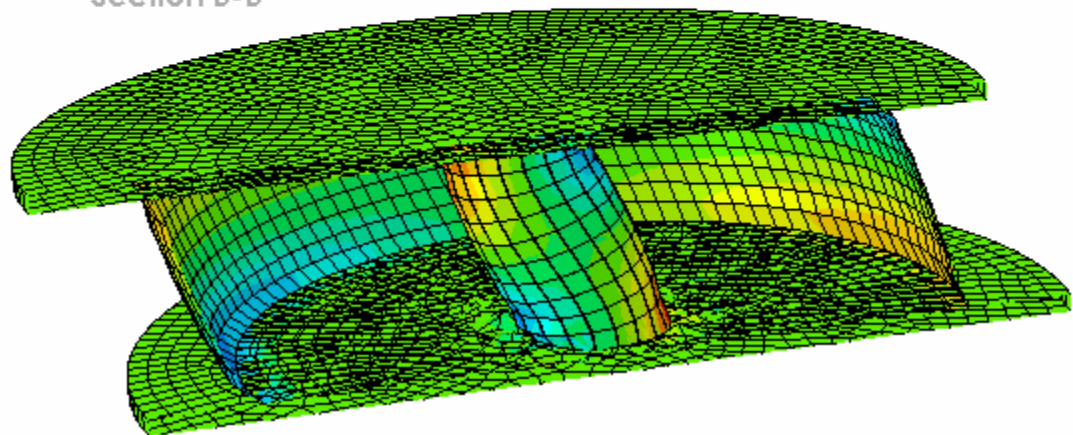


Figure 6-39: 3-D visualization of internal components shows locations with high strains and deformation at critical points, (Device: LRB1300)

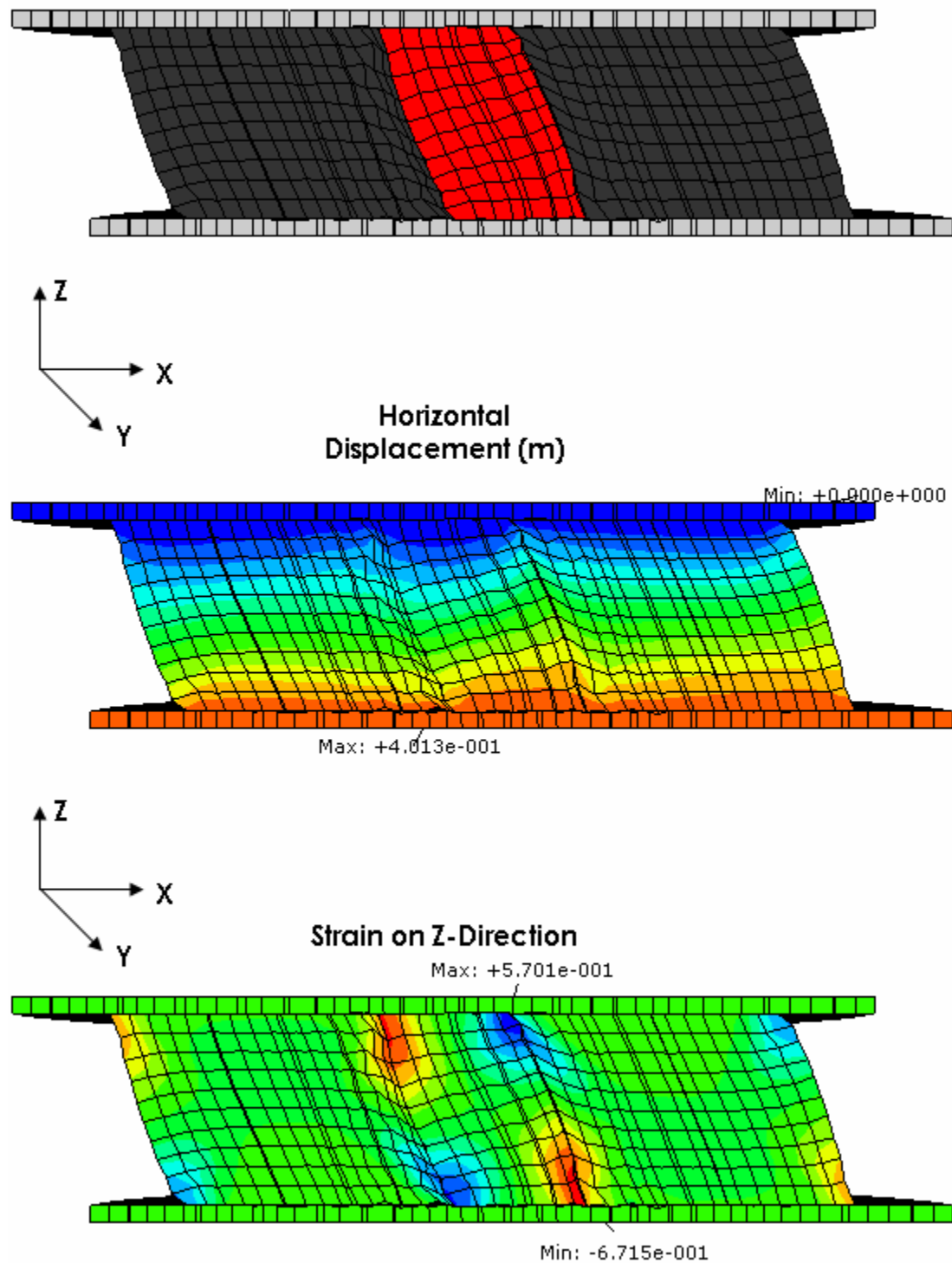


Figure 6-40: At the mid-section view presented on this figure, strain at upper and lower plastic hinges are shown when displacement of 400mm was applied to LRB1300

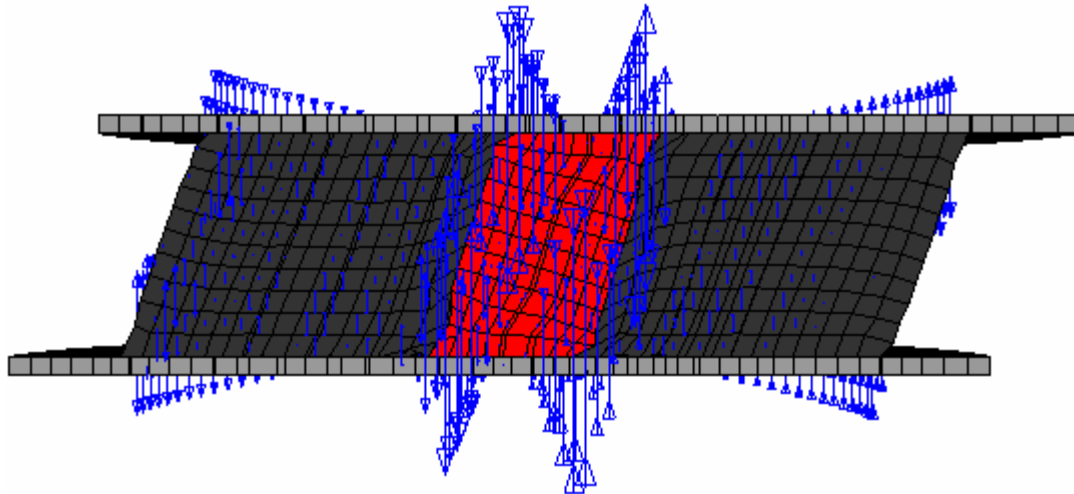


Figure 6-41: Qualitative assessment performed on middle section is shown. Strain vectors are highest at the ends of lead plug relative to the rest of the bearing

The reproduction of Experiment-1 on the F.E. model of LRB1300 gave an insight about the state of stress interaction between internal components of this bearing. It was observed that, the lead plug is subjected to high level of tensile stress as well as non-uniform confining pressure. Each of these imposed constraints can significantly affect performance of lead plug, particularly its energy dissipating characteristics.

The results of modeling also justified a rare type of degradation /failure that happens to the lead plug of elastomeric bearings. It is a failure mechanism through which the lead plug experiences a high shear stress along its axis. This high shear stress causes the plug to slip (Figure 6-42), or to completely break along its axis (Figure 6-43).

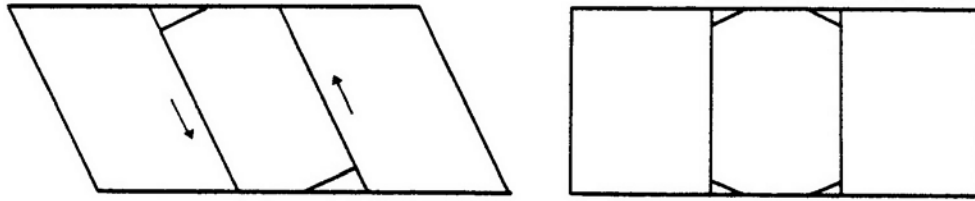


Figure 6-42: Permanent degradation due to slippage of the lead plug in its housing

In rare situations, depending on the rate of applied load or ambient temperature the shear force applied to the lead plug may result in catastrophic shear failure of the lead plug along its axis.

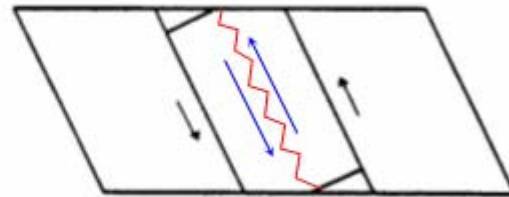


Figure 6-43: Failure of a bearing due to shear failure along the axis. (Source: Report No. 289, S.M Built, Dept. of Civil Engineering, University of Auckland, New Zealand)

6.10 Highlight of the Chapter

Ambient harmonic vibration causes the bearing to warm up gradually and steadily. The final thermal stage is called steady state. At steady state, further variation of temperature with time is small and negligible. Steady state heat analysis is needed for prediction of a bearing's internal temperature when subjected to harmonic dynamic excitation.

The superimposed plots of temperature at each thermocouple as functions of their locations were prepared. A Careful observation on the plots indicated an agreement existed between the data obtained experimentally and those obtained by the finite element modeling. This approved the credibility of the finite element modeling for parametric studies intended for further studies.

Through parametric analysis of this chapter a model was proposed to predict internal temperature of an elastomeric bearing with respect to ambient conditions. This model can serve its purpose when information about ambient and surface temperatures or ambient temperature and heat-flux is available. This could link the equation proposed for EDC in Experiment-1 to the prediction ultimate temperature at a lead plug.

This information will be conveyed to Chapter 7 to be used in the mythology proposed for property loss assessment of elastomeric bearings.

7

Assessment of Thermal Deterioration of Lead Plugs

The low melting temperature of lead (327 °C), and its consequential malleability at room temperature, has made this metal a suitable material for engineering applications where it is subjected to high deformation. Also, the high energy absorbing capacity of lead and its good heat diffusivity, make it ideal for damping applications. Its tendency to recrystallize during deformation, and anneal at room temperature, make this metal a maintenance-free damping material, with limited susceptibility to fatigue during high cycle plastic deformation. Studies were conducted by researchers [32], in order to find a correlation between the tensile strength of lead and the temperature to which it is exposed. The common failure mechanism for lead in tension is microvoid coalescence. At a transition temperature the fracture mechanism has been observed to change from void coalescence to fracture via highly localized bands of intense shear deformation [29]. In this chapter the steady state and transient property loss of lead will be discussed, as highlighted in Figure 7-1.

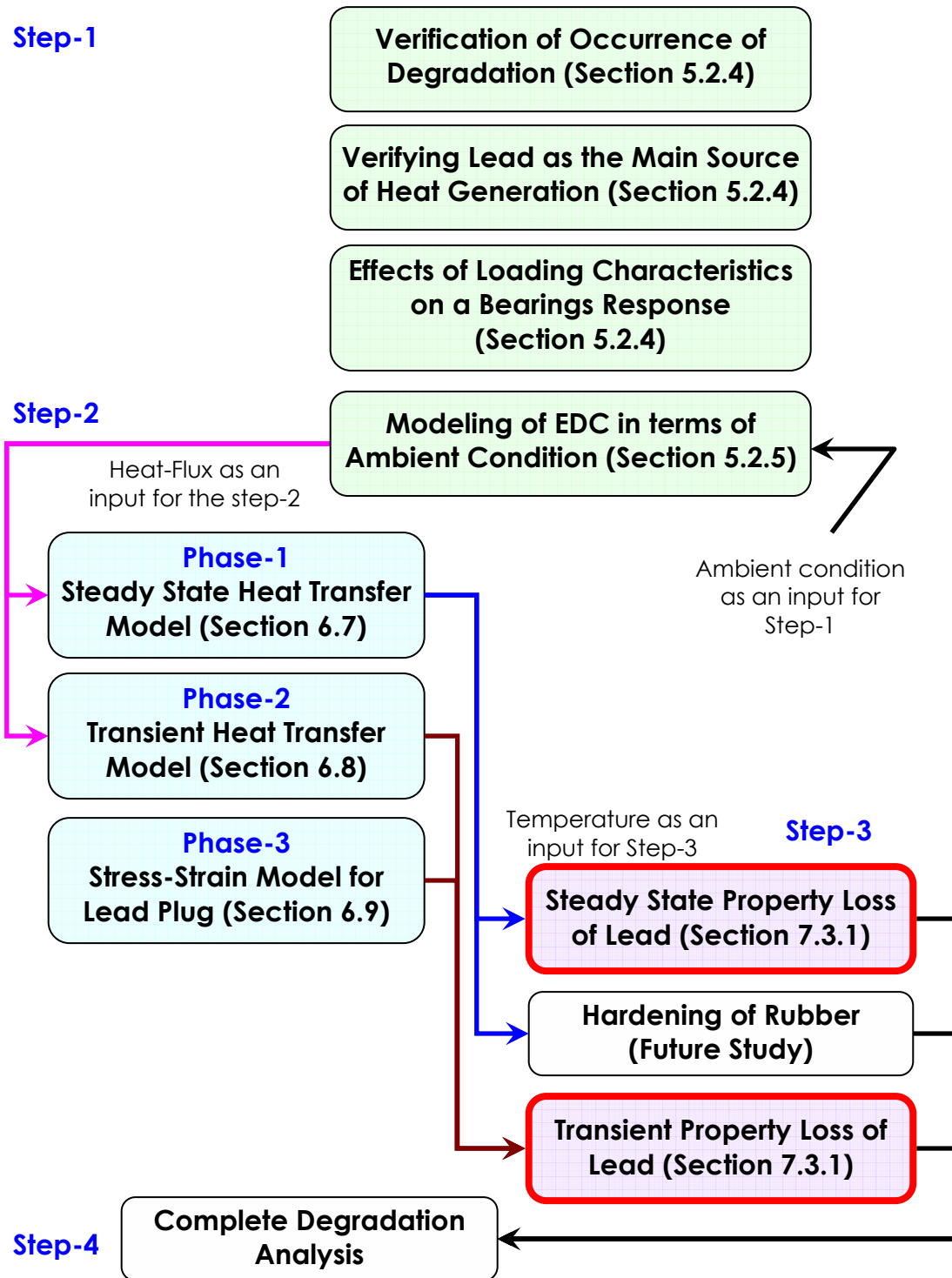


Figure 7-1: The sections highlighted in red are the steps taken at the present chapter

7.1 Relation between Temperature and Tensile Strength of Lead

The finite element modeling together with infrared imaging confirmed the theory that energy dissipation of a lead plug takes place mainly in plastic hinges, the locations where tensile strains along the plug are at the highest, (Figure 7-2). The theory suggests that the reduction in EDC sequential cycles is due to the decrease in ultimate tensile stress of the lead plug when its temperature is raised.

The blue arrows in Figure 7-2 show the magnitude of the strain at the core of LRB1300 relative to the rest of the section when a 400 mm displacement was imposed to the bearing.



Section View at A-A

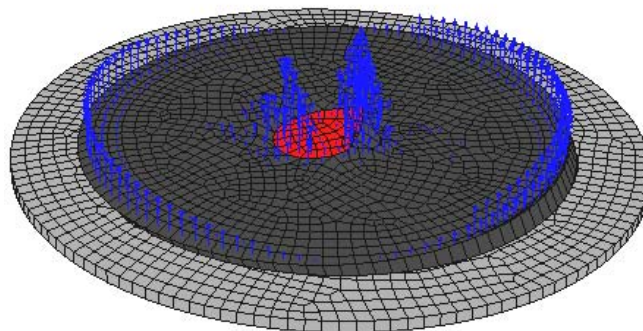


Figure 7-2: Section view of LRB1300 provided by the finite element modeling shows the lead plug experienced high tensile strain at locations of the plastic hinges

Constantinou [32], proposed a relation between temperature and ultimate tensile strength of lead. It was done by performing multiple tensile tests on lead coupons at two widely apart straining rates of 0.25 sec^{-1} and 0.0075 sec^{-1} . The results are reported in Figure 7-3. For a relative fast straining (marked in blue), a linear relationship exists between the tensile strength and the temperature. For slow straining, however, a linear variation can be assumed for the temperature up to 100°C . For the temperatures higher than this point tensile strength behaves nonlinearly with variation of temperature. Higher drops in tensile strength are resulted for increments of temperature change at temperatures higher than 100°C , Figure 7-3.

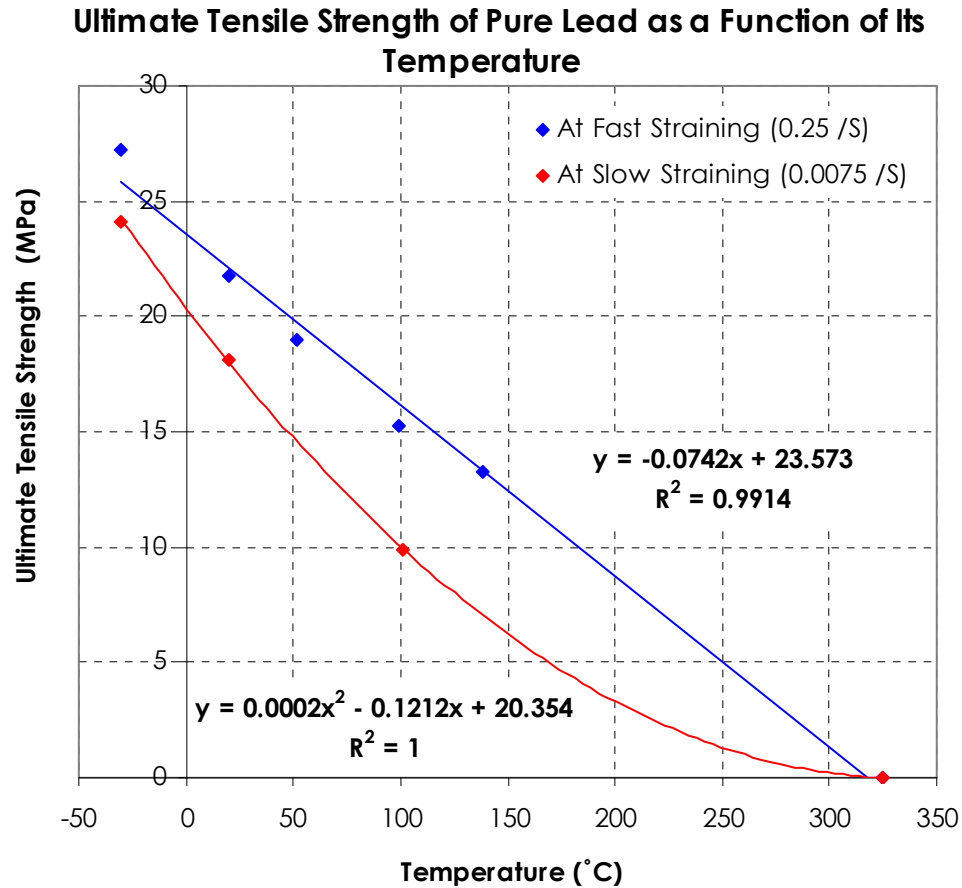


Figure 7-3: Ultimate tensile strength of lead as a function of time at two straining rates of 0.25 sec^{-1} and 0.0075 sec^{-1}

7.2 Proposed Model

The proposed model comprised of a number of linked methodologies, each of which provides inputs for the next link. The methodology was initiated by proposing an empirical equation for calculating EDC of a bearing in terms of the characteristics of input motion. This equation was obtained and validated by experiments that were performed in a wide range of input data (see Section 5.1.5). Figure 5-22 and 5-23 shows the plot of the functions governing the

existing relation between these variables for the test bearings of Experiment-1.

The EDC, calculated from the equation obtained at previous step, was used as an input for two finite element heat transfer models to estimate the temperature of the plug at steady as well as transient states. The thermal results of this analysis were validated by performance of the Experiment-2 (Sections 6.5), and by theoretical studies through substitution of an equivalent material for laminated rubber.

The temperatures variation resulted from the finite element modeling were submitted to one of the existing models to calculate the reduction in tensile strength of the lead plug, associated with the obtained temperature variation. This new tensile strength was compared to the one obtained at initial temperature. This reduction can be interpreted as the reduction in damping property of the lead plug.

7.3 Implementation of the Proposed Model

7.3.1 Reproduction of Tests Performed on Robinson Bearing

The Robinson bearing was selected for verification of the model proposed in Section 7.2. This selection was based on availability of data

from Experiment-1 which included a range of variation for both amplitude and velocity. The bearing was modeled using Explicit Dynamic Analysis, a finite element computational tool available in Abaqus 6.9.

From the result of infrared thermography (Figure 7-7) as well as the finite element 3-D stress analysis (Figure 7.6), it was inferred that a large portion of energy is dissipated by the plastic hinges formed at each end of the lead plugs. In Figure 7-4 the results of test T1, T5a and T5e indicated a consistent drop in EDC between cycles in the order of nearly 10 % (indicated by red arrows in the Figure 7-4). It has to be noted that these tests were performed in identical manner. It was observed that an almost perfect recovery took place within 20 minutes after completion of each test, (see tests T1, T5a, T5e, in Figure 7-4). The recovery from subsequent tests in terms of EDC is indicated by the blue arrows in Figure 7-4. Lead is characterized by its unique capability of recrystallization which can take place at room temperature. Therefore, upon interruption between each two tests the lost properties was expected to be recovered. This justifies the relatively fast recovery of the bearing.

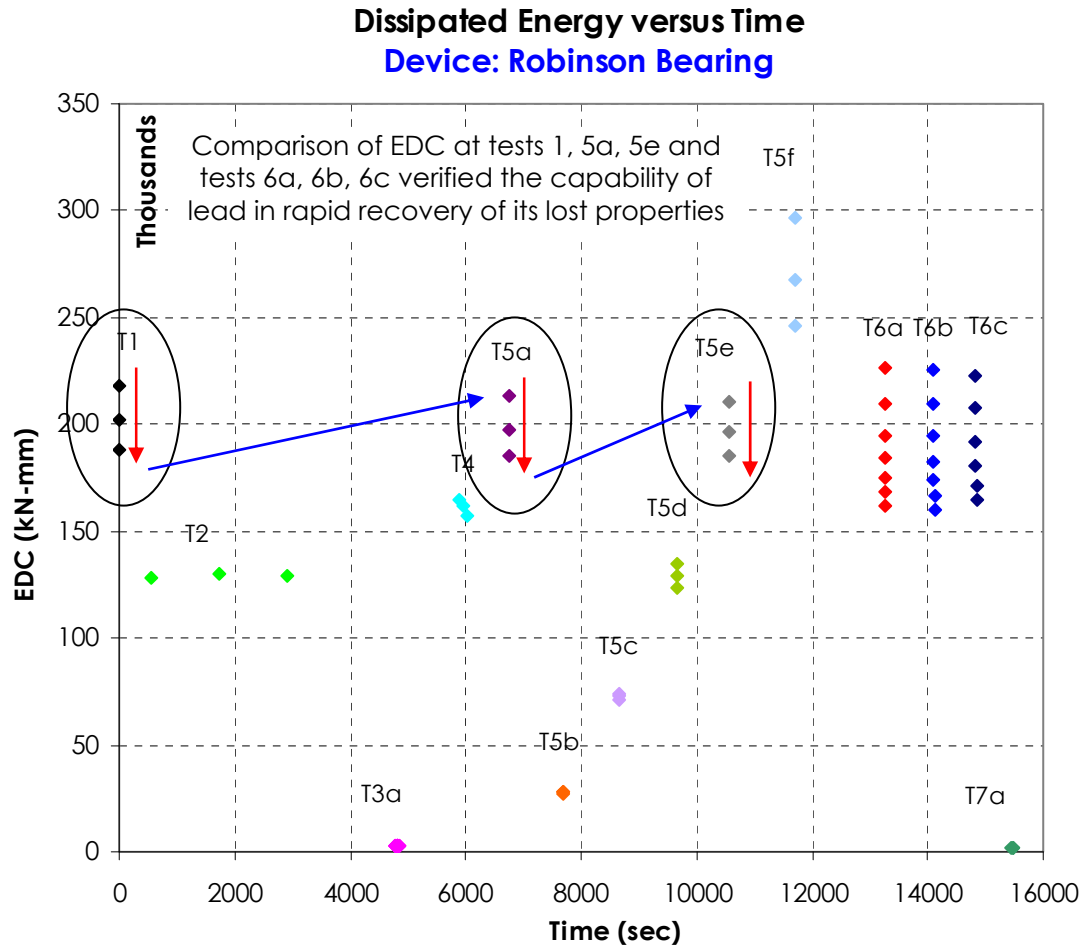
Tests T6a, T6b and T6c were also identical in loading characteristics. They exhibited the similar behavior as the previous tests

in terms of dropping in EDC values. However, recovery was less complete due to short time interval between tests.

It was postulated that there could be a link between property loss and the temperature of the lead plug which is raised by EDC.

At each hysteretic loop, EDC is a function of two variables of stiffness and maximum horizontal force. The EDC was observed to be mainly affected by the maximum force at each hysteretic loop. This conclusion was made by investigating and comparing the effects of cyclic loads on all three characteristics.

These specifications were reproduced by the F.E. model at specific combinations of shear strain and rate that was reported in Figure 7-4. Especially, the condition of shear strain equal to 0.371 and rate equal to 0.9 sec^{-1} was implemented. The rational behind using this selection was the presence of three tests of identical characteristics, which allowed comparison for recovery verifications.



◆ Test 1, Shear Strain= 0.371,	T(sec)=2.6, Shear Strain Rate (/s)=0.9
◆ Test 2, Shear Strain= 0.390,	T(sec)=1180, Shear Strain Rate (/s)=0.0017
◆ Test 3a, Shear Strain= 0.0152,	T(sec)=2.6, Shear Strain Rate (/s)=0.039
◆ Test 4, Shear Strain= 0.371,	T(sec)=70.25, Shear Strain Rate (/s)=0.039
◆ Test 5a, Shear Strain= 0.371,	T(sec)=2.6, Shear Strain Rate (/s)=0.9
◆ Test 5b, Shear Strain= 0.0935,	T(sec)=2.6, Shear Strain Rate (/s)=0.23
◆ Test 5c, Shear Strain= 0.1870,	T(sec)=2.6, Shear Strain Rate (/s)=0.45
◆ Test 5d, Shear Strain= 0.278,	T(sec)=2.6, Shear Strain Rate (/s)=0.675
◆ Test 5e, Shear Strain= 0.371,	T(sec)=2.6, Shear Strain Rate (/s)=0.9
◆ Test 5f, Shear Strain= 0.465,	T(sec)=2.6, Shear Strain Rate (/s)=1.12
◆ Test 6a, Shear Strain= 0.371,	T(sec)=2.6, Shear Strain Rate (/s)=0.9
◆ Test 6b, Shear Strain= 0.371,	T(sec)=2.6, Shear Strain Rate (/s)=0.9
◆ Test 6c, Shear Strain= 0.371,	T(sec)=2.6, Shear Strain Rate (/s)=0.9
◆ Test 7a, Shear Strain= 0.0152,	T(sec)=2.6, Shear Strain Rate (/s)=0.039

Figure 7-4: The Robinson bearing experienced significant per-cycle decrease in dissipated energy but also rapid loss recovery

The purpose of implementation of the finite element model was to investigate the state of tensile strain at the core. This must be used to verify, whether or not is the strain at the core, within the range that could affect the tensile strength.

Figure 7-5 shows the strain contour of one of the lead plugs of the Robinson bearing from the F.E. model. The locations and magnitude of maximum strain at each end of a lead plug of the Robinson bearing are visible in the figure.

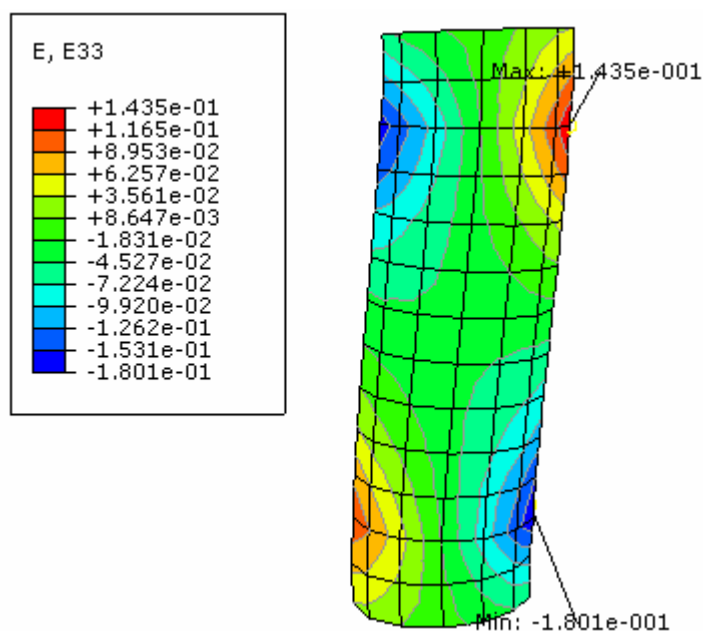


Figure 7-5: Strain contour on one of the four lead plugs shows the location where the magnitude of strain is at maximum

The results of F.E. post yield investigation matched the observation 4 of Section 5.1.4, "The Post-yield behavior of Lead". The post yield shear stress of lead remains at the range of 4.6 (MPa) to 5 (MPa) for strains of up to 1.2 (the highest imposed strain). According to

the results of Section 5.1.4 and the F.E. model, the strain at the either ends of the lead plug of the Robinson bearing remained in a range on which the tensile strength is not varied significantly. Maximum strain at the ends of the plug showing in Figure 7-5 was 0.14 and 0.18 for the top and bottom respectively.

Figure 7-6 is a visualization obtained from the complete numerical model of the bearing, and portions of the lead plugs inside of the bearing. The propagation of high strain levels to the surface of rubber is also indicated by red and blue colored area located at top and bottom of the bearing.

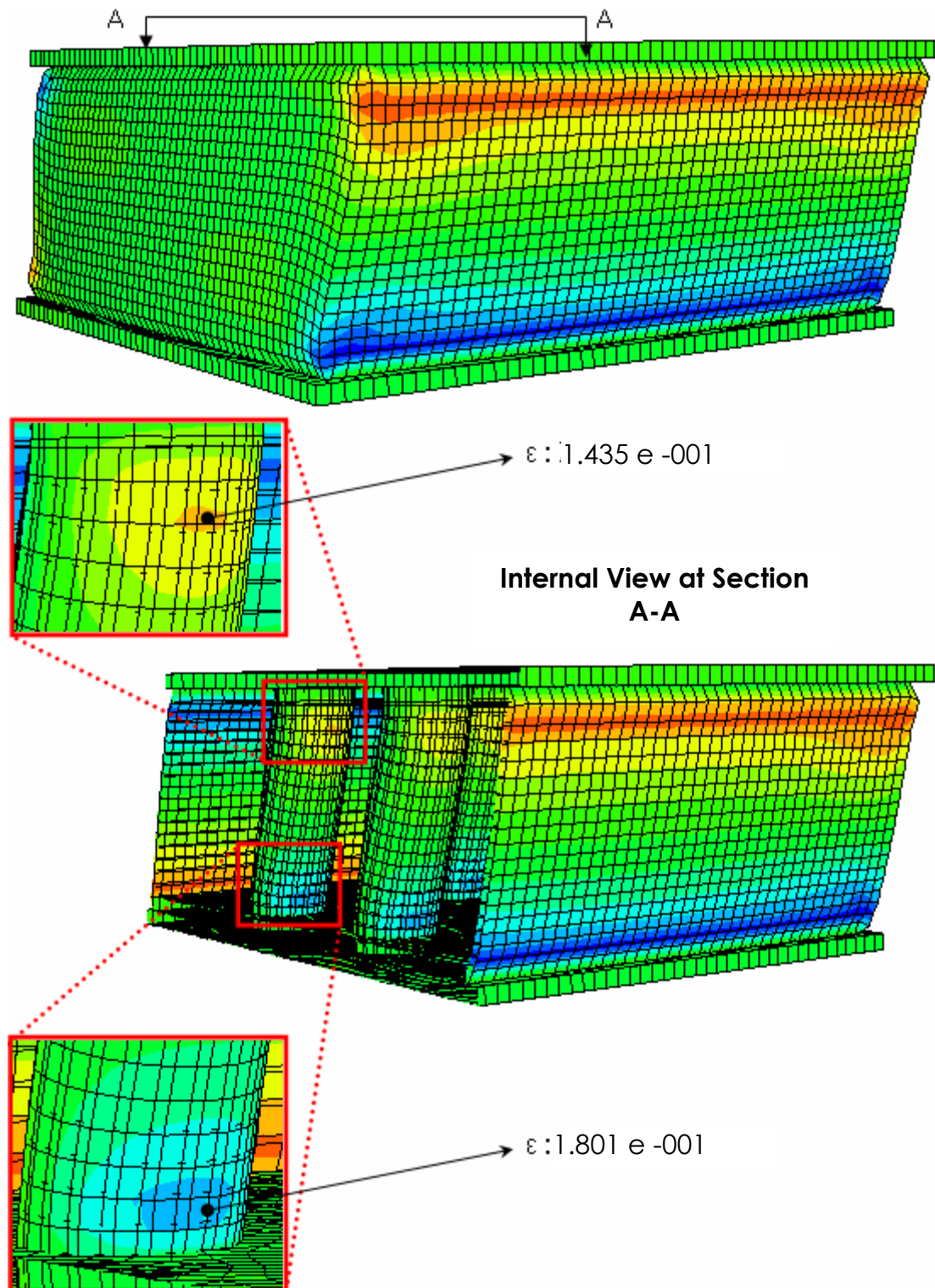


Figure 7-6: Plugs experienced different strain at location of plastic hinges

Infrared imaging was utilized during experimental activities of the Experiment-1. The thermal images, taken from the surface of the Robinson bearing (Figure 7-7), show two regions of different sizes on the surface with temperatures higher than the rest of the surface. These areas are differentiated from the rest of the surface by yellow/red colors.

Area in red color indicates a temperature of 28 °C while area in blue color corresponds to 27 °C. The ambient temperature was 25 °C. The loading applied to the bearing supports a uniform distribution of temperature along the axis of the bearing, however, the bottom portion of the bearing indicates generally a higher temperature even at early stages of the test Figures 7-7 and 7-8. The reason for such non-uniformity was justified by the inequality between the level of strains experienced by the lower and upper plastic hinges, confirmed by the F.E. model results (Figure 7.6). Schematic of the set up and the F.E. model results of the Robinson bearing are presented in Figure 7-8.

The result of extensive analysis on infrared thermography proved that the surface may not be used for an adequately accurate estimation of internal temperature.

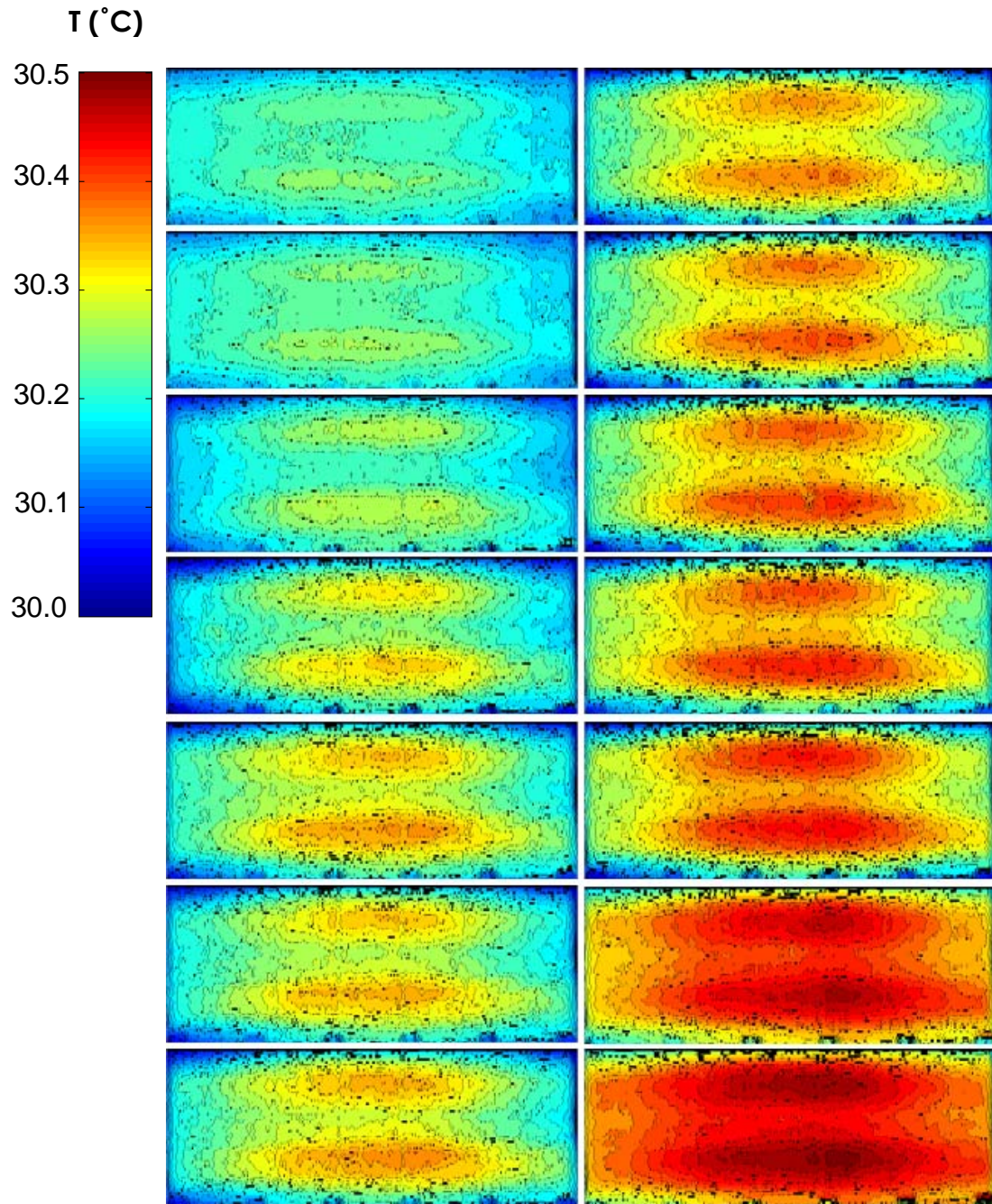


Figure 7-7: Thermography imaging performed on the Robinson bearing. The images from top left to bottom right show the surface temperature at 60 seconds intervals after the test was performed

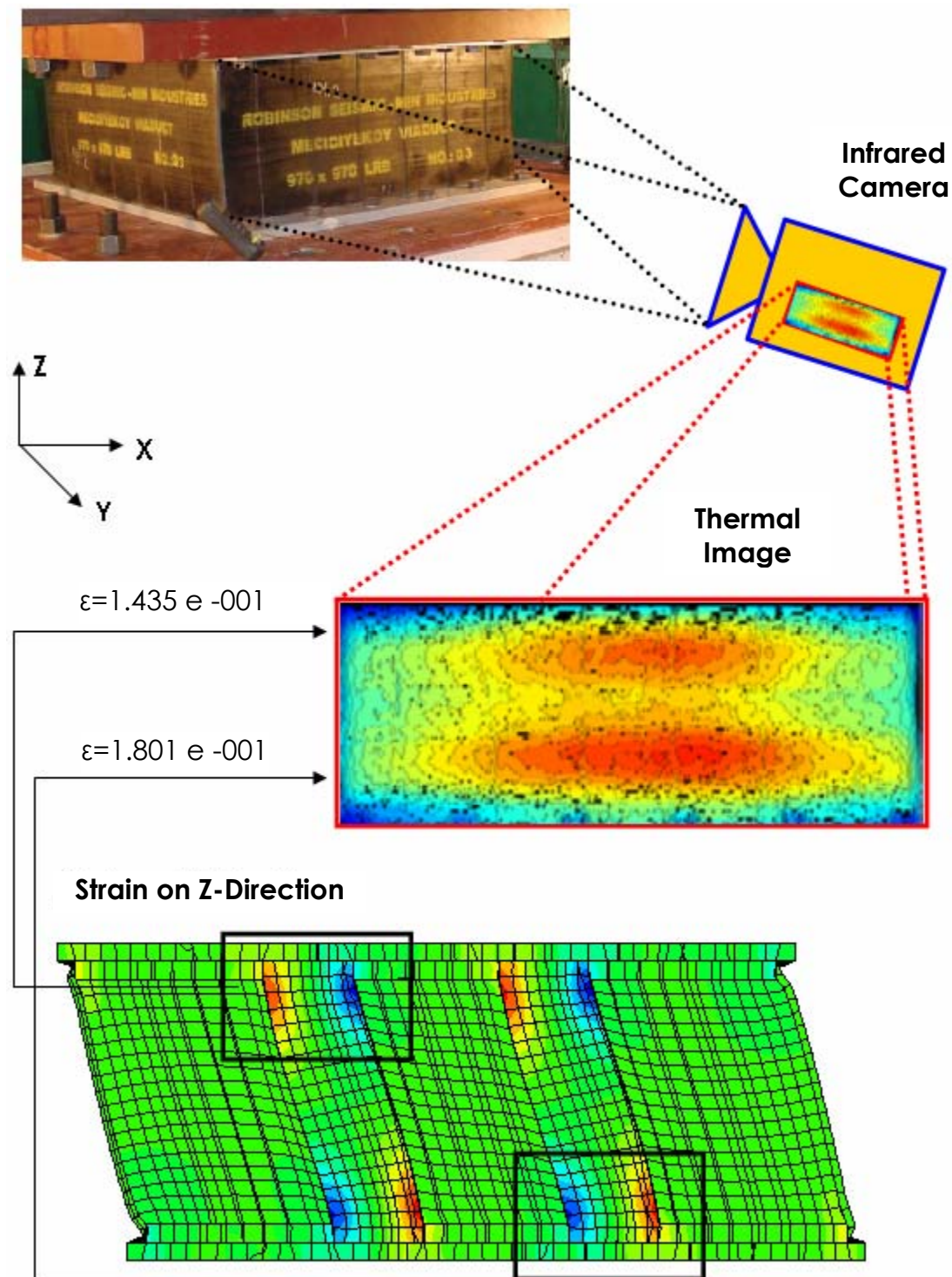


Figure 7-8: Infrared thermography confirmed lead plug strained significantly at the location of plastic hinges. However, strain is higher at the lower plastic hinge

7.3.2 Estimation of per Cycle Degradation

Per-cycle degradation occurs when a relatively high amount of mechanical energy is converted to heat within the core of a bearing. It happens when the rate of the heat generation is much higher than the rate at which the conduction takes place. The abrupt heat generation results in formation of a transient temperature within the core. This high temperature affects the performance of the lead plug at the next cycle. Figure 7.9 indicates how an abrupt energy generation results in temporarily higher temperature within the body of an object.

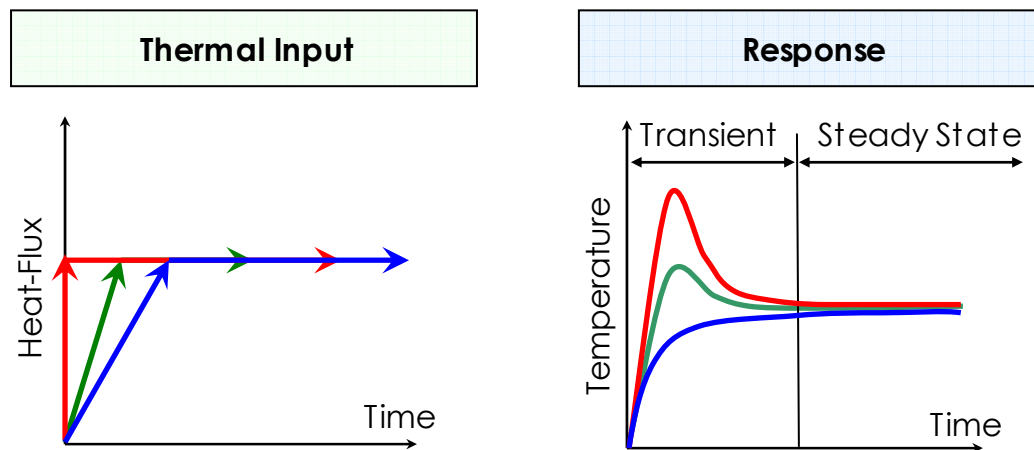


Figure 7-9: schematic representation of thermal transient and steady states

Using the model proposed in Section 5.1.5 for prediction of EDC, a heat-flux of 127000 W/m^2 was calculated for the Test-1 of Experiment-1. Displacement amplitude of 0.371 m was applied at period of 2.5 sec and shear strain rate of 0.9 sec^{-1} through Test-5e. The equation for EDC, obtained in Section 5.1.5 gives:

$$EDC = 265856x^{0.5035}, \quad x = (Shear\ Strain\ Rate)^2 \times Total\ Travel$$

$$EDC = 265856 \times (0.28624 \times 0.9^2)^{0.5035} = 127360\ W/m^2$$

The calculated heat-flux was used as an input for the transient heat transfer model presented in Section 6.8, and a temperature increase of $\Delta T = 23\ ^\circ\text{C}$ was resulted. As a result of taking the ambient temperature of $25\ ^\circ\text{C}$ into account, the total temperature of the core was calculated to be $T_{total} = 48\ ^\circ\text{C}$.

A visualization of temperature increase is presented in Figure 7-10 and the F.E. results are reported in Figure 7-11 in terms of time history of temperature variation within the period of a single cycle.

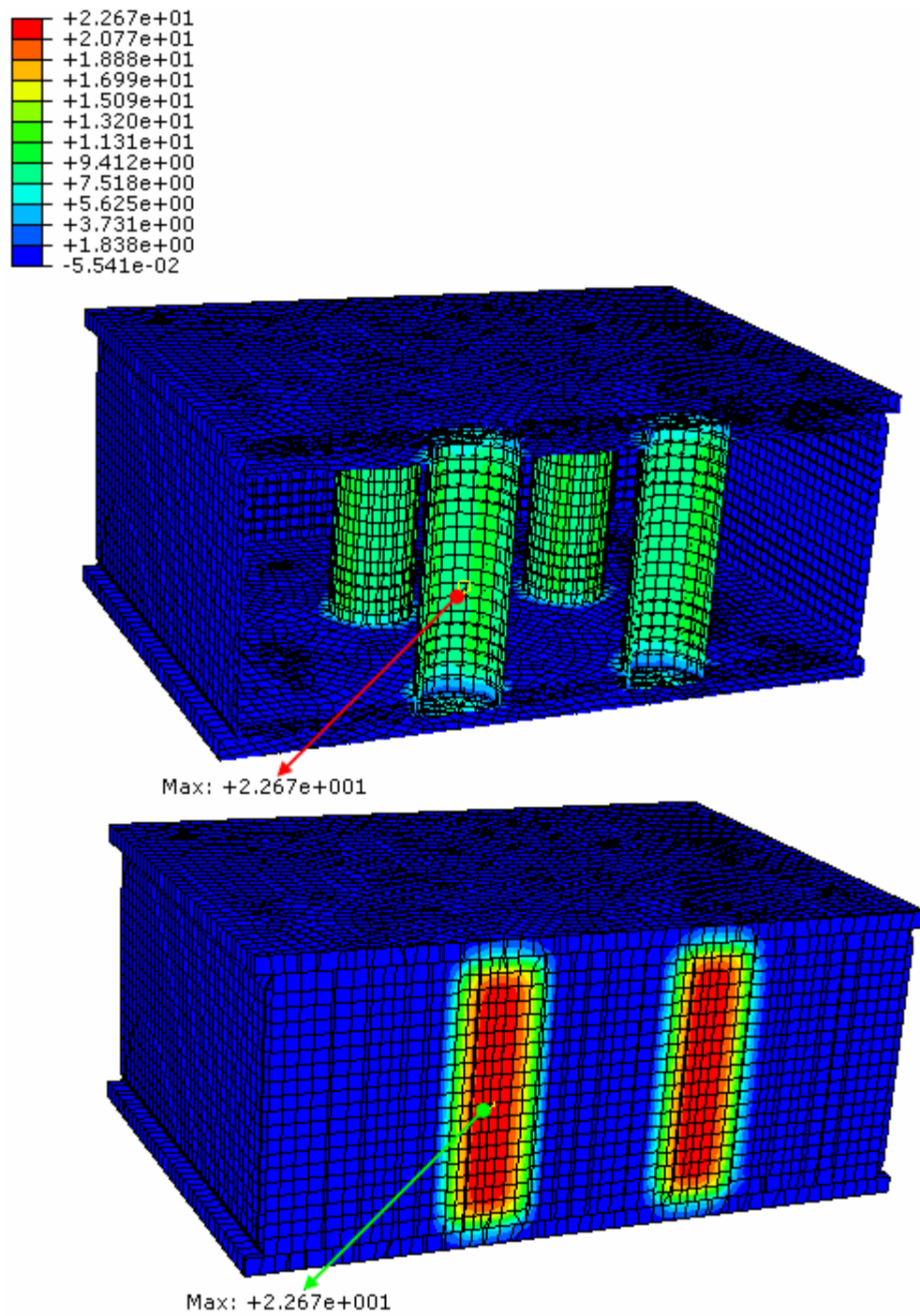


Figure 7-10: Using FEM, a temperature increase of $\Delta T = 23^\circ\text{C}$ at the core of the Robinson bearing was predicted for the first hysteresis loop

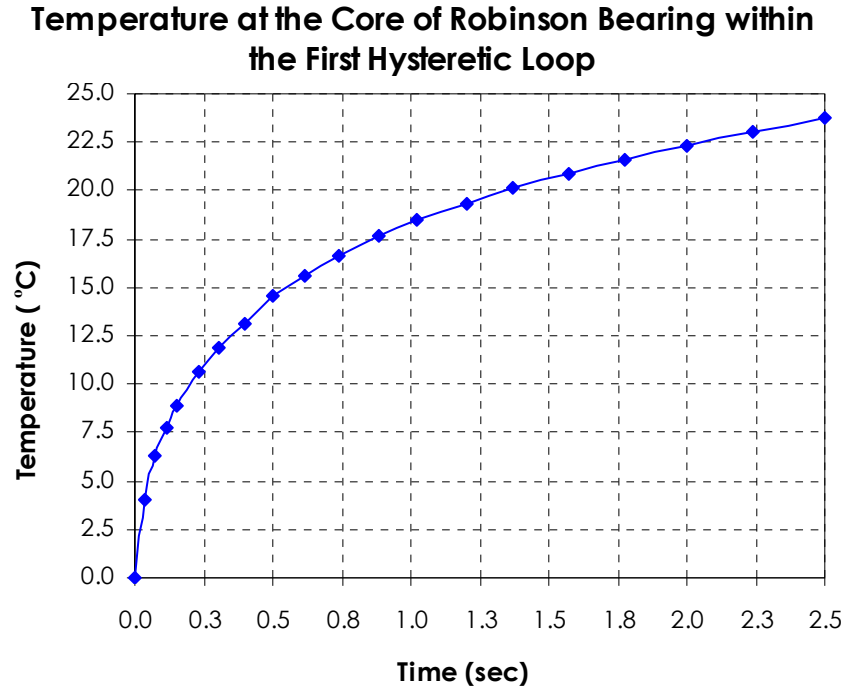


Figure 7-11: Elevation of temperature at Experiment-1 performed on the Robinson bearing reproduced by FEM

The numerically obtained temperature variation of 23 °C can be associated with a tensile strength of lead as proposed by Constantinou [32]. The strain rate used in the model, 0.9 sec⁻¹ is not available in the theory presented by Constantinou [32]. However, it was assumed that higher strain rates present a linear variation of shear strength with temperature (Figure 7-3). For this reason, the linear relation introduced in Figure 7-3, was applied.

$$\sigma_{T(ult)}(MPa) = -0.0742 (T \text{ } ^\circ C) + 23.573$$

$$\sigma_{T(ult)}(MPa) = 21.718 \quad \text{at} \quad T = 25 \text{ } ^\circ C$$

$$\sigma_{T(ult)}(MPa) = 19.937 \quad \text{at} \quad T = 49 \text{ } ^\circ C$$

As a result a temperature rise of $\Delta T = 23.4\text{ }^{\circ}\text{C}$ associated to a drop in ultimate tensile strength of 8% that can be interpreted as an equal drop in terms of EDC. The heat-flux, corresponding to a reduction of EDC in the order of 8 %, is estimated to be 17000 W/m². This procedure repeated in an iterative fashion to obtain the reduction for all three cycles. The results are given in (Table 7-1) for three cycles.

Table 7-1: Experimental and predicted values for EDC and parameters used through the analysis

	Cycle 1	Cycle 2	Cycle 3
Heat-Flux, (Exp) (W/m ²)	133889.22	125185.64	117704.40
EDC, (Exp) kN-mm	210740	196738	185123
Heat-Flux, (Predicted) (W/m ²)	127380.97	116916.00	109334.76
EDC, (Predicted) kN-mm	200189	183742	171826
Ambient Temp ($^{\circ}\text{C}$)	25	25	25
Calculated Transient Temp Rise in 2.5 sec, ΔT ($^{\circ}\text{C}$)	24	17	
Temperature of the Core ($^{\circ}\text{C}$)	25	49	66
Tensile Strength of Lead (MPa)	21.718	19.9372	18.644

The plot of EDC versus cycle number for Robinson bearing is presented in Figure 7-12. The figure contains the plots of experimental

and analytical data superimposed on a single coordinate system for comparison purpose.

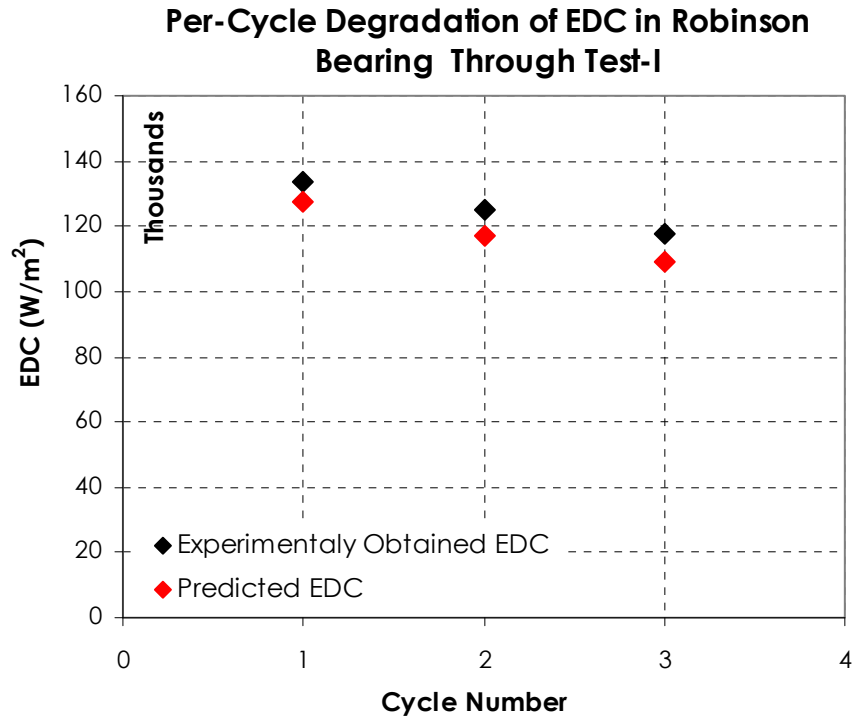


Figure 7-12: Comparison of degradation predicted by analysis that of

The comparison between the experimental and predicted results shows disagreements in the orders of 5 %, 6.6 %, 7 % for cycles 1 to 3, respectively. The procedure was repeated for all performed tests on the Robinson bearing and no error exceeding 8 % was resulted.

It was concluded, and experimentally observed, that the response quality of the bearing deteriorated rapidly when a cyclic load of high amplitude is applied at high rate.

Dynamic response of a structure is defined by its natural period and damping ratio. Knowledge of these two variables allows

determination of pseudo acceleration of a structure during seismic event, using plots of seismic response spectra.

Recalling Equation 2-11, damping is defines through,

$$\beta(eq) = \frac{EDC}{2\pi k_{eff} D_{av}^2} \text{ and natural period, } T_n = 2\pi \sqrt{\frac{M}{k_{eff}}}. \text{ Per the equation for}$$

natural period, this characteristic is depended on the effective stiffness of the bearing. As it was discussed earlier in this research (Section 5.1.4 part 6), the effective stiffness is mainly provided by rubber (nearly 76 % in a standard size bearing) and effective stiffness of the rubber in a bearing remains constant (Figures 5-22, 5-23 and 5-24). With this explanation, the natural period of a bearing is expected to experience insignificant per-cycle degradation.

With the same justification, it can be inferred that per-cycle degradation of equivalent damping is practically affected only by variation of EDC. The values of equivalent damping obtained experimentally and analytically, were normalized with respect to the damping of the first experimental cycle. In Figure 7-13 normalized values of the equivalent damping is plotted against cycle number for the Robinson bearing. A decrease in the order of nearly 17 % predicted where as the experienced decrease was 13 %.

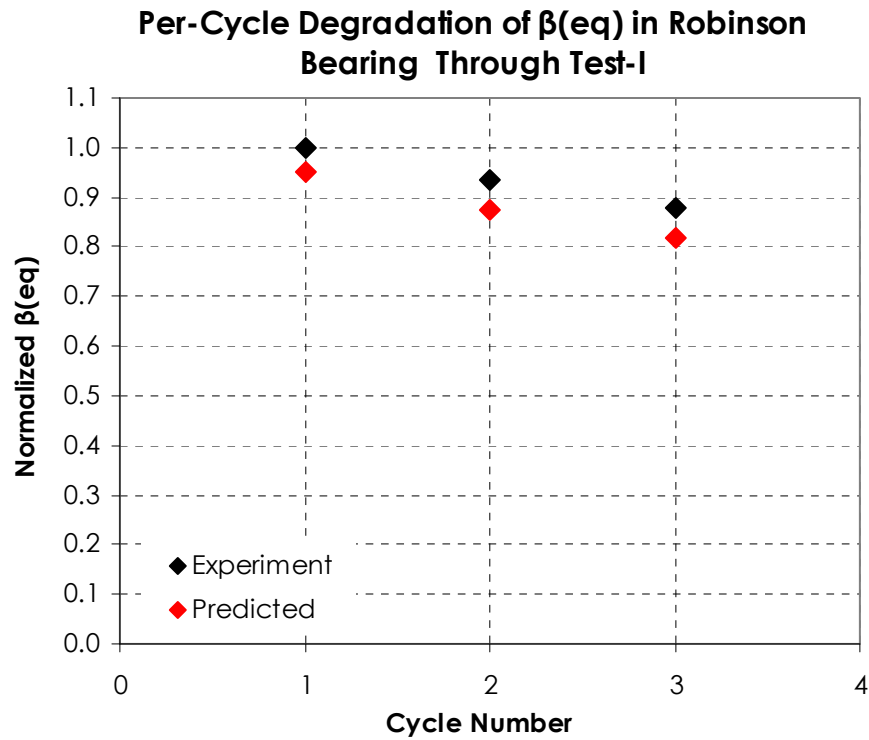


Figure 7-13: Per-cycle degradation of equivalent damping, obtained both analytically and experimentally

Upon continuation of application of load with such characteristics, it was predicted the equivalent damping to drop to 35 % after 10 cycles, Figure 7-14.

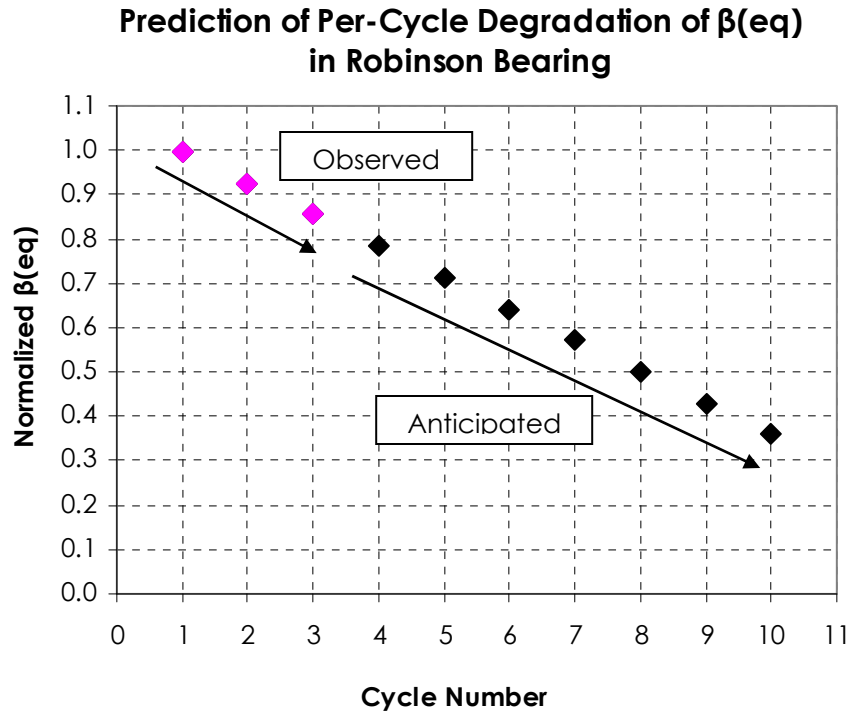


Figure 7-14: Prediction of degradation equivalent damping within 10 cycles

Temperature within the body of lead was expected to reach the melting point of lead (325°C) in less than 20 strokes, (Figure 7-15).

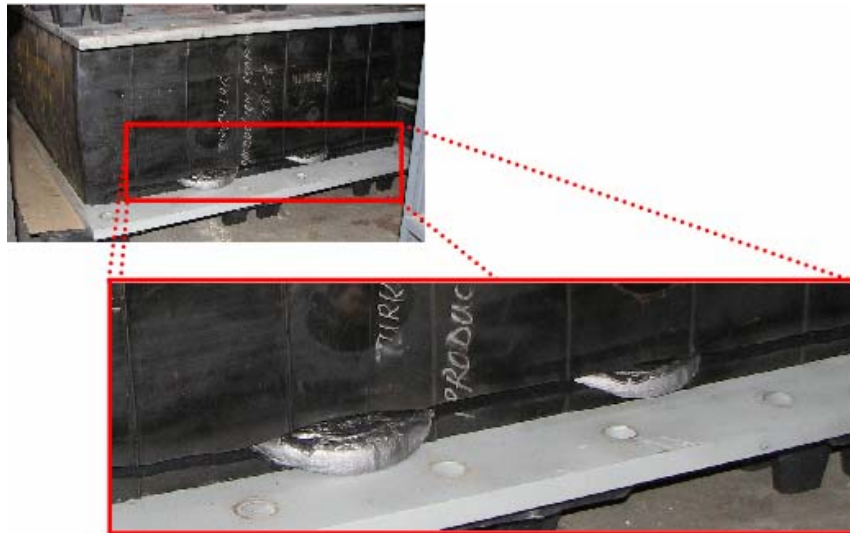


Figure 7-15: Continuous application of high amplitude shear at high rate results in local accumulation of thermal energy which causes lead to melt

7.4 Conclusion and Remarks

The application of the F.E. model to reproduce the experimental results of the Robinson bearing indicates that assessment of the variation of EDC can be reasonably achieved. The overall process indicates that, given certain initial condition (ambient temperature etc.), the application of loading cycle to the bearing can be related to degradation of energy dissipation through a thermal phenomenon which continuously takes place within the bearing. In particular the assessment of the change in EDC activates an iterative cycle due to its effect on the thermal behavior of the bearing. This allows including the prediction of the performance change.

Upon continuation of high rate loading, according to the graph on Figure 7-3, once the temperature reaches 100 °C the plug becomes unstable and loses its property sharply till it completely melts. At that point, it is only rubber that contributes in taking the load (Figure 7-13).

8

Summary, Conclusion and Suggestion for Future Studies

8.1 Summary and Conclusion

As indicated by an extensive literature review, both lead and rubber, as the primary materials used in manufacturing the generic types of lead core elastomeric bearings, is highly subjected to accelerated property loss by exposure to high temperature, [1], [6], [9], [10], [13], [15], [28]. It is documented [16], [17], [27] that rubber experiences irreversible accelerated hardening due to over-vulcanization by heat, Figure 8-1.

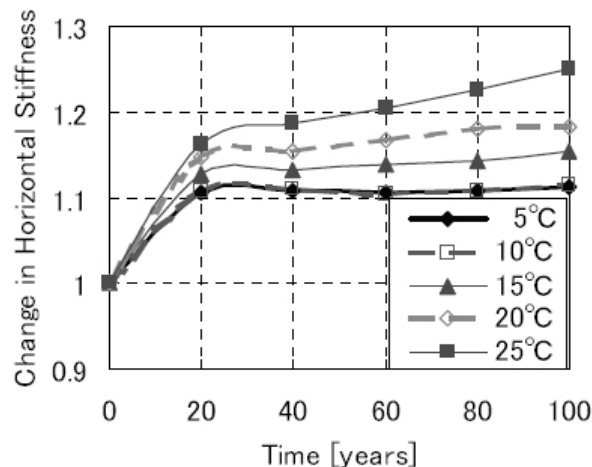


Figure 8-1: Prediction of rubber hardening by over-vulcanization using Arrhenius equation, [10]

It is also documented that the low melting point of lead makes this metal susceptible to loss of mechanical properties even at relatively low temperature variations [32]. However lead recovers almost all of its lost property upon returning to its initial thermal stage (Author, Section 7.2).

There are developed numerical models, capable of quantifying the property loss of both rubber (Arrhenius Equation) and lead [32] when the magnitude of temperature is known. However, a methodology to quantify the amount of temperature, as the key factor to be used in the abovementioned models, is not conclusively presented in the literature.

For this reason, this research was conducted in order to create a link between mechanical energy in the form of dynamic motion and the final temperature of the bearing. This was done by proposing an empirical equation for calculating EDC of a bearing in terms of characteristics of input motion. This equation was obtained and validated by experiments that were performed in a wide range of input data (see Section 5.1.5). Figure 5-22 and 5-23 shows the plot of the functions governing the existing relation between these variables for the test bearings of Experiment-1.

The EDC, calculated from the equation obtained from previous step, was used as an input for two finite element heat transfer models to estimate the temperature of the plug at steady as well as transient states. The thermal results of this analysis were validated by performance of the Experiment-2 (Sections 6.5), and by theoretical studies through substitution of an equivalent material for laminated rubber.

The temperatures resulted from the finite element modeling were submitted to one of the developed numerical models to calculate the tensile strength of the lead plug associated with the temperature obtained from F.E. model. This was compared to the tensile strength, obtained at initial temperature. A reduction was observed and interpreted as the reduction in damping property of the lead plug.

Hardening of rubber, as stated in literature and discussed in Section 4.1.1, is resulted by vulcanization reaction, and like in many other chemical reactions temperature acts like an accelerating agent. The relation between temperature and chemical reaction time is defined by Arrhenius equation. The methodology proposed in this research study can assess the temperature variation associated with specific ranges of motion, and can incorporate this variation with the Arrhenius equation. Knowledge about the range of temperature

variation makes it possible to utilize degradation models, existing in literature, in order to predict the rate and magnitude of changes in performance.

8.2 Suggestion for Future Studies

The proposed procedure appears as a valid tool in support of future studies of degradation phenomenon of elastomeric bearings. The relationship between possible displacement cycles, experienced by bearings in service, and the related thermal phenomenon allows, in fact, the definition of degradation models physically motivated and associated to realistic service conditions. For instance, the development of curves of performance characteristic variations as function of the environmental conditions, as well as of realistic loading of the bearings, represents a logical continuation of the outcomes of this research.

Appendices

Appendix A:	Test Results of Experiment-1
Appendix B:	Experiment-1, Plots of Properties versus Cycle Number
Appendix C:	Experiment-1, Plots of Properties versus Time
Appendix D:	Experiment-2, Plots of Temperature at Thermocouples versus the Distance from a Reference Point
Appendix E:	Experiment-2, Plots of Temperature at Thermocouples with Respect to Ambient Temperature
Appendix F:	Experiment-2, Plots of Temperature at Thermocouples with Respect to Heat-Flux
Appendix G:	Plots of Comparison of the Finite Element Steady State Heat Transfer Model with Results of Experiment- 2
Appendix H:	Plots of Comparison between Direct and Indirect Finite Element Steady State Heat Transfer Models with Results of Experiment-2

Appendix A, Table 1: Test Protocol and Results of Experiment-1, Device: NRB1300

NRB1300			Input Data			Output Data		
Test	Cyl # (total)	Cycle	Disp. Amp. (mm)	Max Vel. (mm/sec)	Ver. load (kN)	EDC (kN-mm)	Fmax (kN)	Kra (kN/mm)
A	1	1	50	13	17800	1045	52.11	1.47
	2	2	50	13	17800	945	46.73	1.52
	3	3	50	13	17800	1077	45.66	1.49
	4	4	50	13	17800	1400	44.34	1.46
	5	5	50	13	17800	1290	46.52	1.52
	6	6	50	13	17800	1438	44.80	1.46
	7	7	50	13	17800	1297	46.28	1.50
	8	8	50	13	17800	1429	47.32	1.46
	9	9	50	13	17800	1628	45.35	1.46
B	10	1	300	13	17800	16661	512.64	1.78
	11	2	300	13	17800	14032	501.09	1.74
C	12	1	100	13	17800	1139	137.02	1.73
	13	2	100	13	17800	654	138.57	1.74
	14	3	100	13	17800	573	137.53	1.74
	15	4	100	13	17800	480	138.01	1.74
D	16	1	400	13	17800	30458	678.68	1.71
	17	2	400	13	17800	28533	667.76	1.69
	18	3	400	13	17800	28522	664.28	1.68
E	19	1	200	13	17800	5339	320.51	1.69
	20	2	200	13	17800	4631	319.65	1.69
	21	3	200	13	17800	4250	324.86	1.69
F	22	1	400	13	17800	28035	664.45	1.69
	23	2	400	13	17800	27582	662.97	1.68
G	24	1	200	13	17800	5382	319.48	1.69
	25	2	200	13	17800	4250	319.04	1.68
	26	3	200	13	17800	4118	322.50	1.69
	27	4	200	13	17800	3977	324.54	1.69
	28	5	200	13	17800	3920	323.87	1.69
	29	6	200	13	17800	3840	324.28	1.69
	30	7	200	13	17800	3840	325.90	1.69
	31	8	200	13	17800	3840	325.64	1.69
	32	9	200	13	17800	3790	326.44	1.69
H	33	1	400	13	17800	27725	669.33	1.69
	34	2	400	13	17800	28246	662.90	1.68
I	35	1	200	13	17800	5205	322.23	1.68
	36	2	200	13	17800	4646	319.70	1.68
	37	3	200	13	17800	4443	319.69	1.68
	38	4	200	13	17800	4185	323.30	1.69
	39	5	200	13	17800	4030	322.48	1.68
	40	6	200	13	17800	3970	323.60	1.69
	41	7	200	13	17800	3917	321.09	1.69
	42	8	200	13	17800	3889	321.48	1.69
J	43	1	50	13	17800	61	43.98	1.69
	44	2	50	13	17800	120	38.11	1.46
	45	3	50	13	17800	174	41.03	1.65
	46	4	50	13	17800	223	42.76	1.67
	47	5	50	13	17800	122	40.27	1.66
	48	6	50	13	17800	149	41.89	1.64
	49	7	50	13	17800	103	39.94	1.66
	50	8	50	13	17800	100	42.10	1.60

Appendix A, Table 2: Test Protocol and Results of Experiment-1, Device: LRB1300

LRB1300			Input Data			Output Data		
Test	Cyl # (total)	Cycle	Disp. Amp. (mm)	Max Vel. (mm/sec)	Ver. load (kN)	EDC (kN-mm)	Fmax (kN)	Kra (kN/mm)
A	1	1	50	13	17800	53793	418.9	2.74
	2	2	50	13	17800	55408	424.8	4.11
	3	3	50	13	17800	53594	407.7	4.03
	4	4	50	13	17800	52713	401.5	4.02
	5	5	50	13	17800	52125	397.9	4.00
	6	6	50	13	17800	51912	391.3	3.95
	7	7	50	13	17800	51813	389.7	3.92
	8	8	50	13	17800	51493	390.5	3.94
	9	9	50	13	17800	51183	384.9	3.91
B	10	1	300	13	17800	372871	780.1	1.85
	11	2	300	13	17800	355692	760.7	1.82
C	12	1	100	13	17800	105279	407.6	2.05
	13	2	100	13	17800	105710	411.4	2.10
	14	3	100	13	17800	105054	408.6	2.09
	15	4	100	13	17800	104676	409.8	2.08
D	16	1	400	13	17800	468008	917.9	1.80
	17	2	400	13	17800	458438	903.8	1.79
	18	3	400	13	17800	453267	900.7	1.78
E	19	1	200	13	17800	212766	569.2	1.79
	20	2	200	13	17800	210630	567.4	1.80
	21	3	200	13	17800	210708	568.1	1.80
F	22	1	400	13	17800	445703	903.3	1.79
	23	2	400	13	17800	442536	895.1	1.79
G	24	1	200	13	17800	209100	568.9	1.80
	25	2	200	13	17800	208110	567.0	1.81
	26	3	200	13	17800	207739	567.9	1.81
	27	4	200	13	17800	207362	567.1	1.81
	28	5	200	13	17800	207267	565.5	1.82
	29	6	200	13	17800	207087	565.8	1.82
	30	7	200	13	17800	206744	565.8	1.82
	31	8	200	13	17800	206621	565.3	1.83
	32	9	200	13	17800	205899	566.6	1.83
H	33	1	400	13	17800	435818	900.0	1.80
	34	2	400	13	17800	434592	893.9	1.80
I	35	1	200	13	17800	205714	565.3	1.82
	36	2	200	13	17800	204516	562.7	1.82
	37	3	200	13	17800	203856	563.9	1.82
	38	4	200	13	17800	204126	563.9	1.83
	39	5	200	13	17800	203544	564.1	1.83
	40	6	200	13	17800	203518	564.9	1.84
	41	7	200	13	17800	203323	564.7	1.84
	42	8	200	13	17800	202994	564.6	1.84
J	43	1	50	13	17800	43904	304.7	3.11
	44	2	50	13	17800	44044	314.3	3.29
	45	3	50	13	17800	43838	309.5	3.29
	46	4	50	13	17800	44029	310.9	3.32
	47	5	50	13	17800	43941	309.3	3.32
	48	6	50	13	17800	44049	308.6	3.32
	49	7	50	13	17800	43757	306.5	3.33
	50	8	50	13	17800	43705	309.4	3.38

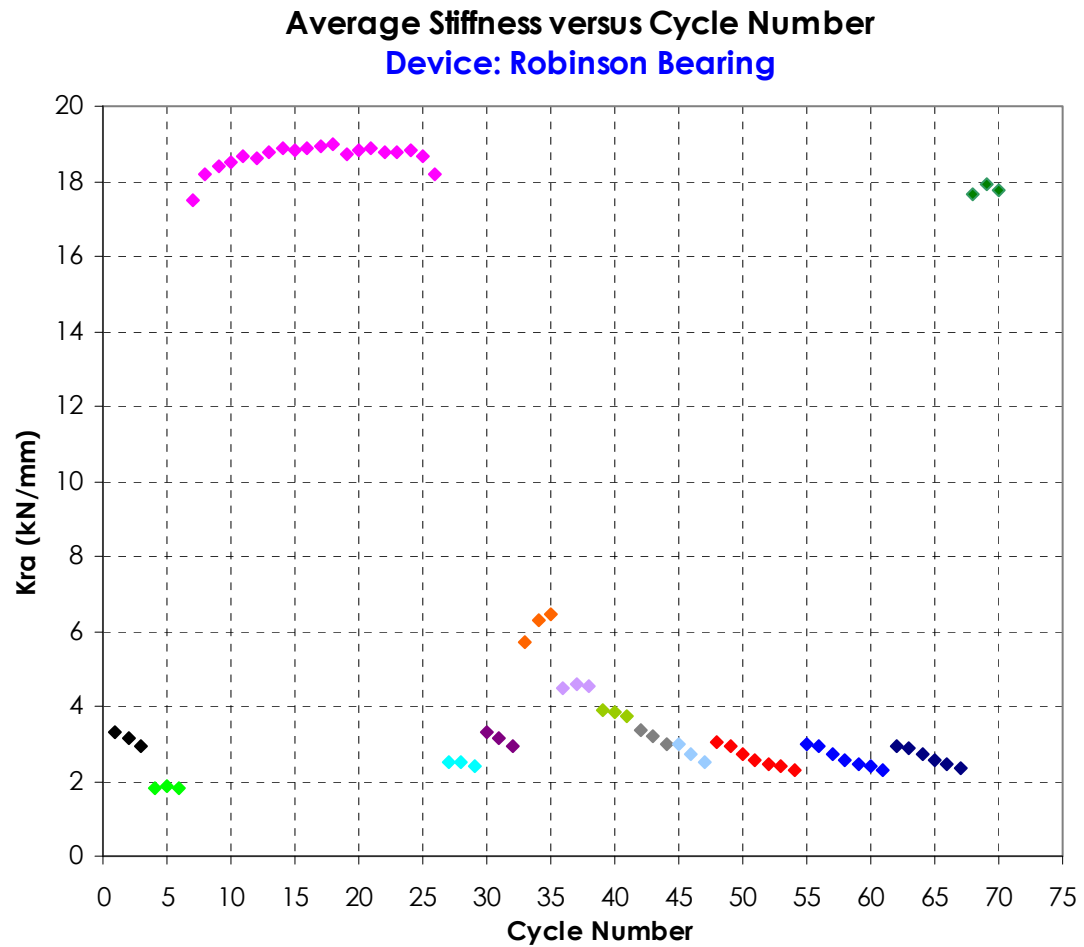
Appendix A, Table 3, Test Protocol and Results of Experiment-1, Device: LRB700

LRB700			Input Data			Output Data		
Test	Cyl # (total)	Cycle	Disp. Amp. (mm)	Max Vel. (mm/sec)	Ver. load (kN)	EDC (kN-mm)	Fmax (kN)	Kra (kN/mm)
A	1	1	50	13	5204	19150	182.8	1290
	2	2	50	13	5204	19368	169.8	1542
	3	3	50	13	5204	18740	165.2	1540
	4	4	50	13	5204	18570	159.5	1478
	5	5	50	13	5204	18397	158.5	1458
	6	6	50	13	5204	18363	157.0	1435
	7	7	50	13	5204	18279	156.6	1415
	8	8	50	13	5204	18229	156.0	1400
	9	9	50	13	5204	18139	154.7	1391
B	10	1	300	13	5204	136379	350.8	854
	11	2	300	13	5204	130117	336.4	824
C	12	1	100	13	5204	37426	185.4	895
	13	2	100	13	5204	37454	186.4	901
	14	3	100	13	5204	37162	186.1	902
	15	4	100	13	5204	37033	184.1	908
D	16	1	400	13	5204	185043	390.5	752
	17	2	400	13	5204	180895	370.6	736
	18	3	400	13	5204	179247	367.9	731
E	19	1	200	13	5204	78216	256.6	834
	20	2	200	13	5204	77507	256.5	833
	21	3	200	13	5204	77441	254.7	834
F	22	1	400	13	5204	178003	369.8	736
	23	2	400	13	5204	176232	363.2	731
G	24	1	200	13	5204	77494	257.5	834
	25	2	200	13	5204	76783	254.9	830
	26	3	200	13	5204	76717	254.3	832
	27	4	200	13	5204	76429	254.1	835
	28	5	200	13	5204	76541	253.6	834
	29	6	200	13	5204	76375	255.6	836
	30	7	200	13	5204	76631	256.6	836
	31	8	200	13	5204	76495	255.6	834
	32	9	200	13	5204	76323	255.2	836
H	33	1	400	13	5204	175075	371.2	743
	34	2	400	13	5204	173947	362.0	735
I	35	1	200	13	5204	76507	255.9	831
	36	2	200	13	5204	75823	253.9	832
	37	3	200	13	5204	75671	254.7	832
	38	4	200	13	5204	75462	255.8	836
	39	5	200	13	5204	75340	254.6	835
	40	6	200	13	5204	75172	256.4	837
	41	7	200	13	5204	74903	254.6	835
	42	8	200	13	5204	74858	255.3	838
J	43	1	50	13	5204	16170	131.8	1068
	44	2	50	13	5204	16094	130.1	1126
	45	3	50	13	5204	16099	132.4	1116
	46	4	50	13	5204	16077	133.7	1139
	47	5	50	13	5204	16163	136.5	1135
	48	6	50	13	5204	16153	131.7	1129
	49	7	50	13	5204	16182	132.3	1131
	50	8	50	13	5204	16122	133.1	1148

Appendix A, Table 4: Test Protocol and Results of Experiment-1, Device: Robinson

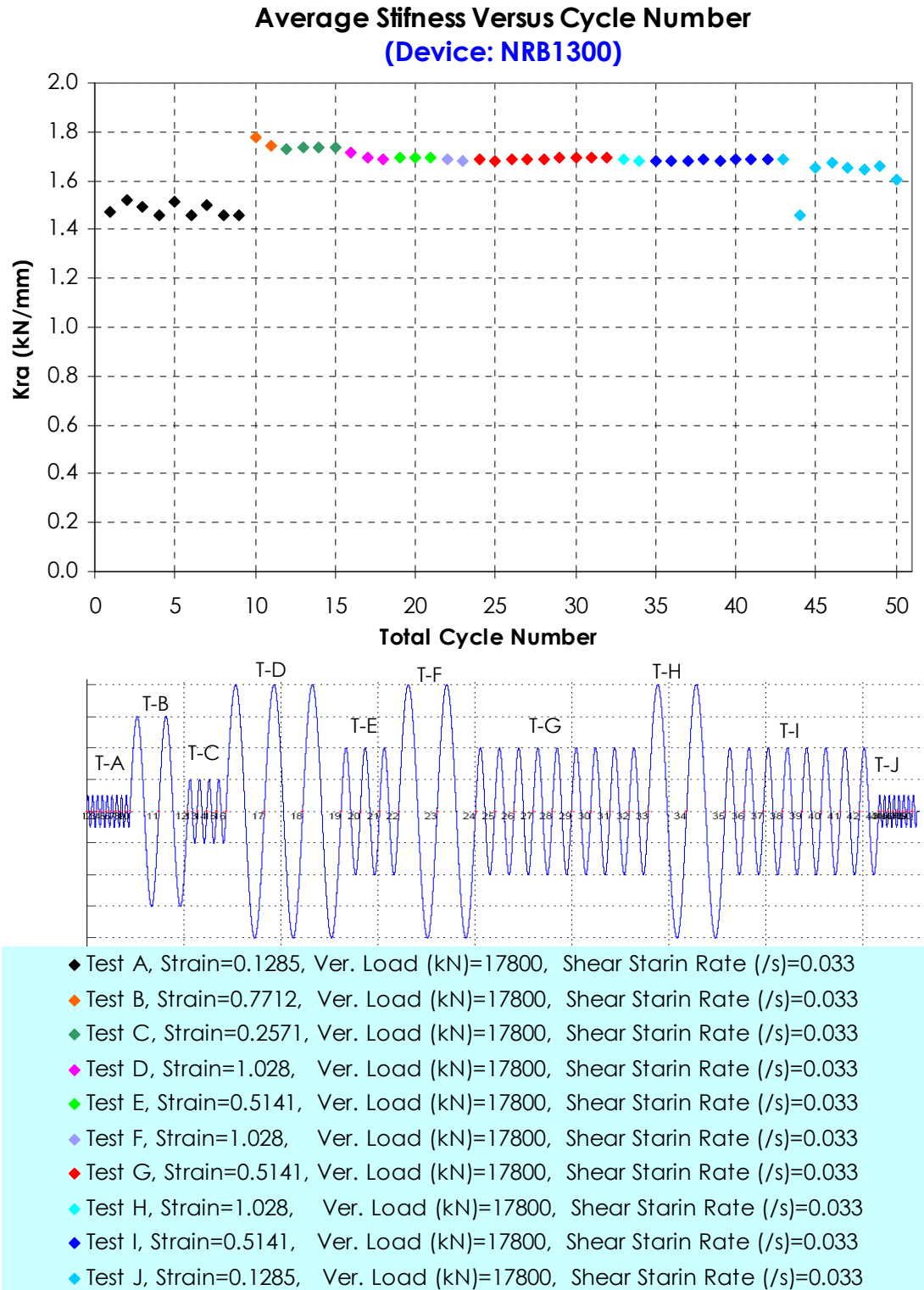
Robinson 970			Input Data			Output Data		
Test	Cyl # (total)	Cycle	Disp. Amp. (mm)	Max Vel. (mm/sec)	Ver. load (kN)	EDC (kN-mm)	Fmax (kN)	Kra (kN/mm)
1	1	1	142.92	345	7882	218457	877.77	3.33
	2	2	142.82	345	7882	202086	834.07	3.17
	3	3	142.77	345	7882	188470	772.65	2.95
2	4	1	150.09	0.65	9617	127789	576.06	1.83
	5	2	150.09	0.65	9617	130423	571.44	1.85
	6	3	150.06	0.65	9617	129554	571.06	1.84
3a	7	1	5.85	15	9617	2434	257.50	17.48
	8	2	5.84	15	9617	2485	262.55	18.17
	9	3	5.82	15	9617	2493	263.48	18.40
	10	4	5.81	15	9617	2510	265.69	18.51
	11	5	5.79	15	9617	2492	270.74	18.65
	12	6	5.80	15	9617	2522	264.57	18.63
	13	7	5.79	15	9617	2517	263.52	18.77
	14	8	5.79	15	9617	2506	267.45	18.86
	15	9	5.81	15	9617	2534	267.97	18.80
	16	10	5.82	15	9617	2524	268.47	18.89
	17	11	5.82	15	9617	2531	266.67	18.91
	18	12	5.83	15	9617	2541	265.09	19.00
	19	13	5.86	15	9617	2540	263.14	18.70
	20	14	5.86	15	9617	2534	265.71	18.83
	21	15	5.86	15	9617	2540	264.24	18.86
	22	16	5.86	15	9617	2549	263.96	18.77
	23	17	5.86	15	9617	2550	262.18	18.76
	24	18	5.84	15	9617	2536	261.45	18.81
	25	19	5.84	15	9617	2546	261.33	18.66
	26	20	5.84	15	9617	2505	261.58	18.19
4	27	1	142.49	13	7882	164274	697.30	2.52
	28	2	142.55	13	7882	162059	643.24	2.50
	29	3	142.59	13	7882	157370	624.85	2.41
5a	30	1	143.15	345	7882	213577	878.45	3.31
	31	2	143.05	345	7882	197780	817.76	3.12
	32	3	142.79	345	7882	185326	757.63	2.92
5b	33	1	35.82	88	7882	27562	390.56	5.69
	34	2	35.78	88	7882	28278	415.87	6.31
	35	3	35.73	88	7882	28166	422.07	6.46
5c	36	1	71.66	175	7882	73977	580.78	4.48
	37	2	71.60	175	7882	73051	587.27	4.61
	38	3	71.59	175	7882	70843	580.06	4.53
5d	39	1	107.42	260	7882	134481	738.98	3.87
	40	2	107.36	260	7882	128837	729.63	3.85
	41	3	107.33	260	7882	123473	705.85	3.71
5e	42	1	143.24	345	7882	210740	878.01	3.34
	43	2	143.17	345	7882	196738	829.91	3.19
	44	3	142.99	345	7882	185123	768.87	2.98
5f	45	1	178.96	433	7882	296644	992.79	2.97
	46	2	178.82	433	7882	267309	888.08	2.72
	47	3	178.62	433	7882	245981	812.22	2.52

Continued Table								
Test	Cyl # (total)	Cycle	Disp. Amp. (mm)	Max Vel. (mm/sec)	Ver. load (kN)	EDC (kN-mm)	Fmax (kN)	Kra (kN/mm)
6a	48	1	143.38	345	7882	226738	1036.00	3.04
	49	2	143.33	345	7882	209466	980.90	2.93
	50	3	143.26	345	7882	194756	912.40	2.73
	51	4	142.98	345	7882	184119	862.10	2.58
	52	5	142.85	345	7882	175361	825.70	2.47
	53	6	142.81	345	7882	168536	796.00	2.38
	54	7	142.72	345	7882	162233	771.50	2.31
6b	55	1	143.30	345	7882	225395	1017.50	2.99
	56	2	143.24	345	7882	209690	972.80	2.91
	57	3	143.19	345	7882	194298	905.50	2.72
	58	4	142.93	345	7882	182746	852.70	2.57
	59	5	142.84	345	7882	174412	813.90	2.46
	60	6	142.82	345	7882	166643	783.40	2.37
	61	7	142.69	345	7882	160171	758.60	2.30
6c	62	1	143.21	345	7882	222473	1001.60	2.94
	63	2	143.15	345	7882	207729	960.90	2.87
	64	3	143.05	345	7882	191724	894.80	2.70
	65	4	142.82	345	7882	180564	842.90	2.55
	66	5	142.75	345	7882	171707	804.80	2.45
	67	6	142.73	345	7882	164454	774.60	2.36
7a	68	1	5.88	15	9617	2184	194.27	17.67
	69	2	5.82	15	9617	2225	197.19	17.92
	70	3	5.78	15	9617	2202	203.68	17.78

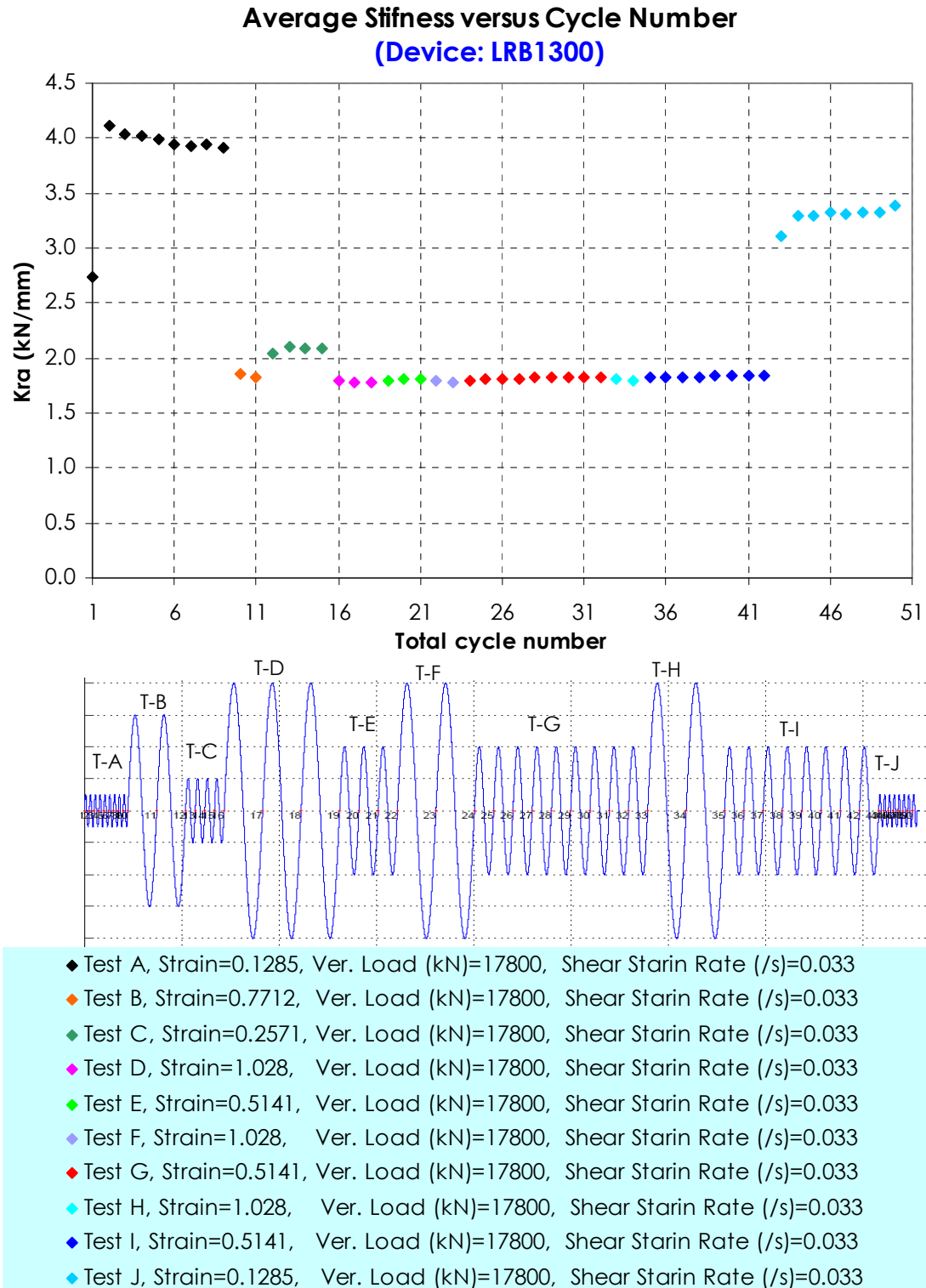


◆ Test 1, Shear Strain= 0.371,	T(sec)=2.6, Shear Strain Rate (/s)=0.9
◆ Test 2, Shear Strain= 0.390,	T(sec)=1180, Shear Strain Rate (/s)=0.0017
◆ Test 3a, Shear Strain= 0.0152,	T(sec)=2.6, Shear Strain Rate (/s)=0.039
◆ Test 4, Shear Strain= 0.371,	T(sec)=70.25, Shear Strain Rate (/s)=0.039
◆ Test 5a, Shear Strain= 0.371,	T(sec)=2.6, Shear Strain Rate (/s)=0.9
◆ Test 5b, Shear Strain= 0.0935,	T(sec)=2.6, Shear Strain Rate (/s)=0.23
◆ Test 5c, Shear Strain= 0.1870,	T(sec)=2.6, Shear Strain Rate (/s)=0.45
◆ Test 5d, Shear Strain= 0.278,	T(sec)=2.6, Shear Strain Rate (/s)=0.675
◆ Test 5e, Shear Strain= 0.371,	T(sec)=2.6, Shear Strain Rate (/s)=0.9
◆ Test 5f, Shear Strain= 0.465,	T(sec)=2.6, Shear Strain Rate (/s)=1.12
◆ Test 6a, Shear Strain= 0.371,	T(sec)=2.6, Shear Strain Rate (/s)=0.9
◆ Test 6b, Shear Strain= 0.371,	T(sec)=2.6, Shear Strain Rate (/s)=0.9
◆ Test 6c, Shear Strain= 0.371,	T(sec)=2.6, Shear Strain Rate (/s)=0.9
◆ Test 7a, Shear Strain= 0.0152,	T(sec)=2.6, Shear Strain Rate (/s)=0.039

Appendix B, Figure 1: Average stiffness at each cycle, Robinson bearing

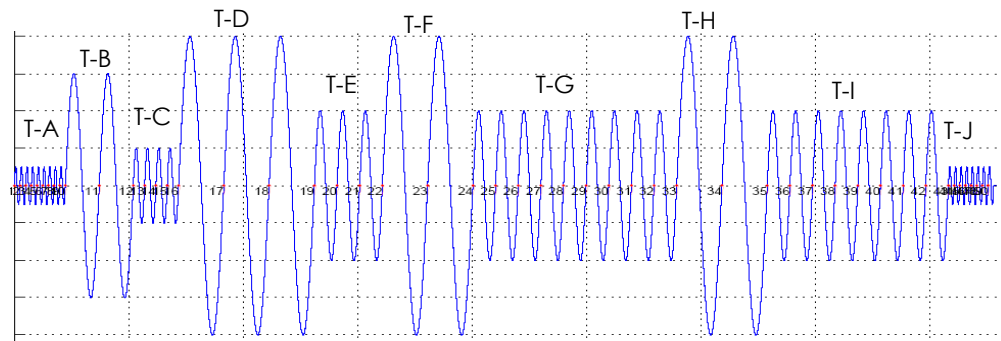
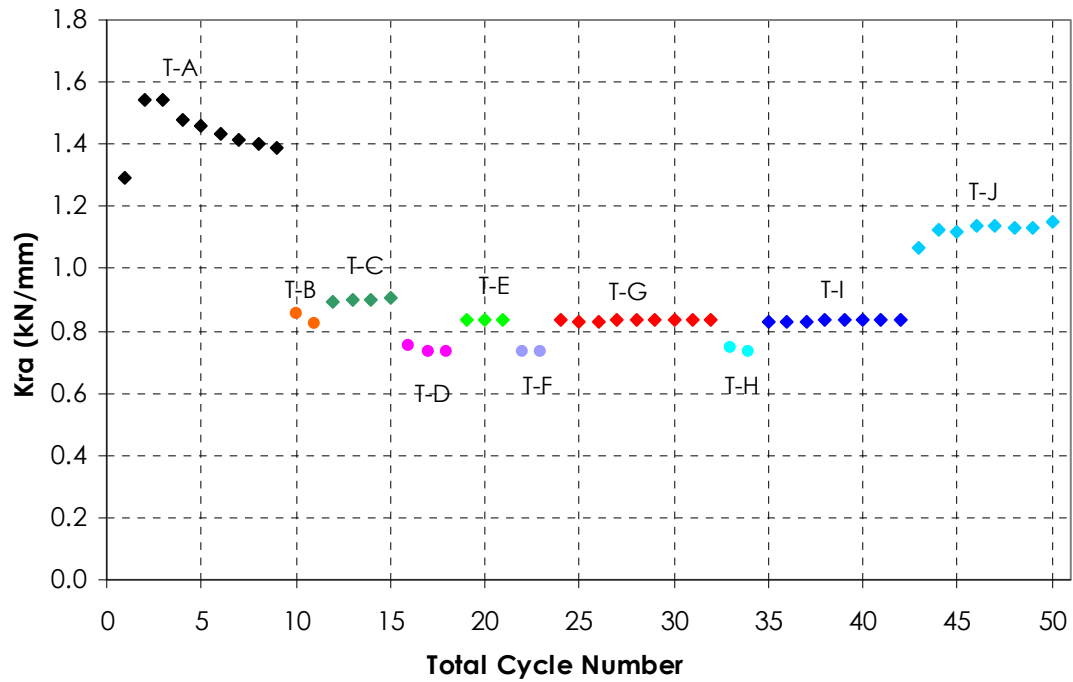


Appendix B, Figure 2: Average stiffness at each cycle, NRB1300



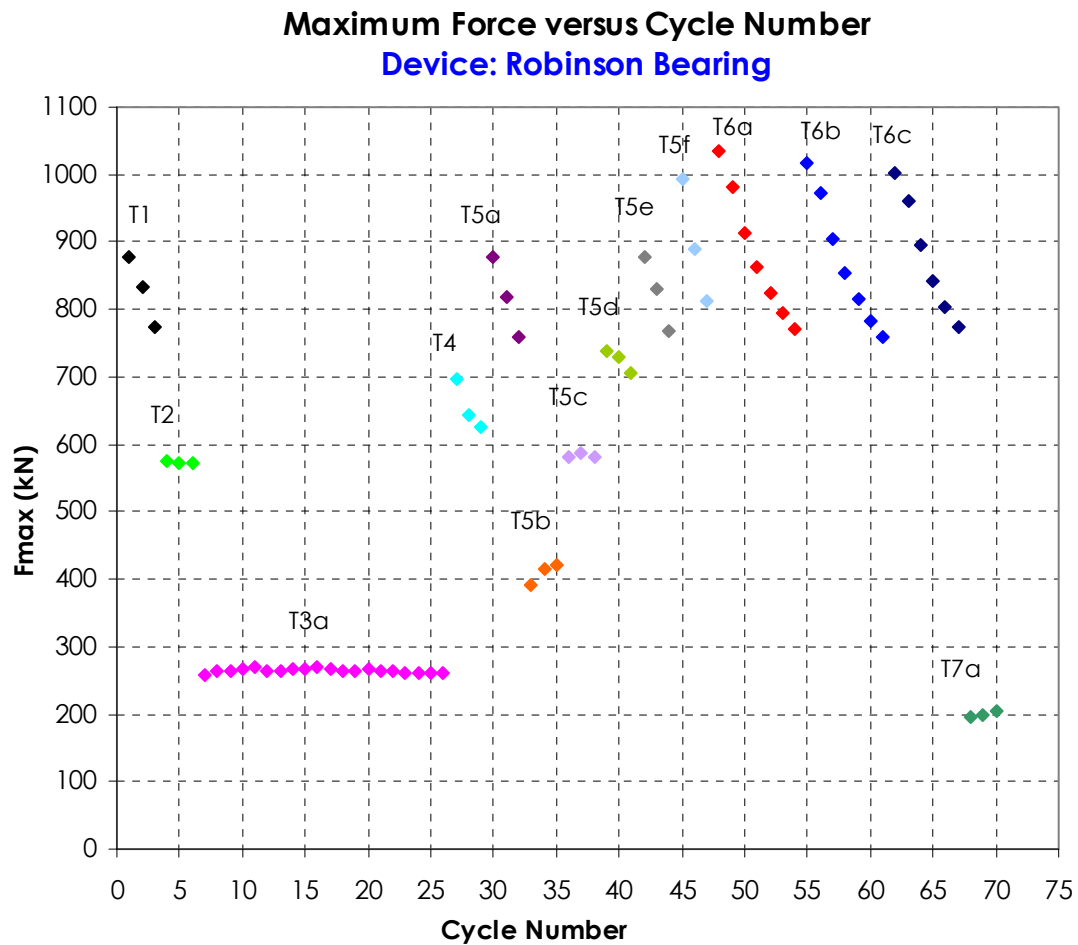
Appendix B, Figure 3: Average stiffness at each cycle, LRB1300

Average Stiffness versus Cycle Number
(Device: LRB700)



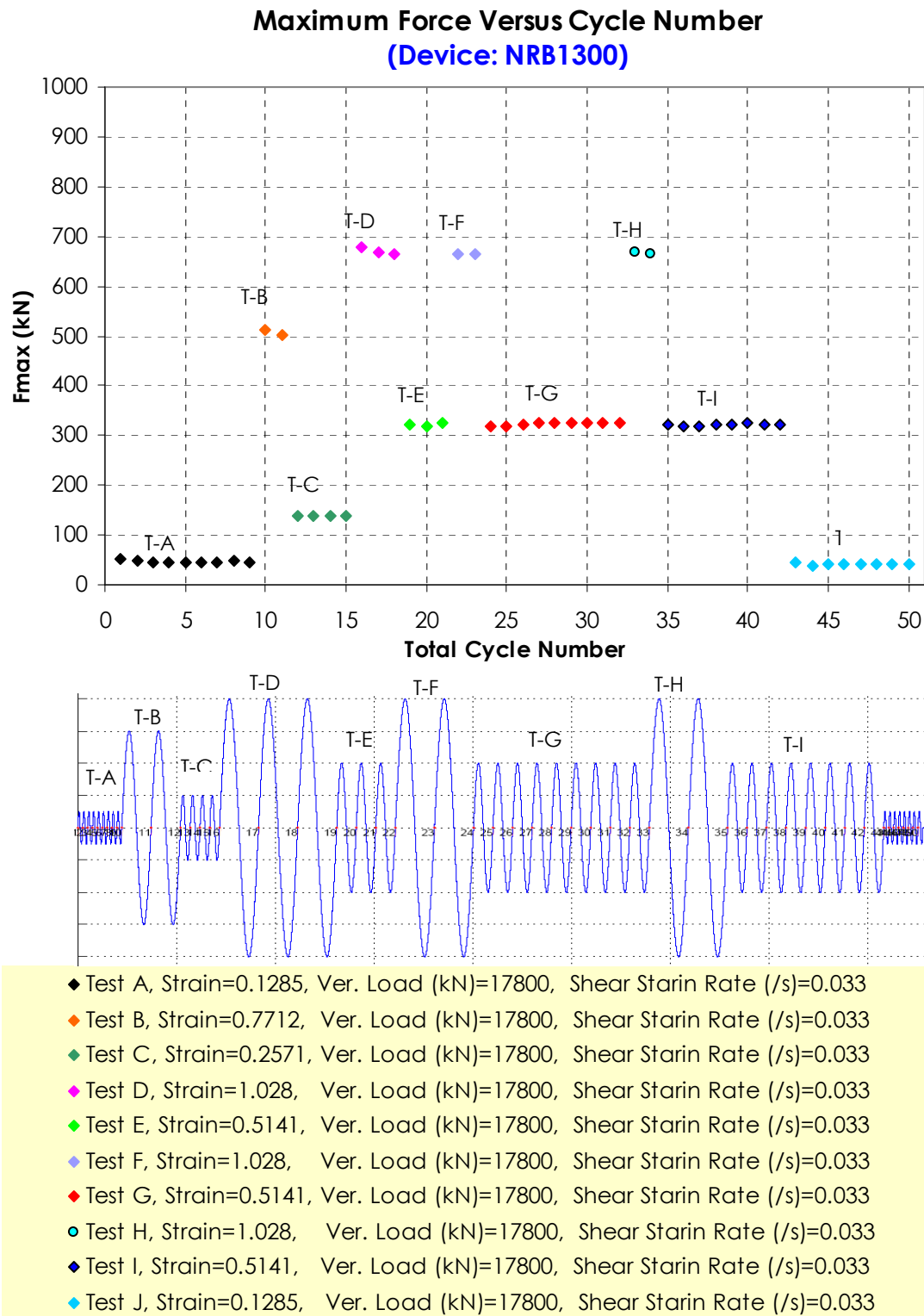
◆ Test A, Shear Strain=0.2164,	Ver. Load (kN)=5204,	Shear Strain Rate (/s)=0.056
● Test B, Shear Strain=1.3,	Ver. Load (kN)=5204,	Shear Strain Rate (/s)=0.056
◆ Test C, Shear Strain=0.433,	Ver. Load (kN)=5204,	Shear Strain Rate (/s)=0.056
● Test D, Shear Strain=1.7316	Ver. Load (kN)=5204,	Shear Strain Rate (/s)=0.056
◆ Test E, Shear Strain=0.8658,	Ver. Load (kN)=5204,	Shear Strain Rate (/s)=0.056
● Test F, Shear Strain=1.7316,	Ver. Load (kN)=5204,	Shear Strain Rate (/s)=0.056
◆ Test G, Shear Strain=0.8658,	Ver. Load (kN)=5204,	Shear Strain Rate (/s)=0.056
● Test H, Shear Strain=1.7316,	Ver. Load (kN)=5204,	Shear Strain Rate (/s)=0.056
◆ Test I, Shear Strain=0.8658,	Ver. Load (kN)=5204,	Shear Strain Rate (/s)=0.056
● Test J, Shear Strain=0.2164,	Ver. Load (kN)=5204,	Shear Strain Rate (/s)=0.056

Appendix B, Figure 4: Average stiffness at each cycle, LRB700

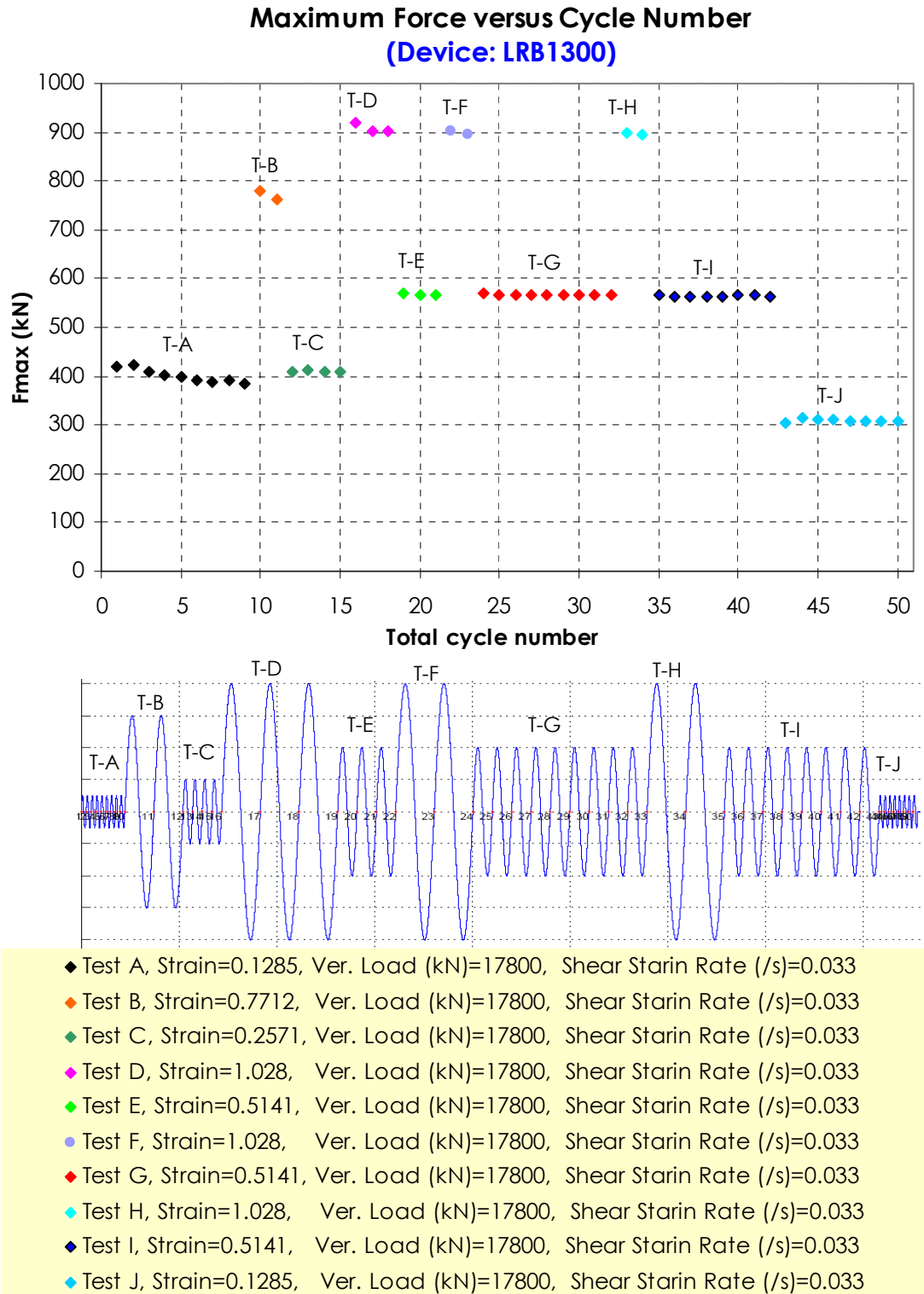


- ◆ Test 1, Shear Strain= 0.371, T(sec)=2.6, Shear Strain Rate (/s)=0.9
- ◆ Test 2, Shear Strain= 0.390, T(sec)=1180, Shear Strain Rate (/s)=0.0017
- ◆ Test 3a, Shear Strain= 0.0152, T(sec)=2.6, Shear Strain Rate (/s)=0.039
- ◆ Test 4, Shear Strain= 0.371, T(sec)=70.25, Shear Strain Rate (/s)=0.039
- ◆ Test 5a, Shear Strain= 0.371, T(sec)=2.6, Shear Strain Rate (/s)=0.9
- ◆ Test 5b, Shear Strain= 0.0935, T(sec)=2.6, Shear Strain Rate (/s)=0.23
- ◆ Test 5c, Shear Strain= 0.1870, T(sec)=2.6, Shear Strain Rate (/s)=0.45
- ◆ Test 5d, Shear Strain= 0.278, T(sec)=2.6, Shear Strain Rate (/s)=0.675
- ◆ Test 5e, Shear Strain= 0.371, T(sec)=2.6, Shear Strain Rate (/s)=0.9
- ◆ Test 5f, Shear Strain= 0.465, T(sec)=2.6, Shear Strain Rate (/s)=1.12
- ◆ Test 6a, Shear Strain= 0.371, T(sec)=2.6, Shear Strain Rate (/s)=0.9
- ◆ Test 6b, Shear Strain= 0.371, T(sec)=2.6, Shear Strain Rate (/s)=0.9
- ◆ Test 6c, Shear Strain= 0.371, T(sec)=2.6, Shear Strain Rate (/s)=0.9
- ◆ Test 7a, Shear Strain= 0.0152, T(sec)=2.6, Shear Strain Rate (/s)=0.039

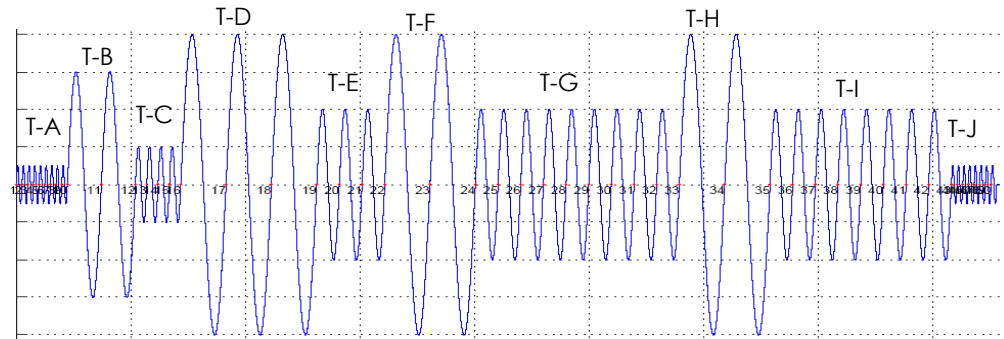
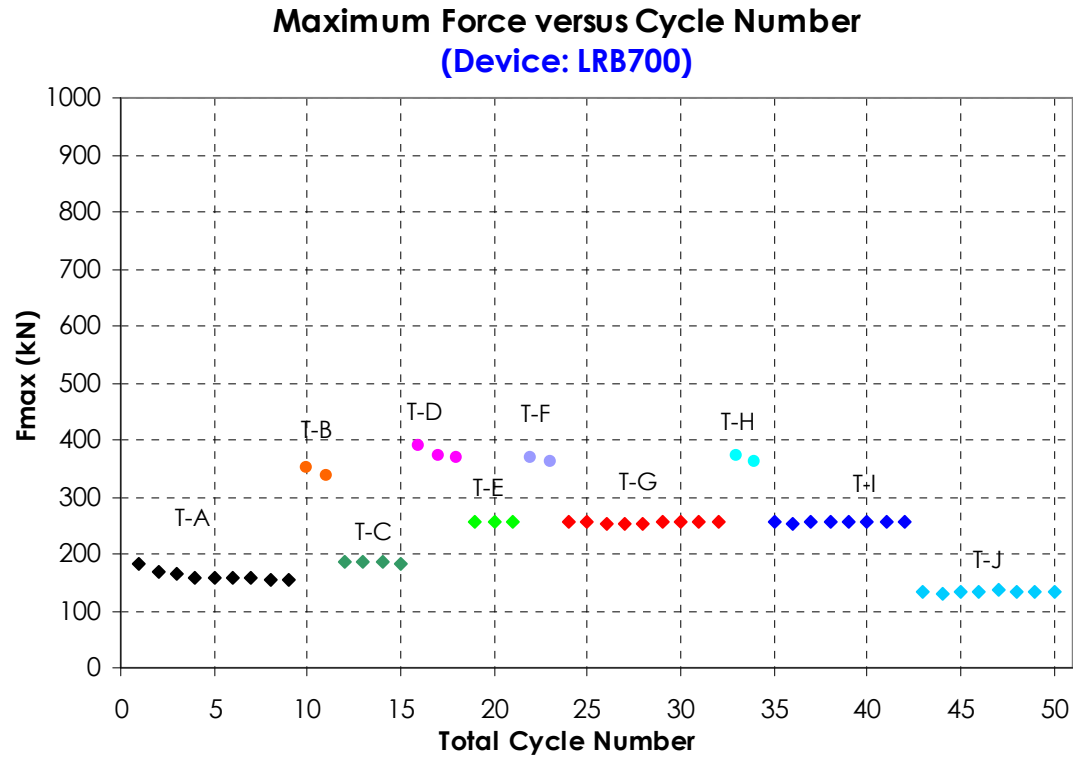
Appendix B, Figure 5: Maximum force at each hysteresis loop, Robinson bearing



Appendix B, Figure 6: Maximum force at each hysteresis loop, NRB1300

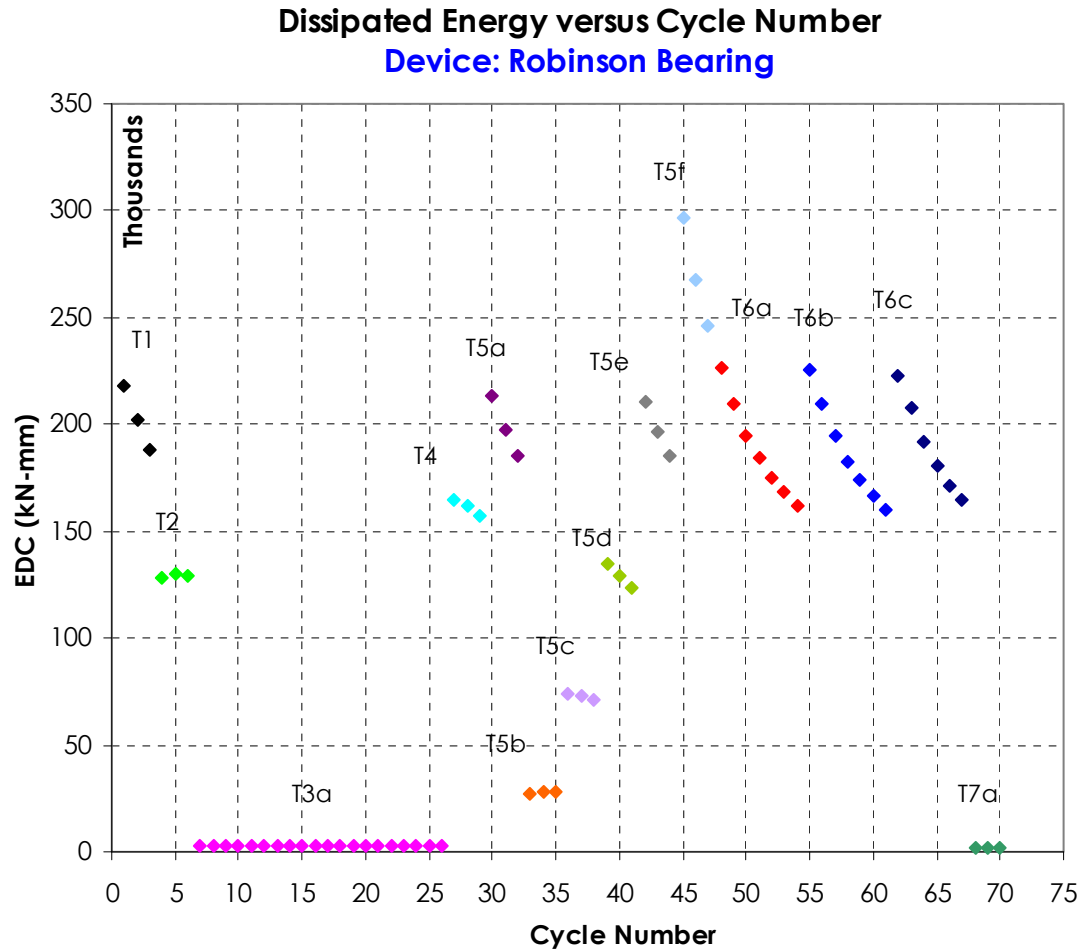


Appendix B, Figure 7: Maximum force at each hysteresis loop, LRB1300



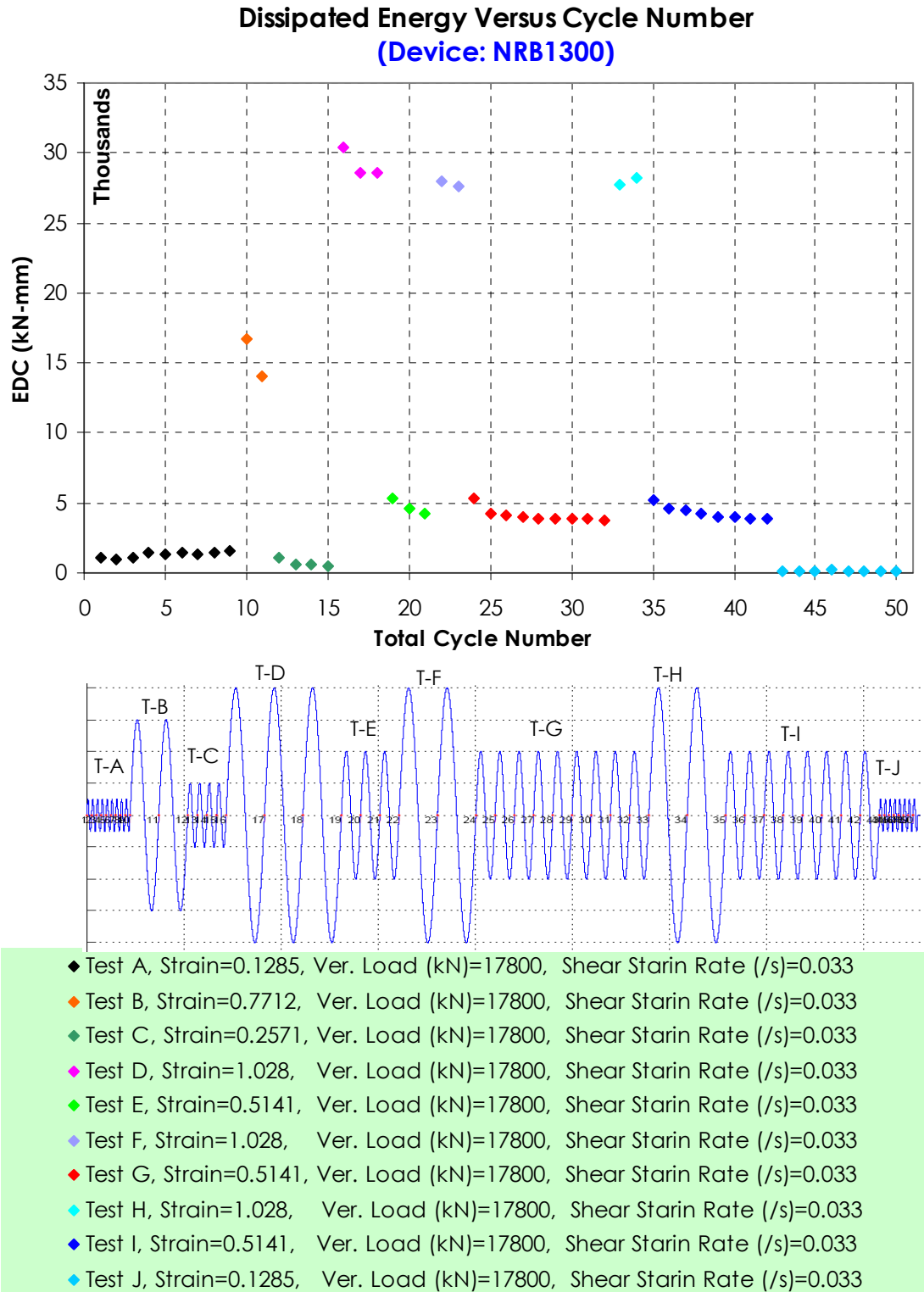
- | | | |
|--------------------------------|----------------------|------------------------------|
| ◆ Test A, Shear Strain=0.2164, | Ver. Load (kN)=5204, | Shear Strain Rate (/s)=0.056 |
| ● Test B, Shear Strain=1.3, | Ver. Load (kN)=5204, | Shear Strain Rate (/s)=0.056 |
| ◆ Test C, Shear Strain=0.433, | Ver. Load (kN)=5204, | Shear Strain Rate (/s)=0.056 |
| ● Test D, Shear Strain=1.7316 | Ver. Load (kN)=5204, | Shear Strain Rate (/s)=0.056 |
| ◆ Test E, Shear Strain=0.8658, | Ver. Load (kN)=5204, | Shear Strain Rate (/s)=0.056 |
| ● Test F, Shear Strain=1.7316, | Ver. Load (kN)=5204, | Shear Strain Rate (/s)=0.056 |
| ◆ Test G, Shear Strain=0.8658, | Ver. Load (kN)=5204, | Shear Strain Rate (/s)=0.056 |
| ● Test H, Shear Strain=1.7316, | Ver. Load (kN)=5204, | Shear Strain Rate (/s)=0.056 |
| ◆ Test I, Shear Strain=0.8658, | Ver. Load (kN)=5204, | Shear Strain Rate (/s)=0.056 |
| ● Test J, Shear Strain=0.2164, | Ver. Load (kN)=5204, | Shear Strain Rate (/s)=0.056 |

Appendix B, Figure 8: Maximum force at each hysteresis loop, LRB700

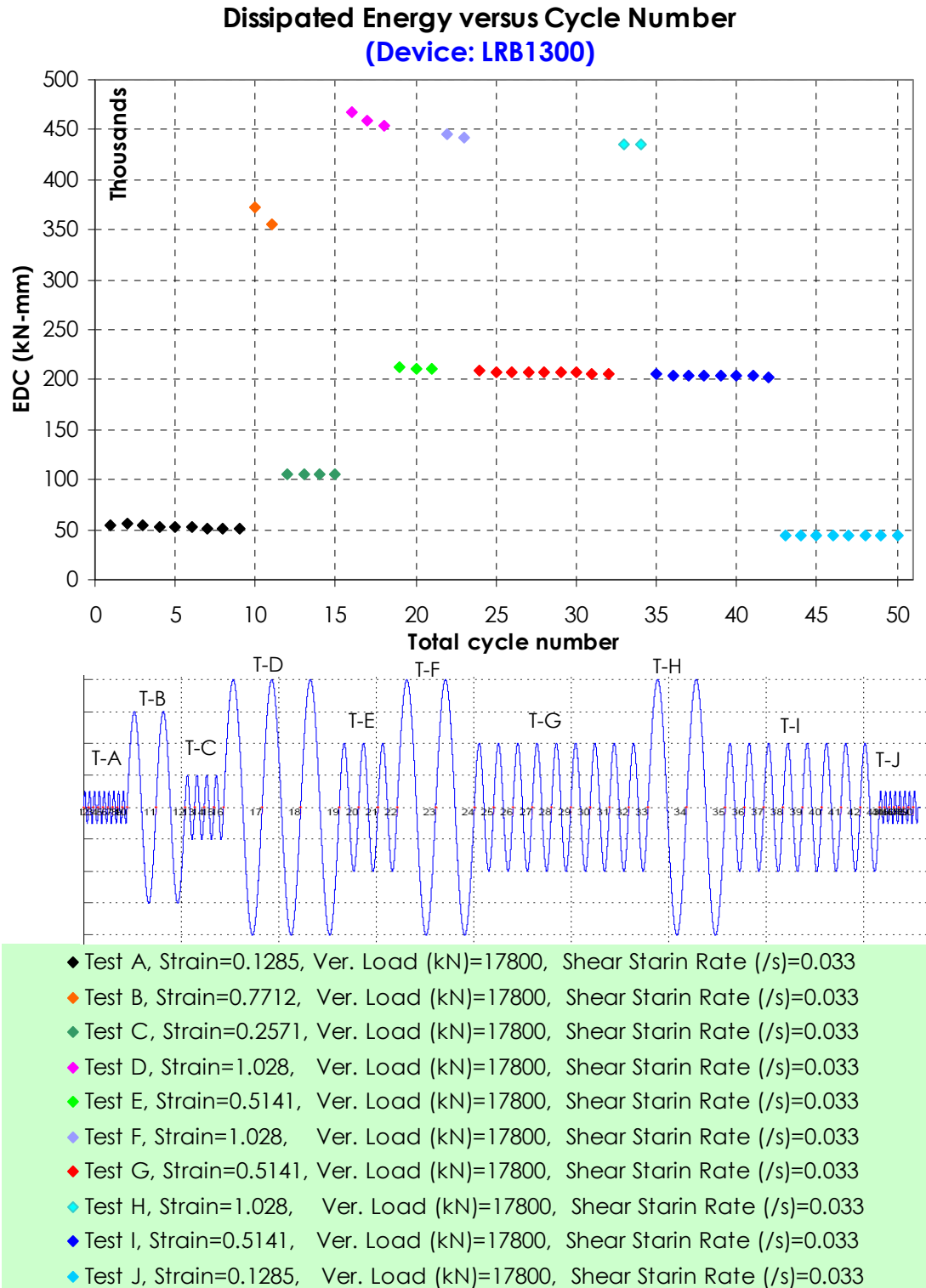


◆ Test 1, Shear Strain= 0.371,	T(sec)=2.6, Shear Strain Rate (/s)=0.9
◆ Test 2, Shear Strain= 0.390,	T(sec)=1180, Shear Strain Rate (/s)=0.0017
◆ Test 3a, Shear Strain= 0.0152,	T(sec)=2.6, Shear Strain Rate (/s)=0.039
◆ Test 4, Shear Strain= 0.371,	T(sec)=70.25, Shear Strain Rate (/s)=0.039
◆ Test 5a, Shear Strain= 0.371,	T(sec)=2.6, Shear Strain Rate (/s)=0.9
◆ Test 5b, Shear Strain= 0.0935,	T(sec)=2.6, Shear Strain Rate (/s)=0.23
◆ Test 5c, Shear Strain= 0.1870,	T(sec)=2.6, Shear Strain Rate (/s)=0.45
◆ Test 5d, Shear Strain= 0.278,	T(sec)=2.6, Shear Strain Rate (/s)=0.675
◆ Test 5e, Shear Strain= 0.371,	T(sec)=2.6, Shear Strain Rate (/s)=0.9
◆ Test 5f, Shear Strain= 0.465,	T(sec)=2.6, Shear Strain Rate (/s)=1.12
◆ Test 6a, Shear Strain= 0.371,	T(sec)=2.6, Shear Strain Rate (/s)=0.9
◆ Test 6b, Shear Strain= 0.371,	T(sec)=2.6, Shear Strain Rate (/s)=0.9
◆ Test 6c, Shear Strain= 0.371,	T(sec)=2.6, Shear Strain Rate (/s)=0.9
◆ Test 7a, Shear Strain= 0.0152,	T(sec)=2.6, Shear Strain Rate (/s)=0.039

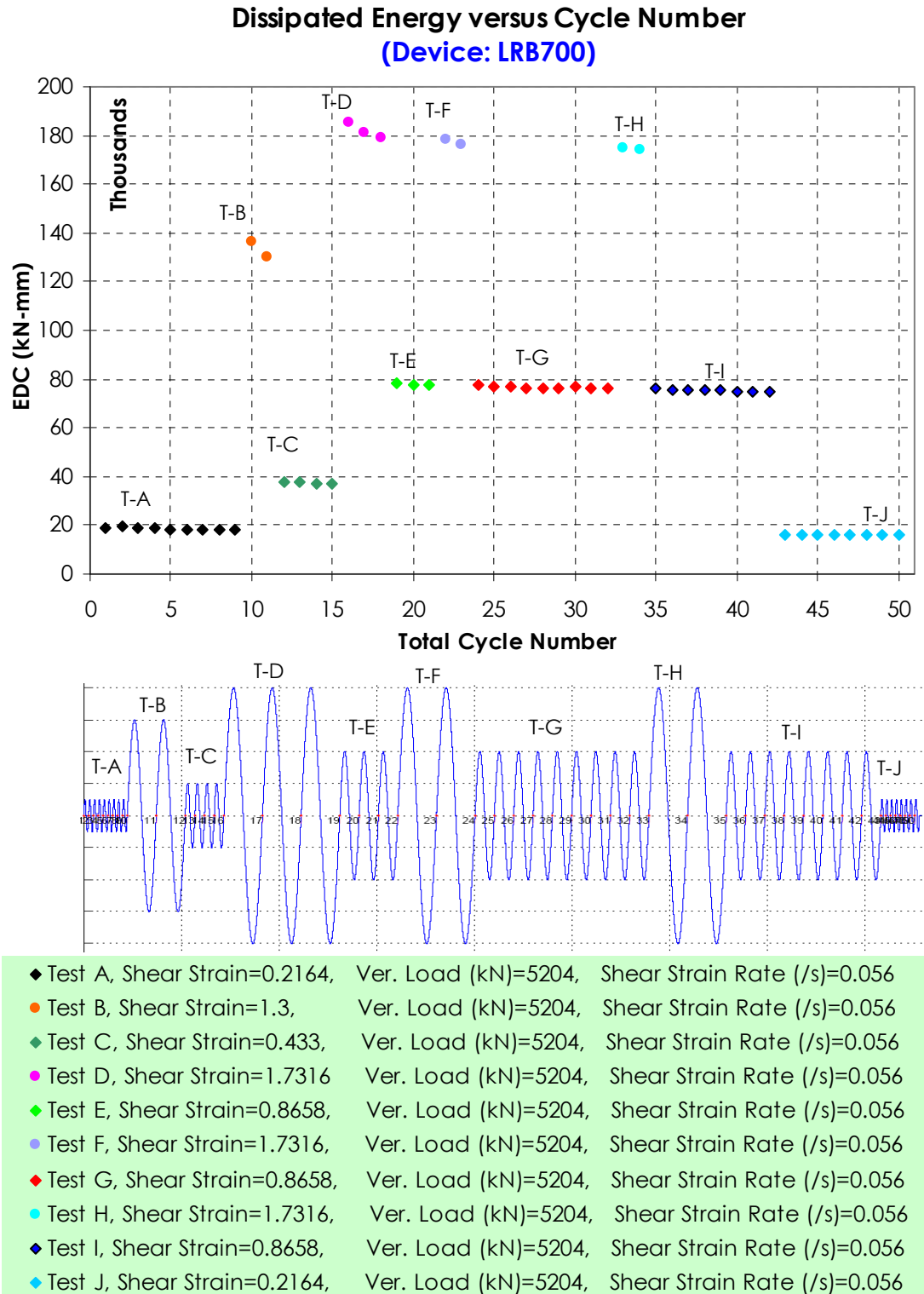
Appendix B, Figure 9: Energy dissipated per cycle, Robinson bearing



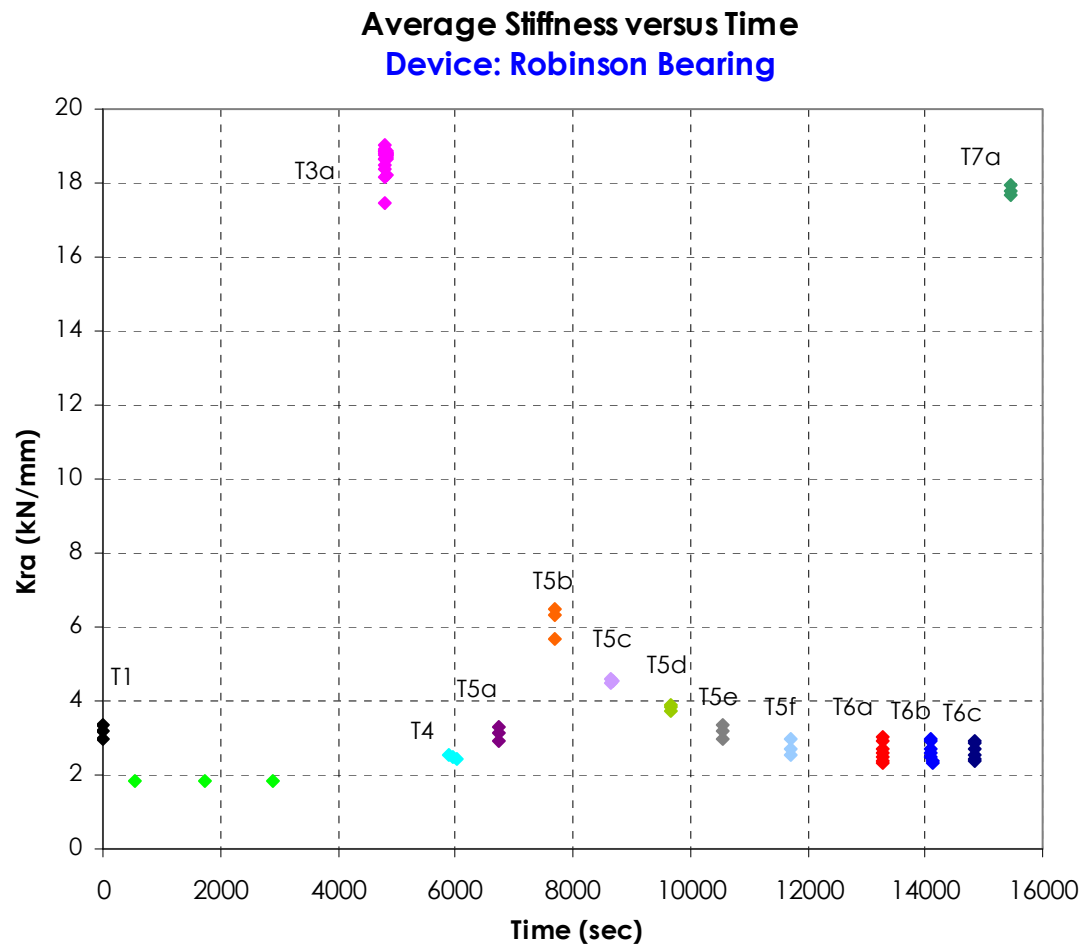
Appendix B, Figure 10: Energy dissipated per cycle, NRB1300



Appendix B, Figure 11: Energy dissipated per cycle, LRB1300

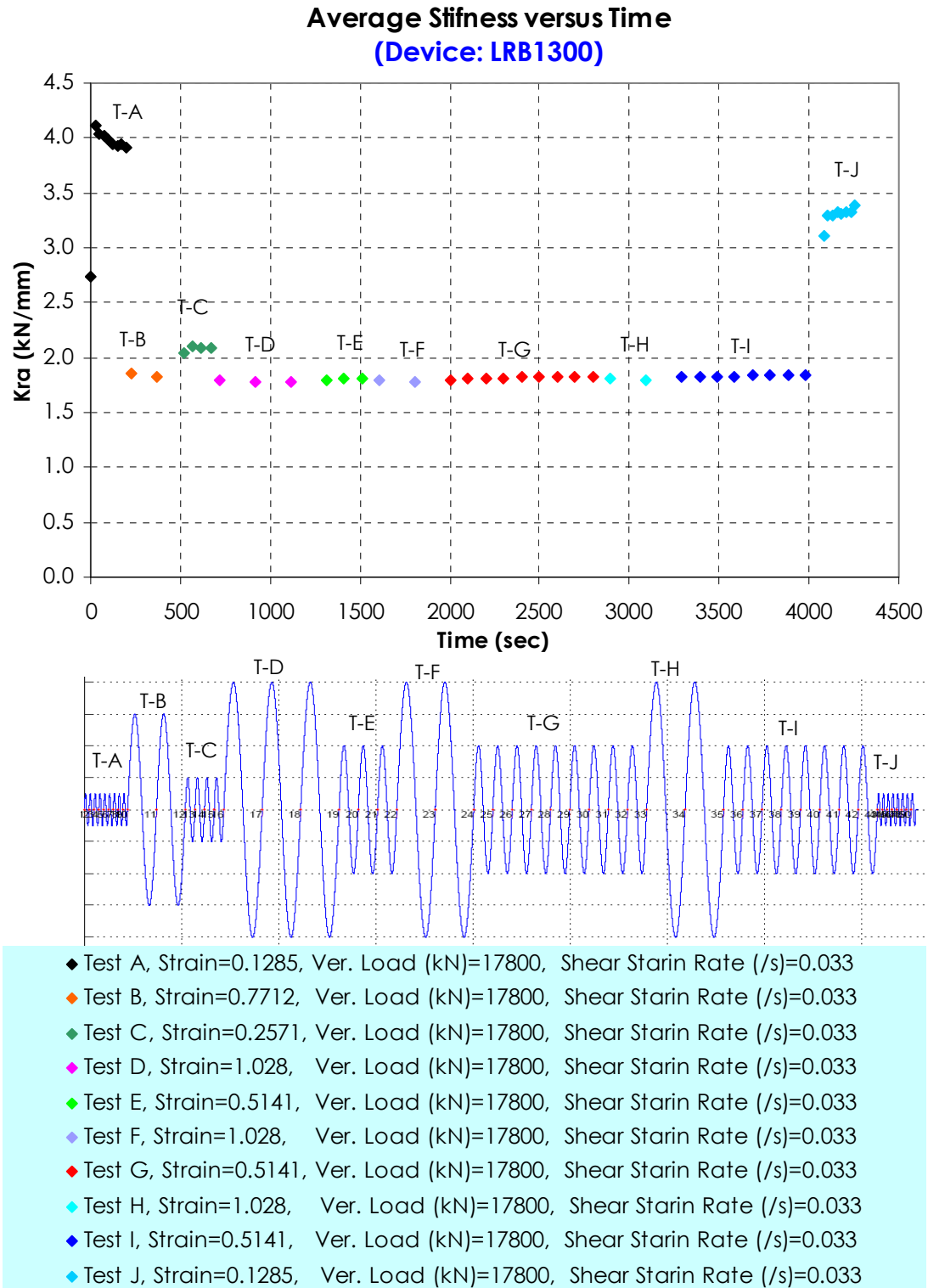


Appendix B, Figure 12: Energy dissipated per cycle, LRB700

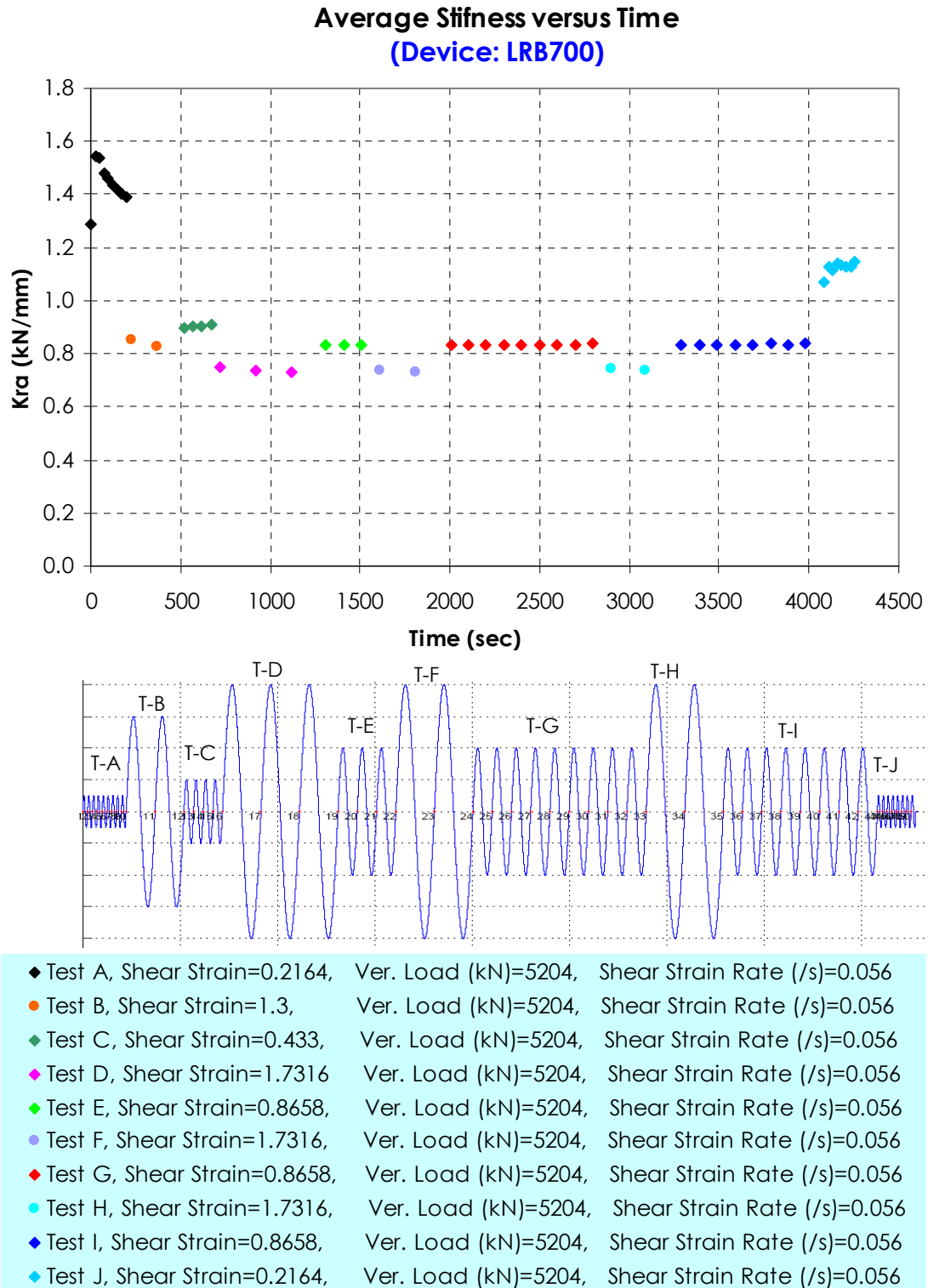


- ◆ Test 1, Shear Strain= 0.371, T(sec)=2.6, Shear Strain Rate (/s)=0.9
- ◆ Test 2, Shear Strain= 0.390, T(sec)=1180, Shear Strain Rate (/s)=0.0017
- ◆ Test 3a, Shear Strain= 0.0152, T(sec)=2.6, Shear Strain Rate (/s)=0.039
- ◆ Test 4, Shear Strain= 0.371, T(sec)=70.25, Shear Strain Rate (/s)=0.039
- ◆ Test 5a, Shear Strain= 0.371, T(sec)=2.6, Shear Strain Rate (/s)=0.9
- ◆ Test 5b, Shear Strain= 0.0935, T(sec)=2.6, Shear Strain Rate (/s)=0.23
- ◆ Test 5c, Shear Strain= 0.1870, T(sec)=2.6, Shear Strain Rate (/s)=0.45
- ◆ Test 5d, Shear Strain= 0.278, T(sec)=2.6, Shear Strain Rate (/s)=0.675
- ◆ Test 5e, Shear Strain= 0.371, T(sec)=2.6, Shear Strain Rate (/s)=0.9
- ◆ Test 5f, Shear Strain= 0.465, T(sec)=2.6, Shear Strain Rate (/s)=1.12
- ◆ Test 6a, Shear Strain= 0.371, T(sec)=2.6, Shear Strain Rate (/s)=0.9
- ◆ Test 6b, Shear Strain= 0.371, T(sec)=2.6, Shear Strain Rate (/s)=0.9
- ◆ Test 6c, Shear Strain= 0.371, T(sec)=2.6, Shear Strain Rate (/s)=0.9
- ◆ Test 7a, Shear Strain= 0.0152, T(sec)=2.6, Shear Strain Rate (/s)=0.039

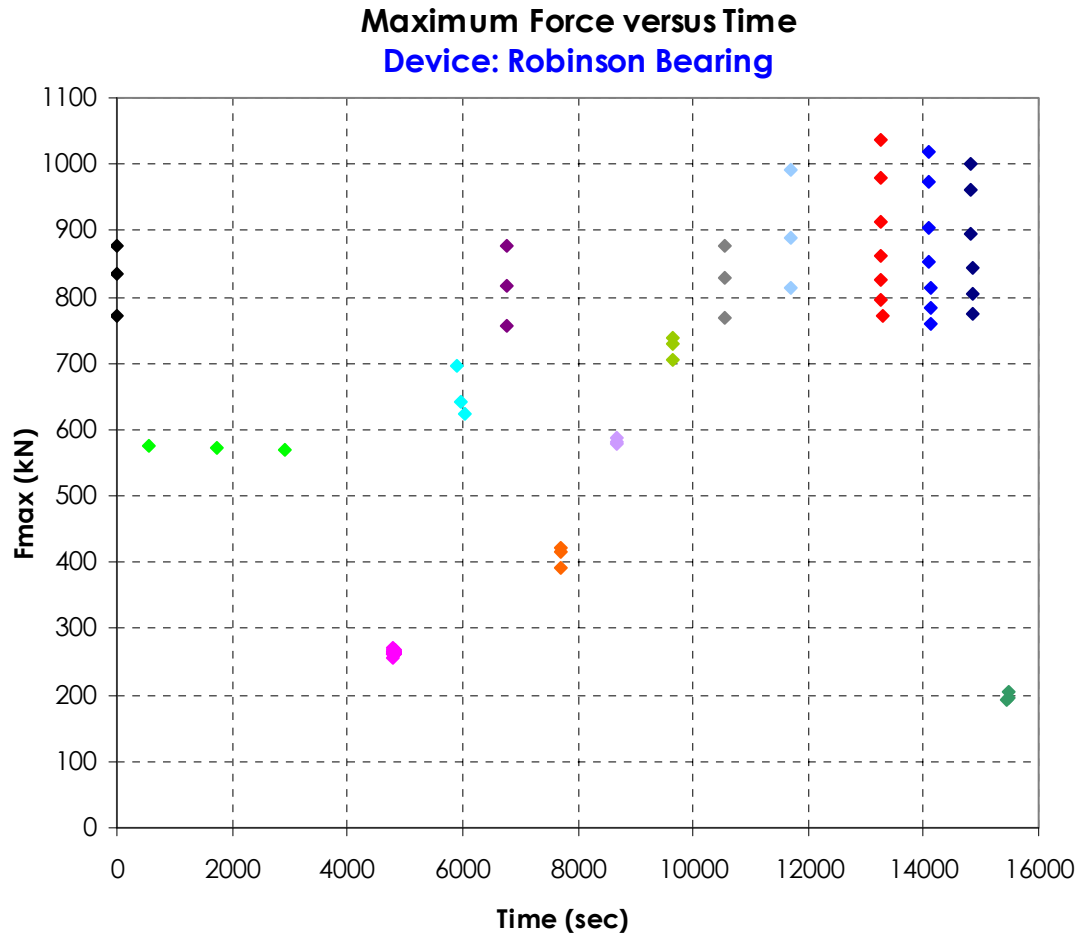
Appendix C, Figure 1: Experiment-1, average stiffness, Robinson bearing



Appendix C, Figure 2: Experiment-1, average stiffness, LRB1300

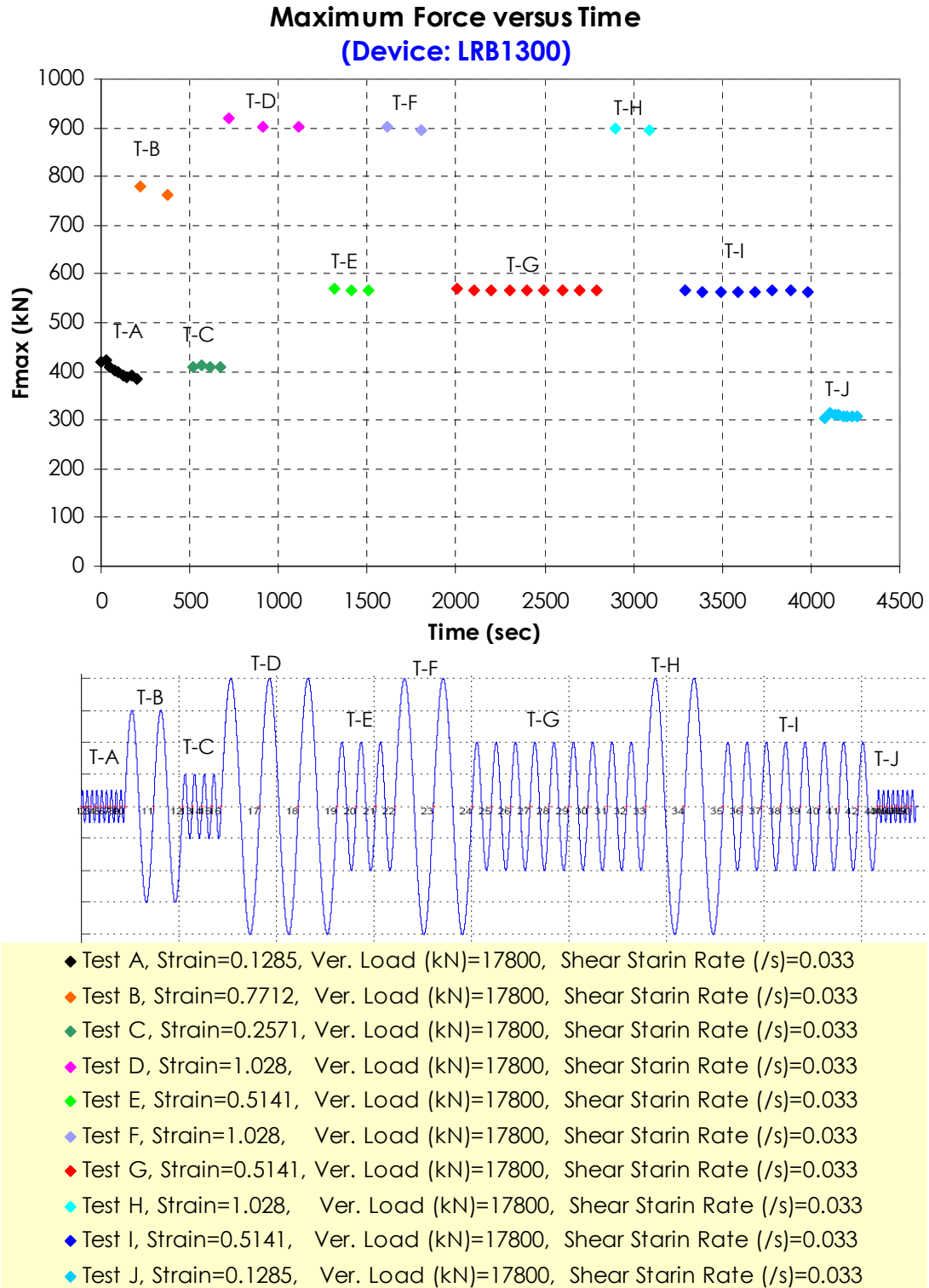


Appendix C, Figure 3: Experiment-1, average stiffness, LRB700

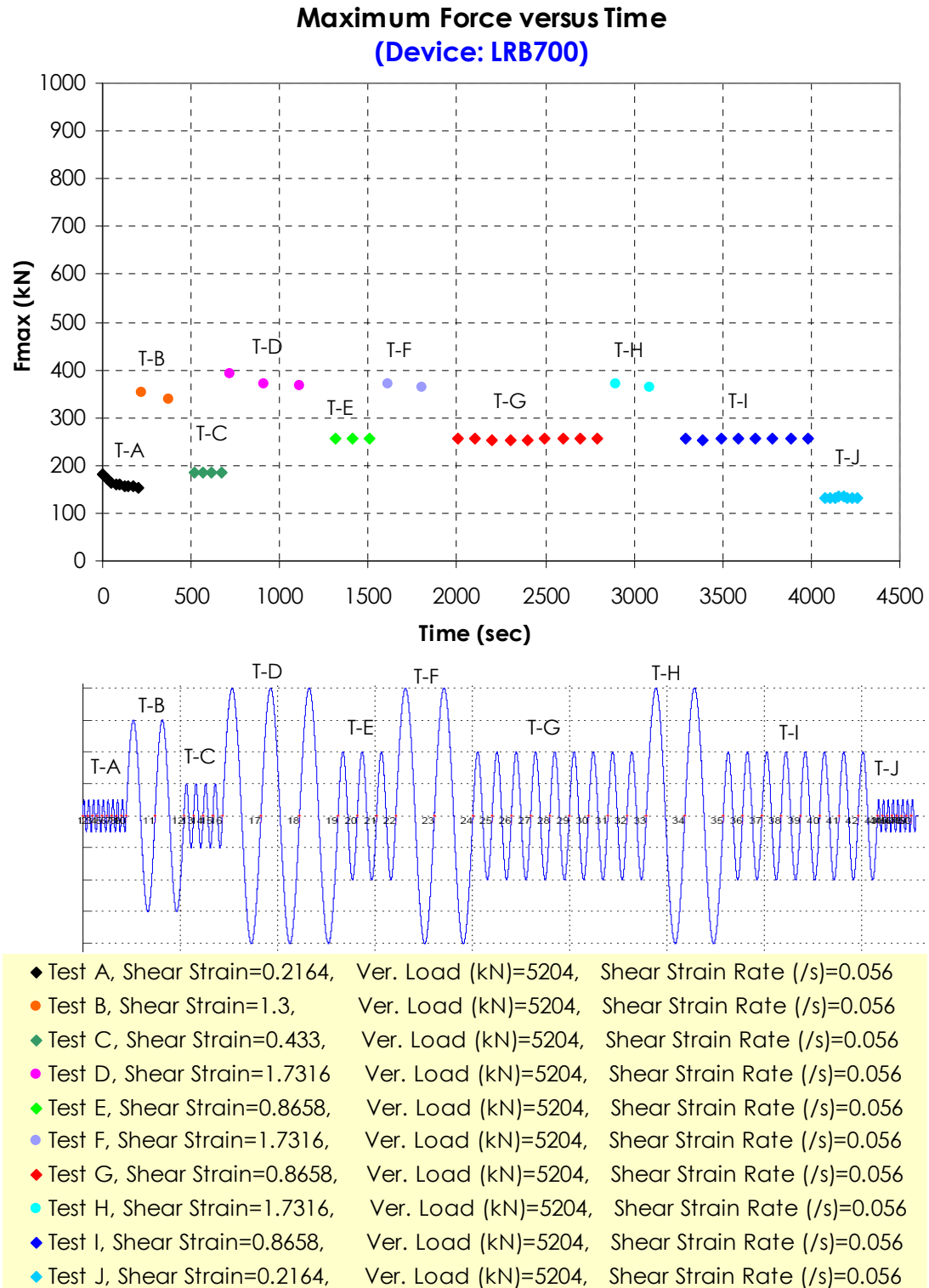


◆ Test 1,	Shear Strain= 0.371,	T(sec)=2.6,	Shear Strain Rate (/s)=0.9
◆ Test 2,	Shear Strain= 0.390,	T(sec)=1180,	Shear Strain Rate (/s)=0.0017
◆ Test 3a,	Shear Strain= 0.0152,	T(sec)=2.6,	Shear Strain Rate (/s)=0.039
◆ Test 4,	Shear Strain= 0.371,	T(sec)=70.25,	Shear Strain Rate (/s)=0.039
◆ Test 5a,	Shear Strain= 0.371,	T(sec)=2.6,	Shear Strain Rate (/s)=0.9
◆ Test 5b,	Shear Strain= 0.0935,	T(sec)=2.6,	Shear Strain Rate (/s)=0.23
◆ Test 5c,	Shear Strain= 0.1870,	T(sec)=2.6,	Shear Strain Rate (/s)=0.45
◆ Test 5d,	Shear Strain= 0.278,	T(sec)=2.6,	Shear Strain Rate (/s)=0.675
◆ Test 5e,	Shear Strain= 0.371,	T(sec)=2.6,	Shear Strain Rate (/s)=0.9
◆ Test 5f,	Shear Strain= 0.465,	T(sec)=2.6,	Shear Strain Rate (/s)=1.12
◆ Test 6a,	Shear Strain= 0.371,	T(sec)=2.6,	Shear Strain Rate (/s)=0.9
◆ Test 6b,	Shear Strain= 0.371,	T(sec)=2.6,	Shear Strain Rate (/s)=0.9
◆ Test 6c,	Shear Strain= 0.371,	T(sec)=2.6,	Shear Strain Rate (/s)=0.9
◆ Test 7a,	Shear Strain= 0.0152,	T(sec)=2.6,	Shear Strain Rate (/s)=0.039

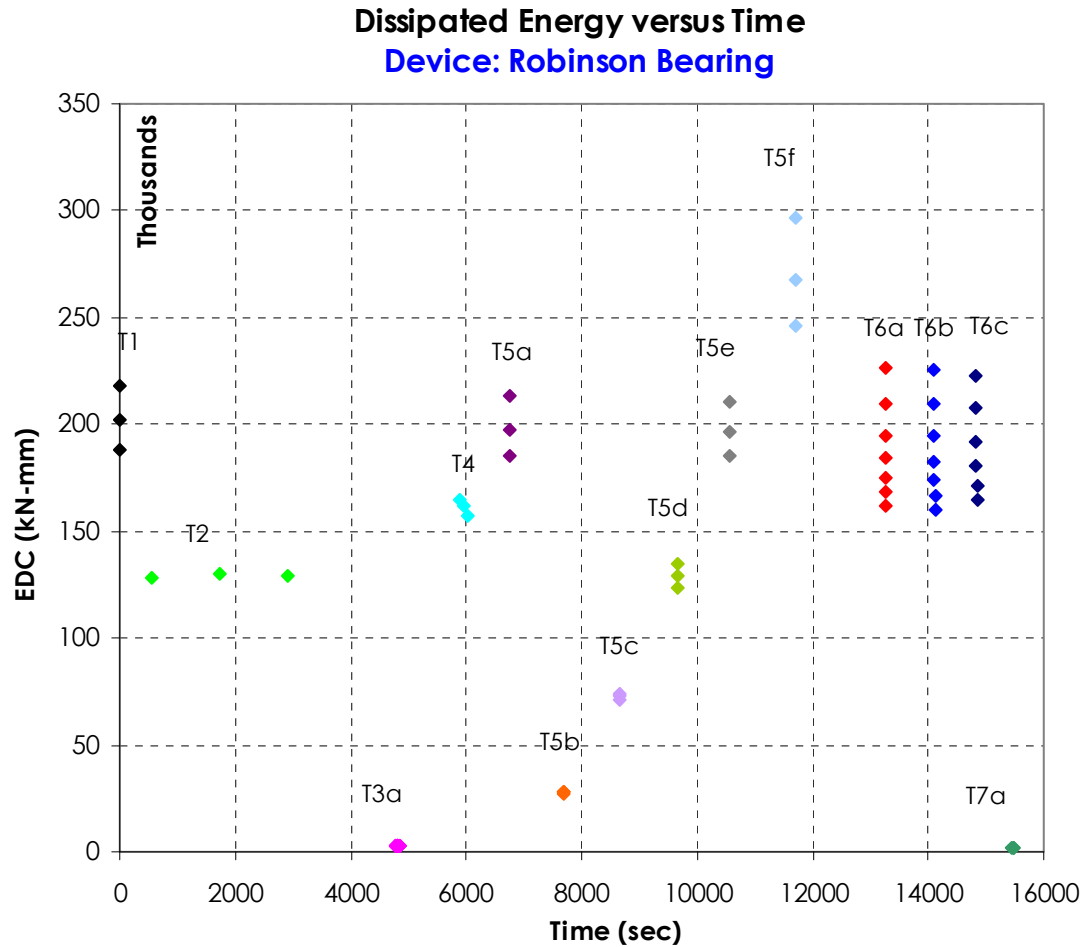
Appendix C, Figure 4: Experiment-1, maximum force, Robinson bearing



Appendix C, Figure 5: Experiment-1, maximum force, LRB1300

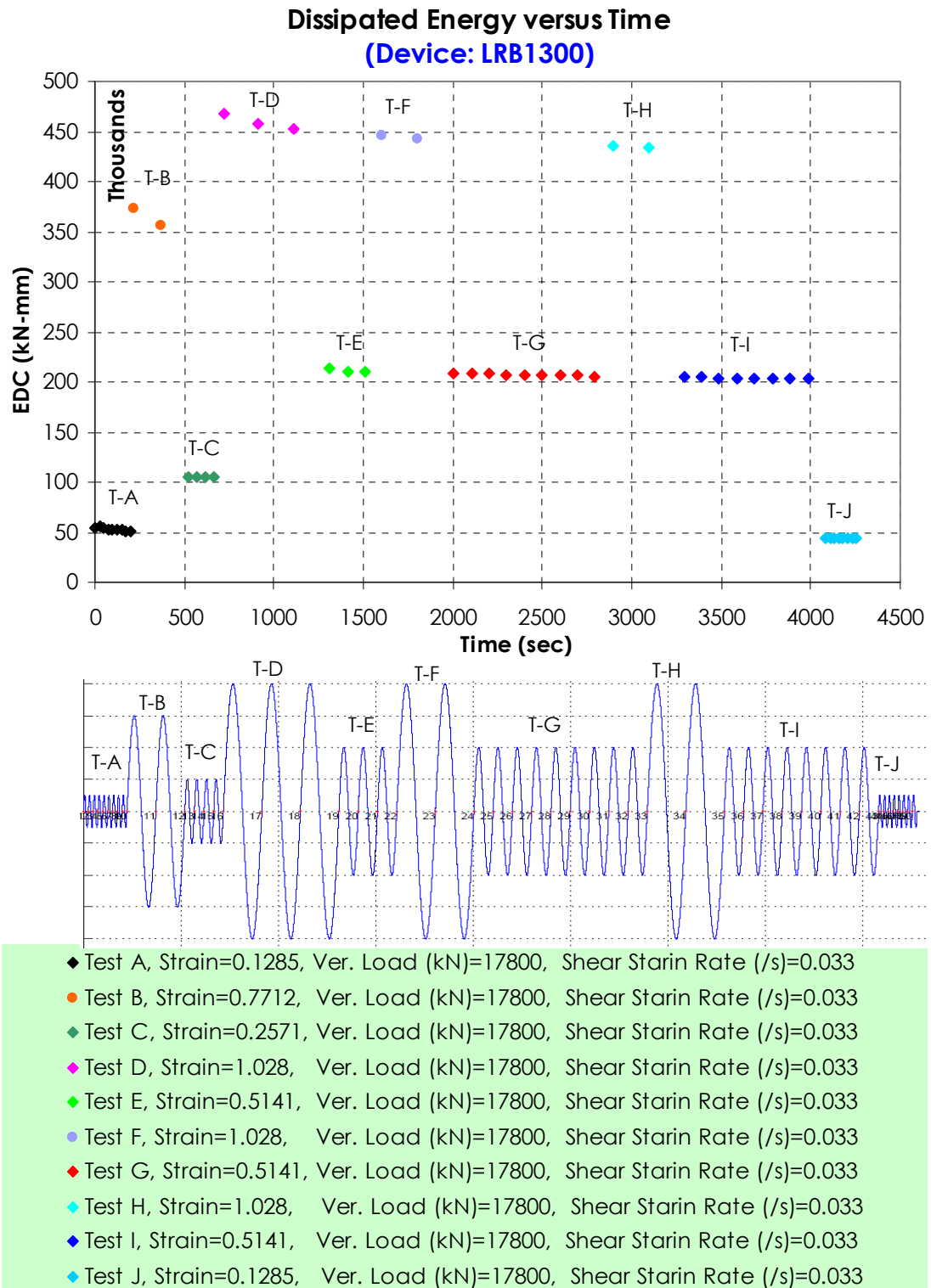


Appendix C, Figure 6: Experiment-1, maximum force, LRB700

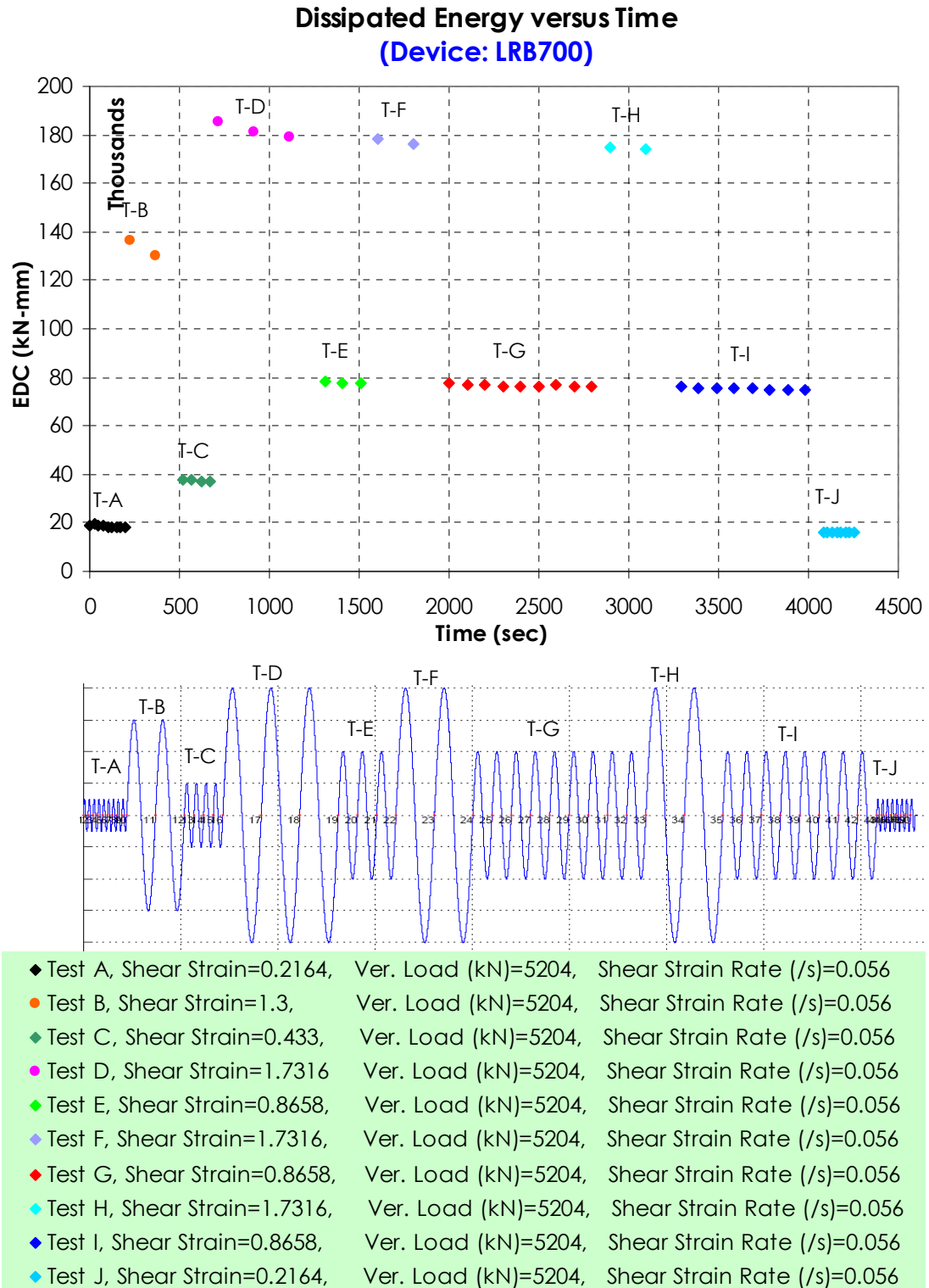


◆ Test 1, Shear Strain= 0.371,	T(sec)=2.6, Shear Strain Rate (/s)=0.9
◆ Test 2, Shear Strain= 0.390,	T(sec)=1180, Shear Strain Rate (/s)=0.0017
◆ Test 3a, Shear Strain= 0.0152,	T(sec)=2.6, Shear Strain Rate (/s)=0.039
◆ Test 4, Shear Strain= 0.371,	T(sec)=70.25, Shear Strain Rate (/s)=0.039
◆ Test 5a, Shear Strain= 0.371,	T(sec)=2.6, Shear Strain Rate (/s)=0.9
◆ Test 5b, Shear Strain= 0.0935,	T(sec)=2.6, Shear Strain Rate (/s)=0.23
◆ Test 5c, Shear Strain= 0.1870,	T(sec)=2.6, Shear Strain Rate (/s)=0.45
◆ Test 5d, Shear Strain= 0.278,	T(sec)=2.6, Shear Strain Rate (/s)=0.675
◆ Test 5e, Shear Strain= 0.371,	T(sec)=2.6, Shear Strain Rate (/s)=0.9
◆ Test 5f, Shear Strain= 0.465,	T(sec)=2.6, Shear Strain Rate (/s)=1.12
◆ Test 6a, Shear Strain= 0.371,	T(sec)=2.6, Shear Strain Rate (/s)=0.9
◆ Test 6b, Shear Strain= 0.371,	T(sec)=2.6, Shear Strain Rate (/s)=0.9
◆ Test 6c, Shear Strain= 0.371,	T(sec)=2.6, Shear Strain Rate (/s)=0.9
◆ Test 7a, Shear Strain= 0.0152,	T(sec)=2.6, Shear Strain Rate (/s)=0.039

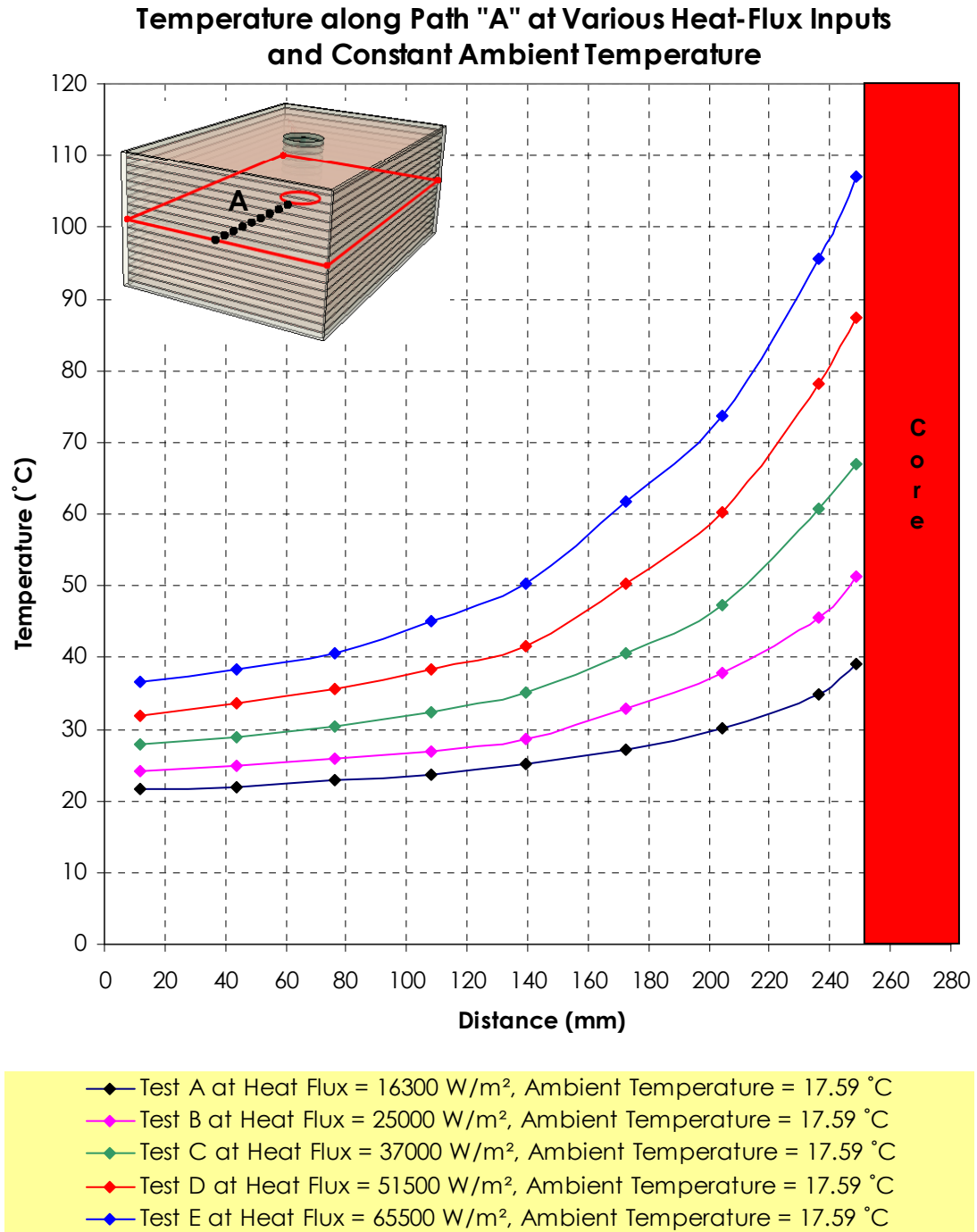
Appendix C, Figure 7: Experiment-1, EDC, Robinson bearing



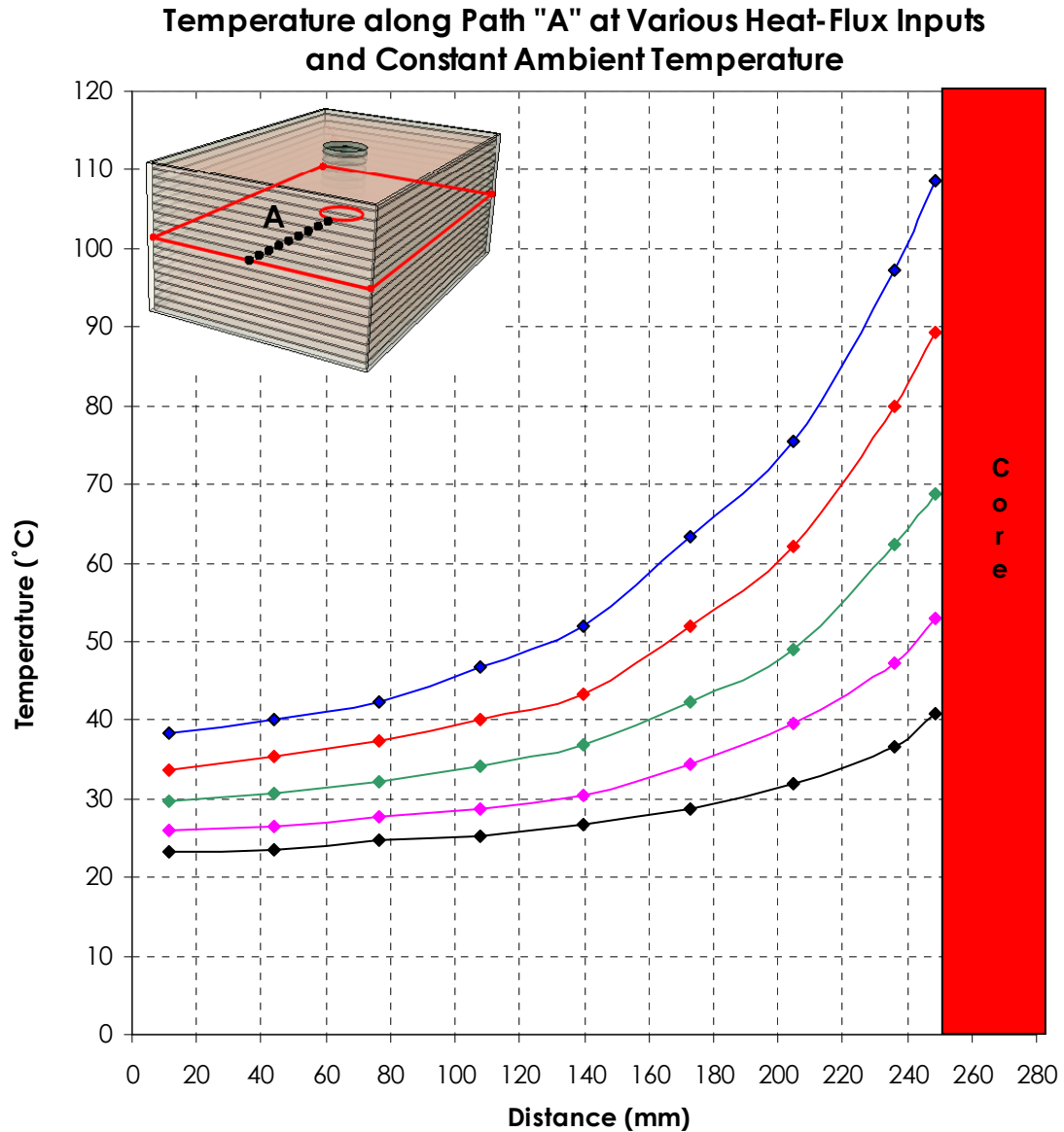
Appendix C, Figure 8: Experiment-1, EDC, LRB1300



Appendix C, Figure 9: Experiment-1, EDC, LRB700

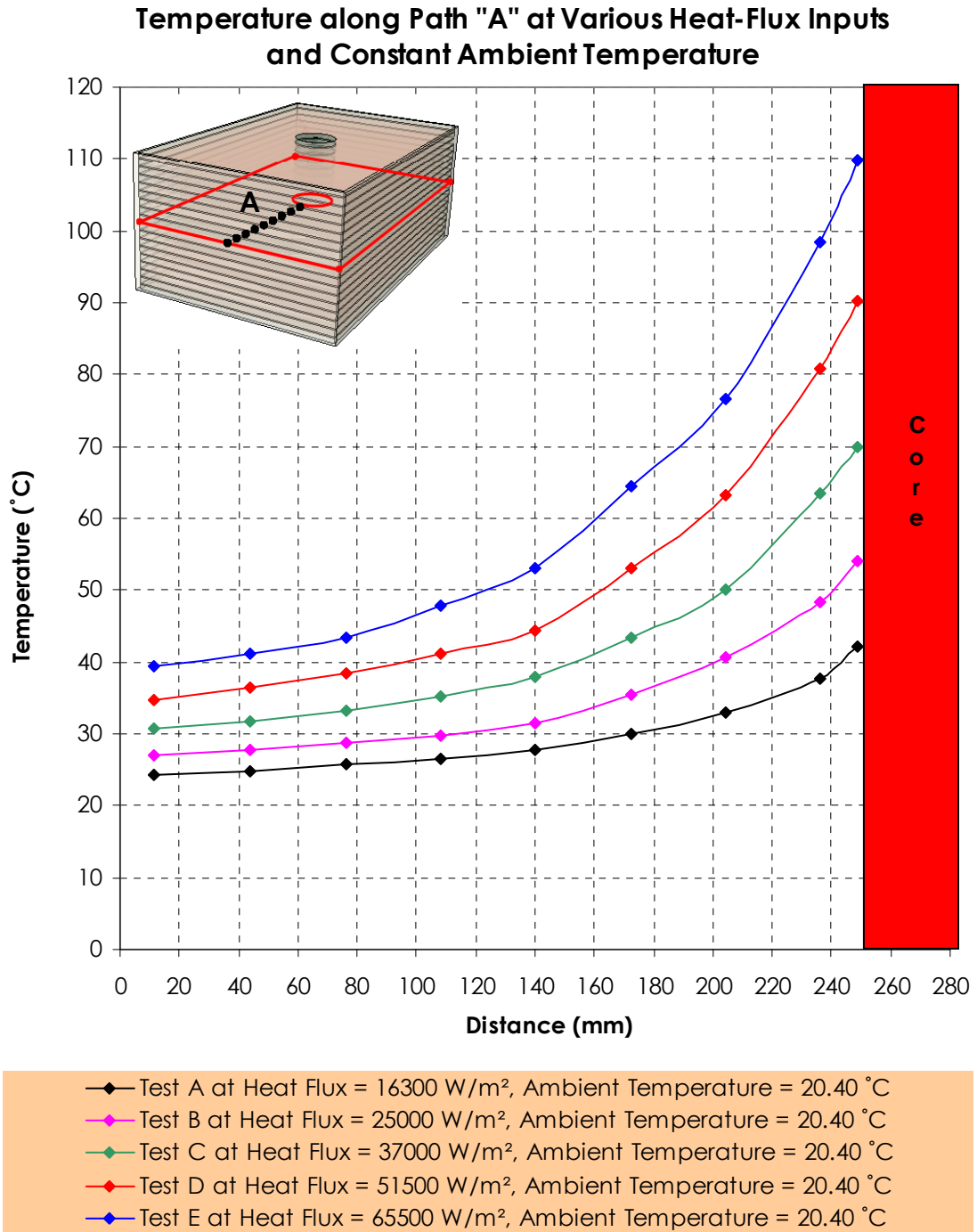


Appendix D, Figure 1: Temperature profile across the bearing shows nonlinear trend across the body of the bearing, ambient temperature was 17.59°C

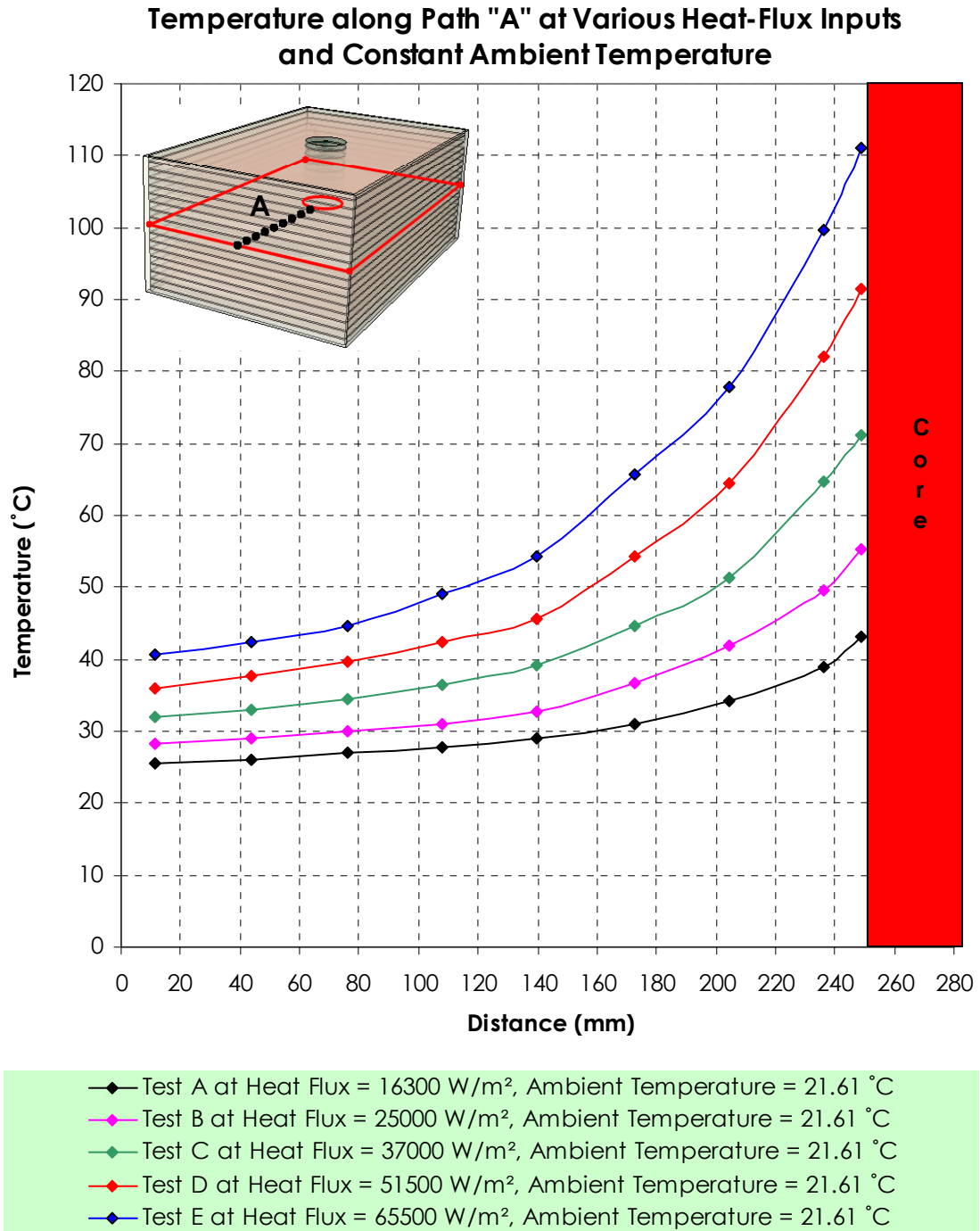


- ◆— Test A at Heat Flux = 16300 W/m², Ambient Temperature = 19.30 °C
- ◆— Test B at Heat Flux = 25000 W/m², Ambient Temperature = 19.30 °C
- ◆— Test C at Heat Flux = 37000 W/m², Ambient Temperature = 19.30 °C
- ◆— Test D at Heat Flux = 51500 W/m², Ambient Temperature = 19.30 °C
- ◆— Test E at Heat Flux = 65500 W/m², Ambient Temperature = 19.30 °C

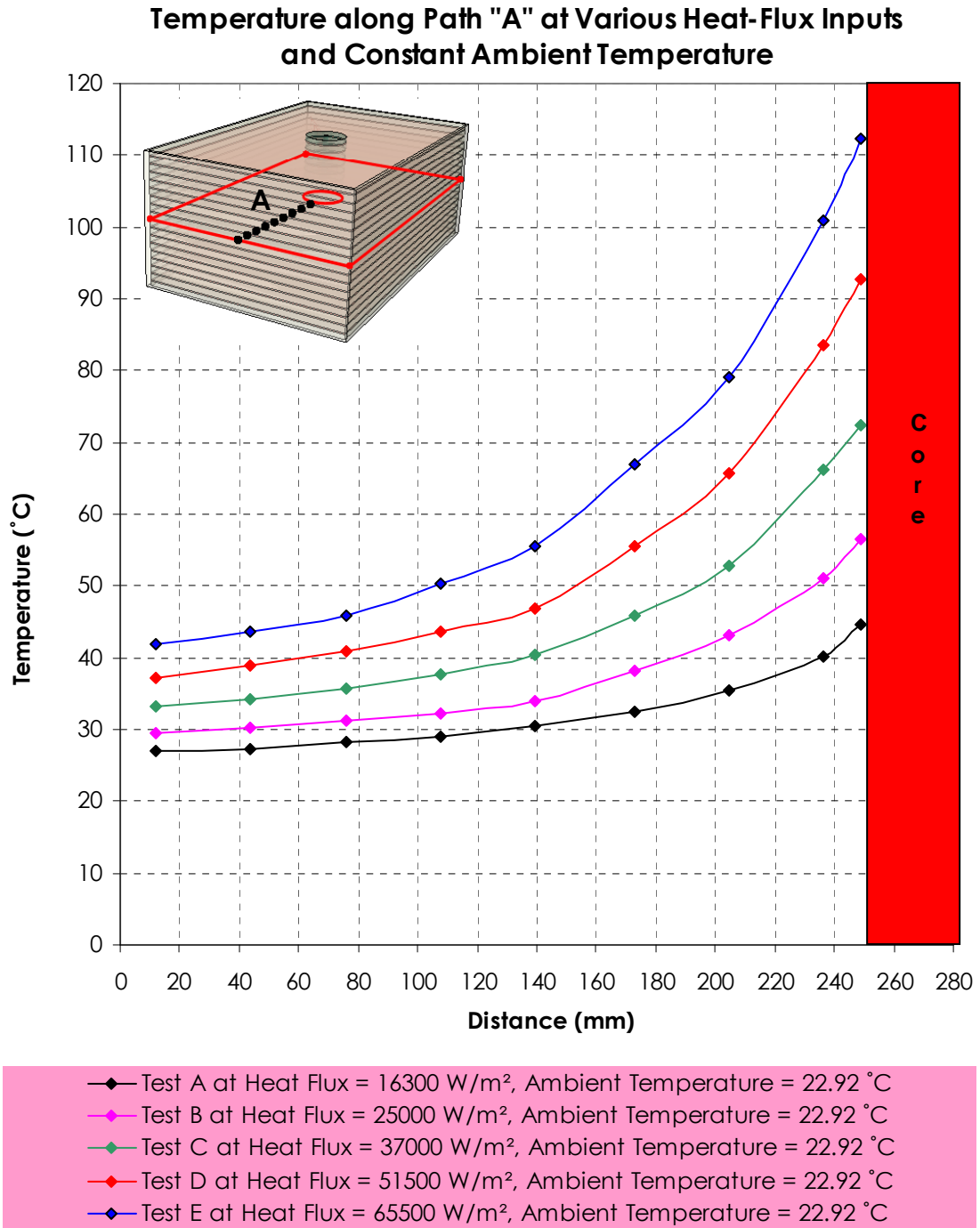
Appendix D, Figure 2 Temperature profile across the bearing shows nonlinear trend across the body of the bearing, ambient temperature was 19.30 °C



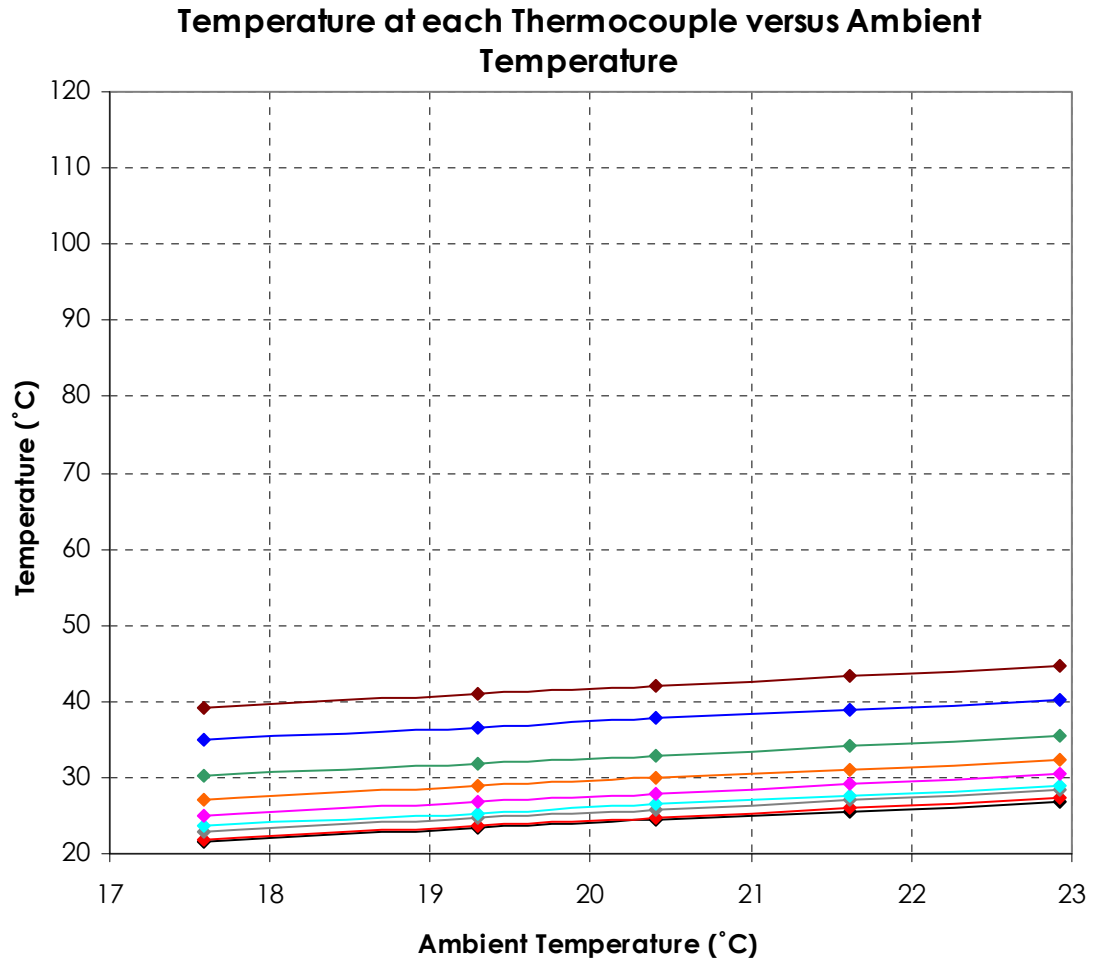
Appendix D, Figure 3: Temperature profile across the bearing shows nonlinear trend across the body of the bearing, ambient temperature was 20.40 °C



Appendix D, Figure 4: Temperature profile across the bearing shows nonlinear trend across the body of the bearing, ambient temperature was 21.61 °C

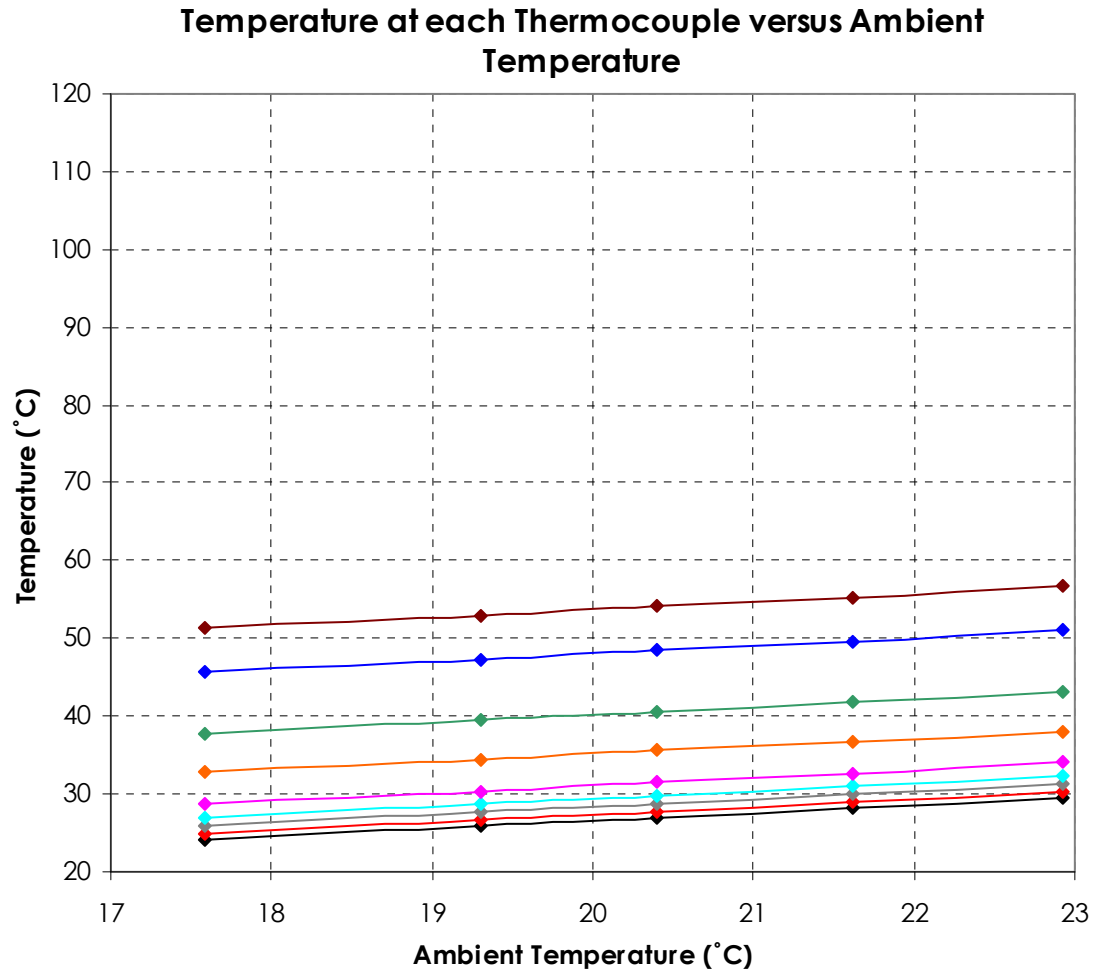


Appendix D, Figure 5: Temperature profile across the bearing shows nonlinear trend across the body of the bearing, ambient temperature was 22.92 °C



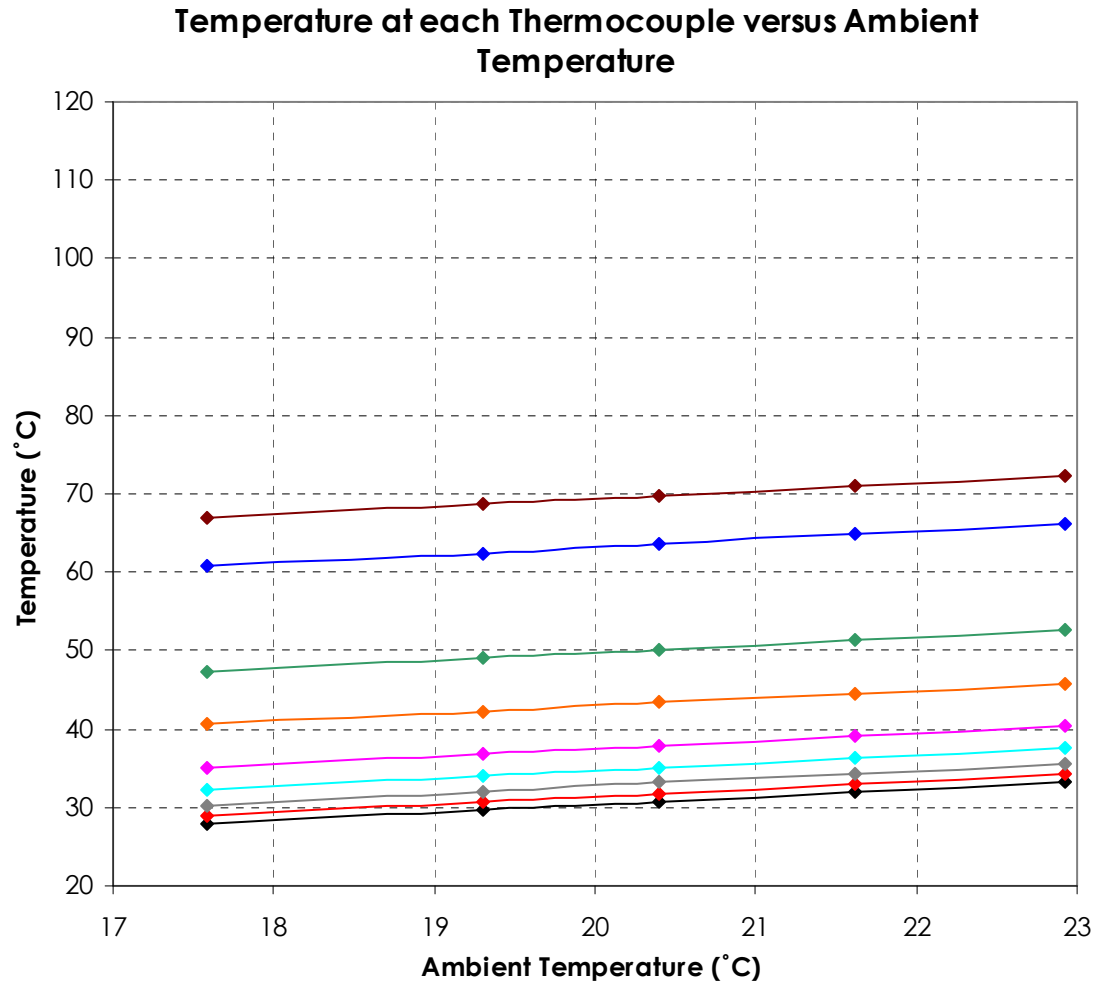
- ◆— Thermocouple #1 at Distance = 11.68 mm, Heat-Flux = 16300 W/m²
- ◆— Thermocouple #2 at Distance = 43.94 mm, Heat-Flux = 16300 W/m²
- ◆— Thermocouple #3 at Distance = 76.20 mm, Heat-Flux = 16300 W/m²
- ◆— Thermocouple #4 at Distance = 107.95 mm, Heat-Flux = 16300 W/m²
- ◆— Thermocouple #5 at Distance = 139.70 mm, Heat-Flux = 16300 W/m²
- ◆— Thermocouple #6 at Distance = 172.72 mm, Heat-Flux = 16300 W/m²
- ◆— Thermocouple #7 at Distance = 204.47 mm, Heat-Flux = 16300 W/m²
- ◆— Thermocouple #8 at Distance = 236.22 mm, Heat-Flux = 16300 W/m²
- ◆— Thermocouple #9 at Distance = 248.92 mm, Heat-Flux = 16300 W/m²

Appendix E, Figure 1: Variation of temperature at each thermocouple with respect to ambient temperature at constant heat-flux of 16300 W/m²



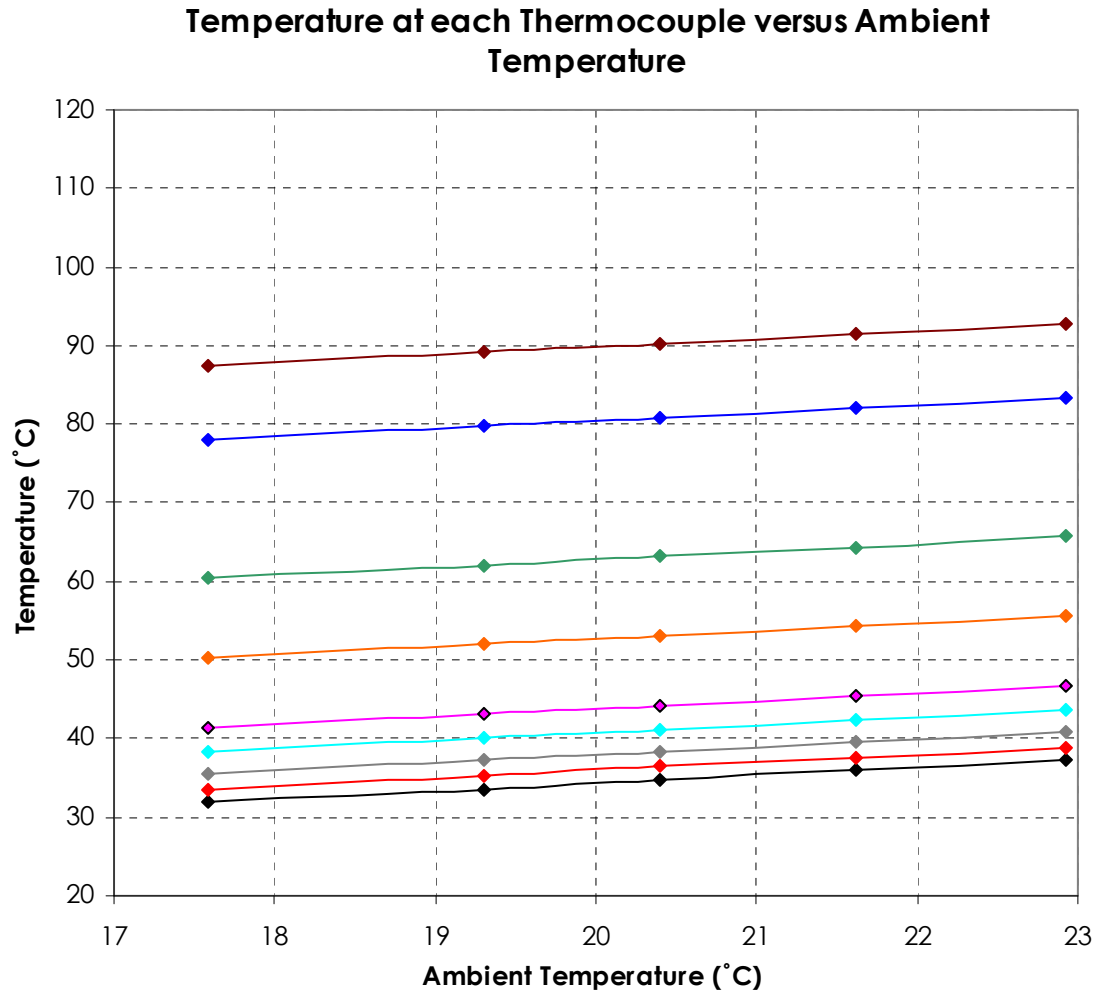
- ◆— Thermocouple #1 at Distance = 11.68 mm, Heat-Flux = 25000 W/m²
- ◆— Thermocouple #2 at Distance = 43.94 mm, Heat-Flux = 25000 W/m²
- ◆— Thermocouple #3 at Distance = 76.20 mm, Heat-Flux = 25000 W/m²
- ◆— Thermocouple #4 at Distance = 107.95 mm, Heat-Flux = 25000 W/m²
- ◆— Thermocouple #5 at Distance = 139.70 mm, Heat-Flux = 25000 W/m²
- ◆— Thermocouple #6 at Distance = 172.72 mm, Heat-Flux = 25000 W/m²
- ◆— Thermocouple #7 at Distance = 204.47 mm, Heat-Flux = 25000 W/m²
- ◆— Thermocouple #8 at Distance = 236.22 mm, Heat-Flux = 25000 W/m²
- ◆— Thermocouple #9 at Distance = 248.92 mm, Heat-Flux = 25000 W/m²

Appendix E, Figure 2: Variation of temperature at each thermocouple with respect to ambient temperature at constant heat-flux of 25000 W/m²



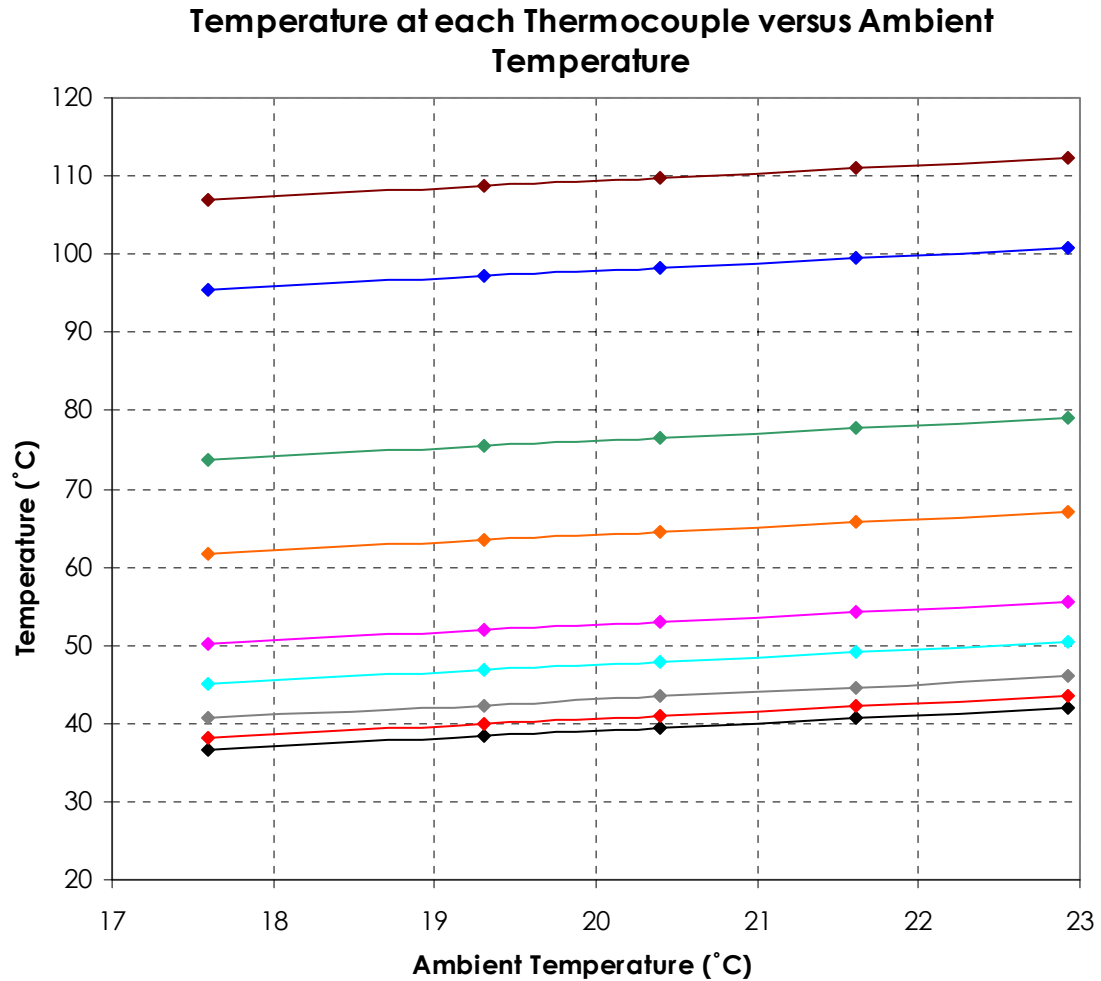
- ◆— Thermocouple #1 at Distance = 11.68 mm, Heat-Flux = 37000 W/m²
- ◆— Thermocouple #2 at Distance = 43.94 mm, Heat-Flux = 37000 W/m²
- ◆— Thermocouple #3 at Distance = 76.20 mm, Heat-Flux = 37000 W/m²
- ◆— Thermocouple #4 at Distance = 107.95 mm, Heat-Flux = 37000 W/m²
- ◆— Thermocouple #5 at Distance = 139.70 mm, Heat-Flux = 37000 W/m²
- ◆— Thermocouple #6 at Distance = 172.72 mm, Heat-Flux = 37000 W/m²
- ◆— Thermocouple #7 at Distance = 204.47 mm, Heat-Flux = 37000 W/m²
- ◆— Thermocouple #8 at Distance = 236.22 mm, Heat-Flux = 37000 W/m²
- ◆— Thermocouple #9 at Distance = 248.92 mm, Heat-Flux = 37000 W/m²

Appendix E, Figure 3: Variation of temperature at each thermocouple with respect to ambient temperature at constant heat-flux of 37000 W/m²



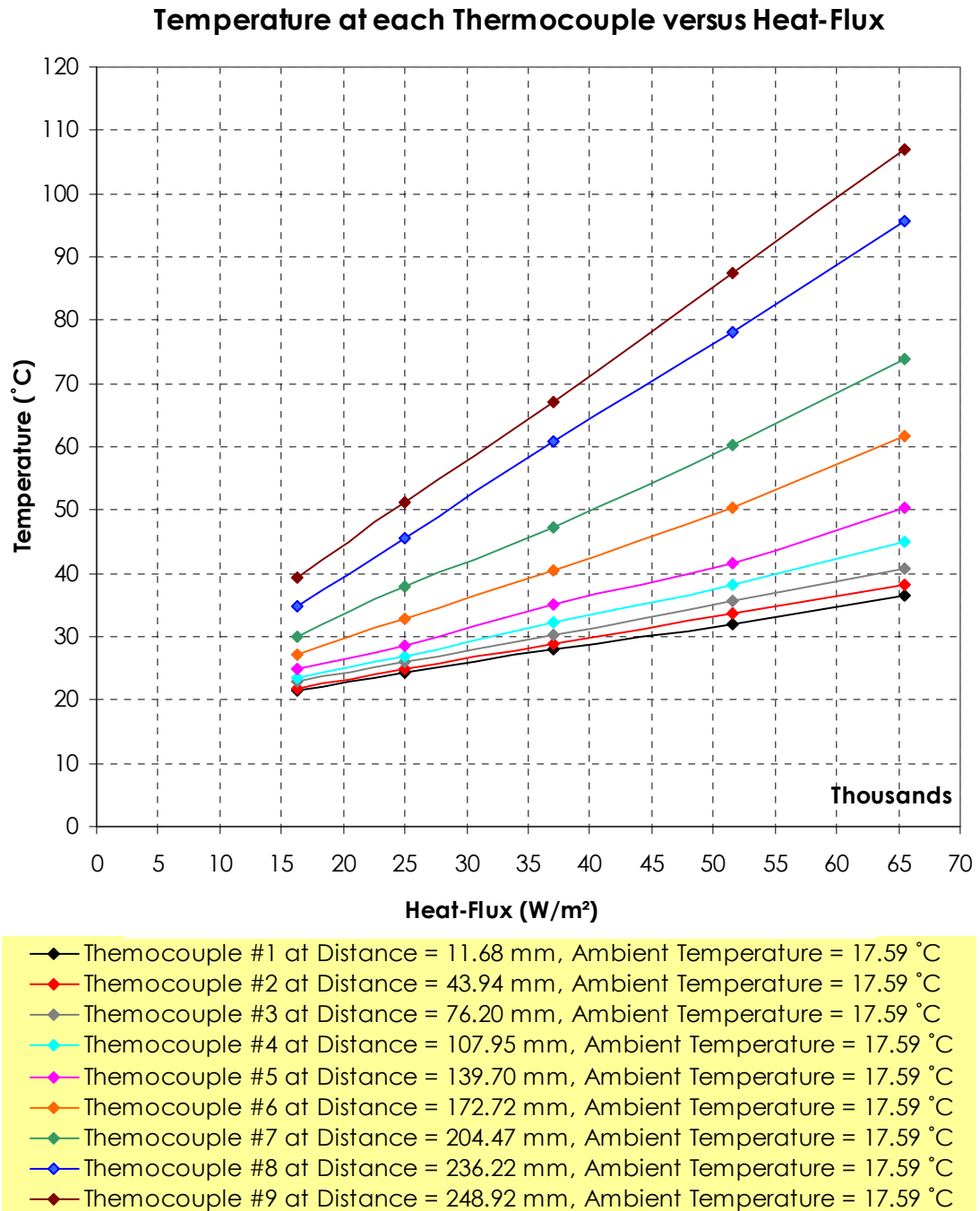
- ◆— Thermocouple #1 at Distance = 11.68 mm, Heat-Flux = 37000 W/m²
- ◆— Thermocouple #2 at Distance = 43.94 mm, Heat-Flux = 37000 W/m²
- ◆— Thermocouple #3 at Distance = 76.20 mm, Heat-Flux = 37000 W/m²
- ◆— Thermocouple #4 at Distance = 107.95 mm, Heat-Flux = 37000 W/m²
- ◆— Thermocouple #5 at Distance = 139.70 mm, Heat-Flux = 37000 W/m²
- ◆— Thermocouple #6 at Distance = 172.72 mm, Heat-Flux = 37000 W/m²
- ◆— Thermocouple #7 at Distance = 204.47 mm, Heat-Flux = 37000 W/m²
- ◆— Thermocouple #8 at Distance = 236.22 mm, Heat-Flux = 37000 W/m²
- ◆— Thermocouple #9 at Distance = 248.92 mm, Heat-Flux = 37000 W/m²

Appendix E, Figure 4: Variation of temperature at each thermocouple with respect to ambient temperature at constant heat-flux of 51500 W/m²

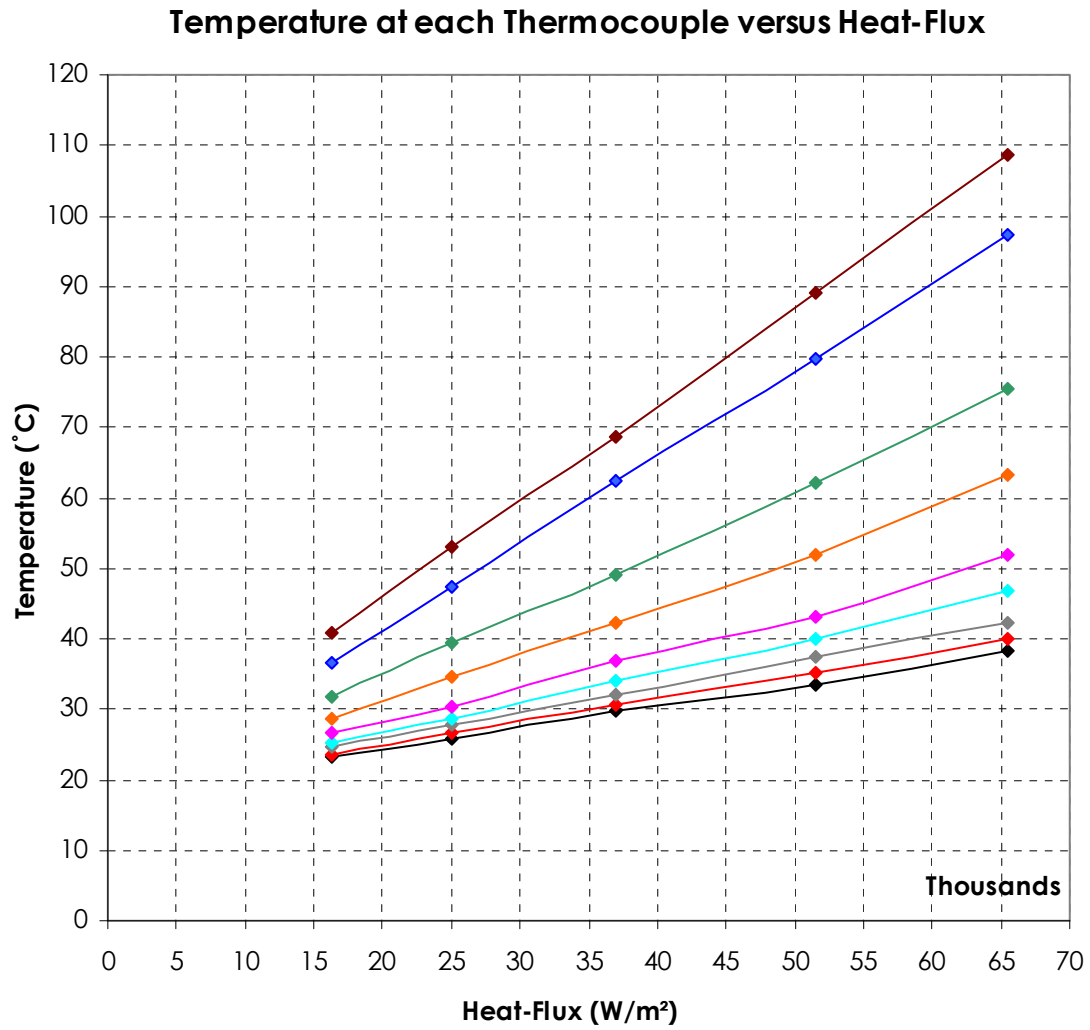


- ◆— Thermocouple #1 at Distance = 11.68 mm, Heat-Flux = 65500 W/m²
- ◆— Thermocouple #2 at Distance = 43.94 mm, Heat-Flux = 65500 W/m²
- ◆— Thermocouple #3 at Distance = 76.20 mm, Heat-Flux = 65500 W/m²
- ◆— Thermocouple #4 at Distance = 107.95 mm, Heat-Flux = 65500 W/m²
- ◆— Thermocouple #5 at Distance = 139.70 mm, Heat-Flux = 65500 W/m²
- ◆— Thermocouple #6 at Distance = 172.72 mm, Heat-Flux = 65500 W/m²
- ◆— Thermocouple #7 at Distance = 204.47 mm, Heat-Flux = 65500 W/m²
- ◆— Thermocouple #8 at Distance = 236.22 mm, Heat-Flux = 65500 W/m²
- ◆— Thermocouple #9 at Distance = 248.92 mm, Heat-Flux = 65500 W/m²

Appendix E, Figure 5: Variation of temperature at each thermocouple with respect to ambient temperature at constant heat-flux of 65500 W/m²

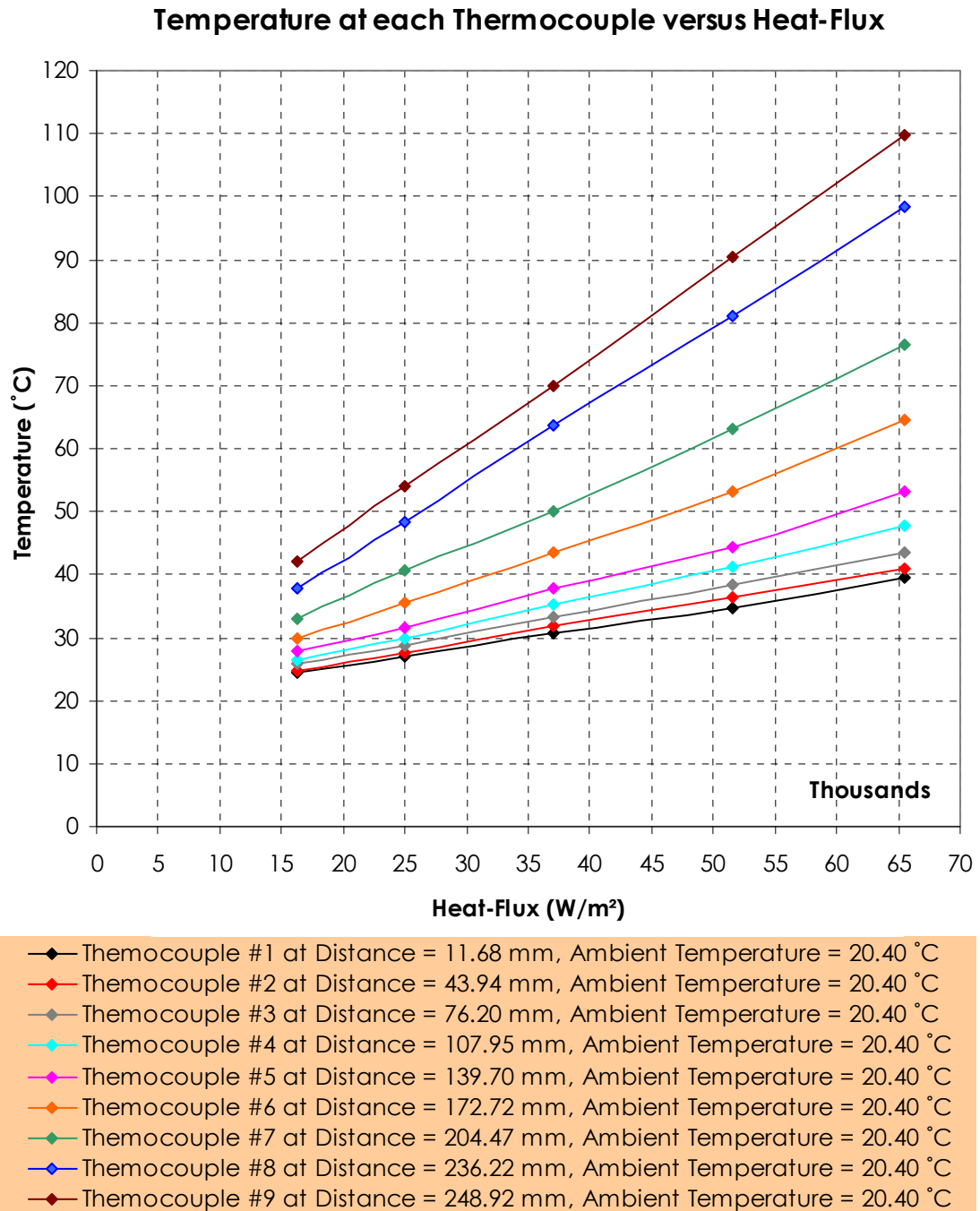


Appendix F, Figure 1: Variation of temperature at each thermocouple with respect to input heat-flux at ambient temperature of 17.59 °C

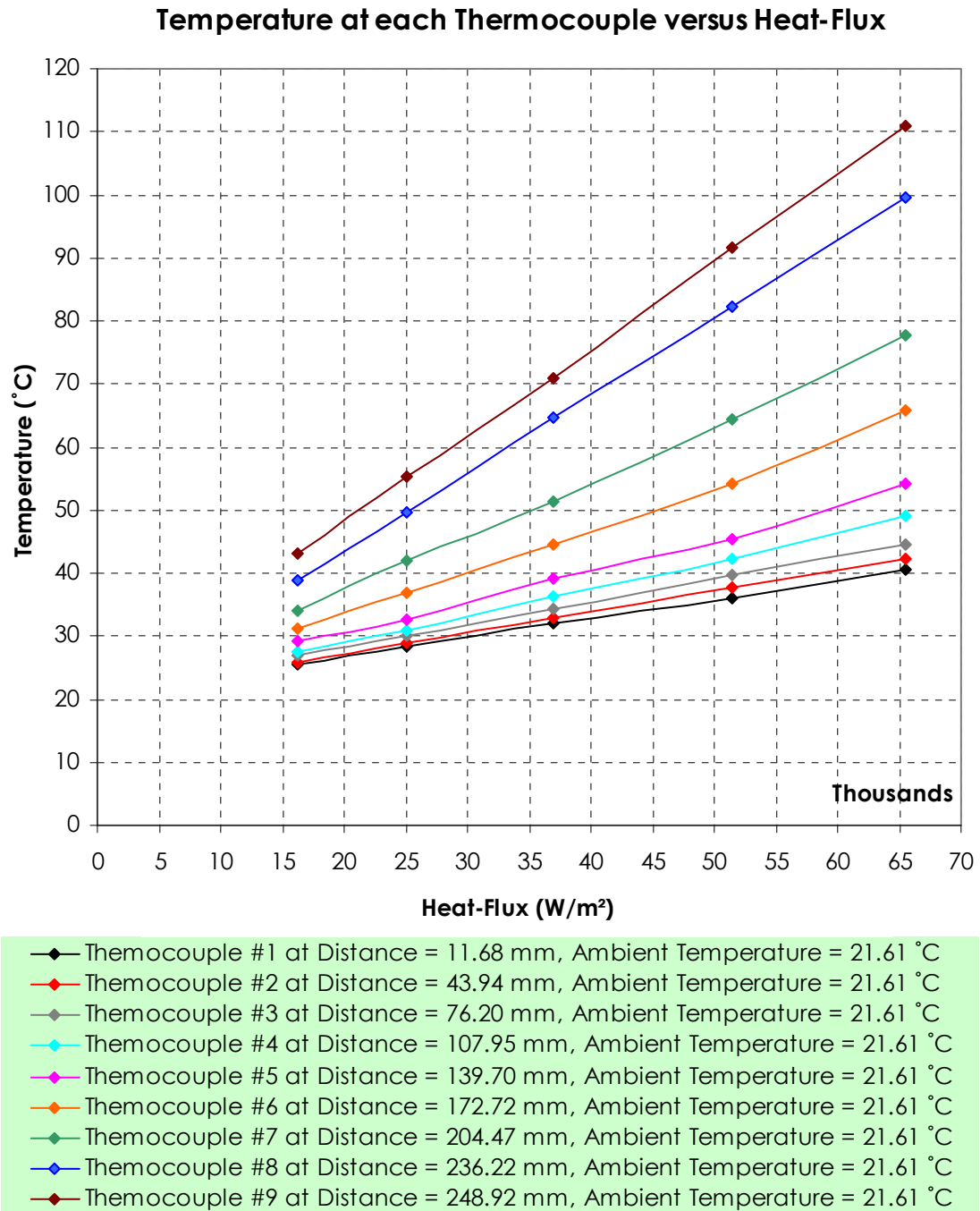


- ◆— Thermocouple #1 at Distance = 11.68 mm, Ambient Temperature = 19.30 °C
- ◆— Thermocouple #2 at Distance = 43.94 mm, Ambient Temperature = 19.30 °C
- ◆— Thermocouple #3 at Distance = 76.20 mm, Ambient Temperature = 19.30 °C
- ◆— Thermocouple #4 at Distance = 107.95mm, Ambient Temperature = 19.30 °C
- ◆— Thermocouple #5 at Distance = 139.70 mm, Ambient Temperature = 19.30 °C
- ◆— Thermocouple #6 at Distance = 172.72 mm, Ambient Temperature = 19.30 °C
- ◆— Thermocouple #7 at Distance = 204.47 mm, Ambient Temperature = 19.30 °C
- ◆— Thermocouple #8 at Distance = 236.22 mm, Ambient Temperature = 19.30 °C
- ◆— Thermocouple #9 at Distance = 248.92 mm, Ambient Temperature = 19.30 °C

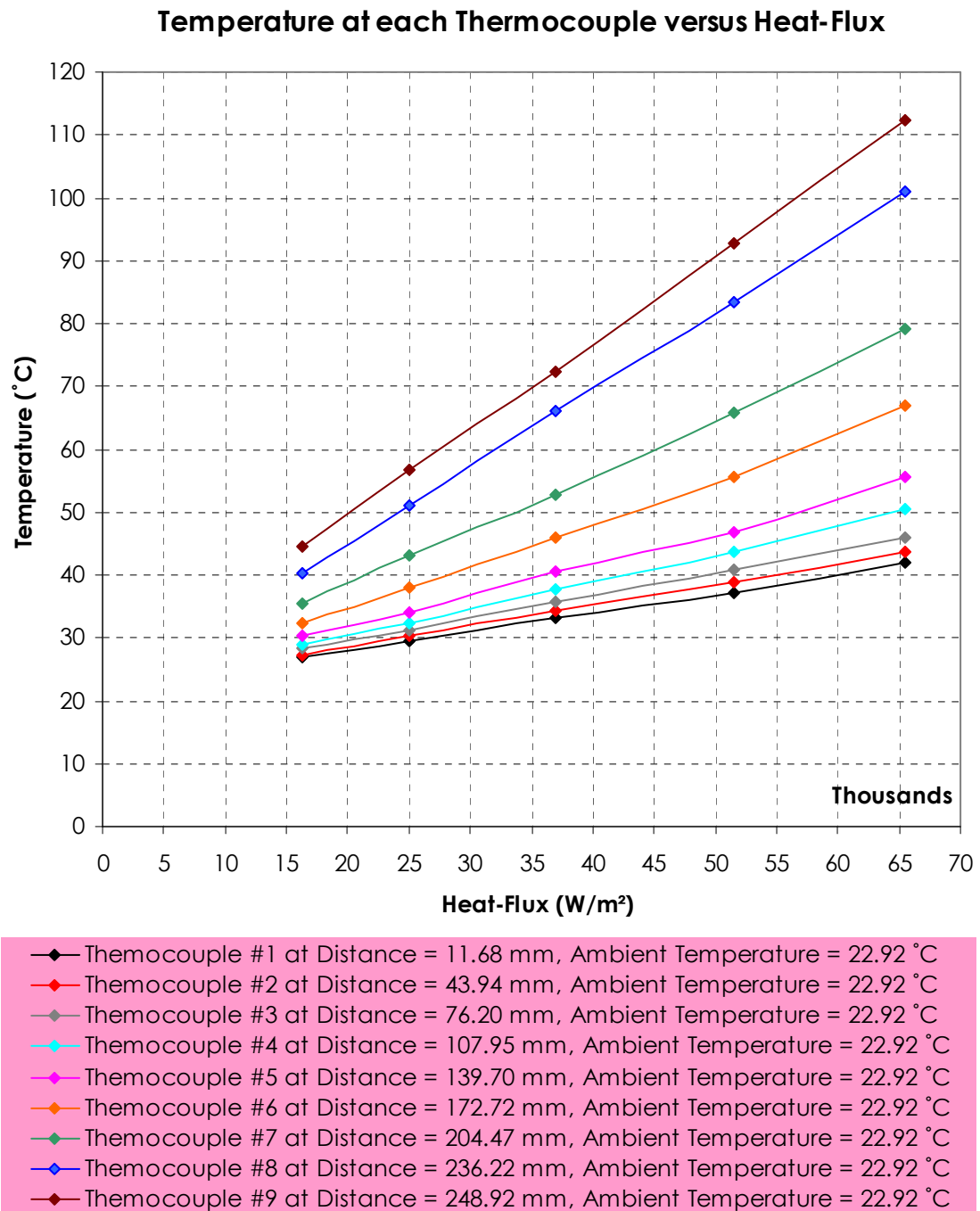
Appendix F, Figure 2: Variation of temperature at each thermocouple with respect to input heat-flux at ambient temperature of 19.30 °C



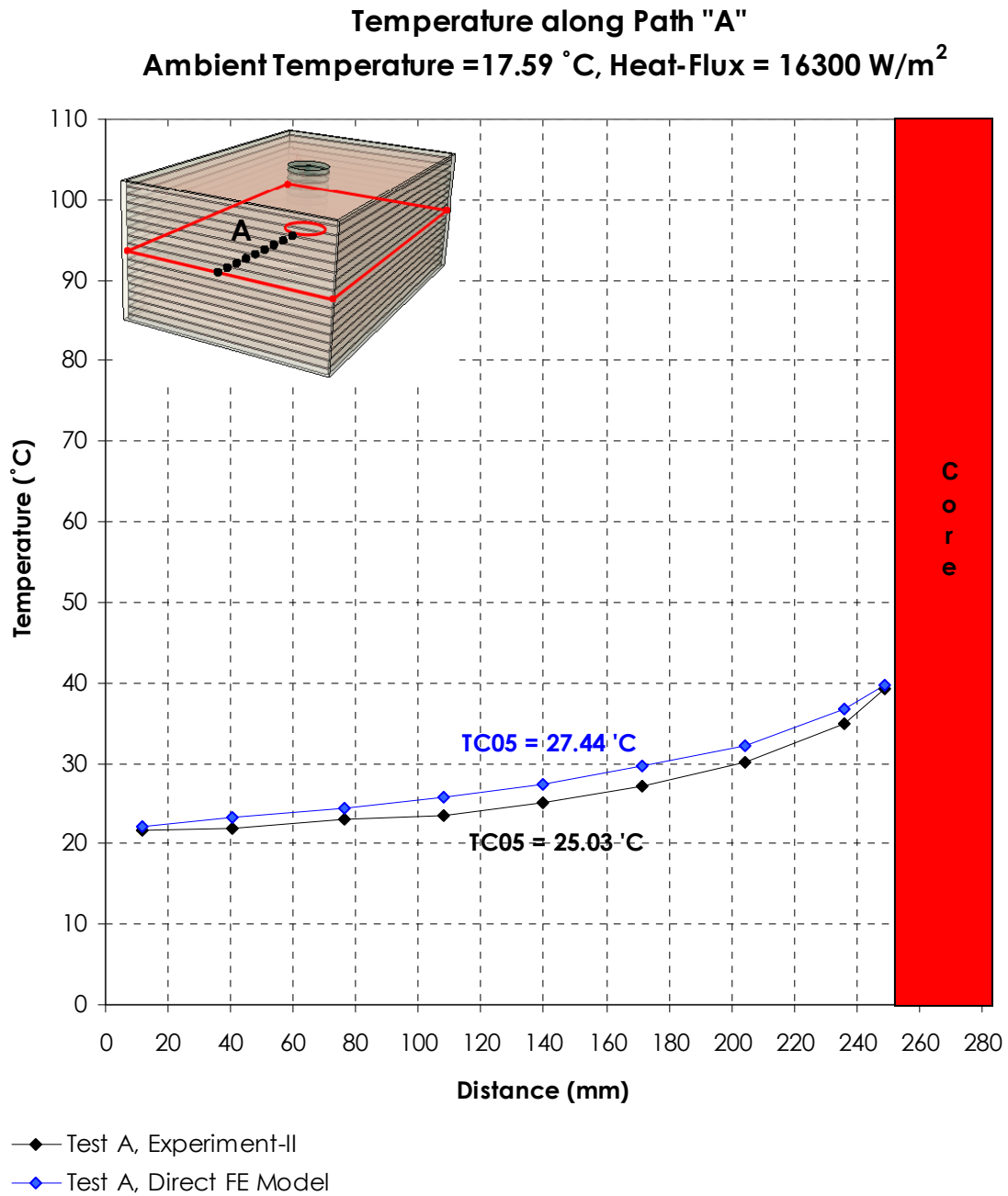
Appendix F, Figure 3: Variation of temperature at each thermocouple with respect to input heat-flux at ambient temperature of 20.40 °C



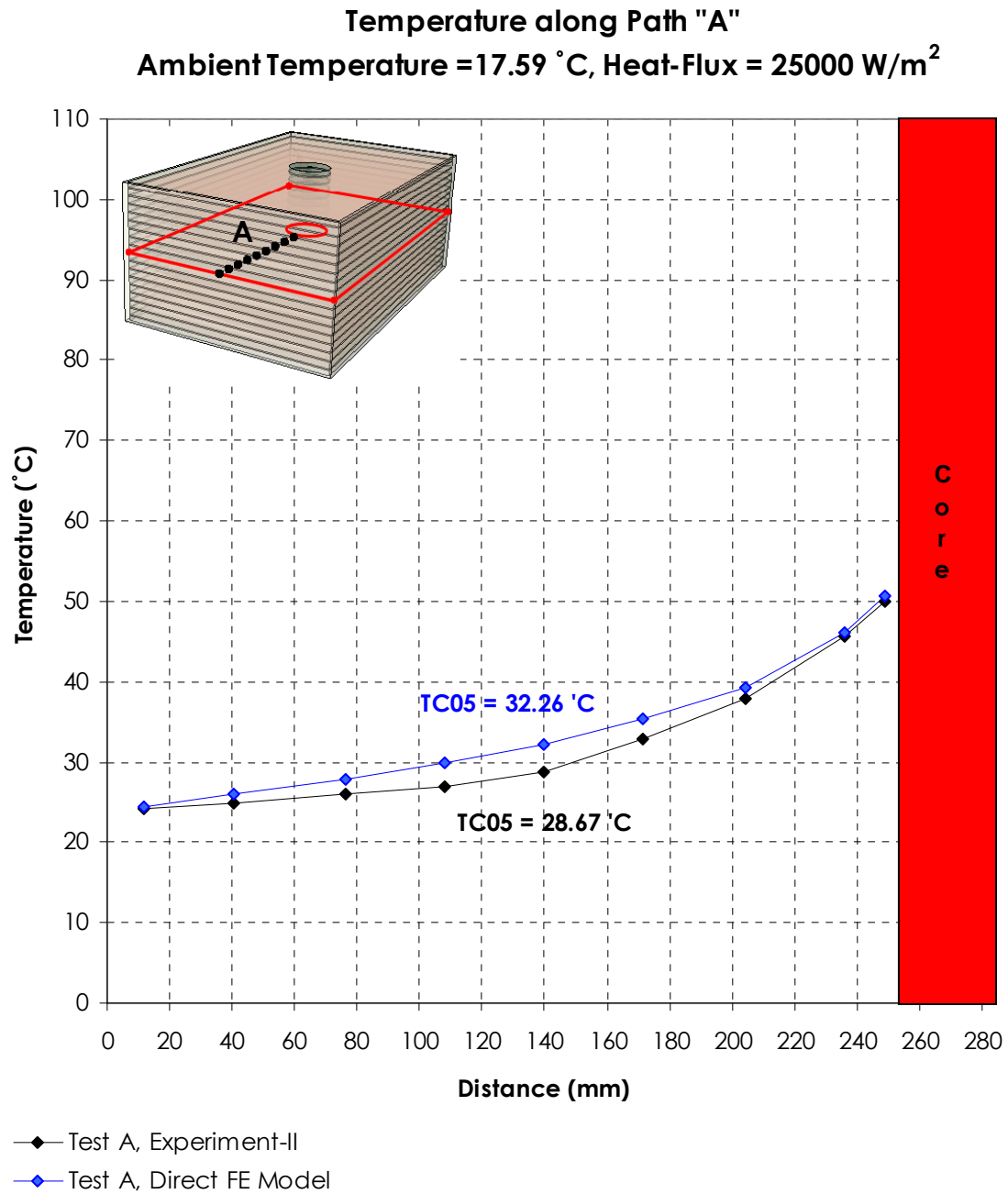
Appendix F, Figure 4: Variation of temperature at each thermocouple with respect to input heat-flux at ambient temperature of 21.61 °C



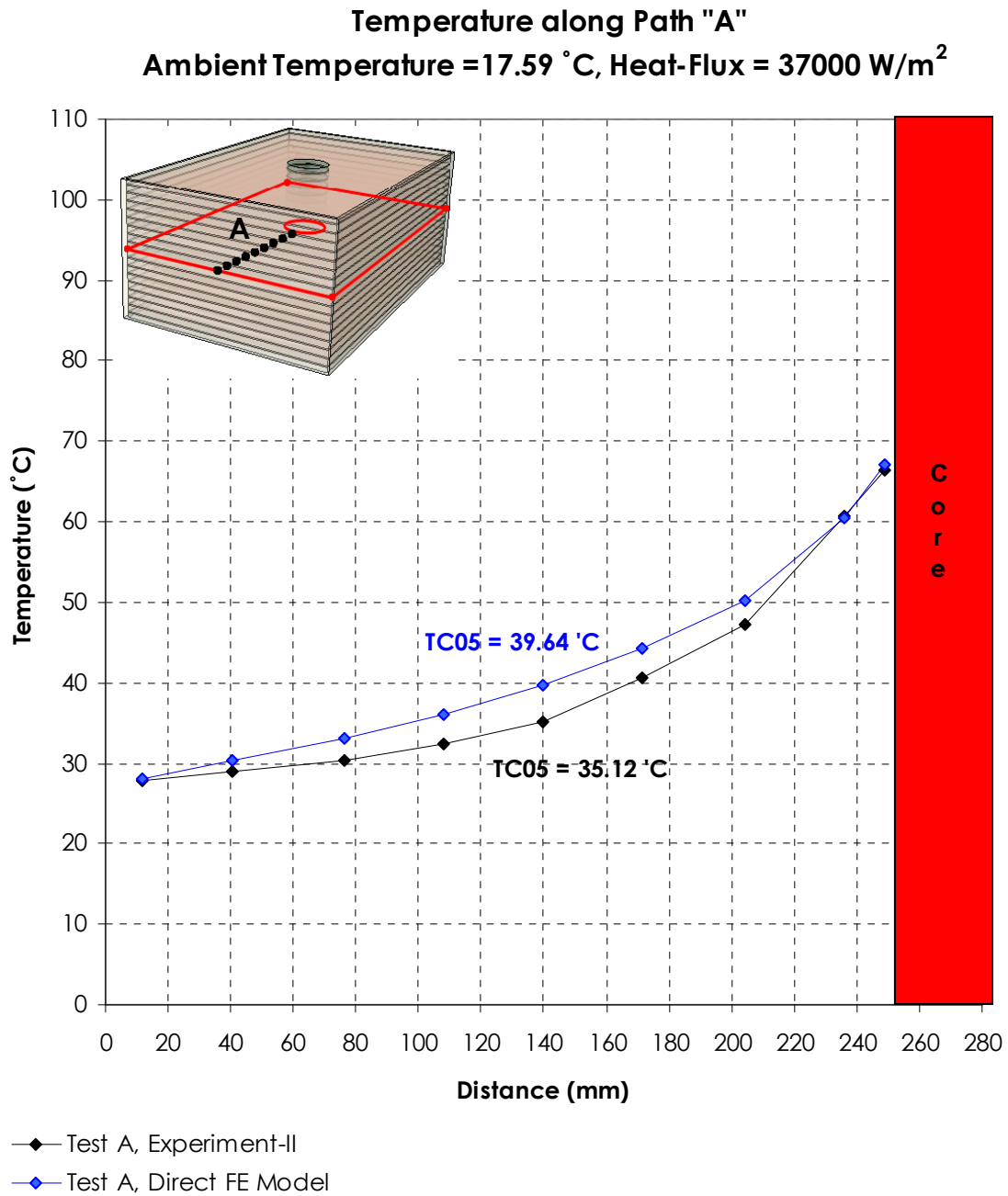
Appendix F, Figure 5: Variation of temperature at each thermocouple with respect to input heat-flux at ambient temperature of 22.92 °C



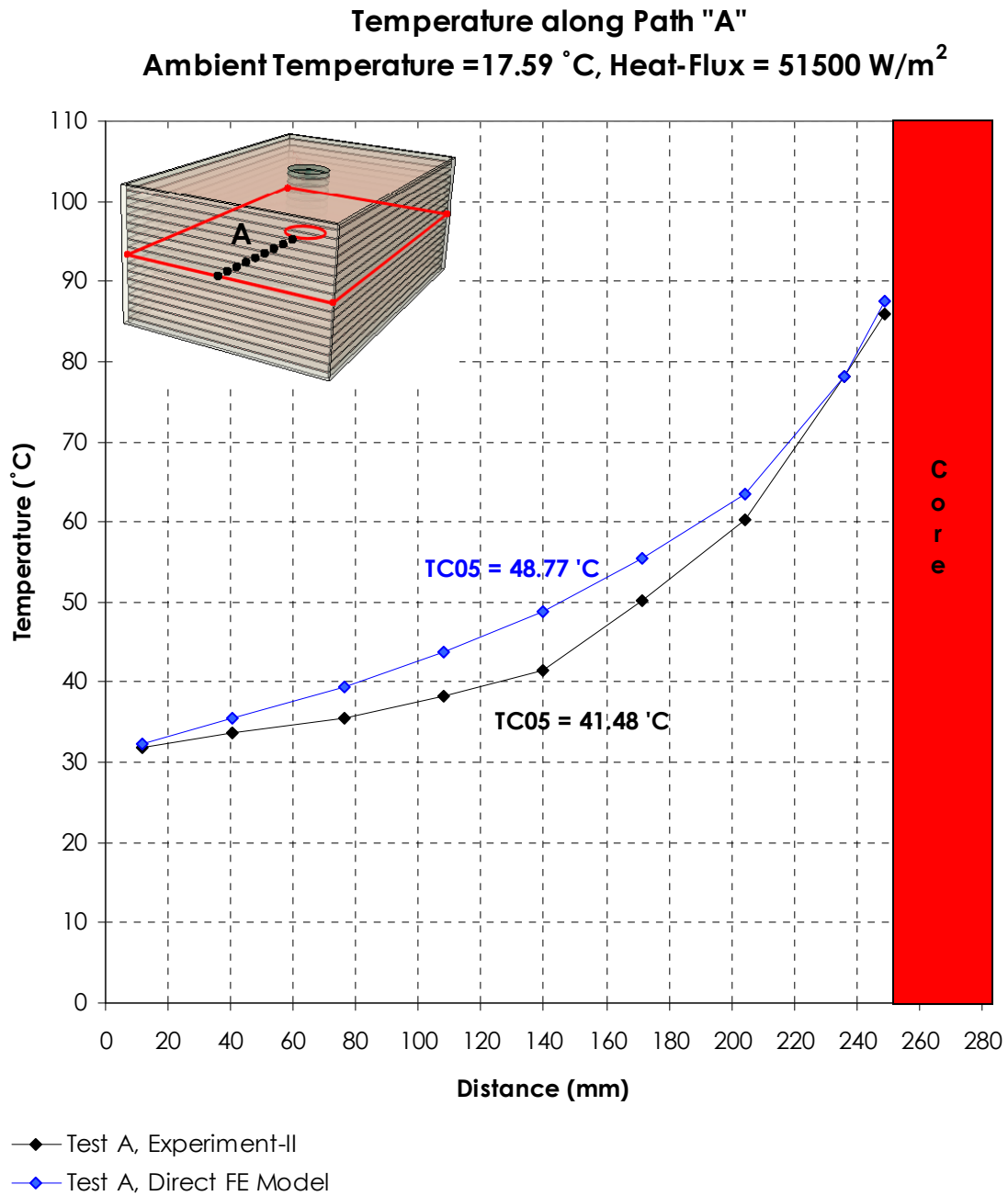
Appendix G, Figure 1: Temperature profile along path "A", obtained from the direct F.E. model and Experiment-2. Heat-Flux = 16300 W/m², Ambient temperature = 17.59 °C. The difference at highest was ~8%



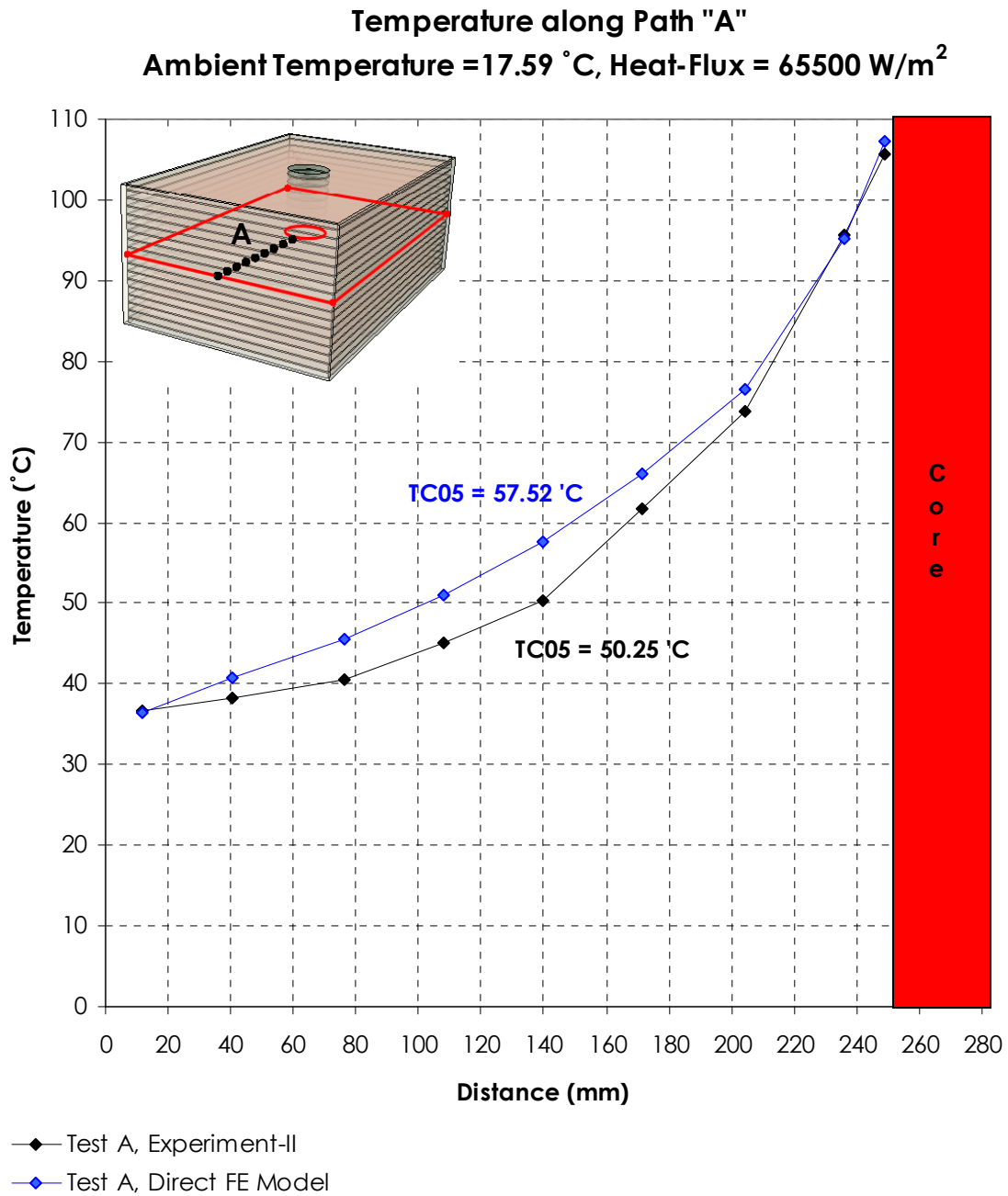
Appendix G, Figure 2: Temperature profile along path "A", obtained from the direct F.E. model and Experiment-2. Heat-Flux = 25000 W/m², Ambient temperature = 17.59 °C. The difference at highest was ~7%



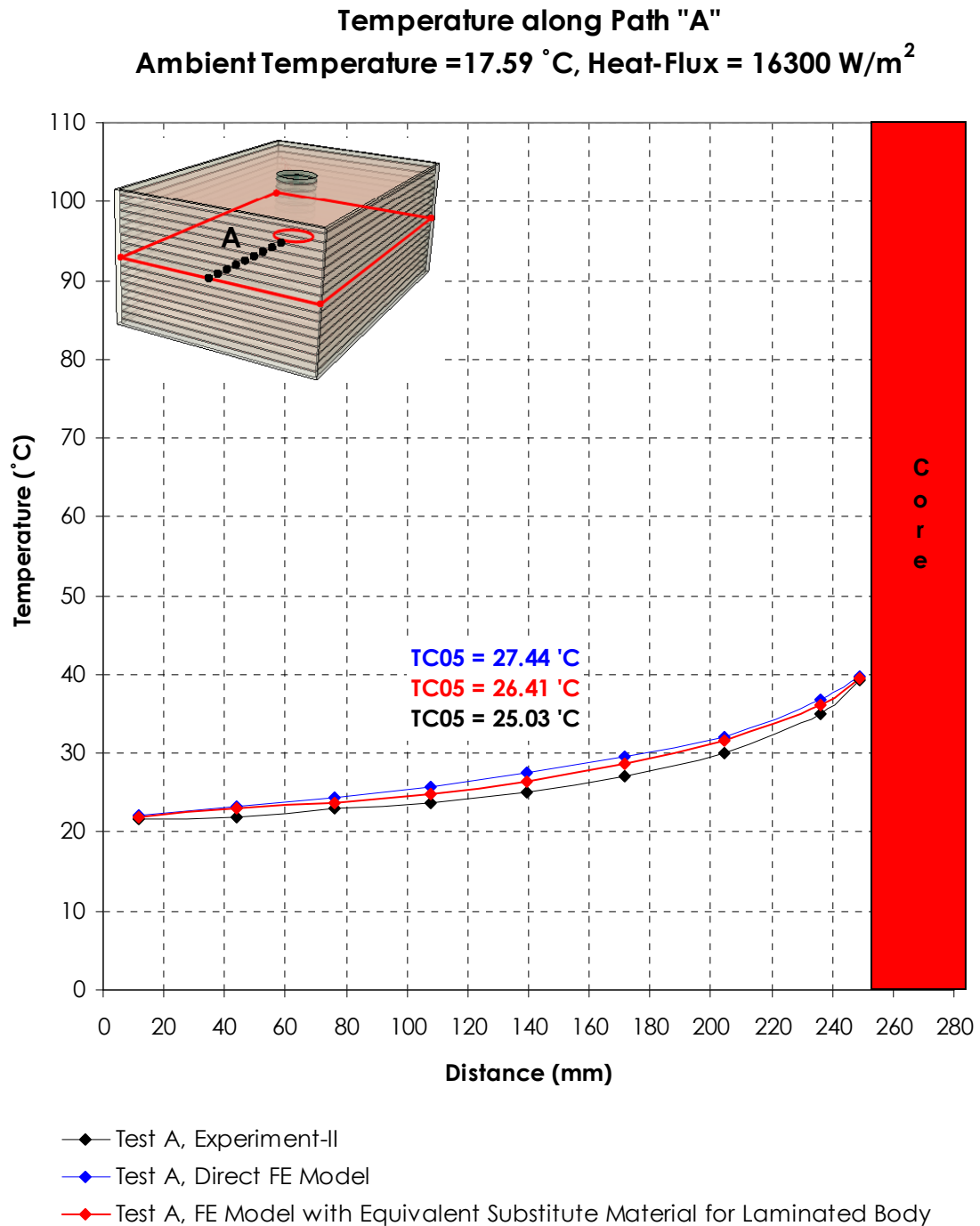
Appendix G, Figure 3: Temperature profile along path "A", obtained from the direct F.E. model and Experiment-2. Heat-Flux = 37000 W/m², Ambient temperature = 17.59 °C. The difference at highest was ~7%



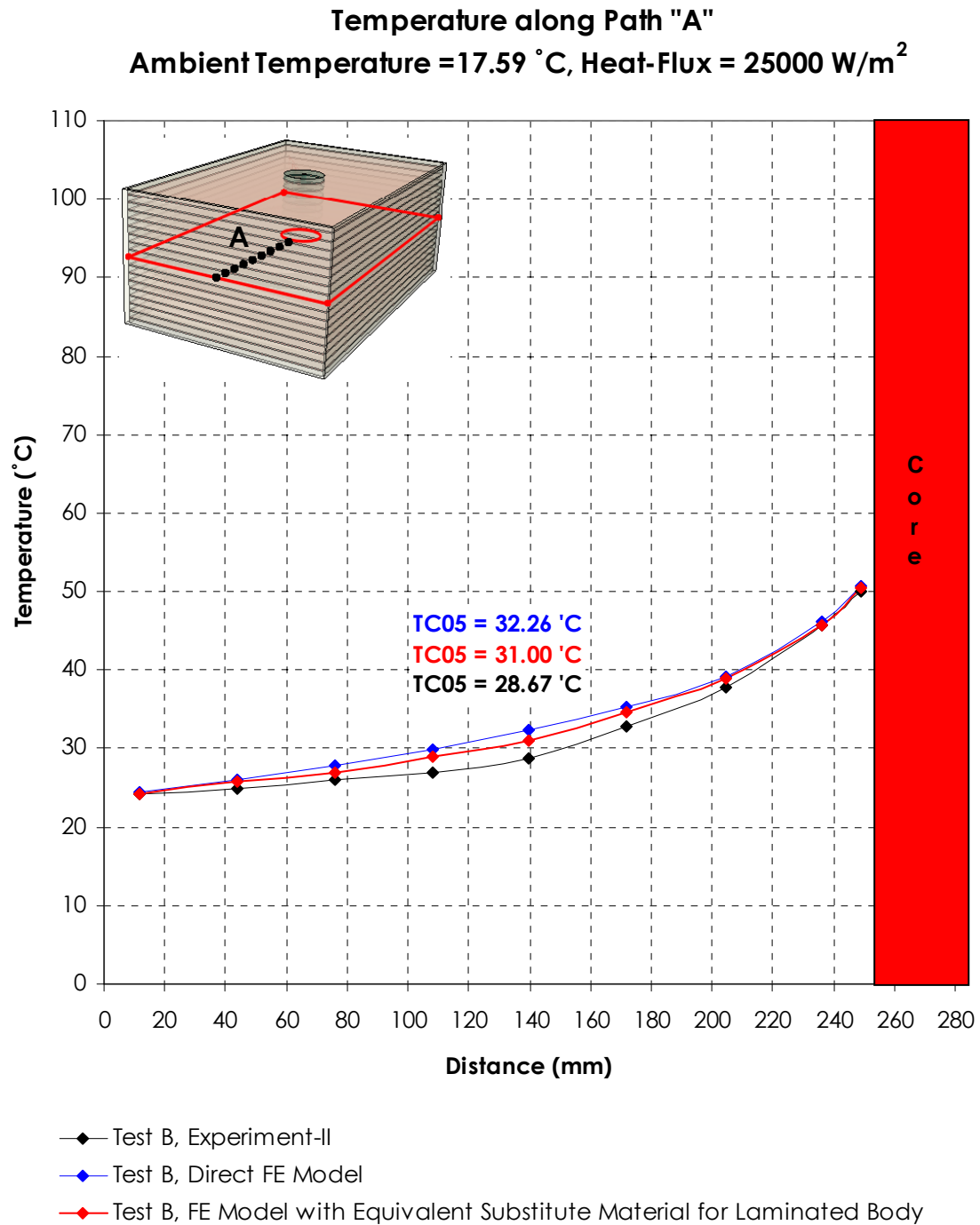
Appendix G, Figure 4: Temperature profile along path "A", obtained from the direct F.E. model and Experiment-2. Heat-Flux = 51500 W/m², Ambient temperature = 17.59 °C. The difference at highest was ~13%



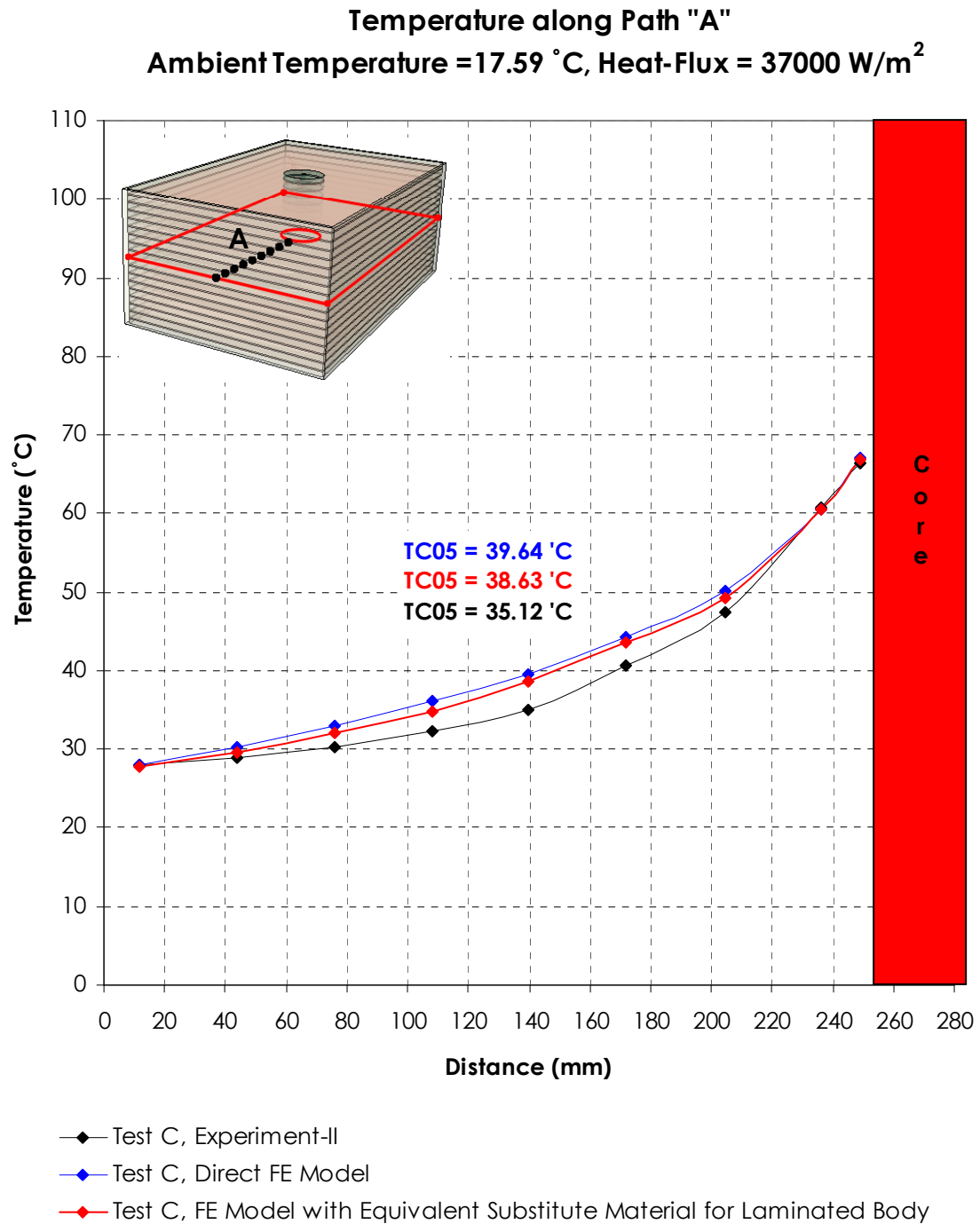
Appendix G, Figure 5: Temperature profile along path "A", obtained from the direct F.E. model and Experiment-2. Heat-Flux = 65500 W/m², Ambient temperature = 17.59 °C. The difference at highest was ~10%



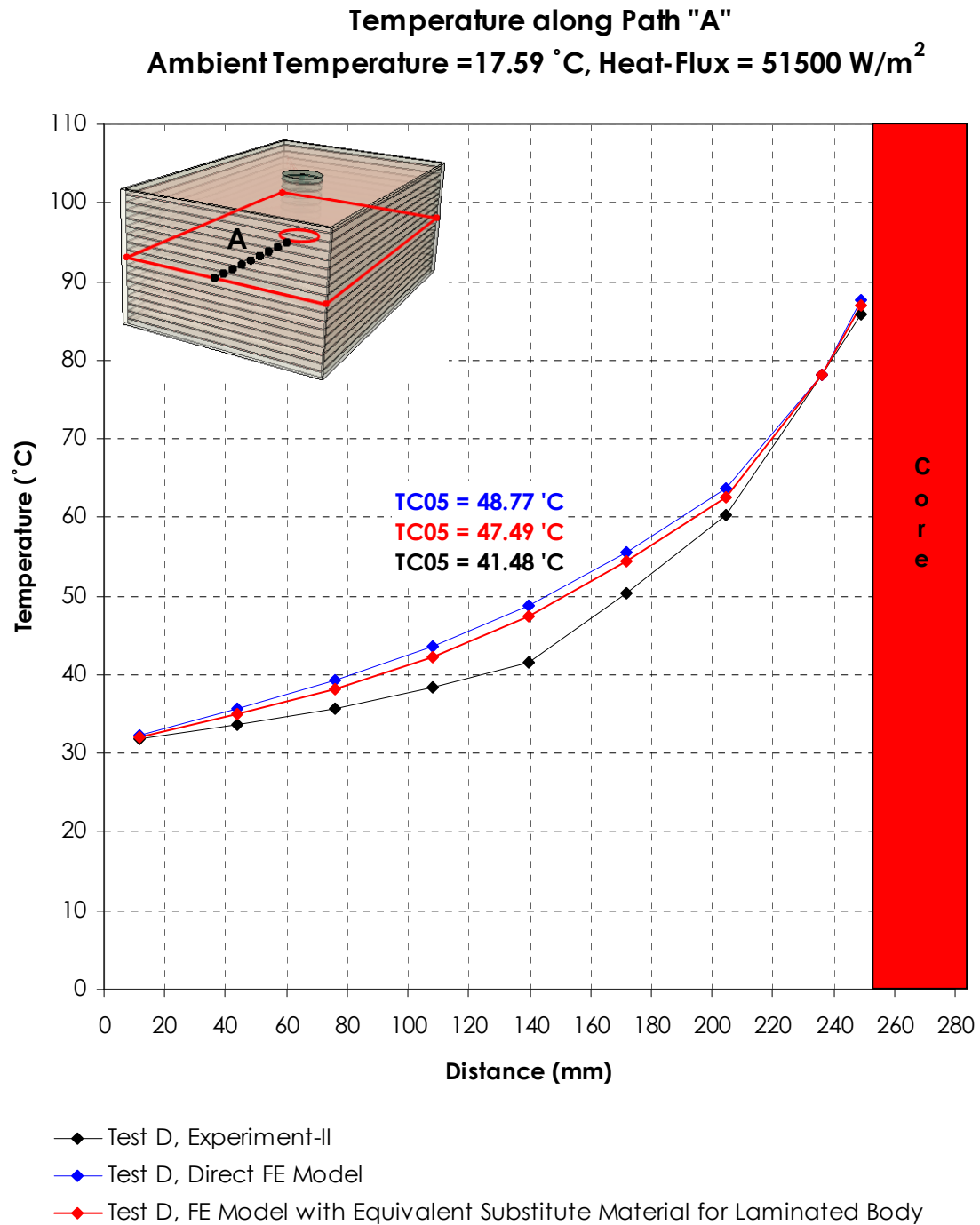
Appendix H, Figure 1: Temperature profile along path "A" for the direct and indirect F.E.M. together with the results of Experiment-2, superimposed on a single coordinate system, at 16300 W/m²



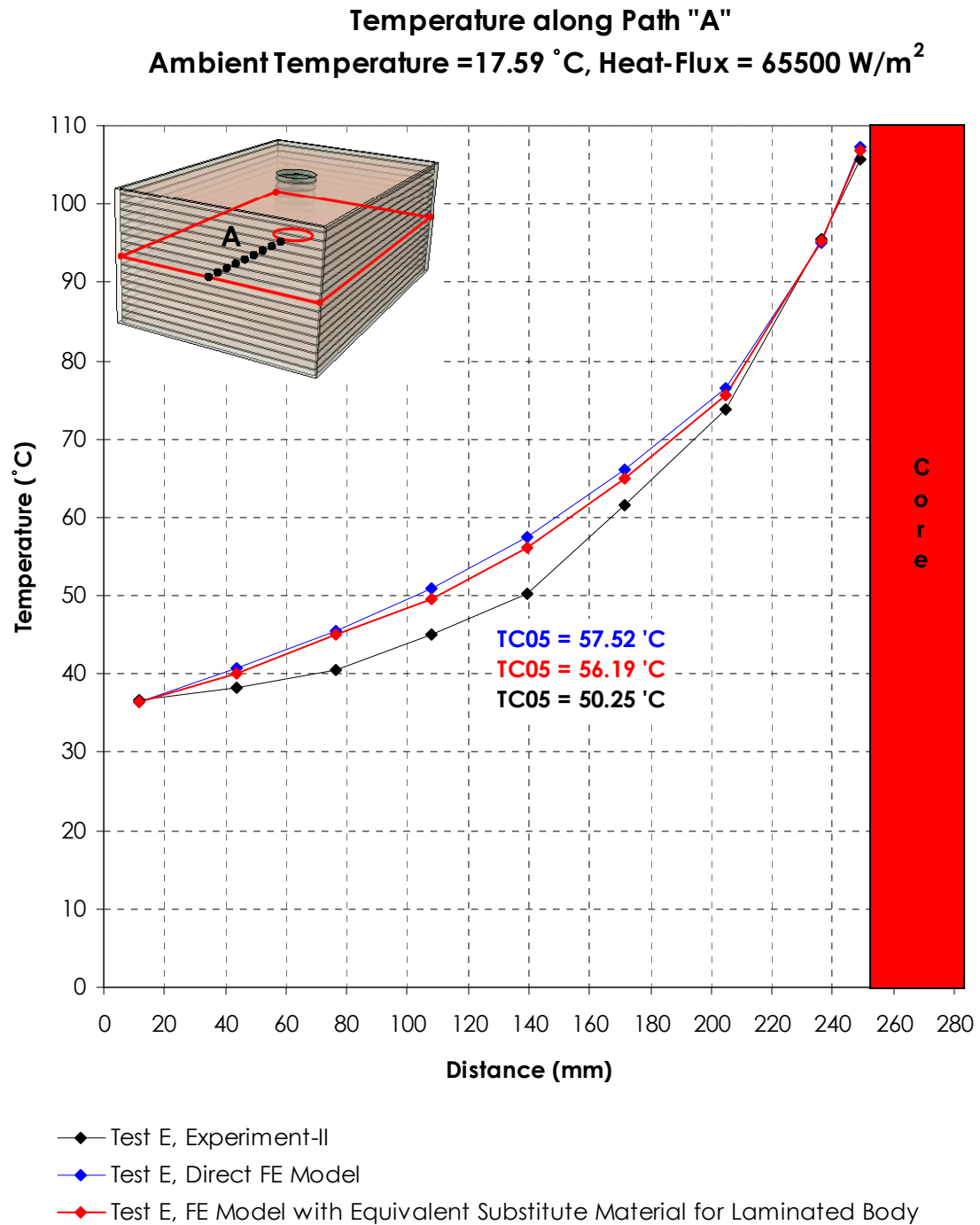
Appendix H, Figure 2: Temperature profile along path "A" for the direct and indirect F.E.M. together with the results of Experiment-2, superimposed on a single coordinate system, at 25000 W/m²



Appendix H, Figure 3: Temperature profile along path "A" for the direct and indirect F.E.M. together with the results of Experiment-2, superimposed on a single coordinate system, at 37000 W/m²



Appendix H, Figure 4: Temperature profile along path "A" for the direct and indirect F.E.M. together with the results of Experiment-2, superimposed on a single coordinate system, at 51500 W/m²



Appendix H, Figure 5: Temperature profile along path "A" for the direct and indirect F.E.M. together with the results of Experiment-2, superimposed on a single coordinate system, at 65500 W/m²

References

- [1] Yoshito Itoh, Haosheng Gu, Kazuya Satuh, Yoshihisa Yamato, "Long-Term Deterioration of High Damping Rubber Bridge Bearing", *Structural Eng./Earthquake Eng.*, JSCE, Vol. 23, No. 2, pp. 215-227, 2006.
- [2] William T. Thomson, Marie Dillon Dahleh, "Theory of Vibration with Application", 5th Ed, Prentice Hall, 1998.
- [3] Hsoun-Wei Chou, Jong-Shin Huang, "Effect of Cyclic Compression and Thermal Aging on Dynamic Properties of Neoprene Rubber Bearings", *Journal of Applied Polymer Science*, Vol. 7, pp. 1635-1641, 2008.
- [4] Charles W. Reoder, John F. Stanton, "Low Temperature Performance of Elastomeric Bearings", *Journal of Cold Region Engineering*, Vol. 4, No. 3, September, 1990.
- [5] Charles W. Reoder, John F. Stanton, "Performance of Elastic Bearings", *National Cooperative Highway Research Program Report 298*, October 1987.
- [6] "Rubber Deterioration in an Air Oven", ASTM, D573, 2007.
- [7] "Elastomeric Bridge Bearing Recommended Test Methods", *National Cooperative Highway Research Program Report 449*, National Academy Press, Washington, D.C., 2001.
- [8] G.J. Lake, "Fatigue and Fracture of Elastomers", *Rubber Chemistry and Technology*, Vol. 68, pp. 435-460, 1995.
- [9] R.P. Brown, T. Butler, "Natural Ageing of Rubber—Changes in Physical Properties over 40 Years", *Rapra Technology Limited*, 2000.
- [10] Yoshito Itoh, Haosheng Gu, Kazuya Satuh, Yokihiro Kutsuna, "Experimental Investigation on Aging Behaviors of Rubbers Used for Bridge Bearings", *Structural Eng./Earthquake Eng.*, JSCE, Vol. 23, No. 1, pp. 17-31, 2006.
- [11] Ryan J. Harbour, Ali Fatemi, Will V. Mars, "Fatigue Life Analysis and Predictions for NR and SBR Under Variable Amplitude and Multi-Axial

Loading Conditions", *International Journal of Fatigue*, pp. 1231–1247, 2008.

[12] Chang-Su Woo, Wan-Doo Kim, "Fatigue Life Prediction of Heat-Aging Vulcanized Natural Rubber", *Key Engineering Materials Vols. 321-323*, pp. 518-521, 2006.

[13] K.N.G. Fuller, J. Gough, T.J. Pond and H.R. Ahmadi, "High Damping Natural Rubber Seismic Isolators", *Journal of Structural Cokirrol*, Vol. 4, No. 2, 1997.

[14] Andrew Ciesielski, "An Introduction to Rubber Technology", Rapra Technology Limited, 1999.

[15] L. R. Treolar, "The Physics of Rubber Elasticity", 3rd Edition, Ciarendon Press, Oxford, UK, 1975.

[16] Ahmadi, H. R. and Muhr, A. H. "Modeling Dynamic Properties of Filled Rubber", *Plastics, Rubber and Composites Processing and Applications*, Vol. 26, No.10, pp. 451–461, 1997.

[17] James M. Kelly, "Earthquake Resistant Design with Rubber", 2nd Ed., Spring Verlag, London, 1996.

[18] M. Arroyo, M. A. Lopez-Manchado, B. Herrero, "Organo-montmorillonite as Substitute of Carbon Black in Natural Rubber Compounds", *Polymer*, Vol. 44, No. 8, pp. 2447-2453, April 2003.

[19] D. Schwarz, D. Askea, B.Lambillotte, "Laboratory Simulated Aging and the Effect on the Oxygen Content in Rubber", *Rubber World*, pp. 26-47, 2004.

[20] Junji Yoshida, Masato Abe, and Yozo Fujino, "Constitutive Model of High-Damping Rubber Materials", *Journal of Mechanical Engineering*, Vol. 130, 2004.

[21] M. Sitti and R S Fearing, "Synthetic Gecko Foot-Hair Micro/Nano-Structures as Dry Adhesives for Future Wall-Climbing Robots", *Journal of Adhesion Science and Technology*, 2003.

[22] Soong T.T. Soong, G.F. Dargush, *Passive Energy Dissipation Systems in Structural Engineering*, Wiley, New York, 1997.

- [23] L.R. Barker, "Accelerated and Long-Term Aging of Rubber Vulcanizates", NR Technology, Vol. 19, No. 2, pp. 28, 1988.
- [24] J.E. Long, "Bearings in Structural Engineering", Wiley, New York, 1997.
- [25] G. Benzoni, C. Casarotti, "The Effect of Vertical Load, Strain Rate and Cycling on the Response of Lead", Journal of Earthquake Engineering, 2006.
- [26] Frank P. Incropera, David P. Dewitt, "Fundamentals of Heat and Mass Transfer", 4th ed, John Wiley and Sons Inc, 1996.
- [27] R. Ding and A. Leonov, "A Kinetic Model for Sulfur Accelerated Vulcanization of a Natural Rubber Compound Polymer" Engineering Department, The University of Akron, Akron, Ohio 44325.
- [28] Feng Demin, Miyama Takafumi¹, Masuda Keiji, "A Detailed Experimental Study on Chinese Lead Rubber Bearings", 1998.
- [29] M.D Monti et al, "High Strain Shear of Lead", "Modeling the Mechanical Response of Structural Materials", pp. 63-69, 1998.
- [30] S. Kustov, S. Golyandin, K. Sapozhnikov, W.H. Robinson "Amplitude-Dependent Internal Friction, Microplastic Strain and Recovery of Lead at Ambient Temperature", 1997.
- [31] Proceeding 11th World Conference on Seismic Isolation, Energy Dissipation and Active Vibration Control of Structures, China, Nov. 17, 2009.
- [32] Ioannis V. Kalapatidis, Michael C. Constantinou, "Effects of Heating and Loading History on the Behavior of Lead Rubber Bearing, Technical Report MCEER-8-0027, 2008